Engineered Electromagnetic Hot-spots for Highly Sensitive (Bio)molecular Detection by Plasmonic Specytroscopies

Rishabh Rastogi

Thèse
de doctorat
de l'UTT

Rishabh RASTOGI

Engineered Electromagnetic Hot-spots for Highly Sensitive (Bio)molecular Detection by Plasmonic Spectrocopies

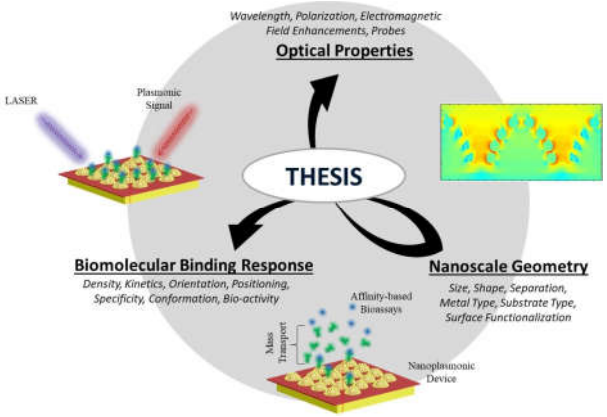

Champ disciplinaire :
Sciences pour l'Ingénieur

2020TROY0018 **Année 2020**

utt
UNIVERSITÉ DE TECHNOLOGIE
TROYES

THESE

pour l'obtention du grade de

DOCTEUR
de l'UNIVERSITE DE TECHNOLOGIE DE TROYES

EN SCIENCES POUR L'INGENIEUR

Spécialité : MATERIAUX, MECANIQUE, OPTIQUE, NANOTECHNOLOGIE

présentée et soutenue par

Rishabh RASTOGI

le 6 novembre 2020

Engineered Electromagnetic Hot-spots for Highly Sensitive (Bio)molecular Detection by Plasmonic Specytroscopies

JURY

Mme Claire MANGENEY	PROFESSEURE DES UNIVERSITES	Présidente
M. Nordin FELIDJ	PROFESSEUR DES UNIVERSITES	Rapporteur
M. Éric FINOT	PROFESSEUR DES UNIVERSITES	Rapporteur
Mme Ana Paula PEGO	PROFESSOR ASSOCIADO	Examinatrice
M. Pierre-Michel ADAM	PROFESSEUR DES UNIVERSITES	Directeur de thèse
M. Sivashankar KRISHNAMOORTHY	Ph.D. - GROUP LEADER LIST	Directeur de thèse

Left Blank Intentionally!

The dissertation has been approved by

Supervisors:

Prof. Pierre Michel-Adam

Dr. Sivashankar Krishnamoorthy

The research in this thesis was carried out at the Luxembourg Institute of Science and Technology (LIST), Luxembourg, and the University of Technology of Troyes, France. This project work was part of the project PLASENS financially supported by the Luxembourg National Research Fund (FNR) under the FNR-CORE program, fellowship number C15/MS/10459961.

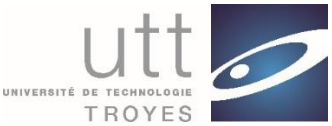

Defense jury

Mme. MANGENEY Claire	Professor de Universitès	Examiner
Mme. PEGO Ana Paula	Professor de Universitès	Examiner
M. FELIDJ Nordin	Professor de Universitès	Rapportuer
M. FINOT Eric	Professor de Universitès	Rapportuer
M. ADAM Pierre-Michel	Professor de Universitès	Directeur de thèse
M. KRISHNAMOORTHY Sivashanakar	Ph.D., Group Leader	Directeur de thèse

Left Blank Intentionally!

"If I say I have the belief that I can do it,
I can surely acquire the capacity to do it,
even if I may not have it at the beginning."

— Mohandas Karamchand Gandhi
(Mahatma Gandhi)

Left Blank Intentionally!

Acknowledgements

First, I would like to thank the National Research Fund of Luxembourg (FNR) for funding the project PLASENS under the core-FNR program, fellowship number C15/MS/10459961 and keeping us (the PhD. candidates) motivated with various campaigns and events. I would like to thank external projects MASSENA and VIRANOSTIC and INTERREG Grand Region V project IMPROVE-STEM that were part of some collaborations involved during this work. I would like to thank EU COST Action BIONECA for providing me with the travel grants to attend ICES, 2019 in Canada.

I would like to express my sincere gratitude to my supervisor at Luxembourg Institute of Science and Technology (LIST), *Dr. Sivashankar Krishnamoorthy*, for choosing me for this position and walking me from the start to the end of this journey. His dynamism, vision, sincerity, and motivation never stopped inspiring me and I am grateful for all the discussions and travels we did together. (I admire you for all that you brought into my life, for the opportunities to travel, to present and to challenge myself, and for continuously inspiring me to step out of my comfort zone.)

I am also very grateful to my supervisor at the University of Technology of Troyes (UTT), *Prof. Pierre-Michel Adam* for his efforts to welcome and integrate me with the team at UTT and contributing to the research with his constructive comments, and suggestions. He always left me with questions that I should be asking myself. It was always fun with him exploring different cuisines, drinks, and places while discussing science.

I am thankful to the *collaborating* teams from Australia (*H. Arianfard, Prof. S. Juodikazis,* and *Prof. D. Moss*) and France (*E. Dogbe-Foli* and *Prof. R. Vincent*) for their inputs and discussions related to numerical simulations and from Belgium (*Dr. S. Poovathingal* and *Prof. C. Dupont-Gillain*) for their inputs and discussion related to Biological aspects of the project. The work in this thesis would not have been of the same quality without your help and support.

I would like to thank the Director of the Material Research Technology (MRT) department *Dr. Damien Lenoble* and all researchers and staff who supported me directly or indirectly during the project. A big thanks to each and every member of the Nano-Enabled

Medicine and Cosmetics (NEMC) group at LIST for sharing their work during group meetings and engaging discussions.

I would like to thank my colleague (and friend!) *Matteo Beggiato* for his inputs and collaboration related to geometric modeling for biomolecular absorption and for all the discussions related to science and life in general!.

I would also like to acknowledge all the Ph.D. candidates with whom I shared the office and for making F1.14 the best office of the department and a great environment to work in. Thanks also to my earlier colleagues - *Serena*, *Divya*, and *Nohora, and especially the new ones Sabrina*, *Raoul*, *Joao (for awkward questions)*, *Shiv (for being weird)*, *Tai (for late evenings in the office)*, *Nikhar*, *and Rutuja.*

Finally I thank my family for staying by my side, keeping faith in my decisions for so many years, while I was busy chasing my dreams. I could not have done without their their love and support. I would like to give special thanks to my wife *Nitika*, for making my life easier even while she was away and busy with her own doctorate in another country and for her continuous support and motivation from the start till the end of my PhD.

I am grateful for so many people for having been part of this challenging yet beautiful journey, for helping me accomplish my goals and having faith me. At last, I would like to thank myself, for bringing in my strength, discipline, and determination. I would like to acknowledge myself for never giving-up through the difficult times and the can-do attitude that never let me lose and achieve what I was called for. I have given my best throughout.

Abstract

Detection of molecular biomarkers at ultra-low concentrations (~nM or lower) within miniaturized footprints and quick response times is critical to meet emerging demands in healthcare diagnostics. State of the art technologies suffer from the trade-off between sensitivity with response times, with a gap capabilities in delivering for nano to picomolar sensitivity with response time of few minutes. Surface-enhanced spectroscopies (SES) have the unique potential to address this gap. SES relies on ligh-matter interactions taking place at nanostructured plasmonic interfaces resulting in enhancement of electromagnetic (EM) fields at the vicinity of the metal surface. Such EM enhancements are heterogeneously distributed resulting in 'hot-spots' at sharp corners or junctions between adjacent nanostructures. Non-linear enhancements of the EM fields as function of closing separation at junctions or gaps are capable of enabling detection of trace quantities of analytes from their Raman or Fluorescence signals.

EM fields at nanoscale gaps between noble metal nanostructures are known to present high-intensity enhancements that increase non-linearly with decreasing gap distances. These enhanced intensities maximize at gap distances of only a few nanometers, which, however imposes significant spatial constraints for the analyte to enter and leverage these EM hot-spots. This presents a trade-off between closing separations needed for high spectroscopic enhancements, and spatial needs for biomolecular adsorption, thus leading to the inability of biomolecular analytes to access highly enhancing EM hot-spots.

The investigations in this thesis are aimed at the rational design of plasmonic nanoarrays that present a high density of EM hot-spots and engineering their structure and functionality to improve the sensitivity of biomolecular detection using surface-enhanced spectroscopies. This thesis identifies configurations that enhance leverage over electromagnetic (EM) hot-spots driving sensitivity down to picomolar concentrations. The investigations presented in this demonstrates robust correlations between the geometry ⇔ optical/spectroscopic properties ⇔ sensitivity in molecular assays with experiments supported with numerical simulations. The findings open new opportunities to the rational design of plasmonic sensors by factoring in the dimensions of analyte molecules into the geometry of nanoplasmonic assemblies.

Left Blank Intentionally!

List of Abbreviations

AFM	Atomic Force Microscopy
BCP	Block Copolymer
BPT	Biotin-PEG-thiol
BSA	Bovine Serum Albumin
Cy5	Cyanine-5
EM	Electromagnetic
EMF	Electromagnetic Fields
LSPR	Localised Surface Plasmon Resonance
MEF	Metal-Enhanced Fluorescence
NCA	Nanocluster Arrays
NP	Nanoparticle
NPA	Nanopillar Arrays
NT	Naphthalene Thiol
PS - P2VP	Polystyrene-block-poly(2-vinylpyridine)
PDI	Polydispersity Index
PDMS	Polydimethylsiloxane
PS	Polystyrene
QCM	Quartz Crystal Microbalance
RIE	Reactive Ion Etching
SA	Streptavidin
SEF	Surface-enhanced Fluorescence
SEM	Scanning Electron Microscopy
SERS	Surface-Enhanced Raman Spectroscopy
SES	Surface-enhanced Spectroscopy
SPR	Surface Plasmon Resonance
UV	Ultraviolet

Left Blank Intentionally!

General Introduction

This thesis entitled **"Engineered Electromagnetic Hot-Spots For Highly Sensitive (Bio)molecular Detection by Plasmonic Spectrocopies"** is an outcome of the project PLASENS (C15/MS/10459961) funded by Luxembourg National Research Fund (FNR) as part of FNR-CORE program and carried out within Nano-Enabled Medicine and Cosmetics Group at Luxembourg Institute of Science and Technology (LIST), Luxembourg.

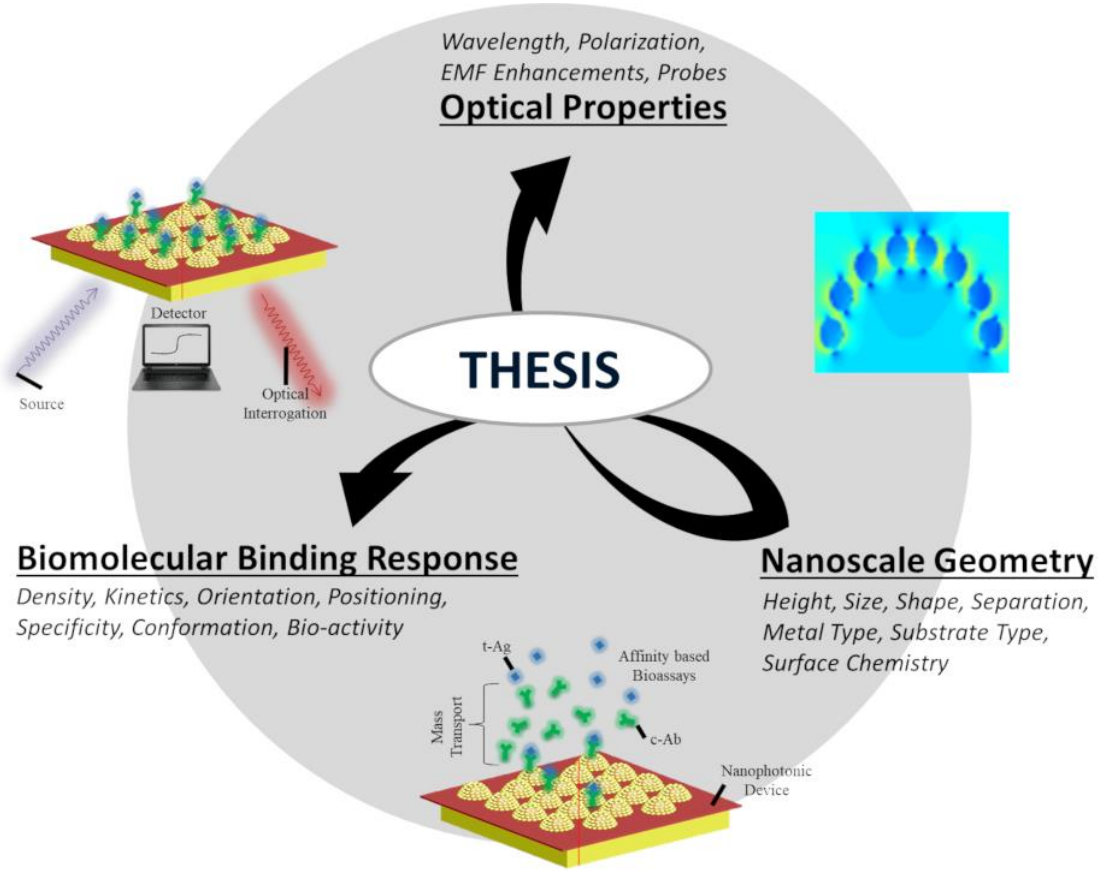

Figure 1. Schematic representing trade-off in developing biosensor based on nanoplasmonically enhanced spectropscopies.

Nanoplasmonic sensing relies on significantly enhanced electromagnetic fields at the vicinity of a nanostructured metal surface to detect molecules at ultra-low concentrations. The EM enhancements are strongly pronounced at junctions between adjacent nanostructures resulting in gap hot-spots. EM enhancements at these hot-spots increase non-linearly as a function of gap distance down to the sub-10 regime. Analyte molecules

present at these gaps can leverage these EM enhancements, resulting in ultra-high sensitivity in detection by surface-enhanced Raman or Fluorescence spectroscopies. However, such confining gaps affect the ability of large analytes such as biomolecules to enter and thereby leverage EM fields within the gaps. This presents spatial needs to enhance EM fields at odds with those for accommodating biomolecular interactions. This thesis demonstrates the rational design of array configurations that allows the EM hotspots to be better leveraged by the reporter of a biomolecular binding event. The thesis uses molecular self-assembly based approach to prepare well-defined and reproducible plasmonic nanoarrays on macroscopic areas. Multiple parameters are considered including the dimension, shape, and density of hotspots, surface functionalization, and the choice of substrates, to demonstrate quantitative detection of proteins and smaller organic molecules down to picomolar concentrations.

Thesis Outline

Chapter 1 reviews state of the art and presents the motivation behind the highly sensitive detection of molecular biomarkers and its significance in addressing emerging demands in healthcare diagnostics. The chapter reviews the gap in the state-of-the-art technologies reviews potential of nanoplasmonic sensors in addressing the gap. State of the art in nanoplasmonic sensors based on surface-enhanced spectroscopies is considered with specific attention to surface-enhanced Raman and surface-enhanced Fluorescence Spectroscopies. The role of electromagnetic (EM) enhancements close to the surface, and the specific role of electromagnetic hot-spots towards the sensitivity in molecular detection is discussed. Metal nanostructure geometries that deliver highly enhancing EM hot-spots and the means to produce them are reviewed. The challenges in state of the art technologies towards delivering highly enhancing EM hot-spots, with spatial resolutions down to the sub-10nm, along with high quality and throughput is highlighted. The strategies adopted in literature to leverage the EM hot-spots by molecular co-localization at the hot-spots is reviewed, while highlighting the challenges in adopting them in the context of biomolecular detection. Additional factors of importance to consider in affinity biosensing, which would also be applicable for nanoplasmonic biosensing platforms, are presented and reviewed.

Chapter 2 gives an overview of the fundamentals of the nanofabrication of plasmonic nanoarrays with engineered EM hot-spots, and experimental techniques related

to the investigation of optical, spectroscopic, and analytical performance, reflecting the basis of approaches employed throughout this thesis. The chapter discusses in detail the process ⇔ structure correlations and fabrication features offered by self-assembled block copolymer template with spatial control of resulting geometries down to the molecular level. The basis, significance and the challenge in different techniques used to characterize the nanoplasmonic substrate geometries, optical/spectroscopic response, and bio-nano interactions are presented.

Chapter 3 present nanoparticle cluster arrays with unique hybrid geometries that present dual-length scale EM hot-spots, viz. inter-particle hot-spots with typical dimensions <1 nm, and inter-cluster hot-spots dimensions in the sub-10nm regime. The contribution of inter-particle hot-spots and inter-cluster hot-spots in detection sensitivities based on the size of the analyte molecules is studied on glass substrates. SERS and MEF assays, along with numerical simulations of EM field profiles show the biomolecular interactions to benefit from inter-cluster EM hot-spots, and to be detected with higher sensitivity by use of configuration that maximizes the density of inter-cluster hot-spots.

Chapter 4 investigates nanoparticle cluster arrays fabricated on gold substrate the impact of substituting the glass substrate with gold on the resulting sensitivity towards detection of small and large molecular analytes. The strong increase in sensitivity of the nanoparticle cluster arrays on gold, and the ability to differentially enhance the EM field at the inter-cluster hot-spots for larger clusters is demonstrated with experiments in combination with FDTD simulations. The NCAs on gold substrate is shown to increase sensitivity in relation to glass. The higher and better sensitivity in detection of small and larger analytes were achieved by leveraging the NCA geometry that presented greater inter-cluster EM enhancements.

Chapter 5 demonstrate NCA fabricated on QCM sensors to correlate MEF signal intensities with surface density of bioanalyte. This enables geometric modelling of biomolecular adsorption on the NCA to attain clarity of the precise distribution of analyte with respect to the inter-particle and inter-cluster EM hot-spots. The measurements further show the significant gain from the use of MEF with respect to the equivalent sensitivities as obtained with QCM, but, with footprints that are 8 orders of magnitude smaller. The approach is shown to pave way to rational design of plasmonic interfaces with an informed

understanding of the relative role of EM enhancement at EM hot-spots versus molecular distributions with respect to the EM hot-spots.

Chapter 6 investigates gold nanopillar arrays with inter-pillar EM hot-spots systematically controlled down to sub-10nm lengthscales. The strong impact of the sensitivity of the pillar arrays towards detection of molecular analytes smaller and larger than the hot-spot dimensions is shown. Numerical simulations together with spectroscopic assays show picomolar sensitivity in detection of biomolecular analytes in SERS and MEF assays. Switching from SERS to MEF based detection is found to be advantageous, as the lengthscale of biomolecular interaction offers separation of the fluorophore from the metal surface.

Chapter 7 gives the summary and the conclusion of the presented work and future prospects.

Table of Contents

Left Blank Intentionally!

Chapter 1. Introduction

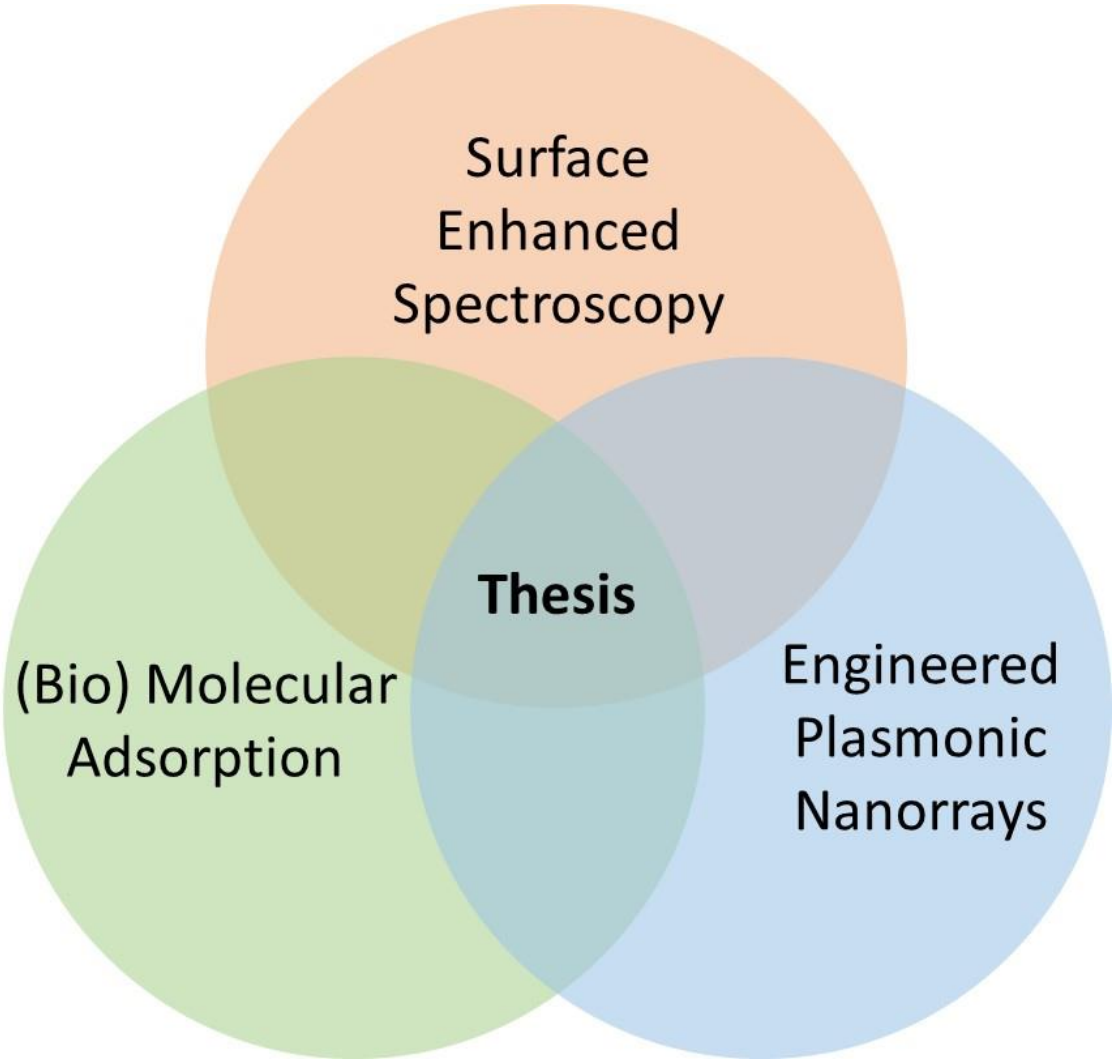

This chapter presents the highly sensitive detection of molecular biomarkers and its significance in addressing emerging demands in healthcare diagnostics and reviews the gap in the state-of-the-art technologies and the solution based on nanoplasmonics. State of the art in nanoplasmonic sensors based on surface-enhanced spectroscopies is considered with specific attention to surface-enhanced Raman and surface-enhanced Fluorescence Spectroscopies. I discuss the role of electromagnetic enhancements close to the surface, and the specific role of electromagnetic hot-spots presenting intense and locally confined electromagnetic fields towards the sensitivity in molecular detection and review the geometries that deliver highly enhancing EM hot-spots and the means to produce them. Furthermore, this chapter analyzes the challenges in literature towards delivering highly enhancing EM hot-spots, with spatial resolutions down to the sub-10nm, and reviews the strategies to leverage the EM hot-spots by molecular colocalization at the hot-spots, highlighting the challenges in adopting them specifically for biomolecular analysis. The additional factors of importance to consider in affinity biosensing, which would also be applicable for nanoplasmonic biosensing platforms, are presented and reviewed.

1.1. Healthcare and Diagnostics

Healthcare and diagnostics encompass a wide variety of efforts made by medical professionals and researchers around the globe to support the healthcare needs of society. Such efforts can underpin the recommended preventive measures to avoid diseases or improve the current state of the art available for controlling disease progression in the living system. These include performing risk stratification,[1] designing and discovering new medicines or vaccines,[2] driving personalized therapies,[3] and predicting diseases.[4] While human diseases could be broadly categorized as hereditary,[5] infectious,[6] or chronic,[7] their pathogenesis remains unique within different patients. Despite exponential advancements in healthcare and diagnostics technologies, thoroughly understanding the behaviors of a disease that are rooted down to the genetic levels of the living system remains a challenge. Illnesses that are avoidable at early stages demand an ultra-sensitive detection tool that can detect the presence of disease markers at such an early stage. Furthermore, it should be able to perform faster with reliable results to expedite prognosis and treatments. This is especially true in low-income countries, where just a few infectious diseases already claim millions of lives every year. Together, these diseases, which could have been prevented or cured, account for 1 in 8 deaths globally.[8] The causation of such diseases can be monitored by the genomic and proteomic analysis in the targeted cells.[9] A pandemic (such as Covid-19), whose growth rate is on an unmatched scale throughout the world, has already exposed the need for sensitive and rapid detection in a cost-effective way. In such cases, large-scale testing is required to match the rising speed of the pandemic.[10] Hence, the ability for multiplexed sensing can support us in addressing such issues.[11] However, to provide detection technologies in the array configurations, the miniaturization of the sensing platforms would also become necessary, enabling lab-on-a-chip settings.[12] Highly sensitive and miniaturized sensing platforms would also underpin the transformation of treatments from ‘one-size-fits-all’ or ‘trial-and-error’ medicine towards personalized or precision drugs,[3,13] ensuring patient-specific therapy with low failure risks, time and cost. The key to understanding disease functionality lies in the molecular behavior of the biological components (such as cells, proteins, or genes) present inside the human body, which can help report the healthcare status of the patient, e.g., the risk, presence, progression, and prognosis of diseases. The tools and techniques aiming to detect molecular biomarkers to

diagnose the healthcare status of an individual would constitute the domain of Molecular Diagnostics.

1.1.1. Targeting Molecular Biomarkers For Diagnostics

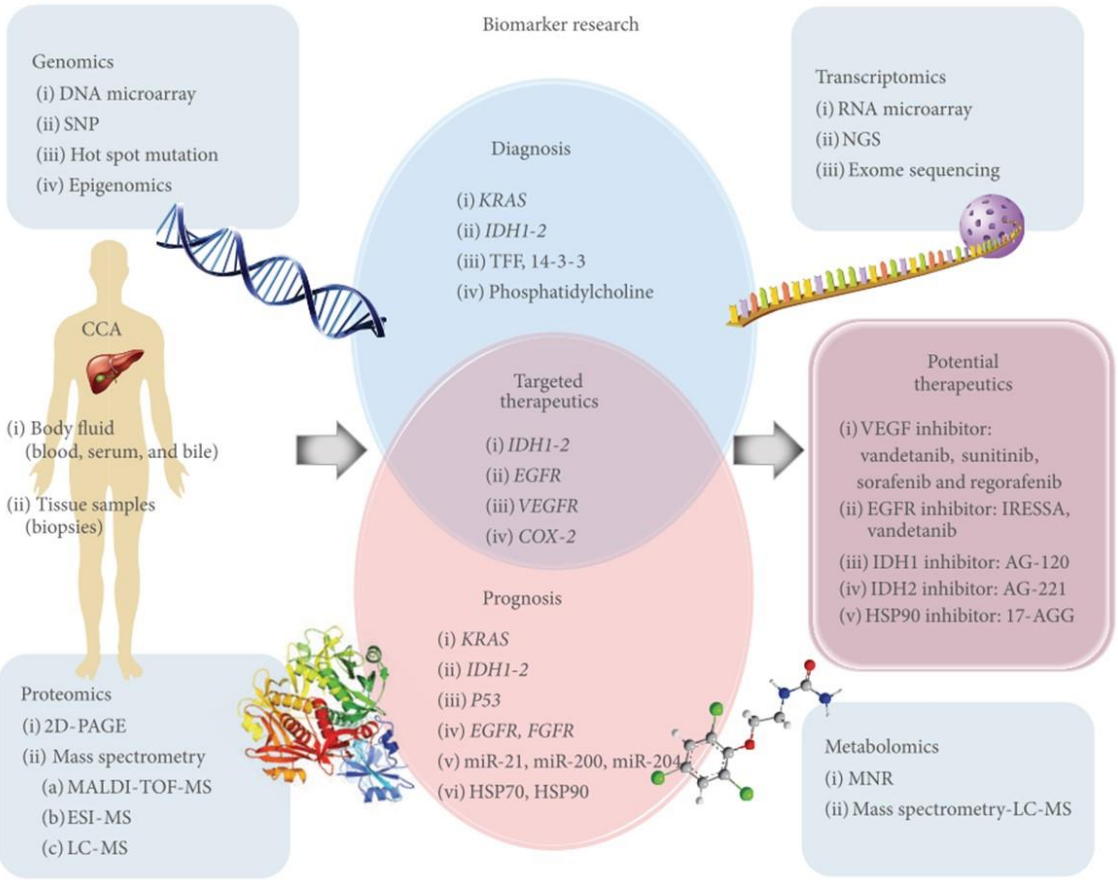

Figure 1.1. Representation of molecular biomarker types and their use in early diagnostics, prognostics, and therapeutics. As an example, the biomarker for Cholangiocarcinoma (CCA) is shown in this figure. [Reprinted with permission from Seeree et al. (2015) Ref.[14]; Copyright © 2015 Hindawi]

Biomarkers refer to the presence or changes to biological or biochemical species that are capable of accurately reporting information related to the health of the patient (**Figure 1.1**).[14] A single droplet of blood contains millions of cells, proteins, and amino acids, which include a plethora of information about the health of the patient and can all be considered biomarkers.[15] For example, glycated hemoglobin (HbA1c) is one of the biomarkers for diabetes found in blood,[16] human chorionic gonadotrophin (hCG) is a biomarker for pregnancy found in urine,[17] and there are many other biomarkers for different types of

cancer, such as PSA, CEA, Bladder Tumor Antigen, etc.,[18] as well as genetic variations known as single polymorphisms (SNPs) biomarkers,[19] which are relevant to genetic disorders, such as Alzheimer's disease.[20] At the onset stage of disease progression, biomarkers present in complex mediums at a concentration *as low as femtomolar* in the case of cancer, pose critical challenges. Therefore, the capability to probe such biomarkers at levels that are clinically-relevant **(Figure 1.2)**,[21] has become a primary focus of bio-sensing technologies.

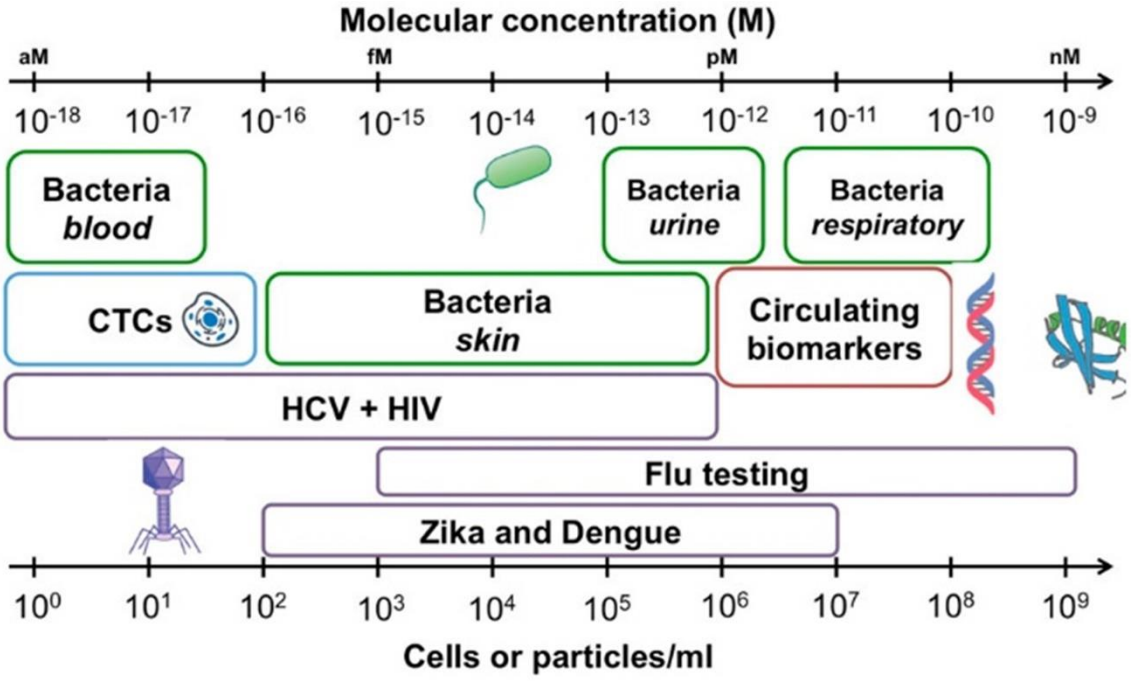

Figure 1.2. Clinically relevant levels of diseases. [Reprinted with permission from Shana O. Kelly. (2017) Ref.[21]; Copyright © 2016 American Chemical Society]

Molecular diagnostics (MDx) deals with the analysis of biological markers in the genome and proteome, that is, the individual genetic code and how the cells express their genes in proteins.[22] Molecular diagnostics have been around for more than four decades,[23] since then, systematic efforts have been made to identify, quantify, and monitor pathogens by applying molecular biology to medical testing. The approach itself manifests the prospect of a personalized treatment approach owing to its miniaturized footprints and multiplexed analysis capabilities. Benefitting from the increasing interest of the researchers and promising outcomes, the molecular diagnostics market is predicted to rise almost $9.9 billion by 2022, having a CAGR of 8.5%. It is important to note that nearly 62% of the

market was already dominated by the diagnosis of infectious diseases before this estimation **(Figure 1.3)**.[24]

Figure 1.3. a) Market Share of different players in in-vitro diagnostics,[25] b) Global MDx Market Size,[24] and c) Global MDx Market.[24]

MDx deals with the specific and robust interaction of biomolecules such as antibody-antigens or a pair of complementary nucleic acid chains.[22] Immunoassay-based techniques such as ELISA (enzyme-linked immunosandwich assays) or PCR (polymerase chain reaction), relying on endpoint detection using fluorescence, are capable of detecting biomarkers that have an in-blood concentration range from the micromolar to picomolar range. However, they are typically carried out in centralized facilities, executing step-wise biochemical processes to achieve quantitative results, resulting in high costs and long durations of time for the analysis. To decrease the cost of healthcare and provide tailored treatments, it is crucial to reduce the reliance on centralized laboratories by making low-cost, efficient, and miniaturized biosensing tools available for deployment at the point of care. Such devices can be made available to "front-line" medical professionals so that they can obtain reliable information quickly enough to make decisions.[26] Examples of such devices include those for self-monitoring blood sugar levels or pregnancy testing kits. A detailed report was published by the World Health Organization (WHO) in 2015, describing the urgent need for such devices for the aging population.[27] Snyderman et al., in their study, summarized the correlation of disease progression with its severity, burden, and the extent of patient suffering, indicating an exponential behavior of progression after infections **(Figure 1.4)**,[28] enforcing the need for early detection. MDx provides opportunities to analyze risks at a healthy stage, in order to detect and prepare personalized treatments at an early stage, when the intervention is most effective in preventing an exponential rise in severity.

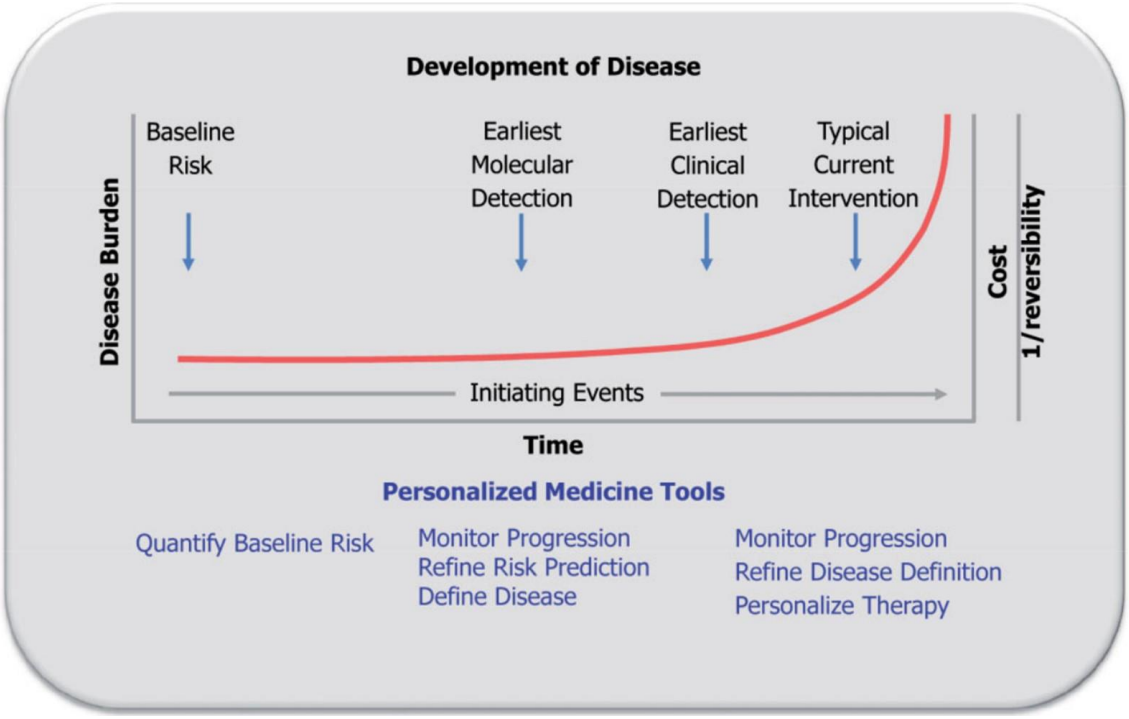

Figure 1.4. Disease progression curve. [Reprinted with permission from Snyderman et al. (2012) Ref.[28]; Copyright © 2012 WILEY-VCH Verlag GmbH & Co. KGaA, Weinheim]

1.1.2. Conventional Bio-Assays

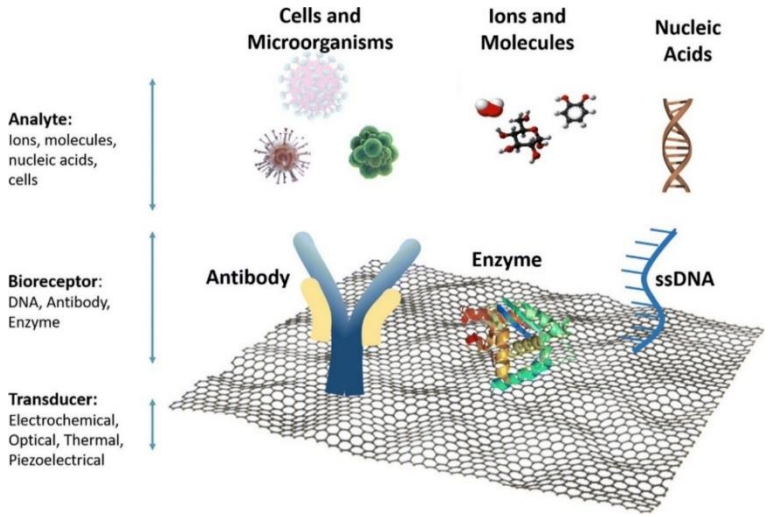

Figure 1.5. Schematic representation of biological species on a transduction platform constituting Molecular Biosensors. [Reprinted with permission from Peña-Bahamonde et al. (2018) Ref.[32]; Copyright © 2018 The Authors]

Taking in to account the increasing awareness of the behavior of cells, proteins, or genes at diminishing length scales reaching nanoscopic levels and their physical interpretation in relation to disease functionality, many innovations have been made in bio-diagnostics tools. Detecting analytes (i.e., biomarkers) specifically and directly according to their physical properties (including mass, size, or charge) is extremely complicated. Additionally, it circumvents one of the underlying requirements for modern biosensors, i.e., the selectivity or targeted detection of a molecule of interest.[29] Hence, biosensing based on immunoassays that use sandwich configurations of biological species as receptors (for example, protein or nucleic acid) has been widely used for clinical as well as research purposes.[30] They are employed in different formats to capture the analyte of interest **(Figure 1.6)**.[31] These analytes can be another protein (antigen or antibody), cell, nucleic acid, or in some cases small molecules, or ions (such as Mg^{+}, NA^{+}, Pb^{+}, etc.).[30,32]

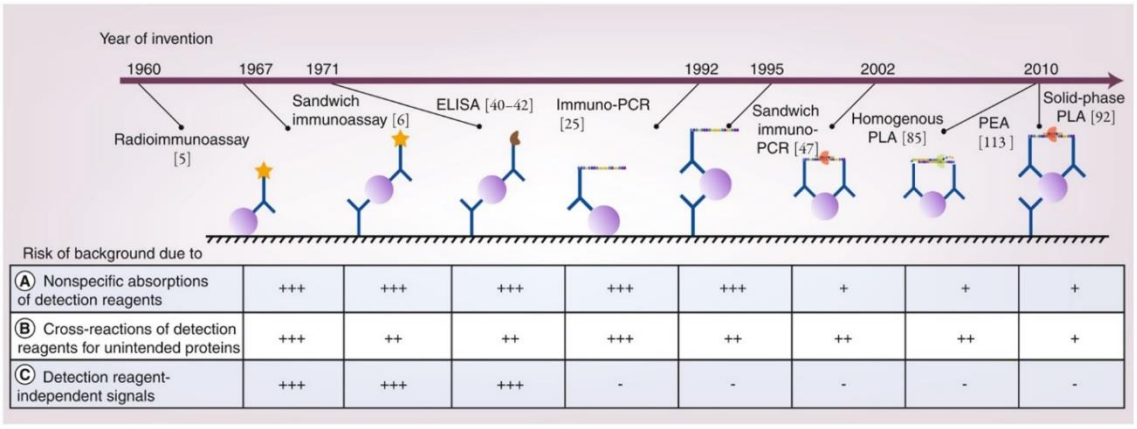

Risk of background due to								
(A) Nonspecific absorptions of detection reagents	+++	+++	+++	+++	+++	+	+	+
(B) Cross-reactions of detection reagents for unintended proteins	+++	++	++	+++	++	++	++	+
(C) Detection reagent-independent signals	+++	+++	+++	-	-	-	-	-

Figure 1.6. (Above) Advancements in the affinity-based detection of proteins and (bottom) background signal contributors and their magnitude. [Reprinted with permission from Nong et al. (2012) Ref.[31]; Copyright © 2012 Expert Reviews Ltd.]

The DNA hybridization assay (based on PCR),[31] immunosandwich assays (ISA), and DNA encoded chemical library,[33] are a few examples of affinity-based bioassays that allow the very selective capturing of the analyte from a complex sample. Relying on the growth of chemistry, nanotechnology, and biotechnology, sandwich assays have been widely developed in order to extend its signaling mechanism from radiolabeling to simpler transduction schemes for example electricity, fluorescence, or enzyme catalysis.[30]

The sandwich assay has been extensively developed, relying on progress in chemistry, biotechnology, and nanotechnology to extend its signaling mechanism from

radiolabeling to more advanced transduction schemes such as enzyme catalysis, fluorescence, or electricity. Moreover, employing nanoparticle labeling techniques to amplify their output signals pushes down their detection limits further **(Figure 1.7)**.

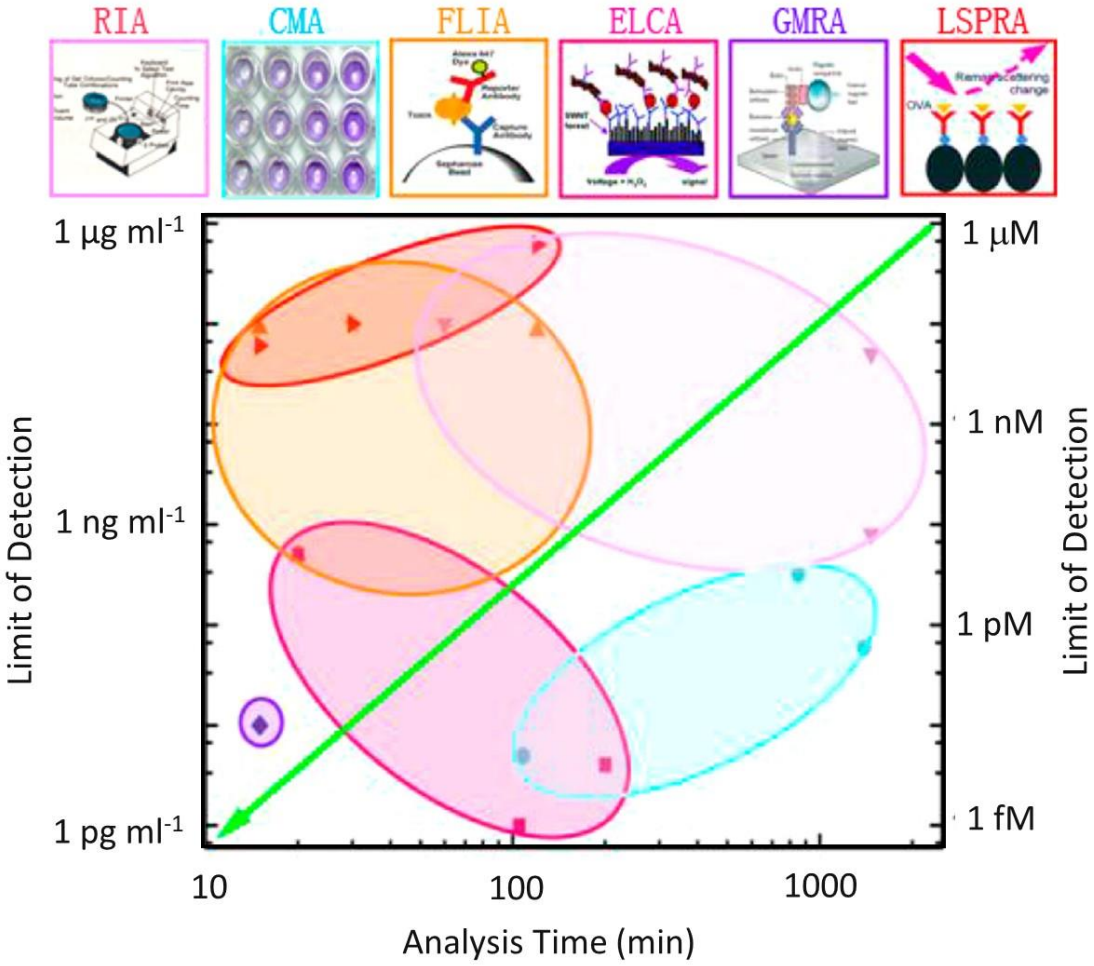

Figure 1.7. Categories of the sandwich assays including sandwich radioimmunoassay (RIA), sandwich colorimetric assay (CMA), sandwich fluorescence immunoassay (FLIA), sandwich electrochemical assay (ELCA), sandwich giant magnetoresistive assay (GMRA), and sandwich localized surface plasmon resonance assay (LSPRA). [Adapted with permission from Shen et al. (2014) Ref.[30]; Copyright © 2014 American Chemical Society]

Although some of these technologies offer detection limits down to the femtomolar range within a few tens of minutes **(Figure 1.7)**,[30] they involve intricate sample pre-treatment processes, medically trained users, sophisticated laboratories, and lengthy and complicated steps (such as washing, drying, and separation stages), which all increase their operational costs. There is an urgent need to develop simpler and more efficient ways of

approaching sensitivities down to single molecules in a shorter timeframe. Incorporating nanoscale structures within modern affinity-based molecular diagnostic techniques has revolutionized the field of in-vivo as well as in-vitro biosensors in recent decades.[34] Their inherent advantages, such as higher surface to volume ratios within miniaturized footprints, favorable electronic/optical or mechanical properties arising at the nanoscale, and fast response time, have been combined to advance molecular biosensing. The nanobiosensing technologies have paved the way for gaining a comprehensive insight into dynamic cellular metabolic events and, subsequently, the human body metabolism. For example, in 2012, Costa et al. demonstrated a more straightforward strategy for monitoring cancer circulating cells (CTCs) labeled with gold NP,[35] and in 2009, Zhang et al. showed that they were able to monitor mammalian brain cell activity relying on the localized surface plasmonic resonance shift of the gold NP.[36]

1.1.3. Emerging Micro-/Nanotechnologies For Molecular Diagnostics

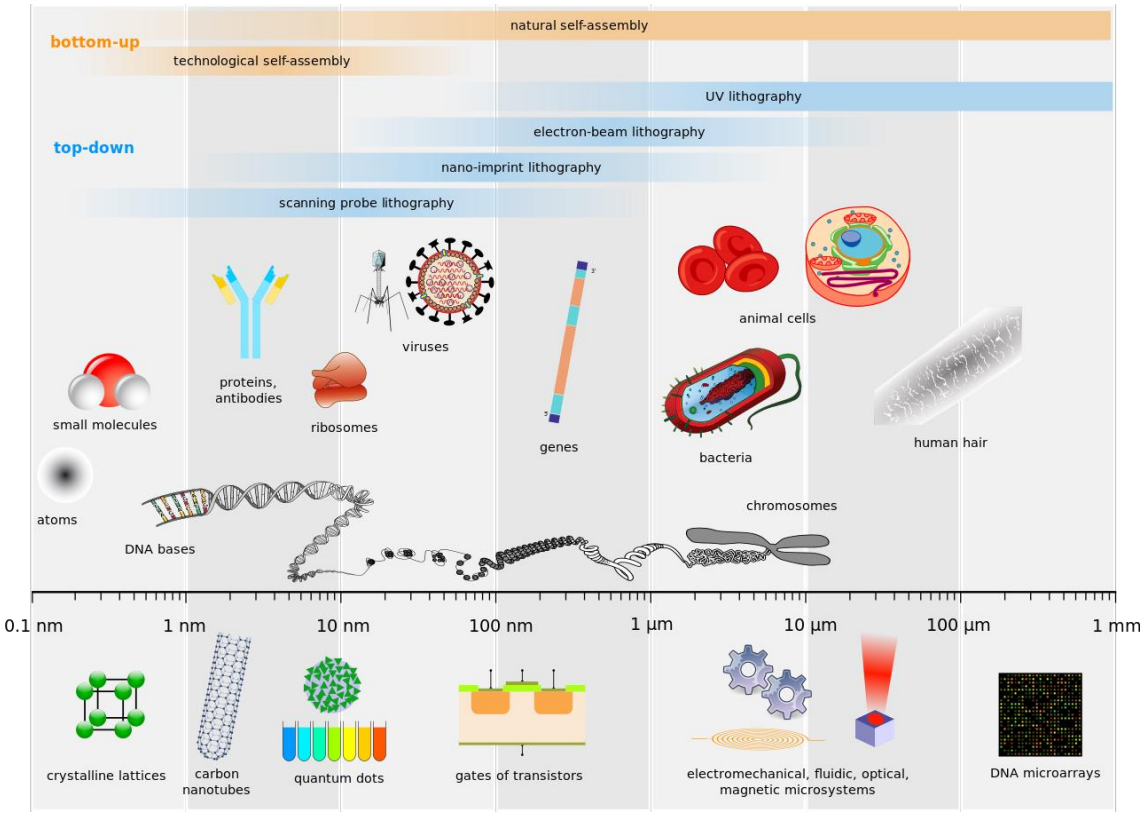

Figure 1.8. Schematic comparison of typical length scales of (above) biological species and (below) length scales relevant to micro and nanotechnolgically engineered surfaces.[37]

The advancement in micro- and nanofabrication technology has unveiled several possibilities for fabricating nanosized structures using modern semiconductor fabrication processes, enabling them to interrogate or influence biomolecular interactions at the molecular length scales. These technologies allow the output signal from conventional bioassays such as immunoassays, DNA hybridization, etc. to be amplified in order to develop practical state-of-the-art biosensors. Such biosensors leverage the advantages of nanoscale structures to improve the signal-to-noise ratios within miniaturized sensor footprints. Nanoscale biosensing platforms relying on nanoscale geometries have already shown themselves capable of sensing down single molecules. However, such a capability does not readily translate into workable solutions in real-life applications. Several challenges need to be addressed before the sensors can perform reliably to quantify the desired biomolecular target in complex media, with specifications that satisfy end-user needs from both the clinic and the industry.

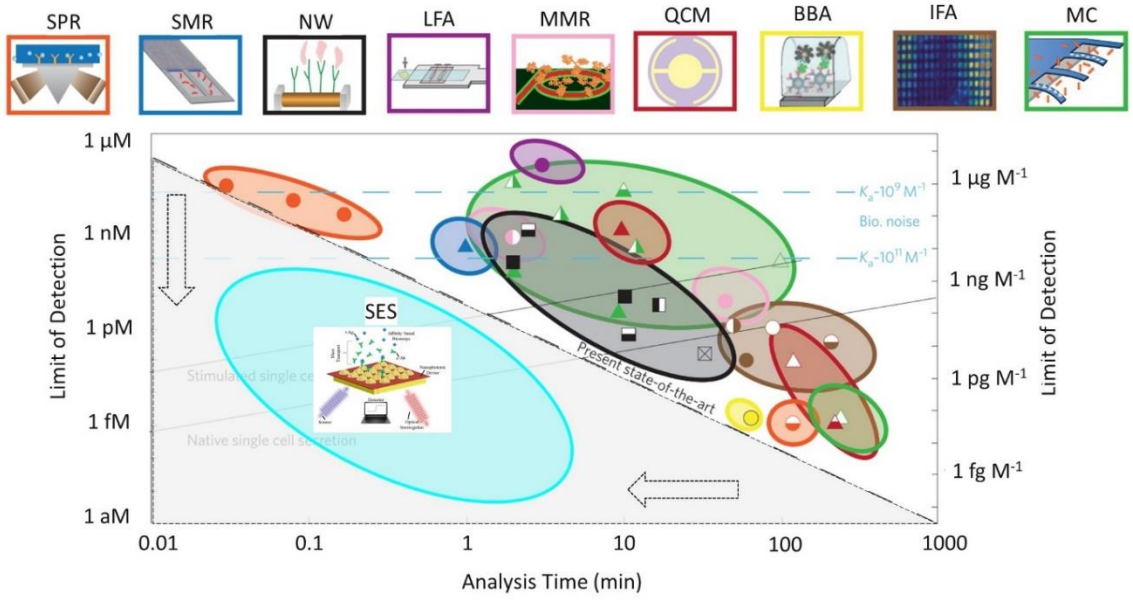

Figure 1.9. Categories of the biosensing transducer including surface plasmon resonance (SPR), suspended microchannel resonator (SMR), nanowire (NW), lateral flow assay (LSA), microring resonator (MMR), quartz crystal microbalance (QMC), bio-barcode amplification assay (BBA), immunofluorescent assay (IFA), microcantilever (MC). [Adapted with permission from Arlette et al. (2011) Ref.[38]; Copyright © 2011 Macmillan Publishers Limited]

In a detailed review by Arlette et al., they compared the state of the art techniques based on their *Analysis time* and *Limits of Detection* relying on optical, mechanical, and

electrical transduction **(Figure 1.9)**.[38] The techniques that deliver high sensitivity do so at the expense of long response times and those which deliver quick results do so at the expense of sensitivity. Such a trade-off exposes a gap for sensing technologies that reliably deliver nano to the picomolar range with response times of a few minutes, which would considerably meet the emerging diagnostic demands. For example, using standard lithography techniques, microcantilever structures were demonstrated to sense prostate static antigen (PSA) down to 1.5 fM concentration relying on the shift in their resonance frequency in a vacuum.[39] While the sensing platform is highly sensitive to surface stress generated due to the binding of biomolecules to the cantilever surface, the time involved for sensing was extended to a few hours.

The standard enzyme-linked immunosandwich assays (ELISA) use an enzymatic enhancement to the colorimetric product as a function of time. The technique can deliver sub-nanomolar sensitivities but is limited by the slow response times, typically over an hour for only the enzyme-catalyzed reaction step. Techniques such as SPR and QCM are capable of real-time monitoring of the sub-monolayer of molecules on the surface but are limited in the number of molecules needed in order to obtain a noticeable signal.[40] For QCM, this typically requires at least a billion molecules on the surface. Plasmon-enhanced spectroscopies that rely on plasmonic signal enhancement over vibrational Raman or Fluorescence signals can clearly address the gap, as they have sensitivity down to a few molecules,[41,42] within microscopic footprints, with typical acquisition times spanning from seconds to minutes.[43,44] In the following section, surface-enhanced spectroscopies, the means to enhance their signals using tailored plasmonic interfaces, are reviewed and discussed.

The ability to detect molecular biomarkers down to sub-nanomolar concentrations is critical to emerging personalized healthcare applications. Popular technologies and the alternative emerging technologies suffer from the trade-off of delivering high sensitivity with quick response times, within miniaturized sensing footprints. With a proven sensitivity down to few molecules within microscopic footprints and a response time of a few seconds to minutes, Plasmon-enhanced spectroscopies have the unique potential to address this gap relying on light-matter interactions.

1.2. Surface-Enhanced Spectroscopies (SES)

Surface-enhanced spectroscopies (SES) rely on the enhancement of spectroscopic signals originating from the analyte molecules attached to or in the close vicinity to the metallic nanostructures. The spectroscopic techniques such as infrared (IR), Raman, or Fluorescence, probe light-matter interactions based on absorption, emission, or the scattering of electromagnetic radiation as a function of wavelength or frequency to detect the presence of molecular analyte based on its vibrational or electronic structure. The presence of metallic nanostructures that can concentrate and enhance EM fields, results in enhanced spectroscopic signals from the analyte. These mainly include Surface-enhanced infrared absorption (SIERA),[45,46] Surface-enhanced chiroptical spectroscopy (SEC),[47–50] Surface-enhanced Raman spectroscopy (SERS),[51,52] and Surface-enhanced fluorescence (SEF).[53,54]

With strongly enhanced signals, SES compensates for the lower signal cross-section of the analyte molecules, allowing usefulness beyond spectroscopic characterization into a tool for molecular detection with limits of detection (LOD) down to few molecules. Different SE spectroscopic techniques have previously been shown for biosensing applications depending on the probe, incident wavelength, nature of the analyte, and assay configuration.[55] Among various SE techniques, SERS and SEF are highly promising due to their compatibility with visible wavelength ranges, ability to reduce sensor footprints, and ease of extending to portable configurations. The following section discusses the origin of enhancements in SERS and SEF signals from nanoplasmonic interfaces.

1.2.1. Surface-Enhanced Raman Spectroscopy (SERS)

Raman spectroscopy allows the structural information of the analytes based on their vibrational frequencies, which are specific to the chemical bonds and the symmetry of the atoms in the molecule. By probing molecular vibrational states, Raman spectroscopy reveals the structural information in the form of a Raman spectrum of the molecule. Therefore, such characteristic Raman spectrums are often referred to as fingerprints of the molecules that allow the identification in a multiplexed environment.

In principle, Raman scattering can be explained from a classical as well as a quantum mechanical point of view. According to the classical wave interpretation, Raman scattering relies on the interaction of EM radiation with oscillating electric fields and with the polarizability of the molecule, i.e., the extent to which the electron cloud on the molecule can be distorted in the presence of an electric field. For example, an aromatic molecule, such as benzene, is a soft molecule (higher polarizability) that tends to be a stronger Raman scatterer, unlike a water molecule (lower polarizability) that has fairly weak Raman signals.

On the other hand, according to quantum mechanical interpretation, when a Raman active molecule is irradiated with incident photons, a large number of photons scatter elastically (a.k.a. *Rayleigh* scattering). This occurs due to the oscillating electron of the molecules in resonance with the incident electric fields. However, few photons undergo energy transformation resulting in inelastic scattering (a.k.a. Raman scattering). Energy changes occur because of the vibration of the molecule that might occur during the resonance between the oscillating electrons and the incident field.

These Raman scattered photons can have either higher or lower energy photons resulting in anti-*Stokes* or *Stokes* bands **(Figure 1.10)**. Raman spectra commonly report *Stokes* bands due to their stronger intensities. Thus, Raman scattering is observed at a longer wavelength or higher energy in relation to incident light.

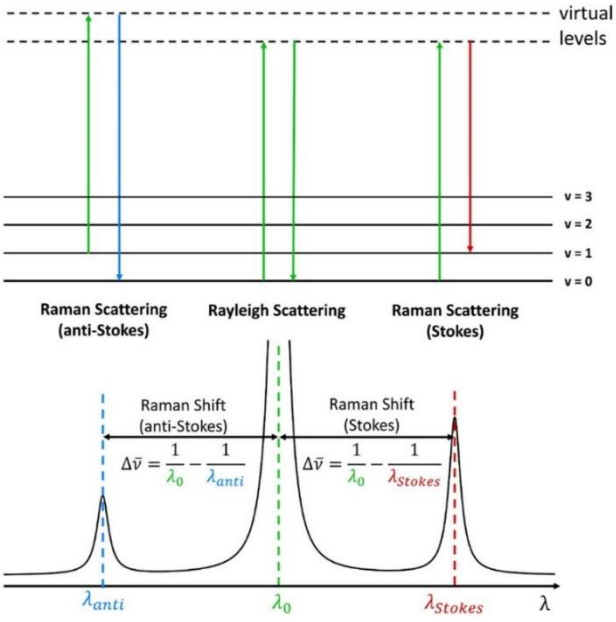

Figure 1.10. Stokes and anti-Stokes Raman scattering.[56]

Raman signal (intended as Stokes-Raman) generated from analytes can be written as:

$$P_{Raman} = KN\sigma_R I \quad \text{Eq. 1.1}$$

Here, P_{Raman} (photon/s) is the Raman signal power measured by the detector, K accounts for a fraction of the photons scattered from the molecule (stokes shifted) converted to electrons by the detector, N is the number of molecules illuminated, σ_R (cm^2/sterade.molecule) is the Raman-cross section of the molecule, and I (photon/(cm^2.s)) is the intensity of the incident laser. This implies its dependency on the chemical nature of the analyte molecule through its cross-section, as well as the incident field.

Raman Spectroscopy offers fingerprint recognition, multiplexing in different environments, and non-invasive interrogative capabilities. However, Raman scattering is an inherently weak phenomenon. In comparison with fluorescence, it is crucial to note that the scattering that occurs has very low efficiency. The fluorescence cross-sections are typically in the range of 10^{-16} cm^2/molecule,[57] whereas, the *Rayleigh* and *Stokes* Raman cross-sections, are approximately in the range of 10^{-26} cm^2/molecule and ~10^{-29} cm^2/molecule, respectively.[57–59] Furthermore, Resonant Raman excitation can benefit the *Stokes* Raman cross-section to reach only up to ~10^{-22} cm^2/molecule.[57,58] Therefore, it is experimentally difficult to filter the Raman scattered photons from the Rayleigh scattered photons or fluorescence background. The detection of analytes at low concentrations is even more difficult.

The presence of metallic nanostructure suitably near the analyte molecule can improve the low intrinsic efficiency of the Raman scattering. Raman signals under such configurations have been estimated to increase up to ~10^{10} times or more in many studies,[60,61] with 10^7 to 10^8 order of enhancement being considered sufficient for single-molecule detection with efficient Raman probes (with high Raman cross-section).[61] This is known as SERS.[62,63]

This enhancement includes (Eq. 1.1) contributions from two factors, namely, electromagnetic and chemical enhancements.[64]

$$P_{SERS} = G_{SERS}\, P_{Raman} = G_{SERS}^{Em}\, G_{SERS}^{Chem}\, P_{Raman} \quad \text{Eq. 1.2}$$

G_{SERS} is the total SERS enhancement factor and accounts for the amplification induced by the substrate, which involves contribution from EM enhancements (G_{SERS}^{Em}) and chemical enhancements (G_{SERS}^{Chem}).

Electromagnetic Enhancements: EM enhancements are considered to be the dominant contributing factor to the overall SERS enhancements. This is based on numerous studies, typically employing computational thermodynamics calculations to determine the enhanced electric field $E(\omega)$ experienced by the analyte situated near the metallic nanostructures with resonating free electrons at frequency ω (*discussed in detail section 1.3*). Although it is independent of the analyte species and their Raman cross-section, to effectively contribute to the output signals, molecules need to be embedded inside the enhanced EM field environment. The electromagnetic enhancement (G_{SERS}^{EM}) can be expressed as,

$$G_{SERS}^{EM} = |E(\omega)|^2 |E(\omega')|^2 \qquad \text{Eq. 1.3}$$

Where $E(\omega)$ is the local electric field, and $E(\omega')$ is the radiated field ω' as the Raman emitted frequency (a.k.a. dipole reradiation[65]).[66,67] Considering that the difference in ω and ω' is small, the so-called E4 approximation can be applied,[68] and Eq. 1.3 becomes,

$$G_{SERS}^{EM} = |E(\omega)|^4 \qquad \text{Eq. 1.4}$$

Chemical Enhancements: On the other hand, chemical enhancements are independent of EM field enhancements and have weak contributions to overall SERS enhancements. Their contributions lie within the modifications in the polarizability experienced by the molecule due to the transfer of charges with the metal surface or receptor molecule on the metal surface.

The interaction can alter the Raman cross-section of their vibrational modes, and consequently, their Raman intensities. Therefore, it relies on the physio-chemical interaction of the molecule with the metallic surfaces, hence is also considered a short-range effect as it involves contact or very small separations between them (a few Angstroms).[69] Depending upon the nature of the adsorption enthalpies involved that determine the strength of the interaction, the electronic structure of the probe molecule

might change. The impact is less significant in physisorbed molecules, and more meaningful in chemisorbed molecules due to the charge transfer (CT) effect between the molecules adsorbed and the metal surface under certain conditions.[70] Consequently, the intense enhancement of some Raman bands is observed in the event of resonance Raman configurations.[71] The chemical enhancements can be expressed as the ratio between the Raman cross-section of the analyte when it is adsorbed (σ_R^{ads}) on the metal surface (physisorbed or chemisorbed) to when it is in free space (σ_R^{free}) in Eq. 1.5.

$$G_{SERS}^{Chem} = \frac{\sigma_R^{ads}}{\sigma_R^{free}} \qquad \text{Eq. 1.5}$$

Distance-Dependence: The dependence of the SERS enhancement on the distance from the surface can be explained by considering a simple case of the metallic sphere of radius much smaller than the incident wavelength; theoretically it follows $\frac{1}{d^{12}}$ dependence,[59] expressed as,

$$\frac{G_{SERS}^{Em}(d)}{G_{SERS}^{Em}(0)} = \left[\frac{a}{a+d}\right]^{12} \qquad \text{Eq. 1.6}$$

Where a is the radius of the sphere, and d is the distance of the Raman emitter from the surface of the metallic sphere. Therefore, the Raman emitter must be in close proximity with the metal surface in order to leverage from the localized EM fields in the environment it is embedded within, as well as chemical enhancements where possible **(Figure 1.11)**.[59,68]

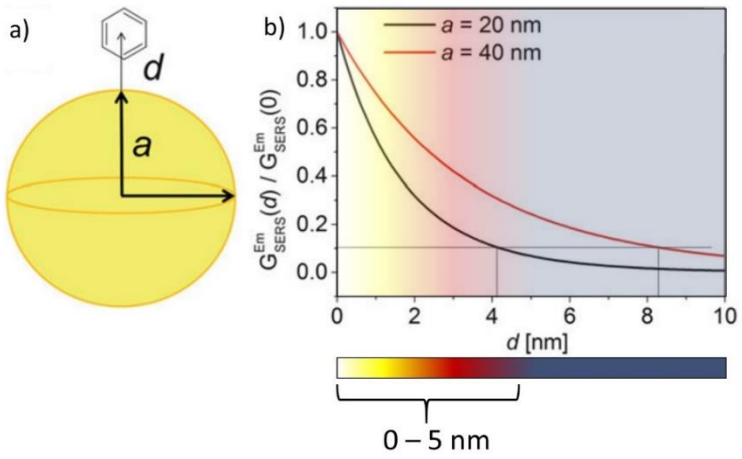

Figure 1.11. (a) Schematic representation of a Raman active molecule placed at a distance d from the metal surface of radius a. [Adapted with permission from Aroca (2006) Ref.[59]; Copyright © 2006 John Wiley & Sons Ltd.] (b) G_{SERS}, normalized to the value at the surface, is plotted as a function of d for a sphere with radius a = 20 nm (black line) and for a sphere with radius a = 40 nm (red line). [Adapted with permission from Pilot et al. (2018) Ref.[68]; Copyright © 2018 Springer International Publishing AG]

Owing to the promising capabilities of SERS in demonstrating highly sensitive probing of the molecules at nanoscale resolution,[52] SERS has gained considerable interest in biomolecular detection applications in body fluids using indirect (label-free), or direct (labeled molecules) biosensing protocols.[64,72] As it combines the advantages of Raman spectroscopy[72] (which includes recognition capabilities using a non-destructive type of analytical technique, minimum preparation of the sample, the possibility of carrying out measurements in solutions (since water has a weak Raman scattering), multiplexed sensing, prospects for portable configurations) with the enhanced Raman signal intensities to overcome that gap and additionally in some cases also enables single-molecule detections.[73] Thus, rationally selecting a Raman reporter based on its Raman cross-section, fingerprint peak positions, excitation wavelength, emission wavelength, surface interaction type (physical/chemical) can help to improve detection sensitivities, provided that the reporter molecule is able to undergo EM and/or chemical enhancements from the localized EM fields at the metal surface.

1.2.2. Surface-Enhanced Fluorescence Spectroscopy (SEF)

The enhancement mechanisms that are relevant to SERS are also applicable in various other spectroscopic techniques that deal with absorption, fluorescence, or the scattering of photons. Fluorescence is widely used for biosensing and imaging for clinical and research purposes due to its high sensitivity and ease of implementation,[74,75] e.g., fluorimetric bioassays,[76] high throughput screening,[77] and the imaging of biological cells and sub-cellular components.[78] However, fluorescence-based biosensors also remained a center of interest for the researchers for the purpose of increasing their sensitivity and overall performance of the biosensors.[79]

The fluorescence signal, like Raman, can be enhanced under appropriate conditions for fluorophores near metal surfaces, and are thus known as SEF.[53] Despite having a much

higher cross-section of fluorescence than Raman, the signal enhancement achievable in the former is much lower (~10^3) than that in the latter (~10^8).[80–83] Although they have similar enhancement mechanisms supporting their signal amplification, there are many important dissimilarities amongst them.

Fluorescence is a multi-step process, unlike SERS, where scattering is instantaneous. This means that the enhanced EM fields (local $E(\omega)$ and re-radiated $E(\omega')$) near the Raman probe will aid to improve the SERS cross-section. While for fluorescence, enhanced local EM fields will provide support to modify the absorption cross-section, the radiative enhancement only contributes to modifying the decay rates, which then compete with each other.[57] The detection techniques based on fluorescence are usually limited to the quantum yield, autofluorescence, and photostability of the fluorophore.[54] During SEF, enhanced EM fields in the environment in which the fluorophore is embedded influences two main optical properties of the fluorophore. This includes, quantum yield, and the absorption cross-section.[57] In other words, enhanced absorption of photon that excites the electron from the ground state to the excited state, does not enhance the energy being extracted from the electron but only extracts it faster. Hence improving the excitation rate.[57]

To understand the mechanism behind the impact of metal surfaces on the fluorophore, the Jablonski diagram is shown in **Figure 1.12**.[84] It briefly explains the excitation and the emission process that takes place in the absence and presence of the metal surface close to the fluorophore. A fluorophore in a free space condition can absorb the energy of the photon (E) and jumps to its excited state (S_1). Following this, the molecules from the excited state can fall back to their ground state (S_0) while undergoing radiative decay by emitting a photon at a rate, Γ, or by undergoing non-radiative decay with a rate of k_{NR}, or they can suffer from a quenching process which results in depopulating the S_1 level with a rate of k_Q. The quantum yield, Q_0, of a fluorophore suggests competition between radiative decay and non-radiative decay processes.

$$Q_0 = \frac{\Gamma}{\Gamma + k_{NR} + k_q} \qquad \text{Eq. 1.7}$$

The decay time accounting for the duration for which a fluorescent molecule stays in the S_1 state is expressed as,

$$\tau_0 = \frac{1}{\Gamma + k_{NR} + k_q} \qquad \text{Eq. 1.8}$$

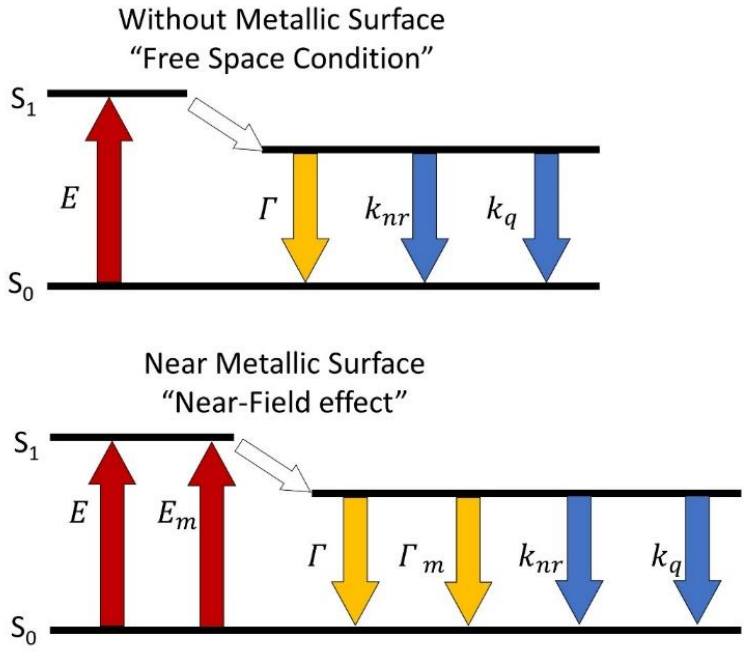

Figure 1.12. Jablonski diagram explaining excitation and emission of a fluorophore a) without the metal surface and b) with the metal surface in the vicinity. [Adapted with permission from Geddes et al. (2003) Ref.[84]; Copyright © 2003 Bentham Science Publishers Ltd.]

A close spatial environment of the fluorophore plays a vital role in influencing its fluorescence lifetime and intensity (due to the changes in k_{NR} and k_q), with less modification to its emission rate, Γ. If Q_0 is lower for a fluorophore, then the Γ is relatively less than $k_{NR} + k_q$, and vice versa. Hence, it is possible to modify spectral properties of the fluorophore by modifying k_{NR} or k_q. Invariably Q_0 and τ_0 change together. Γ depends on the transition probability and oscillation strength of the $S_1 \rightarrow S_0$ transition.[85] Therefore, modification in Γ is typically not significant enough to consider.

However, when such fluorophores are placed in the near vicinity of the metallic nanostructure capable of enhancing near EM fields, the fluorophore can undergo an enhanced rate of radiative decay, Γ_M. Hence, an increase in Γ_M results in an increase in quantum yield, Q_M and a decrease in a lifetime, τ_M, which analogous to free space condition in which both change in unison. This can be expressed as,

$$Q_M = \frac{\Gamma + \Gamma_M}{\Gamma + \Gamma_M + k_{NR} + k_q} \quad \text{Eq. 1.9}$$

$$\tau_M = \frac{1}{\Gamma + \Gamma_M + k_{NR} + k_q} \quad \text{Eq. 1.10}$$

Distance-dependence: Analogous to SERS, the relationship of MEF enhancement and the distance from the metallic surface is not simply proportional. The distance of the fluorophore from the plasmonic surface should be more than a certain threshold distance, where the radiative decay rate can dominate over quenching, while still being able to leverage from the enhanced EM radiations in the local environment near the metal surface **(Figure 1.13)**.[80,86]

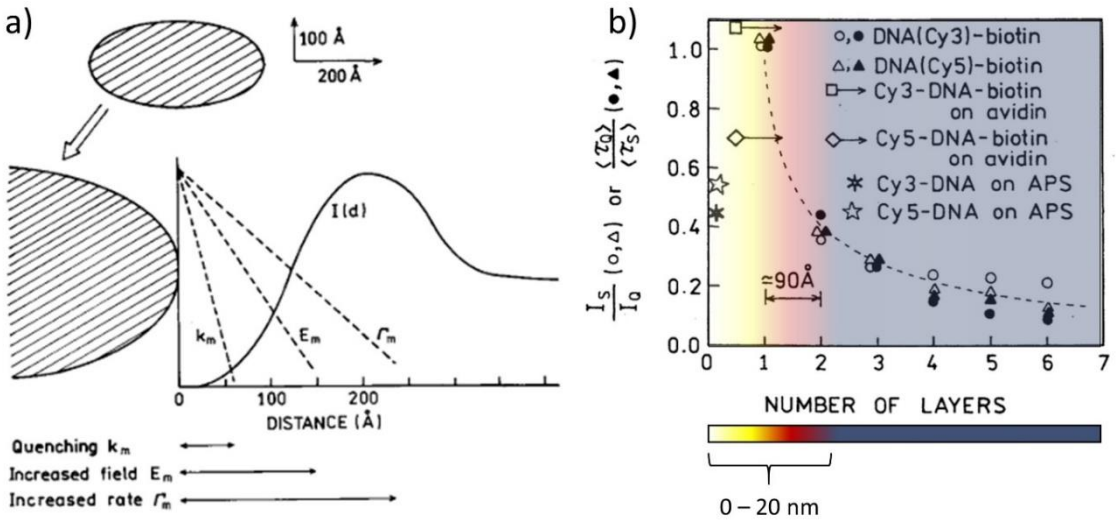

Figure 1.13. a) Effect of metallic NP on electronic transition within a fluorophore as a function of the distance between the fluorophore and the metal surface, [Adapted with permission from Lakowicz (2001) Ref.[80]; Copyright © 2001 by Academic Press], b) Distance dependence of the MEF signal intensity from the surface of the metal. [Adapted with permission from Lakowicz et al. (2003) Ref.[86]; Copyright © 2003 by Academic Press]

The distance from the metal surface depends upon the extent of the electromagnetic field experienced by a fluorophore due to the presence of propagating surface plasmons (PSP) on continuous thin metallic films and localized surface plasmons (LSP) on metallic nanostructures. MEF enhancements obtained in LSP configurations are usually higher.[87] The absolute distances of the fluorophore from the surface, reported in the literature, are

diverse, and justify gaps as low as 1-2 nm,[88] 5nm,[88–90] or 10-20 nm.[80,86,87] It is essential to consider the quenching effect that is prevalent when the fluorophore is at an extremely low distance or in contact with the metal.[90]

Fluorescence has been preferred over normal Raman due to a larger cross-section of fluorescence than Raman for the reporter molecules. The radiative decay rate for a fluorophore has been predicted to increase over 10^3 times when the fluorophore (with high quantum yield, Q_0) is placed at a suitable distance from the metallic surface. In addition, with enhancement in the excitation rate at the same illumination intensity, a fluorophore can produce a remarkable cumulative signal with 10^7 times increase in the fluorescence intensity.[91]

SERS and SEF are highly promising means to achieve highly sensitive detection of analytes at ultra-low concentrations. The highly enhanced EM fields close to nanostructured metal surfaces are significant contributors to the enhancement factors. Achieving high signal intensities would thus need high EM enhancements.

1.3. Nanoplasmonics - Light-Matter Interactions

Nanoplasmonics is a component of nano-optics that deals with the interaction of light and the motion of charges in nanoscale materials.[92] It explores how the electromagnetic fields can be confined over dimensions that are smaller than the wavelength of incident light-concentrating and enhancing their intensity at tiny spatial regions.

Plasmonics, in general, is the physics of plasmons that relates closely to the optical properties of the metal nanostructures.[93] The term “plasmon” is defined as the collective oscillation of conduction electrons that can be excited in the metallic nanostructure (particularly gold and silver),[94] semiconduction NP,[95] metal surfaces,[96] and even in 2D materials like graphene,[97] or in molecules.[98] However, the relevance of plasmonics (or nanoplasmonics) here is mainly due to the inherent electromagnetic effect. As discussed in the previous section, the enhancement of spectroscopic signals relies dominantly on enhanced electromagnetic fields. Hence, nanoplasmonics is a way to create regions that have intense EM fields.

Small note on metals: Noble metals like gold or silver have the lowest losses in the visible and near IR regions, which are most suitable for sensing related applications.[99] Although silver exhibits better optical properties than gold, it is not necessarily the best choice for biomedical applications due to its oxidative and reactive nature.[100] Gold provides superior chemical stability, low toxicity, and biocompatibility.[101]

1.3.1. Propagating And Localized Surface Plasmons

Propagating surface plasmons are referred to as collective oscillation of free electrons present at the metal surface upon irradiation with incident light. When a photon hits the metal surface (usually silver or gold), at a certain angle of incidence (under total internal reflection condition), part of the energy is lost. The energy lost in the metal is absorbed by the free electrons present at the surface of the metal which then starts to oscillate.[99] Hence, the oscillating electrons are now called plasmons, and they propagate parallel to the metal surface (propagating surface plasmons (PSP)). Upon matching the frequency and the *k*-vector of the incident electric field with the oscillating electrons, the plasmons resonate, and this is hence known as surface plasmon resonance (SPR). SPR generates a decaying electric field (evanescent wave) perpendicular from the surface of the metal (decay length ~300nm).[102]

However, controlled fabrication and diminishing the size of metallic structures much smaller than the incident wavelength can result in the localization of these surface plasmons, hence called localized surface plasmons (LSP).[103] At resonances (LSPR), due to small lateral dimensions, the charges accumulate at the surface of the nanostructure leading to an strong electric field in the vicinity of the surface (decay length ~5-30 nm).[104,105] Due to the formation of dipoles, the internal electric field acts as a reinstating force acting on the oscillating charges, and resonance may occur, which is known as localized surface plasmonic resonance (LSPR).[106]

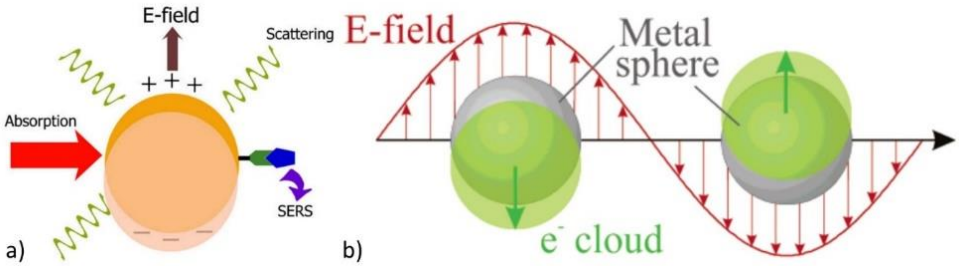

Figure 1.14. (a) Schematic representation of a coherent oscillation of electrons of metal NP resulting in LSPR, [Reprinted with permission from Jain et al. (2010) Ref.[116]; Copyright © 2010 Elsevier B.V.] (b Schematic representation of plasmon oscillation on the spherical nanoparticle, depicting the displacement of the conduction electron charge cloud relative to the nuclei. [Reprinted with permission from Kelly et al. (2003) Ref.[117]; Copyright © 2003 American Chemical Society]

Table 1.1. Comparison between SPR and LSPR techniques. [Reprinted with permission from Haes et al. (2004) Ref.[107]; Copyright © 2004 Springer-Verlag]

Feature/characteristic	SPR	LSPR
Label-free detection	Yes[108–111]	Yes[112–115]
Distance dependence	≈1,000 nm[116]	≈30 nm (size tunable)[104,117]
Refractive index sensitivity	$2x10^6$ nm RIU^{-1}	$2x10^2$ nm RIU^{-1}
Modes	Angle shift,[118] wavelength shift, imaging	Extinction,[112] scattering,[113,119] imaging[113,119]
Temperature control	Yes	No
Chemical identification	SPR-Raman	LSPR-SERS
Field portability	No	Yes
Commercially available	Yes	No
Cost	US $150,000–300,000	US $5,000 (multiple particles), US $50,000 (single nanoparticle)
Spatial resolution	≈10 x 10 μm[118,120]	1 nanoparticle[113,119,121]
Nonspecific binding	Minimal (determined by surface chemistry and rinsing)[111,118,122–124]	Minimal (determined by surface chemistry and rinsing)[112]
Real-time detection	Time scale=10^{-1} – 10^3 s, planar diffusion[109,123,125–127]	Time scale = 10^{-1} – 10^3 s, radial diffusion[113]
Multiplexed capabilities	Yes[128,129]	Yes-possible
Small molecule sensitivity	Good[125]	Better[117]
Microfluidics compatibility	Yes	Possible

As a result of plasmonics in metals, localized EM fields have been demonstrated to serve the enhanced chemical, electrical, magnetic, and, most importantly, optical properties of the materials. Accordingly, their applications include improved chemical reactions,[130] electrical conductivity,[131] energy harvesting,[132] data storage,[133] molecular detection,[55,134] and several others discussed elsewhere.[93,135,136] The evanescent EM waves are much

stronger in intensities as compared to PSP, allowing better sensitivities for changes occurring in the vicinity of the nanostructured surfaces **(Table 1.1)**.[107] Based on the previous discussion, detection using SERS or SEF requires analyte on the metal surface or near the metal surface because of these enhanced and concentrated EM fields that originate from the surface of metal NP **(Figure 1.14)**.[137,138]

1.3.2. Electromagnetic Hot-spots

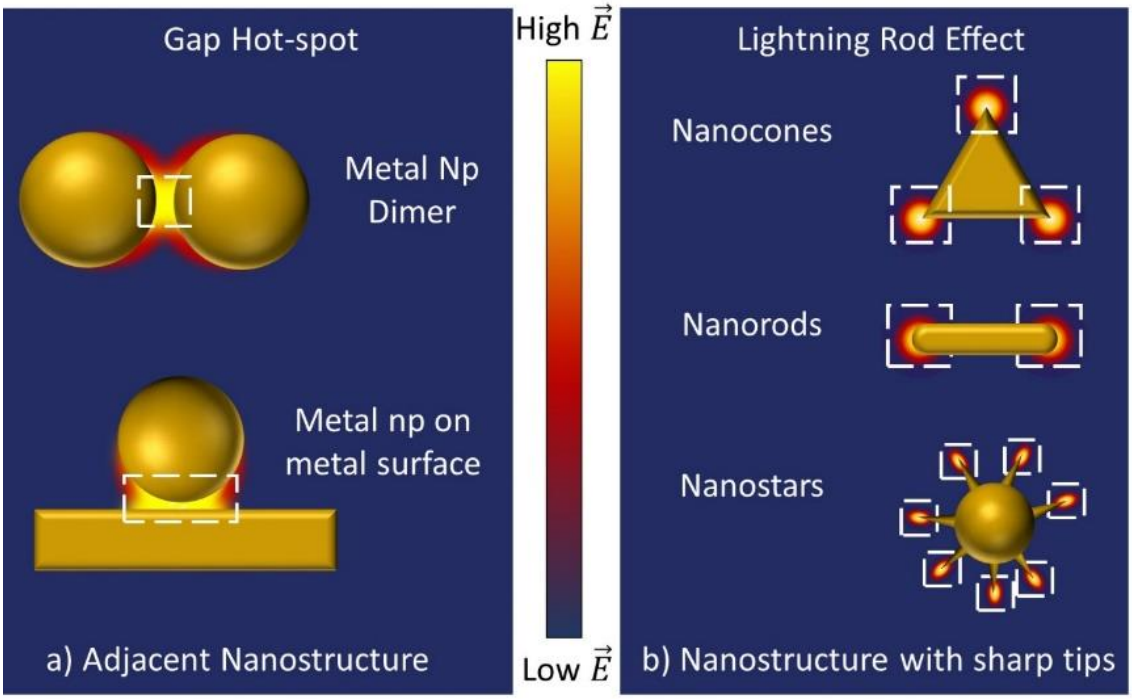

Figure 1.15. An illustration of types of a) coupling gap type hot-spots and b) Lightning rod effect was seen at sharp-tip or curvature type hot-spots.

The emergence of an electromagnetic (EM) 'hot-spot' results from the optical interaction between two metal nanostructures and the EM field distributed on their surface.[139–142] 'Hot-spots' refer to spatial regions in the vicinity of the metallic substrates where the intensity of the local field is higher than that of the incident field. Kleinman defined it as "a junction or close interaction of two or more plasmonic objects where at least one object has a small radius of curvature on the nm scale".[143]

The field intensities are generally distributed heterogeneously around the surface of the nanostructures and are mainly concentrated in very tiny volumes of 'hot-spots'.[144,145]

Such regions can be formed due to the formation of sharp features of an isolated nanostructure,[146] or nanoscale gaps between adjacent nanostructures **(Figure 1.15)**.[147–149] However, field intensities are stronger in gap hot-spots. This occurs due to the coupling between the electric fields that originate on the surface of adjacent metal nanostructures. Several studies in the literature describe the impact of assemblies/arrays of the metal nanostructures, benefitting from their optical interaction with each other to control the near-field intensities.[137,150,151]

1.3.3. Plasmonic Coupling As A Function of the Gap Size

In order to understand better, we can consider the two metallic spherical NP with a much smaller diameter ($d \ll \lambda_i$) than the incident wavelength. The dipole of one particle has the ability to interact with that of the adjacent particle. In close proximity, due to dipole-dipole interactions between nanostructures, the plasmon oscillations couple together.[142,152] The coupling between the plasmonic waves of neighboring NP is governed by the polarization or charge distribution around the surface.[153,154] **(Figure 1.16)** The LSPR spectral band red-shifts when plasmonic coupling occurs between metal NP. The extent of the redshift in the far-field spectra is directly dependent upon the interparticle distance, and their relationship is derived using a plasmonic ruler equation.[151,152,155]

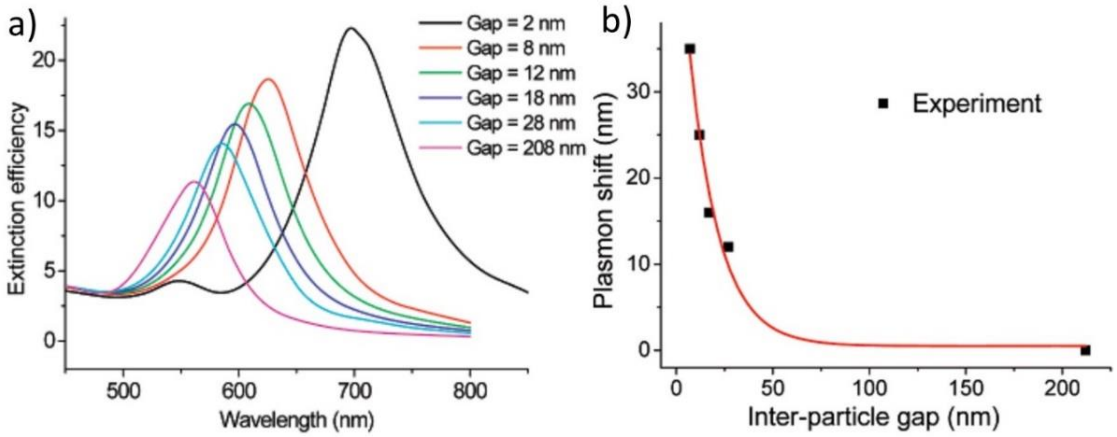

Figure 1.16. a) Red shifted extinction spectra of nanosphere dimers with decreasing interparticle gaps, b) Relationship between the shift in the wavelength and the interparticle distance. [Adapted with permission from Jain et al. (2007) Ref.[151], Copyright © 2007 American Chemical Society]

The plasmonic ruler equation was established for biological systems interacting with NP and later employed in the plasmonic coupling,[156,157] Forster distances in FRET,[158] and photothermal effects.[155] According to the plasmonic ruler equation, the fractional shift in the dipole resonance can be used to estimate the interparticle distance. The plasmon ruler equation is expressed as,

$$\Delta\lambda/\lambda = A * \exp(-(s/D)/\ell) \qquad \text{Eq. 1.11}$$

Where, $\Delta\lambda/\lambda$, is the fractional shift in the plasmonic resonance wavelength, A is the amplitude of the dipole coupling, s is the interparticle edge-to-edge separation, D is the diameter of the spherical nanoparticle, and ℓ is the decay length of the EM field away from the surface. The amplitude and the decay length can be expressed as constant over a range of sizes in a given shape, as shown by Tabor et al. in a detailed study.[152] In another study, Ben et al. reported the exponential behavior of a) the relationship between the diameter of nanoparticle ranging from 20 nm to 100 nm, as a function of interparticle distance, and b) the comparison of the exponential behavior of the wavelength shift in dimer arrangements, and periodic array arrangements of the NP.[159] Their observations show the effect of size or diameter to be weaker for NP arranged in dimer formats due to a significant reduction in structural retardation compared to the array case.

Despite the selection rules based on size, shape, and arrangements (dimers or arrays), the plasmonic ruler equation explains that the coupling behavior between two or more nanostructures is basically exponential in relation to the distance between them. Therefore, it is crucial to notice that to achieve coupling between nanostructures, nanoscale separations are fundamental. Coupling strengths, however, can vary below distances corresponding to the field decay length ℓ for a specific type of nanostructure.

1.3.4. EM Enhancements As A Function of Gap Size

Strong coupling between plasmonic NP allows the intense localization of EM fields in between them.[149,160] However, an interparticle distance lower than the threshold tunnel-distance may encounter quantum mechanical effects of electron tunneling that modify the plasmonic behavior completely.[161] This results in the disappearing of the red-shifting

plasmon wavelength mode and gradually emerging blue-shifted mode related to charge transfer plasmons.[161]

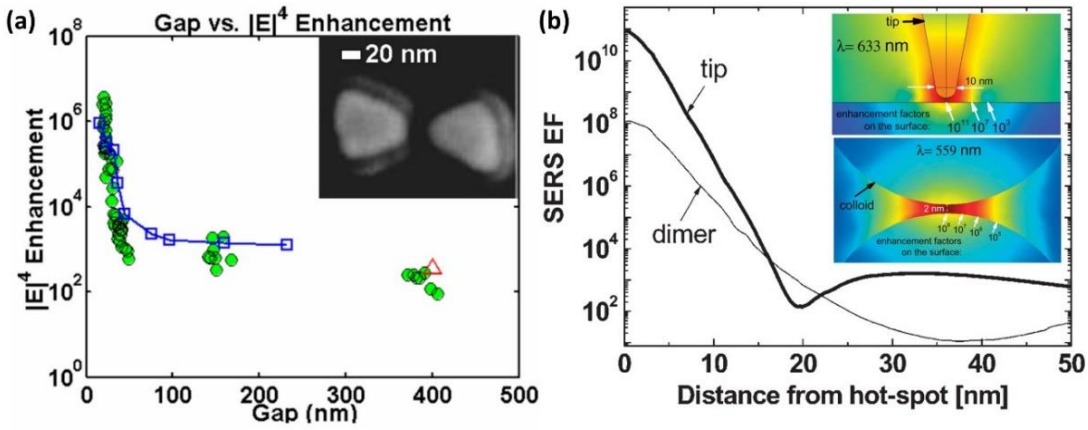

Figure 1.17. a) Exponential behavior of closing gaps between gold bow-tie nanoantennas and the enhancement factors in the center of the gap, [Adapted with permission from Schuck et al. (2005) Ref.[162]. Copyright © 2005 American Physical Society], and b) Enhancement factor distribution at a gap hot-spot in between spherical Au NP and between gold tips close to a gold surface. [Adapted with permission from Etchegoin et al. (2008) Ref.[163]. Copyright © 2008 the Owner Societies]

It is clear that the closing gaps down to extreme distances improve the coupling strength between metal nanostructures and ultimately intensify the localized EM fields between them.[164] This was also observed by Schuck et al. in 2005.[162] They investigated the relationship between the EM field localization with the decreasing interparticle distances using a gold bow-tie nanostructure dimer. EM enhancements increased exponentially when the two nanostructures came closer than ~20 nm, as shown in **Figure 1.17a)**.[162] However, the EM field intensities are observed to be heterogeneously distributed in and around the gap hot-spot, as shown in **Figure 1.17b**.[145,163] The shape of the nanostructure also plays an essential role in deciding the strength of these EM field interactions,[163,165] as well as the plasmonic modes that appear in their extinction spectra.[166]

Achieving high enhancement factors sufficient for single-molecule detection is possible with gap hot-spots. However, there is currently a lack of techniques that can offer precise control to create gap hot-spots with high resolution down to sub-10 nm at pre-determined locations efficiently, or strategically positioning of a given molecule at the hot-spot.

1.4. Impact of Geometries Of EM Hot-spots

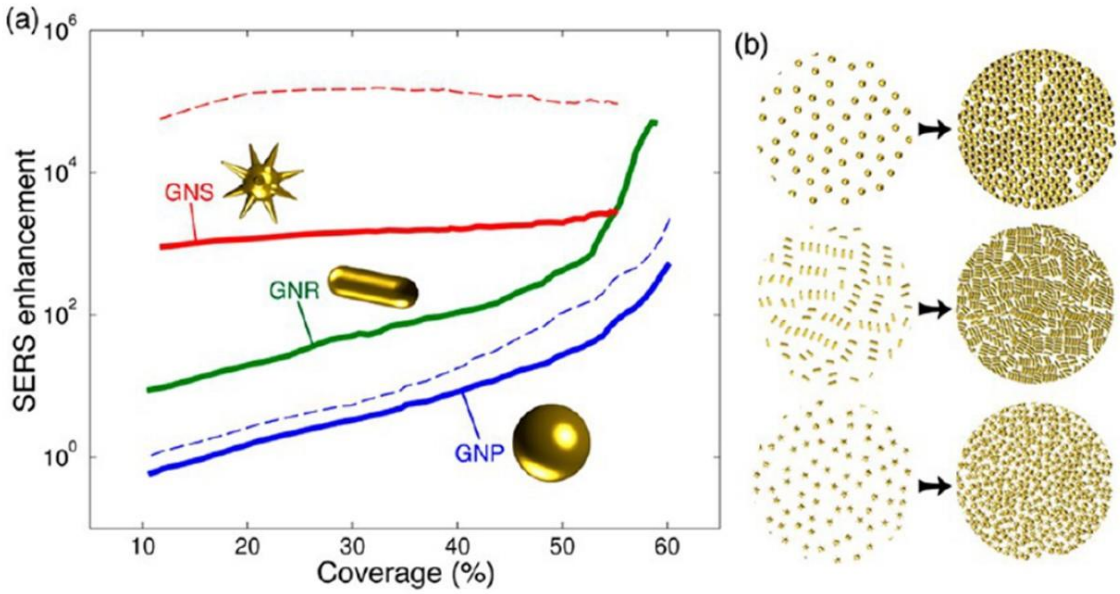

Figure 1.18. SERS enhancement in relation to geometric shape comparing Nanostar, Nanorod, and Nanosphere with increasing surface coverage resulting in smaller interparticle gaps. [Adapted with permission from Solis et al. (2016) Ref.[167]. Copyright © 2016 American Chemical Society.]

Solis et al. recently compared the impact of different geometries and surface coverages of randomly arranged nanostructures using computational techniques.[167] As shown in **Figure 1.18**, there are two main observations: a) The enhancement factor is higher for nanostructures with a higher curvature or sharp apex of the metallic tip. This is also shown in several other studies and has been associated with the lightning rod effect.[168] b) When, organized in closely packed arrangements, enhancement factors improved remarkably for spherical nanoparticles and nanorods. Therefore, despite having lower enhancement factors when in isolation, spherical nanoparticles can undergo stronger coupling between the long-range randomly organized network.

1.4.1. Impact Of Density and Homogeneity Of EM Hot-spots

The enhanced EM field intensities are heterogeneously distributed on the surface that has a large number of EM hot-spots. Consequently, the enhancements experienced by the analyte will depend on its local environment and the intensity of the local EM field. In order to elucidate the impact of variations in the enhancement factors experienced by the analytes

on the total signal arising from the given area, in 2008 Fang et al., carried out an elegant experiment. They profiled the signal contribution from analytes in EM hot-spots with different enhancement factors, by the population of molecules at hot-spots, and by the EF at the hot-spots.[169]

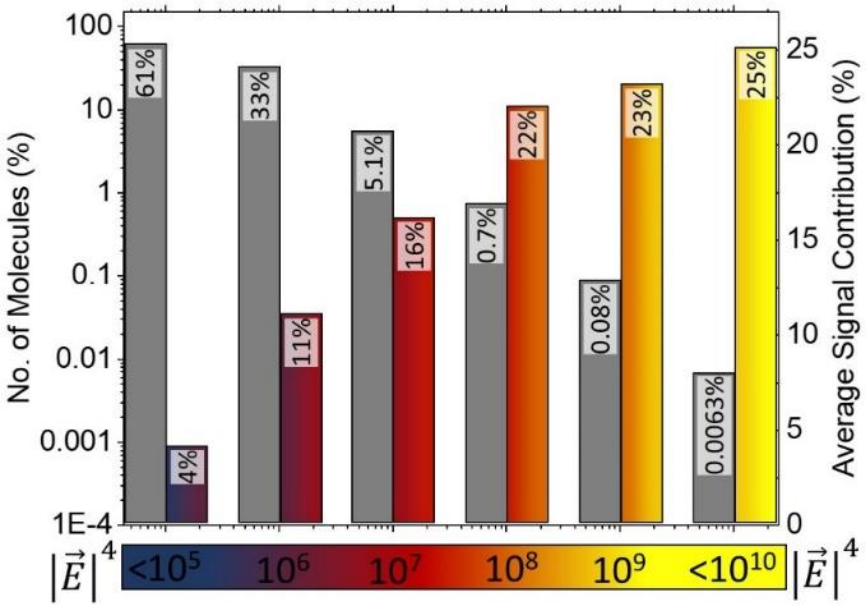

Figure 1.19. Distribution of EFs on the AgFON substrate. a) representation of the molecules adsorbed at different SERS EF and their contribution to the overall signal originating from the surface in percentage. [Adapted with permission from Fang. (2008) Ref.[169], Copyright © 2008, American Association for the Advancement of Science.]

They made use of photon hole burning (PHB) to selectively "burn out" the analyte molecules embedded in varying EM fields in and around the hotspots on the AgFON substrate. The surface was exposed to a carefully chosen intensity of the burning pulse to start destroying molecules that were present in the hottest region of the EM hot-spots. The analyte molecules started to get destroyed from the hottest region as they reached the critical breakdown limit of the field (i.e., ~10^9 V m^{-1}). Subsequently, upon escalation of the incident burning pulse intensity, the molecules embedded in less hot regions (regions with weaker EM fields) were destroyed. In between destroying PHB pulses, a continuous wave laser probed the SERS signal intensities that originated from the remaining active analyte molecules on the surface. This methodology allowed them to estimate the contribution of the analyte molecules into the total overall signals. With their study, they were able to estimate that approximately 25% of the signal intensities originated from the molecules that

were present in the most intense region of the hotspot with an enhancement factor over 10^9, and these molecules constituted less than 0.01% of the total molecules (63 molecules per million) that were present at the hot-spot. In addition, less than 6% of the molecules at a saturated surface site concentration (i.e., a monolayer) were able to take advantage of the sites with an enhancement factor over 10^7 **(Figure 1.19)**.[169]

The study served to highlight the extent to which there is a disproportionate dominance of signal contributions from molecules from highly enhancing EM hot-spots. This means, in order to achieve high sensitivity, it is necessary to achieve highly enhancing EM hot-spots, and large numbers of them. It also means that it is important for molecules to be able to leverage those EM hot-spots. It also highlights how the variation in hot-spot geometries can significantly contribute to signal intensity variations.

At the sub-monolayer concentration of the analyte in the solution, the probability for the analyte to approach the EM hot-spots would be reduced. This can compromise the resulting sensitivity, and lead to false-negative outcomes. Increasing density of EM hot-spots can increase the probability of molecules to adsorb at the enhanced surface sites at the hot-spot, where it can leverage from enhanced EM fields. Attempts to increase such geometric sites have been discussed in detail in the next section, which focuses on various nanofabrication methods.

1.4.2. High-Resolution Geometries For EM Hot-spots

Reports based on single-molecule SERS (SMSERS),[73,170] and giant enhancement factors $>10^{13}$,[171] have attracted the interest of researchers towards SERS and other surface-enhanced spectroscopies **(Table 1.2)**. [143,172] As discussed in previous sections, it was established that such enormous enhancements were arising from the hotspots that were present in between adjacent nanoparticles with the nanoscale interparticle gap.[173] Even though the random distribution of nanoparticle aggregates can harbor some of the highest intensities of localized fields for SMSERS, the lack of control and reproducibility over the resulting geometric hotspot patterns remained a significant concern in their applications for quantitative plasmonic biosensing.

Table 1.2. Comparison between different substrates supporting EM hot-spots. Data in a tabular form. [Adapted with permission from Kleinman et al. (2013) Ref.[143], Copyright © 2013 Royal Society of Chemistry.]

	EF Range	Estimated Gaps (nm)	Cost ($-$$)
Non-hot-spot substrates			
Island Films[174–176]	10^4	10 – 100	$$
Periodic Particle Array[177,178]	10^7	10 – 100	$$
Nanorods[179]	$10^3 – 10^7$	NA	$
Nanoshells[180]	~10^6	NA	$
Fabricated substrates			
MFONs[169,181]	$10^3 – 10^{11}$	0.1 – 10	$$
Lace-shell nanoparticles[182]	~10^2	1 – 10	$$
Fs laser etching[183,184]	<10^9	NR	$$
E-Beam lithography[185–187]	10^3 to 10^5	1 – 100	$$
Templated nanowires[188–190]	$10^2 – 10^3$	5 – 100	$$
Bowtie electromigration[191]	10^8	0.1 – 100	$$
Spheres on E-beam posts[192]	10^8	0 – 1	$$
Assembled Structures			
Aggregated [60,73]	$10^6 – 10^{10}$	0 – 10	$
DNA hybridization[193,194]	$10^8 – 10^{12}$	1 – 100	$$
Embedded polymers[195–197]	~10^5	10 – 100	$
SiO_2 encapsulated cores[198]	$10^6 – 10^8$	0 – 10	$$
Particles in wells[199,200]	10^9	0 – 10	$
Nanofingers[201,202]	$10^{10} – 10^{11}$	0 – 10	$$
TERS[203–205]	$10^4 – 10^9$	0 – 100	$$
SHINERS[206,207]	$10^5 – 10^8$	1 – 10	$

Traditionally, hot-spots with high **resolution** (sub-5 nm) have been attained as a natural consequence of stochastic growth or deposition processes,[208,209] including colloidal nanoparticle aggregates,[210,211] electrochemical growth or roughening de-wetting of nanoparticles,[212] or salts from solution phase,[213,214] and the de-wetting of thin films on the surface. The stochastic processes, by nature, result in a large standard deviation in geometries, which reduces the number of the most efficient hot-spots, and also leads to

greater spot-to-spot variability in signal intensities.[215,216] The randomness in geometry makes it particularly hard to predict a response, identify the source of issues, and adopt a rational approach to optimizing performance. Therefore, a more consistent approach must be realized.

Well-defined, high **quality** arrayed geometries such as spherical nanovoids,[217] or square pyramidal pits in a thin gold film,[218] and gold nano bow-tie structures[162,219,220] have been designed to elicit intense EM localizations for stronger spectroscopic signals. Such geometries with an improved definition (i.e., quality) have remained the forte of top-down lithography tools (e.g., E-beam lithography,[221–223] focused ion-beam milling,[224] X-ray interference lithography[225]) and have enabled several types of geometries such as triangles,[226] nanoshells,[227] nanorods,[228] and nanorings.[229] Consequently, well-defined plasmon resonances can be altered in a controlled manner by changing their geometric dimensions. This grants the ability to perform precise calculations and predict their response; however, their fabrication approaches associated with these benefits demand long processing times for limited surface areas and high input costs **(Table 1.2)**.[143] The throughput and cost of fabrication is not only an issue for manufacturing, but also reduces the efficacy of research due to the limitation in the number of samples available for investigations.[230] From a manufacturing perspective, the throughput of the process would be a key determinant of the cost, which is driven to <$5 per sensor chip for point of care applications.[231]

Techniques such as nanoimprint lithography, polymeric, or colloidal self-assembly techniques allow **throughput** to be enhanced, albeit at the cost of defects. The ability of self-assembly techniques to cater to the parallel fabrication of nanopatterns across arbitrarily large areas at a low cost, as well as the several handles it offers towards the tunability of structure dimensions down to the molecular level, are unmatched by conventional lithography tools. However, self-assembly based approaches carry limitations that demand careful attention to ensure their usefulness: a) Poor uniformity, which is often a result of poor process optimization, and in some cases due to the susceptibility of process parameters to environmental variables. This can be addressed by mapping the impact of environmental variables and factoring them within the process optimization; b) Large standard deviations, either inherent to the primary templates produced by the technique, or those that may creep in during different stages of processing; c) Feature shape. Typically,

self-assembled template patterns have a circular feature cross-section. Rectangular, triangular, or other feature shapes with lower-symmetry are uncommon; d) in the absence of any external guidance, self-assembly techniques typically lead to a polycrystalline 2D hexagonal order. Long-range ordering, square or other lattice types besides hexagonal symmetry remain uncommon and can be attained through guidance from a top-down lithographic tool.[232–237] The lack of long-range order and presence of point or line defects are better tolerated by plasmonic sensing applications, as long as the averaged properties are consistent and reproducible with low standard deviations.

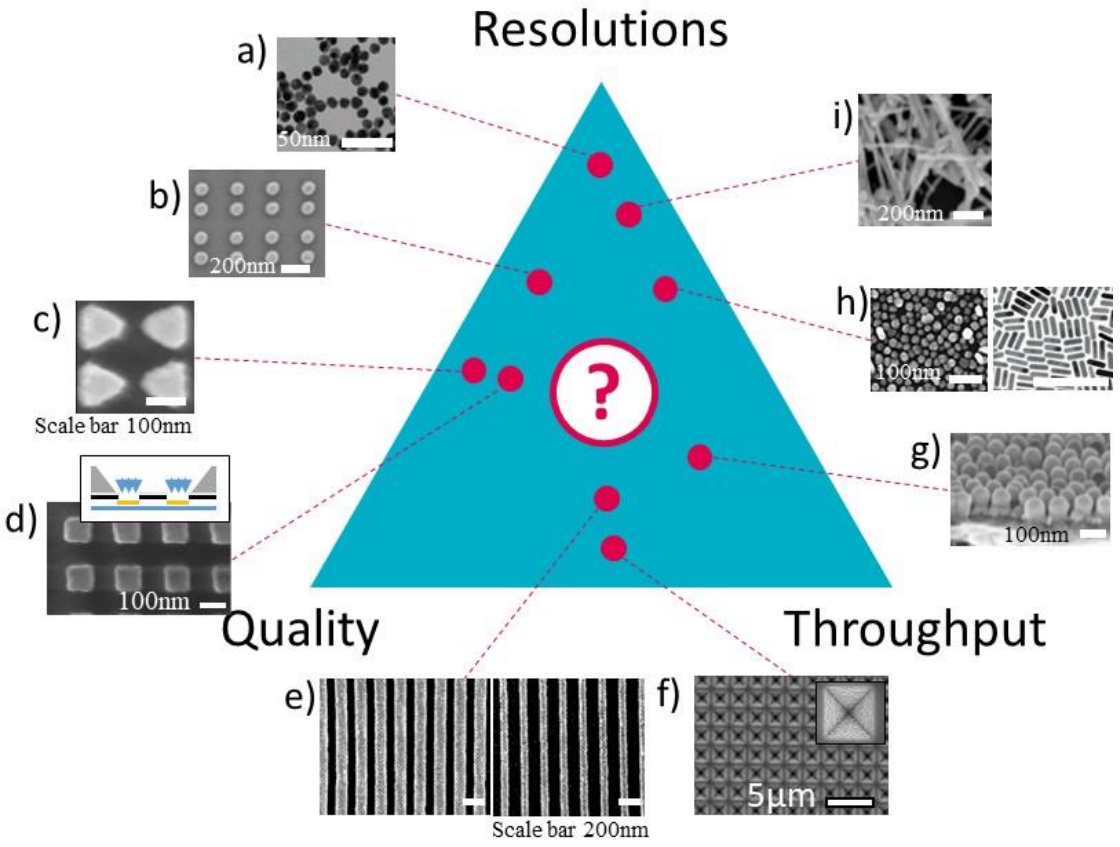

Figure 1.20. Schematic representation of the trade-off between resolution, quality, and throughput in the fabrication of plasmonic nanoarrays with high spatial resolutions, showing the comparative advantages and limits of (a) nanoparticle assemblies,[210] (b) top-down – bottom-up control over nanoparticle assemblies,[223] (c) direct-write techniques,[219] (d) Nanostencil lithography,[238] (e) nanoimprint lithography,[239] (f) photolithography,[240] (g) porous anodized alumina templates,[208] (h) stochastic, random structures, including island film,[209,241] and (i) stochastic chemical growth processes.[242]

Therefore, several of the top-down or bottom-up routes to fabricate nanostructures reported earlier are limited due to the trade-off between resolution ⇔ quality ⇔ throughput. It is necessary to be able to identify drivers that can enable the fabrication of geometries over large areas without heavily compromising with quality and resolution. The thesis will employ an approach developed by Krishnamoorthy et al., to obtain plasmonic nanoarrays with high spatial resolutions relying on the hierarchical self-assembly of amphiphilic di-block copolymers into soft colloids and their subsequent quasi-periodic organization when deposited on a planar surface.[243,244] The approach results in well-defined organic templates on the surface with nanometric control over the width, topography, and pitch, realized by control over parameters of molecular self-assembly. By understanding the impact of the different process parameters on the resulting geometric outcome, it is possible to deliver templates with high reproducibility and uniformity on full wafers, with a yield >90%.[245] These templates are translated into highly sensitive SERS-based plasmonic sensors, with control over metal nanogaps down to the sub-10nm regime.

1.4.3. Co-localization of Molecules In EM Hot-spots

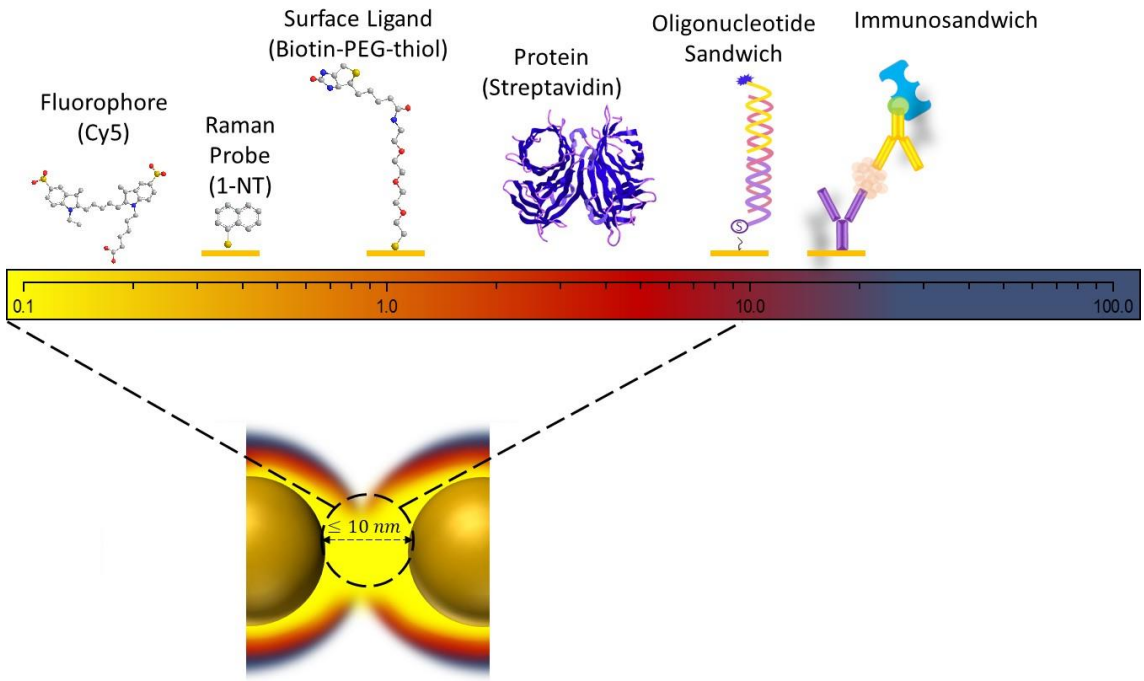

Figure 1.21. Schematic representation of biomolecular length scales in relation to confined geometric spaces within EM hot-spots.

The nanostructured sensing platform and its interaction with the biological entities requires significant attention as it dictates the performance and the sensitivity of the biosensor. Yet another challenge is the application of plasmonic arrays relying on diminishing gap hot-spots for biomolecules with larger footprints **(Figure 1.21)**. The high spatial resolutions sought for maximizing EM enhancements at the gap or curvature hot-spots are not compatible with the spatial requirements to accommodate large biomolecules like proteins. In addition, plasmonic nanostructures are highly resolved and have the potential to change the way biomolecules interact with surfaces; this is known for proteins and their interaction kinetics,[246–251] as well as cell behavior.[252,253]

EM hot-spots play a dominant role in a biosensor relying on SES signals to detect biomarkers, provided that the reporter molecule is strategically positioned in the region where it can leverage from the localized EM yields. EM hot-spots are fundamentally found in the confined gaps between metal nanostructures, which are generally from 1 to 10 nm, with higher EF at lower gaps. There have been cases where researchers have demonstrated large enhancements on substrates using organic reporter molecules that are typically sub-nm in dimensions such as crystal violet (CV), Rhodamine 6G (R6G), or Naphthalenethiol (NT). Positioning such small molecules within gaps as small as 2 nm at the hot-spots is possible due to the small radius of gyration or the spatial footprint of the molecule. For example, between dimers with a gap size of < 2 nm or sandwiched between the nanoparticle and metallic surfaces. Furthermore, the localized EM fields concentrated in the vicinity of the metal surface within a hot-spot extends only to small distances. This makes it difficult for the detection of biomarkers involving hierarchical arrangements of different biomolecular species (such as immunoassays or oligonucleotide sandwiches) to be able to accommodate themselves within the physically constrained regions of EM hot-spots. **Figure 1.22** shows a combination of instances where attempts were made to allow biomarkers to interact with isolated (nanotags),[254] or hybrid nanostructures,[255,256] pre-defined hot-spots,[83,257] 3D/sandwich hot-spots,[258–263] trap within responsive,[264,265] or collapsible surface structures.[266,267]

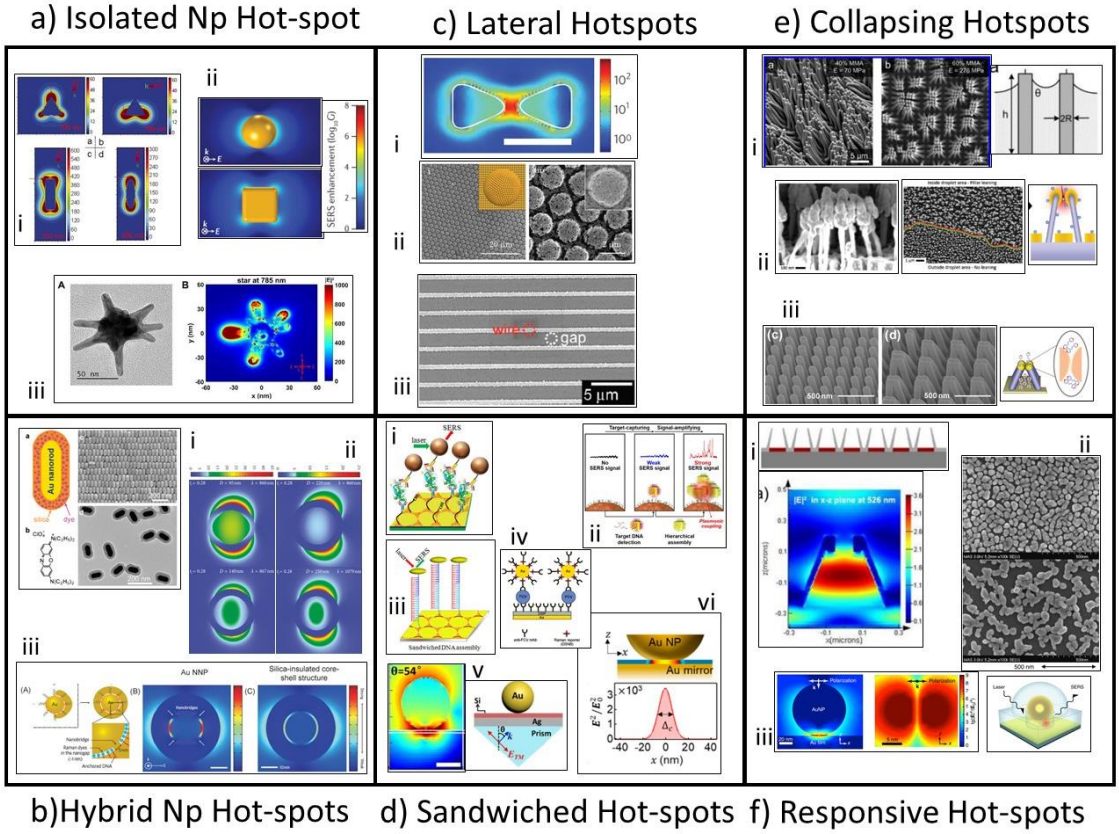

Figure 1.22. Types of nanostructured geometries supporting EM hot-spots. **a) Isolated nanoparticles hot-spot**: i) Ag nanoparticles (Triangular Prism, Rod and Spheroid),[268] ii) nanoparticles and nanocube,[269] and iii) Au nanostar,[254] **b) Hybrid nanoparticles hot-spot**: i) Au-nanorod/SiO_2,[255] ii) Si/Au nanoshell in,[256] and iii) Au nanobridged nanogap particles,[194] **c) Lateral hot-spot**: i) bowtie nanoantenna,[83] ii) Au nanoparticles microhemisphere array,[257] and iii) Metallized Nanowires ,[270] **d) Sandwiched hot-spot**: i) Au nanoparticles assembled on Au triangle nanoarray,[262] ii) Au nanocube clusters assembled on a magnetic microparticle,[260] iii) Au nanorice assembled on Au triangle nanoarray,[263] iv) Au nanoparticles assembled on Au film,[258] v) Au nanoparticles on Ag film on the glass prism,[261] and vi) nanoparticles on a mirror,[259] **e) Collapsing hot-spot**: i) micropillars,[266] ii) leaning nanopillars,[271] and iii) Self-closing of gold fingers,[272] **f) Responsive hot-spot**: i) polymer brush in a cavity of Ag nanovolcano arrays,[265] ii) adaptive silver films,[273] and iii) poly(N-isopropylacrylamide) coated Au nanoparticles on Au/SiO_2 coated silicon substrate.[264]

Further, the plasmonic sensor needs to be adapted to work in complex media, for which the surface functionalization to avoid non-specific binding would also consume part of the sensitive space above the plasmonic interface. While the plasmonic sensors have held high promise for highly sensitive, rapidly responding, and portable configurations,

they need significant transversal development cutting across topics beyond fabrication, physics, and photonics, to ensure reliable devices that address emerging analytical challenges.

It is important to note that there is a need for rational design structures with a nanofabrication route that allows orthogonal control over geometric attributes down to a few nanometers as handles in tailoring near-field profile and intensity of EM field. Consequently, this may result in possibilities to predict biophysical interactions taking place at the surface in nanoscale volumes, using models that can resemble geometric features on the surface.

1.5. Bio-Nano Interactions

In the biosensing application, the fundamental goal of the analyte is to find the answers to the two most important questions: A) *What is it?* and B) *How much is it?* Answering the first question using the enhanced spectroscopic technique can be very efficient. However, quantifying the concentration of molecular biomarkers using enhanced spectroscopies requires the ability to achieve spectroscopic signals that can be directly related to the concentrations of biomarkers and are least affected by the intrinsic standard deviations due to the engineered nanostructures on the biosensing platform, as discussed previously.

1.5.1. Quantitative Plasmonic Bioassays

In the field of biosensors, there is a need for absolute quantification, and technologies making this possible have the edge over other technologies to integrate themselves into the market. Although the urge to introduce techniques that can offer quantification in less time without compromising in their reliability is one of the driving force for the current state of research and development in nanoplasmonic biosensors.[274] This may be within the context of food quality monitoring, where the levels of pesticides or synthetic adulterants need to be regulated.[275] Within environmental health, while monitoring toxic pollutants,[276] or within the medical field, to assess the stage of the disease.[277]

Quantitative analysis is principally dependent upon the calibration curve that can validate the biosensor response in determining the concentration of an analyte. This can be done by applying the most common method relating the spectroscopic signal intensities (or, in some cases, signal peak areas) with the known target concentrations to construct a calibration curve with linear behavior between the signal intensities and the analyte concentrations or sigmoidal (S-shaped) behavior corresponding to Langmuir adsorption isotherm (also discussed in next section) depicting molecular adsorption behavior.[278] Sigmoidal calibration curve consists of a) a lower concentration range, above the noise. This is also used to calculate limit of detection (LOD) or limit of quantification (LOQ) of the system; b) linear range, which demonstrates sensitivity; c) a plateau or decline beyond linear range, where the surface sites at the interface are saturated, and no increment in the signal is observed. A decline in signal intensities can be observed due to the hook effect at high dose, also known as the prozone effect.[279–281] The sigmoidal curve serves to depict the relationship between fraction of the target analyte in the solution near the sensing surface and the adsorbed molecules on the surface. Therefore, sigmoidal behaviour between the analyte concentration and the output signal, validates that the signal originating from the surface relects the nature of the analyte binding to the surface. Also, it highlights the reproducibility and the homogeneity of the surface sites in case of detection based on SES for quantitative analysis.

Most surface-enhanced spectroscopic detection techniques are devoted to demonstrate detection capabilities of biomarkers at lower concentrations with ultra sensitivities in terms of limit of detection or quantification. However, more important is the ability to predict the concentrations accurately in ranges that are relevant to clinical use.[282] The disproportionate enhancements make it particularly difficult to attribute the signal contributions and often can false negative signal outputs.

1.5.2. Specificity and Selectivity

One important criterion is to reproducibly co-localize the analyte or target biomarker into nanostructured regions (EM hot-spots) by identifying appropriate biorecognition elements. In most cases, target molecules do not exhibit affinity or specificity with the plasmonic substrate that enables direct SERS detection. It is, therefore, essential to regulate the surface chemistry in a manner that only the interactions of interest takes place. Although

it is challenging, but it also opens various possibilities benefitting from tailored surface chemistries to assume a variety of applications.

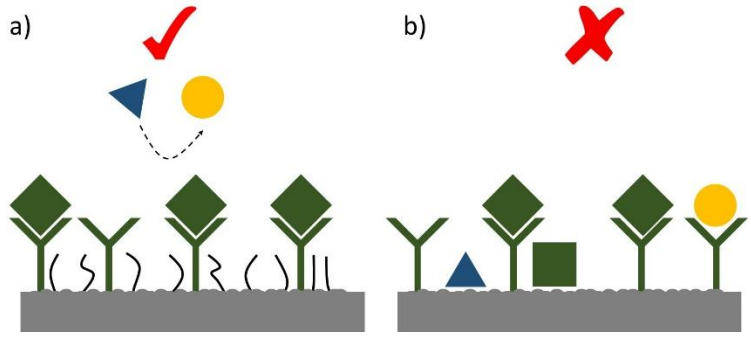

Figure 1.23. Schematic representation of a) favorable condition of both specific and selective binding, and b) unfavorable condition with non-specific adsorption of target and other molecules.

In order to detect, for example, a specific biomolecule from a complex sample (such as blood or urine), the sensor surface chemistries should be should be selective. The surface should be able to capture specifically the targeted molecules and prevent the non-specific binding events **(Figure 1.23)**. It is particularly challenging considering the lower concentration of target biomolecules (nanomolar or lower) and the presence of many other biomolecules in excess (higher order of magnitude). Therefore, anti-fouling molecules or molecules that are inert to biomolecular bindings can be used as the blocking agents to suppress non-specific binding events. This may include organic molecules such as Polyethylene glycol (PEG) in the form of PEG-silane, PEG-thiols, or grafter with poly-L-lysine (PLL-g-PEG) or biomolecules such as Bovine serum albumin (BSA).

1.5.3. Specific Surface Functionalization

It is helpful if the binding of the analyte can be directed at the most sensitive location on the sensor. Surface chemistries can allow selectively modifying surfaces to achieve efficient binding of the target biomolecules, thus improving sensor performance.[283] Therefore, a wide range of affinity-based agents are available that are specific to target species such as antigens, proteins, or cells **(Figure 1.24)**. Methods have been investigated in the literature to immobilize functionalities on the plasmonic surface to capture target species. These methods are typically based on physical, chemical or biospecific interactions

that allow receptor molecules to be anchored and target species or reporter molecules from the solution to be captured.[283]

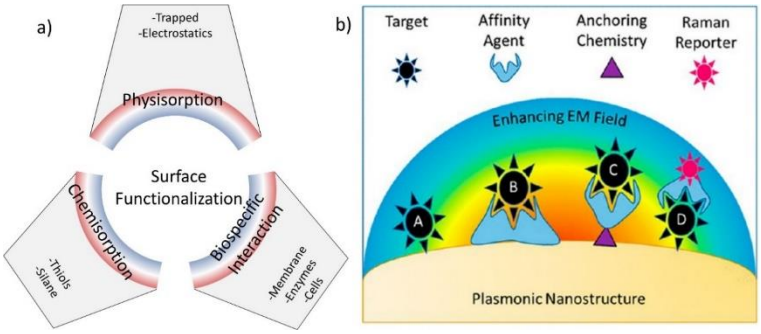

Figure 1.24. a) Type of Surface interactions, b) Representative examples for general SERS sensing schemes: A) Chemisorption-based, b) Affinity-based capture, c) Anchored receptor for Affinity-based capture, and d) Free-floating affinity agent to attach the target to the surface using schemes from A to C. [Reprinted with permission from Szlag et al. (2018) Ref.[283]. Copyright © 2018 American Chemical Society]

Two important factors that are required to consider while selecting biorecognition element are a) the length of the affinity agents, which will determine the distance from the surface or EM field, and b) spectroscopic cross-section of the affinity agents, biological media, and the reporter molecule, which will determine the ability to distinguish the signals from the target molecule in case of a complex environment.

1.5.4. Biomolecular Binding Reactions – Thermodynamic Limitations

Surface coverage of the bound biomolecules in an essential parameter. In fact, the sensor response of the most biosensors is directly related to this parameter. However, biomolecular interactions with the surfaces at ultra-low concentrations pose further challenges due to tailored kinetics of bimolecular adsorptions, which no longer can be ignored; this is the thermodynamic limit. That includes factors that are not intrinsic to the transduction mechanism but are originating from the biorecognition interface.[284–286]

Surface coverage Equilibrium: This can be understood well considering binding kinetics and equilibrium conditions of biomolecules adsorbing on the surface. Biomolecular interaction is, in most cases, reversible. In case of surface-based sensor, this

implies that the targeted molecule will continuously adsorb or desorb to the receptors present on the surface.

The difference in surface coverage Γ (i.e., bound target molecule per unit area) with the time t can be expressed as:

$$\frac{d\Gamma(t)}{dt} = k_{on}c[\Gamma_{max} - \Gamma(t)] - k_{off}\Gamma(t) \qquad \text{Eq. 1.12}$$

Where, k_{on} and k_{off} are the reaction coefficients, Γ_{max} available number of binding sites represents complete coverage, and c is the analyte concentration that sensor surface is exposed to. The first and second part of the right side of the equation represents binding and unbinding events. When the rates of these two events are equal, the equilibrium is reached and relative surface coverage $\Gamma_{\mathrm{eq}}/\Gamma_{\mathrm{max}}$ is obtained as:

$$\frac{\Gamma_{\mathrm{eq}}}{\Gamma_{\mathrm{max}}} = \frac{1}{1 + {k_{off}}/{k_{on}c}} = \frac{1}{1 + {K_D}/{c}} \qquad \text{Eq. 1.13}$$

Where K_D is the equilibrium dissociation constant. The inverse of K_D represents the affinity and thus strength of the interactions. **Figure 1.25** shows that $\Gamma_{\mathrm{eq}}/\Gamma_{\mathrm{max}}$ obeys a sigmoidal behavior with varying concentrations of the target molecule. Adsorption behavior of two molecules with different K_D is represented here.

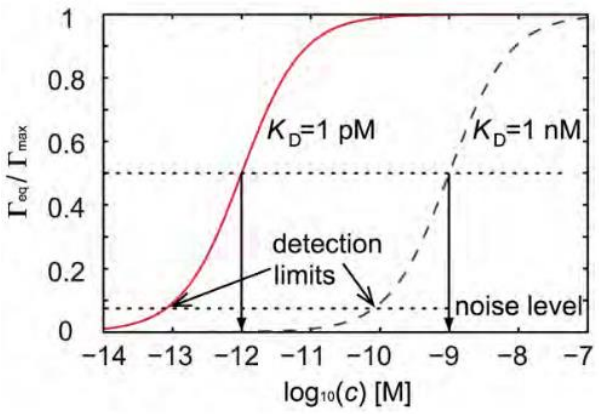

Figure 1.25. Graphical represenation of the equilibrium surface coverage, following to Eq. 1.13 (where, $\Gamma_{eq}/\Gamma_{max} = 1$ represents full surface coverage) in relation to concentration o the analyte corresponding to two interactions with different values of dissociation constant K_D. The red curve

represents the strong interactions (for example streptavidin to biotinylate surfaces) and dashed curve represents weak interactions (for example antigens to antibodies).[287]

Reaction Limited Binding: Yet, it is not just straightforward that the detection limit down to picomolar concentrations can be reached using pairs with stronger strengths. It is not always possible to reach equilibrium binding conditions in reasonable time frames. The solution of the Eq. 1.12 representing the binding kinetics for reaction controlled binding in solutions takes exponential form also called as Langmuir isotherm,[288] (with boundary conditions $\Gamma(0) = 0$ and $\Gamma(\infty) = \Gamma_{eq}$),

$$\frac{\Gamma(t)}{\Gamma_{max}} = \frac{1}{1 + {K_D}/{c}}\left[1 - e^{-(k_{on}c - k_{off})t}\right] \qquad \text{Eq. 1.14}$$

While, Eq. 1.12 explains that similar surface coverages (Γ_{eq}/Γ_{max}) at specific concentrations are obtained from two interactions that have similar K_D. However, the interaction rate can differ with different values of k_{on} and k_{off}. As shown in Eq. 1.14 interaction rate is governed by the exponential term that consists of k_{on} and k_{off}. The time to cover the surface of a certain fraction, x of equilibrium surface coverage can be expresses as:

$$t = \frac{-\ln(1 - x)}{k_{on}c + k_{off}} \qquad \text{Eq. 1.15}$$

For instance, considering the Avidin-biotin binding kinetics, it takes an hour to reach half the equilibrium surface coverage at picomolar concentration (k_{on}~$10^8\ M^{-1}\ s^{-1}$ and k_{off}~$10^{-4}\ s^{-1}$).[288] However, only a few seconds are necessary to reach detectable surface coverage (assuming detection limit of 0.1 ng/cm^2) for a state of the art biosensor such as SPR.[289] Therefore, rapid detection mechanism with low detection limits can potentially dictate the ability of performing fast sensing. Nevertheless, the time scales here only consider the limitations set by the reaction kinetics itself. Following this, transport of molecules to the surface also poses a great concern, as it limits the uptake of the biomolecule which is foreseen in Eq. 1.14 and Eq. 1.15.

Mass transport limitation: The discussion above was based on the assumption that the concentration of the solution in vicinity to the sensor surface is comparable to the

concentration in bulk solution and remains constant throughout the interaction. However, due to binding interactions, the region near the surface becomes depleted of the target molecules, hence reducing the local population of the molecules available for binding. Further binding interactions rely on the transport of more analyte molecules towards the surface. Specifically, at ultra-low concentrations, the binding rate is limited by the ability of the molecule to diffuse through the solution (transport of molecules) to approach the sensor surface.[286] Also known as diffusion limited reaction, typically occurs at an ultra-low concentration (nanomolar or below). At static condition (solution above the sensor surface is stagnant), the target analyte will reach the surface only by diffusion. Considering that all the molecules near the surface bind immediately, the local population of the target molecule will become null and gradually increases in the solution with increasing distance from the surface until the bulk concentration appears. This so called diffusion limited binding to a planar surface can be expressed as,[290]

$$\Gamma(t) = 2c\sqrt{\frac{Dt}{\pi}} \qquad \text{Eq. 1.16}$$

here, D represents analyte molecules' diffusion coefficient in the sample. Eq. 1.16 basically relates to the total number of target species reaching the surface from the bulk solution per unit area in a definite time. Taking an example of streptavidin (60 kDa) that binds to biotin anchored surface (K_D~1 pM), has a diffusion coefficient of around 6x10^{-11} m^2/s.[289] Under these conditions, it would take years to reach equilibrium surface coverage. In addition, the uptake or binding of the target to available sites does not linearly increase with time. A sensor surface that has specific number of sites that can host the target molecule, would initially be limited by mass transport and undergoes reaction limited behavior at some stage due to occupied local binding sites as it reaches equilibrium surface coverage. Hence, at various time points, a balance between the availability of molecules and surface sites, along with the rate of the reaction, governs behavior of the analyte binding to the sensor surface.

The use of plasmonic surfaces that are planar (and are not floating like nanoparticles) do have much of this challenge. However, few reports have demonstrated that surface roughnesses can actually provoke higher densities of proteins to adsorb.[246,251,291] When the total population of the target analyte at ultra-low concentrations (nanomolar or below) is

limited, the capture efficiency of the analyte might stand as a relevant parameter. Here capture efficiency would be the fraction of total molecules that bind to the sensor's surface where they can be detected. In the case of detection based on SES, these surfaces would be further limited to surface sites where EM fields are particularly enhanced (EM hot-spots).

Making use of the strategies offered by various surface chemistries to increase bioreceptor molecules or binding sites at the surface can support higher mass transport in one way.[292] Another way to deal with such limited kinetics is by reducing the sensor footprint, thereby reducing the quantity of analyte that may be necessary for the sensor response.Additionally, use of microfluidics environment with careful consideration and strategic parameters (such as flow rates/static conditions, channel height, channel length and time) can help to improve the surface to volume ratio and hence efficient analyte capturing possibilities.[293]

Strategically positioned biomolecules in the EM hot-spot geometries on the substrate plays a significant role in determining the performance of the molecular biosensor based on SES. At the same time, taking advantage of the biotechnologically advanced tools to capture bioanalytes efficiently. It becomes necessary to identify a substrate that offers consensus about the gap-size in gap hot-spot that can accommodate large biomolecules while concentrating EM fields strong enough to exhibit higher sensitivities in the range of nM to fM.

1.6. Rational Design Of Plasmonic Bioassays

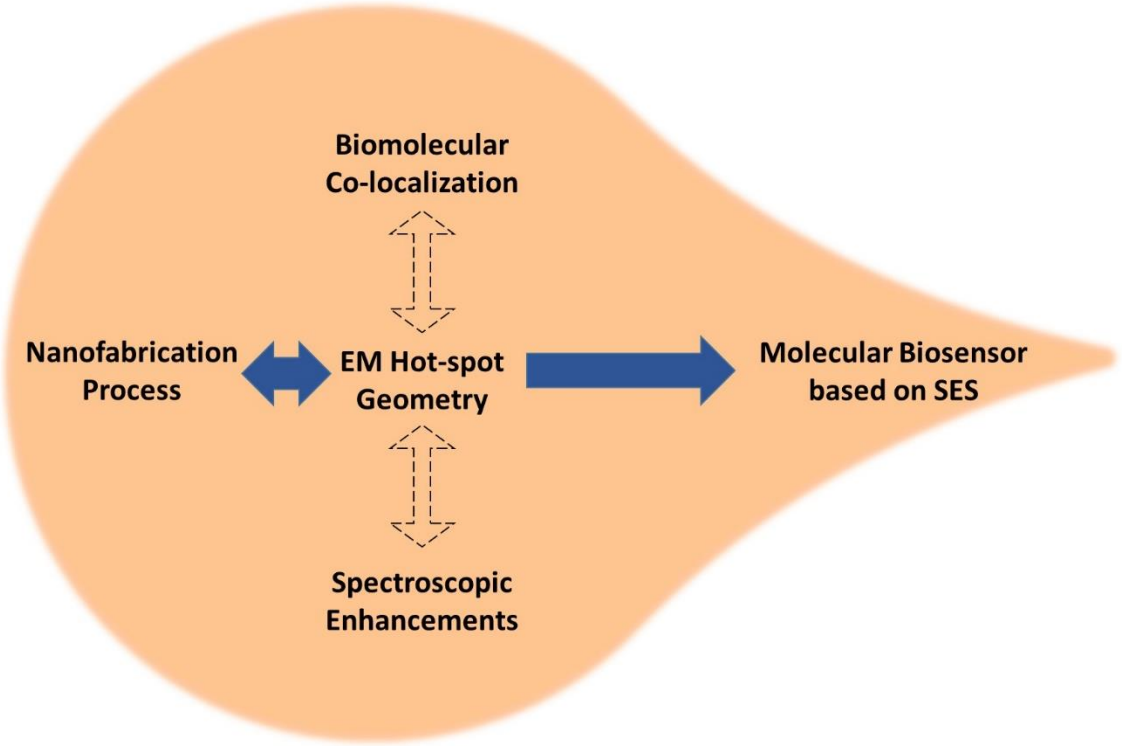

Figure 1. 26. Correlation between the nanofabrication process ⇔ EM hot-spot geometries enables investigation of the correlation between EM hot-spot geometries ⇔ biomolecular co-localization and EM hot-spot geometries ⇔ Spectroscopic enhancements, that can help to build rationally designed molecular biosensor based on SES.

Many challenges remain – from the development of efficient and effective biosensors to address urgent clinical needs.[38,285] The main focus remains to capture the molecules of interest specifically, and then to draw relevant information using transduction techniques that offer rapid feedback with ultra-high sensitivities. Review of the state of the art highlights the need for highly enhancing and uniform EM hot-spots on the sensor surface as means to transduce the binding events reliably at very low concentrations. These areas should then be functionalized optimally using surface chemistries to improve target capture efficiency of the sensor surface. To ensemble such characteristics in the sensor, one would need rational approaches along lines of following key objectives:

✓ *The ability to fabricate with resolutions down to sub-10nm lengthscales, combined with quality and throughput*. Fabrication of electromagnetic hot-spots with resolution down

to sub-10 nm is a challenge, while assuring the quality over large areas, along with scalability and throughput necessary to produce large number of samples for systematic investigations. Plasmonic nanoarrays presenting large enough areas can permit probing using techniques with large physical footprints. The fabrication process used to produce the plasmonic arrays should thus ideally deliver large areas, typically wafers, in a reasonable time, ideally in a matter of a few minutes to an hour.

- ✓ *Orthogonal Control over geometric variables.* Systematic investigations require robust correlation between process parameters ⇔ structural characteristics of the EM hot-spots ⇔ optical/spectroscopic properties ⇔ biosensing performance. This would require process handles to control one variable at a time. This remains often a non-trivial challenge.
- ✓ *The ability to design/model the EM hot-spots*. This requires the ability to achieve geometries of hot-spots experimentally that are close to the idealized models used for calculations. Thus, we will need a technique with well defined geometric features and has low standard deviation in characteristic geometric variables.
- ✓ *The ability for reliable and reproducible signals.* Reliable and reproducible signals are one of the significant factors that limit their application for commercial biosensing based on SES. This requires homogeneity in geometries across a given sample and over multiple batches of samples produced. This is critical to ensure quantitative detection of biomolecular analytes, and to assure reliability in detection.
- ✓ *Quantifying the molecular concentrations on plasmonic nanoarrays.* The signal contribution to the plasmonic sensor is disproportionately dominated by the concentration of analytes present at the hot-spots as function of EM enhancements at the hot-spots. Rational design would require ability to separate the contribution from the overall molecular concentration from those that are present at the EM hot-spots. This would help optimizing the assays to maximize the presence of molecules at the EM-hot spots.

1.7. Summary

Nevertheless, confronting challenges that were discussed above and rationally designing the nanoplasmonic biosensing platform can eventually support the attempt to integrate SES based detection schemes within quantitative biosensing applications. The

next chapter **(Chapter 2)** of this thesis focusses on the nanofabrication technique that enables possibilities to address the gap in the EM hot-spot fabrication technology. Chapter 3 to 6 demonstrates the application of fabrication techniques in understanding the impact of biomolecular sensing behavior with varying EM field distribution in and around the hot-spots.

Chapter 2. Nanofabrication And Characterization Methods

Some parts of this chapter are based on the book chapter published in Intechopen, UK "Nanoplasmonic Arrays with High Spatial Resolutions, Quality, and Throughput for Quantitative Detection of Molecular Analytes", in *Nanoplasmonic* R. Rastogi, M. Beggiato, P. Michel-Adam, S. Juodkazis, S. Krishnamoorthy. DOI: 10.5772/intechopen.89064.

The nanofabrication process of the plasmonic nanostructures was performed in the cleanroom (class 100) facilities of the Materials Research and Technology Department, Luxembourg Institute of Science and Technology, Luxembourg. The ambient humidity was maintained between 45% and 55%, monitored by a hygrometer inside the cleanroom. In **section 2.4**, I discussed characterization tools are that include atomic force microscopy (AFM), and scanning electron microscopy (SEM) for closely following geometric features with varying process controls. Nanoparticle hydrodynamic diameter was observed using dynamic light scattering (DLS). The optical response of geometries, their plasmonic coupling behavior were analyzed using a UV/visible spectrophotometer and a home-made extinction optics set-up at Light, Nanomaterials & Nanotechnologies (L2N) lab, the University of Technology of Troyes, France. The spectroscopic measurements employed microscopic Raman spectrometer for SERS and MEF measurements. Quartz crystal microbalance (QCM), and surface plasmon resonance (SPR) were employed for the analysis of (bio)molecular interactions with nanostructured.

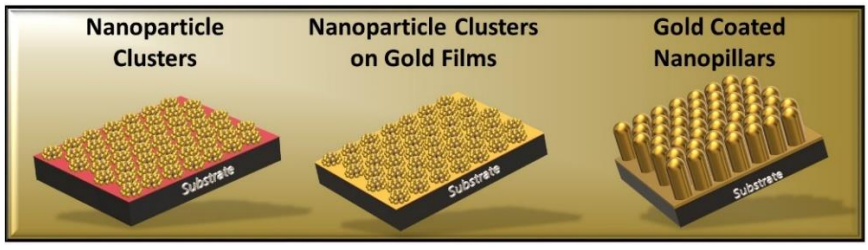

Figure 2.1. Illustration of the correlation between Nanofabrication, surface-enhanced spectroscopies and Bio-nano interactions +

The substrate was cleaned every time before starting coating the substrate with the polymeric template. Organic and inorganic contaminants on the surface of the silicon dioxide (SiO_2) present on Quartz, Glass, or Silicon (with native oxide) were removed using three solvents Aceton, Ethanol, and Isopropanol (solvent cleaning) in the same sequence and drying the surface with Nitrogen (N_2) immediately after. Furthermore, the substrate was exposed to three minutes of Oxygen plasma in the reactive ion etching chamber at low pressure,[294] or ten minutes of UV/Ozone (depending upon availability),[295] to oxidize the surface. For full wafer coatings, CO_2 snow jet cleaning helped further remove hydrocarbon contaminants and the nanoscale dust particles. The cleaning process helps to improve the wettability of the surface, and adhesion of the polymeric template with the surface.

2.1. Molecular Self-Assembly For Highly Resolved Nanolithography

One of the key challenges is to be able to produce surfaces with nanoscale sensing surfaces reliably, at low cost, using manufacturing compatible techniques. This section specifically discusses all the aspects of the nanofabrication technique based on molecular self-assembly of block copolymers to deliver wafer-level fabrication of nanoplasmonic interfaces with spatial resolutions down to a few nanometers, assuring high quality and low costs. The approach permits systematic variation to different geometric variables independent of each other, allowing the significant opportunity for the rational design of nanoplasmonic sensors.

2.1.1. Phase Separated Block-Copolymer Thin-Films

Polymers are long chains of repeating subunits known as a monomer. Polymers that contain similar types of monomers can be called homopolymers, while a mixture of two or more types of monomer chains (polymers) are called copolymers. Block copolymer (BCP) is a type of copolymer in which two or more homopolymer chains are connected end-to-end, providing different functionalities with their distinctive chemical nature **(Figure 2.2)**. Diblock copolymer, which has two dissimilar polymer chains covalently linked to each other are the simplest form of BCP.

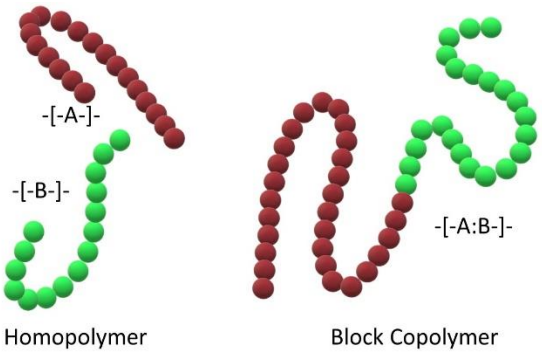

Figure 2.2. Structural representation of linear homopolymer and block copolymer (di-block).

Microphase separation in block copolymers gave rise to several advantages in obtaining lithographic patterns for nanofabrication of three-dimensional architectures.[296–298] With the help theoretically and experimentally developed phase diagram, these morphologies can be predicted, as well as modulated as per requirement.[299,300]

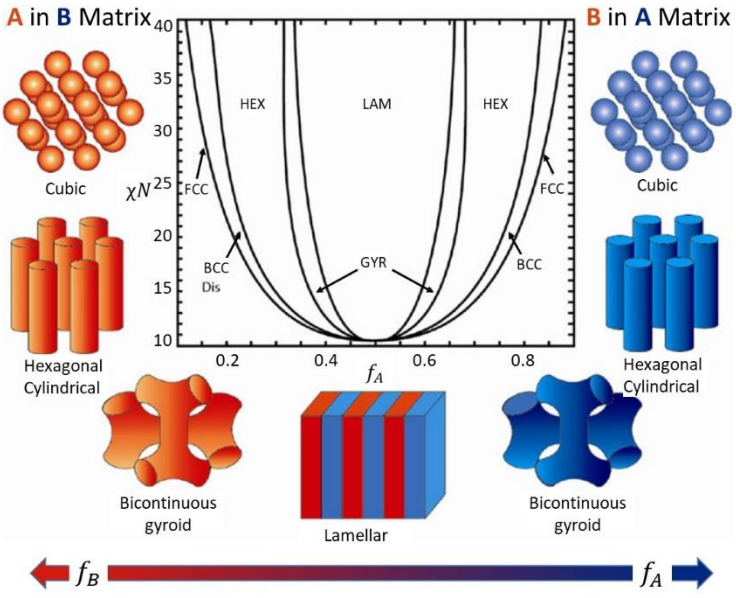

Figure 2.3. Phase diagram for diblock copolymers representing typical mesophases: face-centered cubic (FCC), body-centered cubic (BCC), hexagonal (HEX), bicontinuous gyroid (GYR) and lamellar (LAM) phase. [Adapted with permission from Gromadzki (2010) Ref.[301], Copyright © 2010, Springer Nature]

The assemblies are determined by a set of parameters such as volume fraction of the blocks (f), the polymerization degree of the copolymer (N), and the Flory-Huggins interaction parameter that reflects the enthalpic interaction amongst the blocks (χ). As

shown in **Figure 2.6,** χN is the segregation power that relates to the immiscibility of the two blocks. Above order-disorder transition (ODT), at a higher value of χN, the morphologies are known to exist in five ordered microphase structures. The role of matrix shifts from one block to another depending on the f values of each block. The Flory-Huggins parameter can be expressed as a function of temperature T in the form of:

$$\chi(T) = \chi_S + \chi_H/T \qquad \text{Eq. 2.1}$$

Where the χ_S is assumed to be the contribution originating from the entropy and is independent of T, and χ_H/T is presumed to be the contribution originating from the enthalpy of the polymer. For chemically dissimilar blocks in a BCP, χ is directly proportional to cohesive energy density between the blocks. Therefore, at higher values χ, the driving force for demixing or phase separation is higher.[302,303] Self-assembled structures due to enthalpic modulation in apolar BCPs have been used as templates to grow nanoscale tubes, porous materials, or nanopillars.[304–308] However, phase-separated thin films of BCL, limit the freedom to manipulate further into their periodicities a.k.a. center-to-center spacing without changing the polymer size and composition. Templates made of BCPs are therefore limited to the possible arrangements that the BCL of that composition allows physically on the surface. On the other hand, kinetically driven structures from the micellization of BCP in the solution phase allow orthogonal control over various geometric attributes without needing to change the polymer compositions. Thin-film templates formed out of BCP reverse micelles are kinetically trapped structures on the surface. They are advantageous from the point of view that their size, width, and separation can be orthogonally controlled by modulating solvent quality, concentrations, or evaporation speeds.

2.1.2. Micellization Of Amphiphillic Block Copolymers

Amphiphilic di-block copolymers are those polymers in which one end is hydrophobic and the other end is hydrophilic. Micellization of BCP in solution occurs when the solvent selectively dissolves one of the chains and leading to kinetically driven structures in which one block constitutes the core and the other constitutes the corona such as micelles or reverse micelles. They can arrange themselves into structures such as spherical, rod-like, or vesicle (**Figure 2.4**).

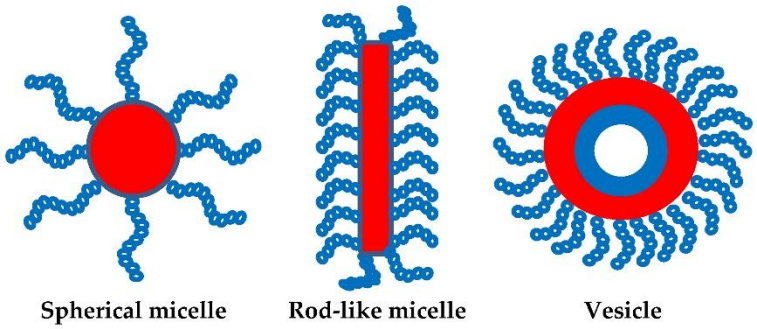

Figure 2.4. Different micelle structures resulting from micellization of amphiphilic di-block copolymer.[309]

The micellization process is highly dependent upon the solvent and the polymer concentration micellization process starts when the concentration of the BCP in the solution is above critical micelle concentration (CMC). Micelles are formed d in polar solvent such as ethanol, or water and the reverse micelles are formed in an apolar solvent such as toluene, or xylene. The shape of the molecule can be determined by its packing parameter, β.

$$\beta = \frac{V_H}{L_C A_0} \qquad \text{Eq. 2.2}$$

whereV_H is the volume occupied by a hydrophobic chain, L_C is the hydrophobic chain length, and A_0 is the surface area of the hydrophilic chain.[310] Spherical micelles are formed when the packing parameter is above zero and below ~ 0.33 ($0 < \beta < 1/3$) **(Figure 2.6)**. The overall size of the micelle is, however, proportional to the total size of the BCP.

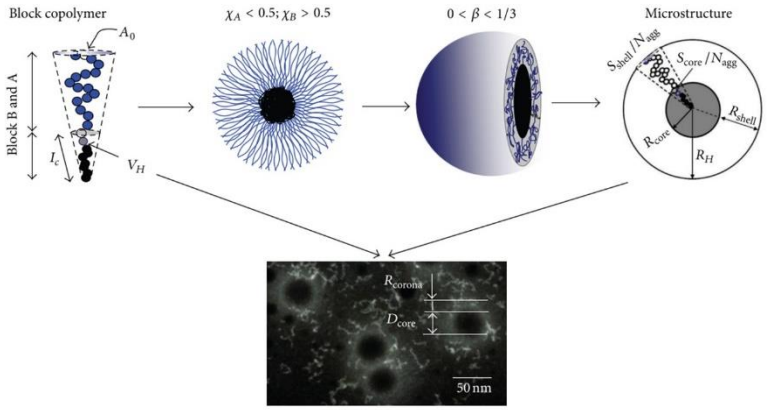

Figure 2.5. Representation of the aggregation number of a spherical micelle in relation to polymer compatibility with the solvent and packing parameter.[310]

Amphiphilic di-block copolymers can self-assemble into reverse micelles when dissolved in a solvent that selectively dissolves only the apolar block of the copolymer. These reverse micelles can be obtained or be induced into attaining a spherical morphology, with a feature size determined by their aggregation number. The micelle aggregation number is not only a function of the molecular weight and composition of the copolymer but also the quality of the solvent used and the presence of additives **(Figure 2.5)**. As a consequence, the size can be varied independent of the molecular weight, using solvent quality and concentration of additives, as useful drivers to fine-tune template geometries and eventually those of resulting plasmonic arrays. The spherical micelles are colloidal structures which can be readily organized on a variety of surfaces to yield a 2D hexagonally ordered dot-array templates. These templates are subjected to physical or chemical means of pattern transfer to produce nanopatterns of desired materials. Pattern formation on surfaces using copolymer reverse micelle approach is fundamentally different from that of microphase separation in BCP thin films.[311–313] The size of reverse micelles in solution, which eventually determines the feature sizes on the surface, is independently varied by engineering the solvent quality or the use of additives. The standard deviation of the templates on the surface is determined by that of the micelles in the solution phase before deposition, which in turn is governed by the inter-micellar exchange process. The exchange process is slow due to the slower diffusion for larger molecular weight polymers or when solvent with high selectivity to the corona-forming blocks is employed.[314]

2.2. Spatially Controlled Molecular Templates

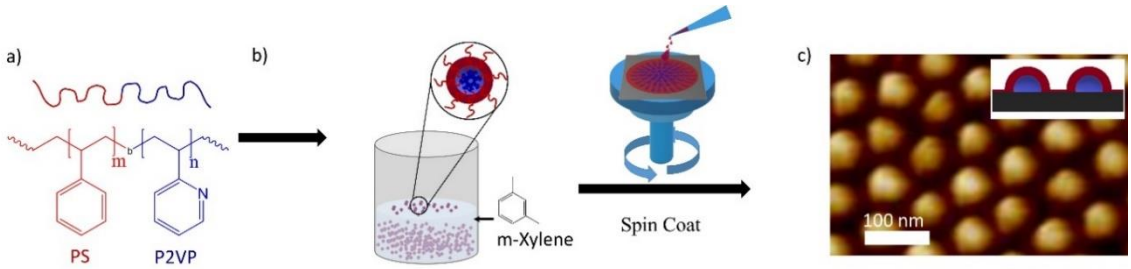

Figure 2.6. Schematic representation of the self-assembly of amphiphilic diblock copolymer into reverse micelles and their subsequent assembly to form two-dimensional arrays on the surface.[244]

During the spin-coating process, the solvent-laden micelles in solution deform on the surface to assume an ellipsoidal shape, with partial fusion of corona from adjacent reverse

micelles resulting in the globally continuous organic film presenting periodic contrast in topography with an ultrathin film (<5 nm) in the background. The pitch of the ensuing pattern on the surface can be varied in steps <5% of its mean value, through control over the evaporation rate or the concentration of the micelles in solution. The evaporation rate can be controlled using spin or dip coating speeds (discussed later in this section). The ability to vary the lattice periodicity within a certain window is attributed to a range of distances for which the PS blocks from the corona of adjacent micelles can still meet upon deformation and film formation. When this condition is not met, namely, at low solution concentrations or high spin speeds, the reverse micelles are spaced too far apart, resulting in patchy coverage. On the other hand, at high solution concentrations or at low spin speeds, the excess concentration beyond what is necessary toward a monolayer appears as multilayers, as shown in **Figure 2.7**.[245] The topography of the reverse micelle film is a variable that can be determined by the relative humidity in the ambient environment during the coating process. This is attributed to the change in moisture that is likely to concentrate at the polar core-forming PVP and consequently increasing the interfacial tension resulting in resistance to collapse and as a result a higher topography. Under optimal conditions of coating, micelle arrays can be produced with a standard deviation of <10% in geometric attributes across a complete wafer.

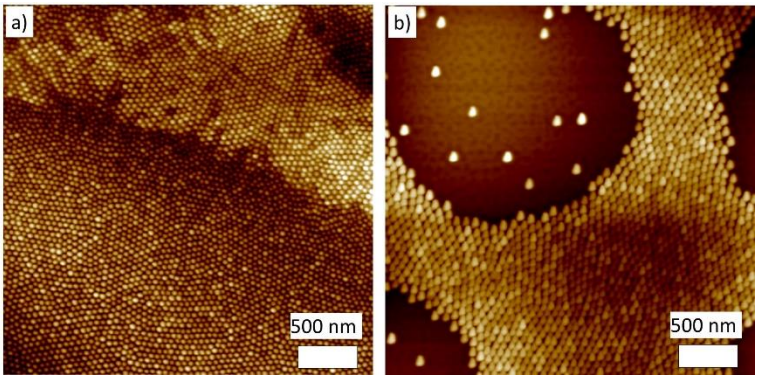

Figure 2.7. AFM images of a) multilayered template and b) patchy template after spin coating

In a specific example shown in **Figure 2.6**, reverse micelles of polystyrene-block-poly (2-vinyl pyridine) (PS-b-P2VP) obtained from dilute solutions of m-xylene. Here, a copolymer with a molecular weight of 81.5 kDa, and a PDI of 1.10, at a concentration of 0.5%w/w in m-xylene is spin-coated on a clean silicon surface at 5000 rpm resulting in a hexagonally ordered array with feature heights of 20 nm and pitch of 69 nm with typical

standard deviations <15% in all geometric variables. During the spin-coating process, the solvent-laden micelles in solution deform on the surface to assume an ellipsoidal shape, with the corona from adjacent reverse micelles coming together resulting in the globally continuous thin film presenting periodic topography and ultra-thin film (<5 nm) in the background. The center-to-center distance or the pitch of the template arrays could be systematically decreased in steps of <5 nm between 50 - 69 nm by increasing the solution concentrations from 0.6 – 1 w/w % at a fixed spin-speed of 5000 rpm or decreasing spin-speeds from 9000-2000 rpm at a fixed concentration of 0.7%. The ranges were found to constitute an optimal window of conditions where a continuous uniform film was obtained. The multilayers above 1 w/w% and patchy layers below 0.5 w/w% were observed, as shown in **Figure 2.7**.

2.2.1. Scalability Across Full Wafers

Among key limitations encountered by self-assembly-based approaches, in general, is the scaling up to practically large areas while ensuring high consistency and reproducibility. The issues of reproducibility arise mainly due to the sensitivity of the process outcome to environmental parameters. Such sensitivity also limits process scalability, due to inconsistencies encountered when coating large areas like full wafers and to limited batch-to-batch reproducibility. These issues are true also for the case of self-assembly of amphiphilic copolymers, and this can be addressed only by adequate investigations directed at mapping the impact of different environmental variables on the process outcomes. Several sources of variability were identified and addressed for the self-assembly of amphiphilic copolymers, including the presence of moisture and contaminants in solution; the history of preparation (agitation and incubation), temperature, and humidity; differences in surface roughness or surface energy (e.g., due to organic or particulate contaminants on the surface); changes to solution concentrations due to solvent evaporation during use; and inadequate mixing of the polymer. Under optimal conditions, the assemblies of reverse micelle feature exhibit standard deviations lower than 15% across full wafers.

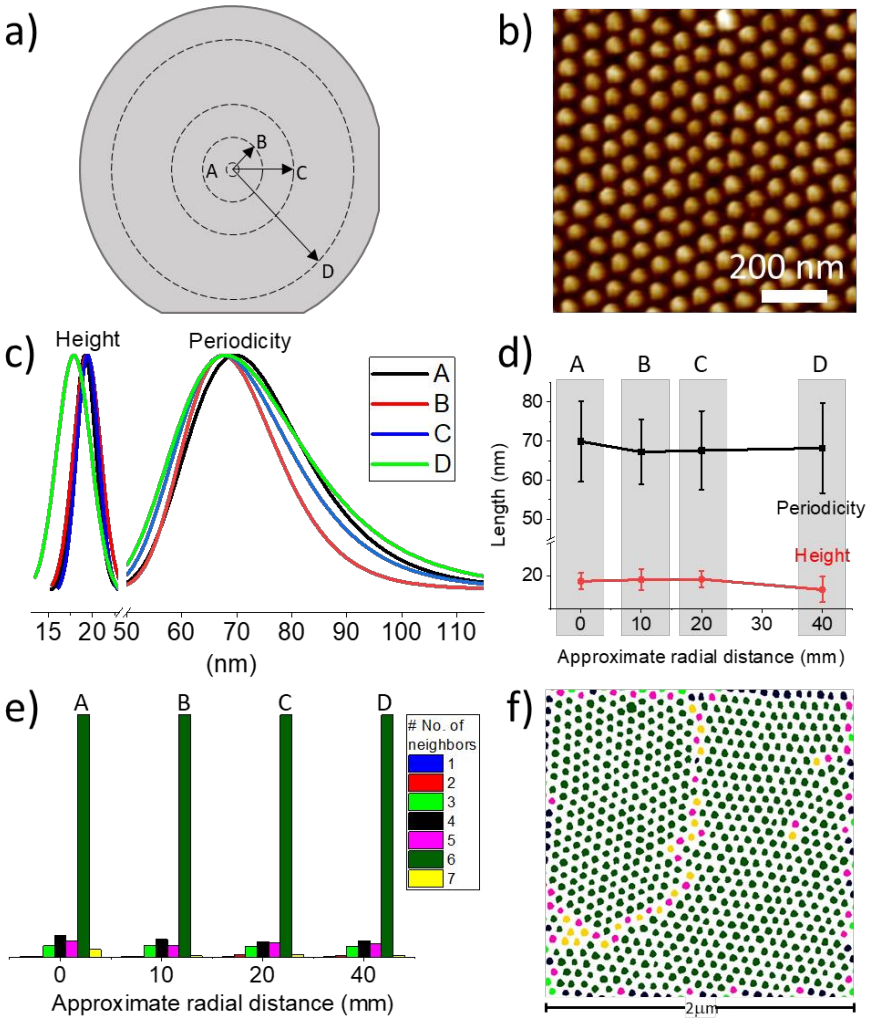

Figure 2.8. Demonstration of scalability combined with uniformity on full wafers of optimized coatings (a) Schematic of radially separated points from center to the edge of 100 mm wafer, (b) where tapping mode AFM measurements are performed (image indicated for point a), (c) The distribution of height and pitch across the full wafer, (d) with mean values plotted as a function of radial distance from the center, and error bars showing standard deviation in corresponding feature dimensions at a single point, (e) Histogram of nearest neighbors showing predominantly six nearest neighbors as expected for hexagonal assembly, maintained across the wafer and (f) representation of nearest neighbors using Voronoi analysis with the features colored corresponding to the number of nearest neighbors as indicated in (e).

A specific outcome of optimization of the templates represented in **Figure 2.6**c on a 100 mm silicon wafer can be seen in **Figure 2.8**, which shows the distribution for height, diameter, pitch, and nearest neighbors, in different regions of the wafer. Typical characterization involves AFM topography for heights and diameters (within errors of

AFM tip-convolution) and SEM top view and image analysis using ImageJ or MATLAB. A representative AFM image recorded in the tapping mode is shown in **Figure 2.8**b. The characterization is critical for each batch of samples, and it is possible to scale the process to several batches of wafers.[252] Points A, B, C, and D correspond to four positions representing systematically increasing radial distances from the center to the edge of the wafer. AFM measurements at these points show a standard deviation of <15% for geometric variables and <10% variation of their mean values across the full wafer. Voronoi analysis of the AFM images shows a predominance of six nearest neighbors as expected for hexagonal packing, which is uniformly maintained across the wafer (**Figure 2.8e, f**). The outcome demonstrates the feasibility of reliable scaling up of the technique to cater to nanostructures over large areas.

2.2.2. Orthogonal Control Over Geometric Attributes

Anhydrous m-Xylene solvent was utilized to prepare the reverse micelles of PS-b-P2VP BCP, at concentrations ranging from 0.3 w/w% to 2 w/w% for different molecular weights. The solutions were prepared in a small pre-cleaned vial with Teflon cap and left overnight for stirring at low speed to ensure equilibrium. Freshly cleaned substrates were mounted on to the chuck held by a low vacuum in the spin coater. 20 to 40 µl of the polymer solution was poured on to the substrate and was coated at the spin speeds between 2000 to 9000 rpm for 60 seconds. The spin speeds and the concentration were varied depending on polymer size to avoid multilayers or patchy coatings of the polymeric features on the surface.

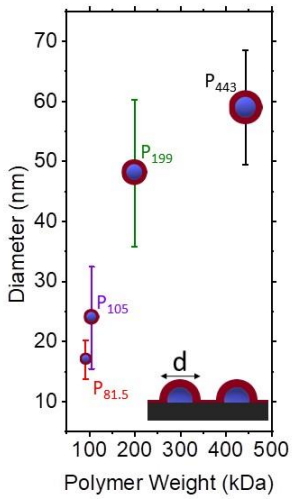

Figure 2.9. Graphical representation of diameter (d) and standard deviation obtained from AFM analysis of each type of polymer coating showing the proportional relationship of diameter of diffused ellipsoids with the molecular weight of the polymer.

As discussed self-assembly based on molecular arrangements, open possibilities to manipulate geometric attributes of the assemblies at the molecular level. The aggregation number of the micelle is also a function of the molecular weight of the BCP, hence the size of the micelle. To start with, four different PS-b-P2VP BCP sizes (81.5, 105, 199, and 443 *kDa*) were compared based on the diameter of diffused micelle structures on the surface using tapping mode AFM images, shown in **Figure 2.9**. Depending on their size there exists the range of periodicities (center to center spacing) that are possible to achieve during the fabrication of the organic templates. In figure **Figure 2.10**, calibration curves are shown with varying periodicities as a function of the concentration of the polymer in the solution and/or the spin speed while coating. The periodicity ranges from ~50 to ~200 nm from BCP of different sized used here. However, the aspect ratio of the diffused features differs from one to another. This also governs the space between the features and can be tuned as per the requirement with sub-5 nm steps.

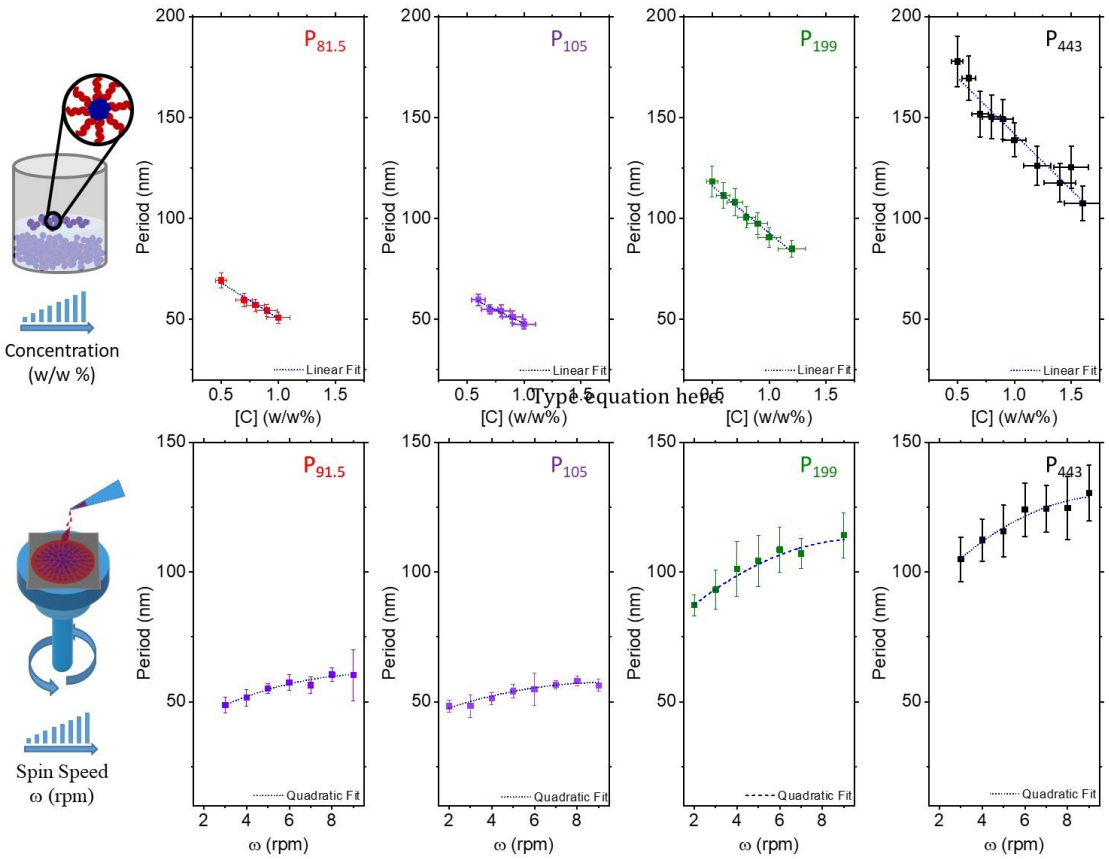

Type equation here.

Figure 2.10. Demonstration of orthogonal control over nanoscale geometries using the fabrication process.

After the coating of the organic template on the substrate with the desired geometric properties (such as period, height, and diameter), the size of the diffused spherical micelle structures could also be modified by exposing them to oxygen plasma. The height systematically decreased to ~0 nm with a gradual increase in time of exposure **(Figure 2.11)**. In the reactive ion etching chamber, the templates were etched at the rate of 0.3nm/s. This was an important factor to consider when the thickness of the polystyrene was needed to be decreased (for transferring pattern to SiO_2) or to expose PVP core (for stronger attraction between negatively charged negative particles and positively charged PVP), discussed in section 0.

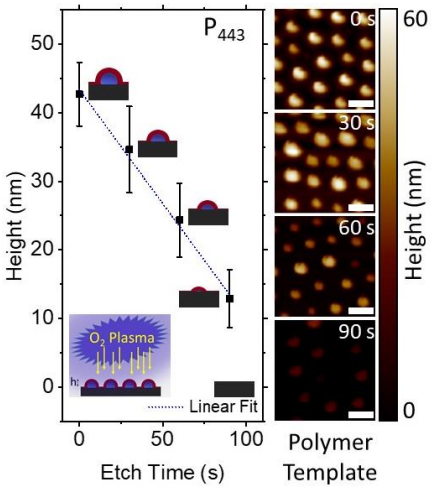

Figure 2.11. Control over dimensions using oxygen plasma etching with etch rate ~0.3 nm/s shown for polymer template#B (443 kDa). Scale bar: 200 nm

The interest of optimization was to identify periodicities or separations ranges associated with the polymer types to define coating conditions to obtain defined templates or masks to investigate various factors that are necessary to achieve high sensitivities (discussed in chapter 3 to 6). Throughout the thesis, two types of nanostructures were deduced from these high-resolution polymeric templates, a) Nanoparticle Cluster Arrays (NCA),[315] and b) Nanopillar Arrays (NPA).[316] However, there exists a variety of possible structures that are possible to fabricate using the pattern transfer process from these organic templates of high resolutions, shown briefly in the next section.

2.3. Nano-Plasmonic Arrays By Pattern Transfer

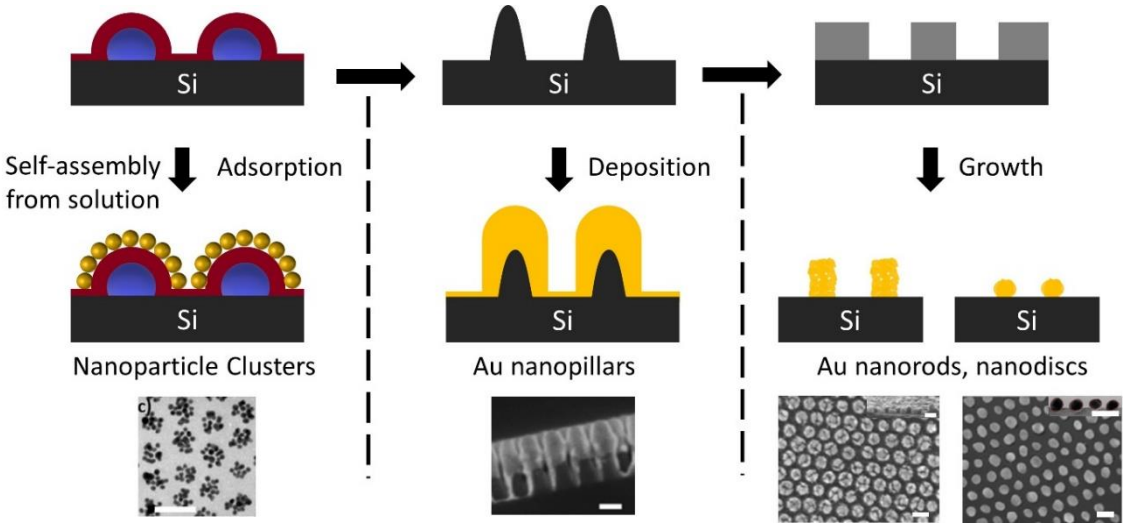

Figure 2.12. Fabrication of plasmonic nanoarrays with different profiles, size, and distribution of metal nanostructures can be attained by control over pattern-transfer processes. In all cases, the advantages of the original templates including the uniformity and scalability are preserved.[316–318] Scale bar: 100 nm

Fabrication of plasmonic nanoarrays starting from organic templates relies on pattern transfer approaches, for example, template-guided growth, deposition, or etching, to define noble metal nanoarrays with the conservation of pitch from the original template. The pattern transfer approaches offer large flexibility in the geometry of the individual features, thus making it possible to fabricate plasmonic nanoarrays of different types, for example, nanoparticle cluster arrays, nanopillars arrays, nanorods, or nanodiscs. The pattern transfer parameters provide independent control over the size, shape, and aspect ratio of the features and should be optimized to ensure that they do not affect the spatial arrangement, uniformity, and reproducibility from the original template. Although the pattern transfer approaches are common in semiconductor fabrication, extending them to work at the scale of few nanometers requires rigorous optimization and quality assurance to ensure low standard deviations and reproducibility in geometries. Further in this section different pattern transfer methods to reach such three different plasmonic nanoarrays have been discussed in detail **(Figure 2.12)**.

2.3.1. Nanoparticle Clusters

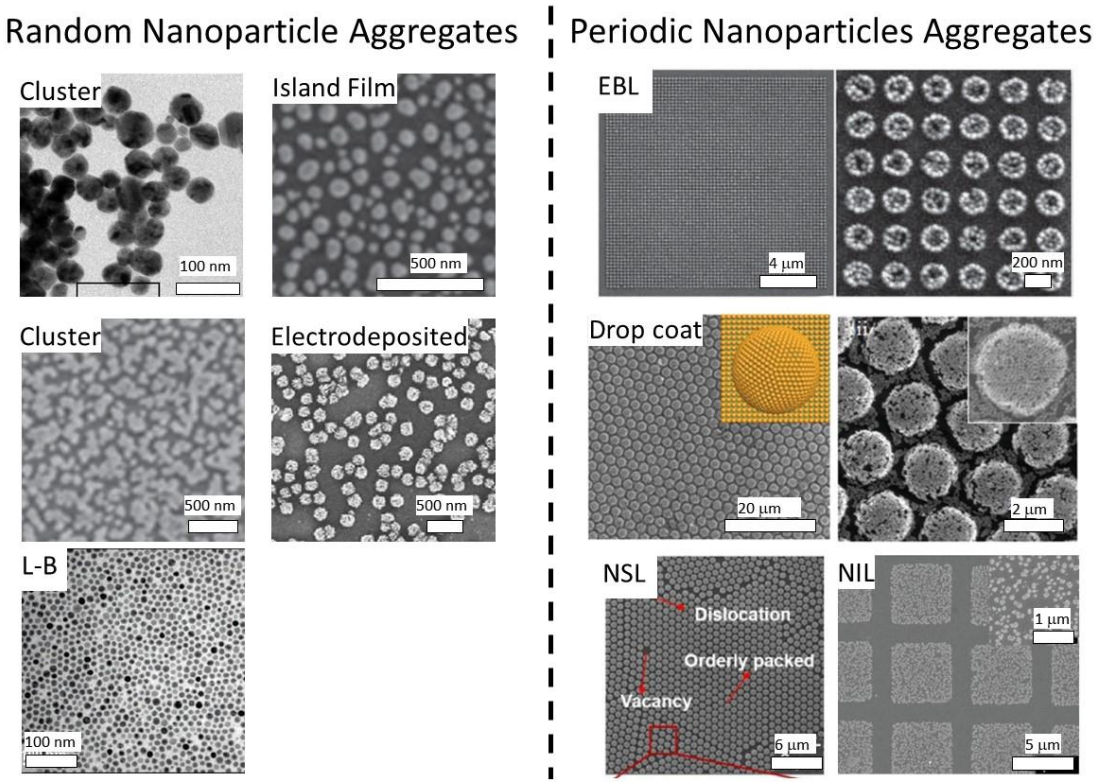

Figure 2.13. Different reported instances in literature of nanoparticle aggregates. Randomly arranged,[82,319–321] and periodically arranged.[322–324]

Clusters (used interchangeably with "aggregates" in this report) of metal nanoparticles behave differently from their isolated counterparts due to the collective optical behavior arising out of plasmonic coupling between the constituent nanoparticles.[325–330] Clusters of nanoparticles are known to behave as hot particles, with significantly enhanced electromagnetic fields at the inter-particle junctions.[331–334] Consequently, clusters exhibit higher extinction cross-sections, with hot spots that can be excited at lower energies than the isolated particles. The aggregation-induced color change of gold nanoparticle suspensions caused by the analyte of interest has been the basis of several biological assays.[335] Such random aggregation typically results in a large distribution in the number of particles per cluster, with a distinct lack of control over those numbers. To achieve clusters with desired optical properties, it is essential to be able to produce them with a narrow distribution in the size, shape, and spatial arrangement between nanoparticles within the cluster and between clusters in an array. Such clusters were

demonstrated using templates fabricated by electron- beam lithography (EBL)[170,326,327,333,336–338] and controlling the size of the template to obtain dimers, trimers, quadromers, and multimers. Since EBL is time-consuming and expensive to achieve high-resolution patterns spanning large areas, other low-cost means to achieve controlled nanoparticle aggregates using template-assisted means have been reported in the literature. These include the use of DNA,[339] surfactants,[340] block copolymers,[340–342] carbon nanotubes,[341] cylindrical micelles,[342] or microorganisms like bacteria or viruses[343] as templates to attach nanoparticles. While the template-assisted cluster formation allows creating clusters with the desired size (or a number of particles per cluster) and shape, they often fall short of abilities to control inter-cluster arrangement within an array. Such an arrangement is important to ensure reproducible inter-cluster plasmonic interactions as well as an ability to engineer them to achieve desired optical properties. In this direction, block copolymers are an excellent solution, as they allow effective control over the spatial arrangement of eventual clusters. Microphase separation of BCP in thin films, as well as BCP reverse micelles, has been utilized as templates to attain clusters of metal nanoparticles on surfaces. These techniques have exploited the BCP templates either to organize one or more particles from solution phase,[344–346] or to drive selective complexation of metal ions and in situ reductions to form clusters.[347] However, these fall short of opportunities for the rational design of the cluster properties. The approach based on copolymer reverse micelle template allows preparing clusters based on electrostatic self-assembly of preformed gold NP from the solution phase on to the features on the surface. The cluster dimensions (the number of NP per cluster) and the inter-cluster separation were controlled by control over the template size and their separation. The low standard deviation of the template enables low standard deviation in the geometric attributes of the clusters as well.[315]

2.3.2. Gold Nanoparticle Cluster Arrays By Electrostatic Self-Assembly

Gold nanoparticle was synthesized using the citrate reduction method developed by Turkevich et al. and improved by Frens.[348,349] Gold chloride ($HAuCl_4$) was reduced by sodium citrate at high temperatures, generating fairly monodispersed gold NP. In this method, citrate plays the role of reducing agents as well as a capping agent for gold. The size of the nanoparticle can be tuned by changing the ratio of the salt and the capping agent.

The diameter of ~11 nm of Au NP with optical extinction spectral peak at 520 nm, which corresponds to the spherical shape **(Figure 2.14a-b)**.

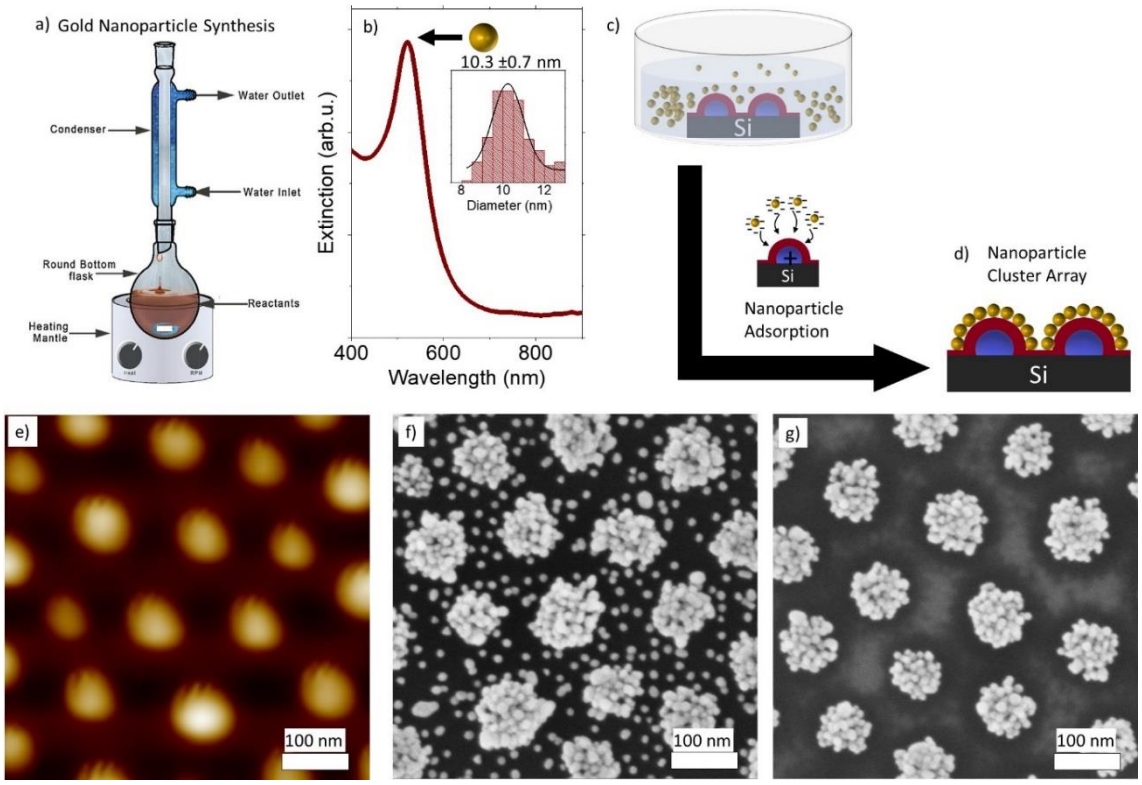

Figure 2.14. a) Schematic representation of the setup used for synthesizing Au NP via wet chemical route, b) Statistical analysis of size distribution of Au NP from SEM images, c-d) Schematic of the fabrication of gold nanoparticle cluster arrays by electrostatic attraction of negatively charged Au NP to positively charged templates on the surface, e) AFM image of the polymeric template, and Au-NCA f) without short oxygen plasma etching (before NP adsorption), and g) after oxygen plasma etching (before NP adsorption).

In a typical experiment, the reverse micelle arrays prepared from PS-b-P2VP with a molecular weight of 443 kDa and PDI of 1.1 were spin-coated from m-xylene solutions and subsequently exposed to an aqueous suspension of gold NP **(Figure 2.14c)**. Due to the presence of the pyridyl groups of PVP in the core of the features, the reverse micelle features are positively charged, and attract negatively charged citrate-stabilized gold NP from the suspension **(Figure 2.14d-g)**. The electrostatic attraction between the NP occurs locally on the features, and not in-between them, therefore resulting in a patterned array of nanoparticle clusters. The number of NP in each feature is a function of its size. The inter-cluster separations are controlled by the control over the periodicity of the template.

Extinction spectra of the nanoparticle clusters showed a peak at 647 nm (discussed in the next chapter), which was over 100 nm red-shifted from the plasmon resonance band of isolated Au NP. This is attributed to the strong plasmonic coupling between the NP within the cluster. Further, the absence of a strong contribution at 520 nm would confirm the geometric observation of the absence of isolated NP. The substrate was exposed briefly to oxygen plasma (10 to 30 s) before nanoparticle attachment. This ensured, stronger spatial confinement of the NP adsorbed electrostatically on the positively charges ellipsoidal features of the template **(Figure 2.14f-g)**.

2.3.3. High Aspect Ratio Nanostructures For Three Dimensional EM Hot-Spots

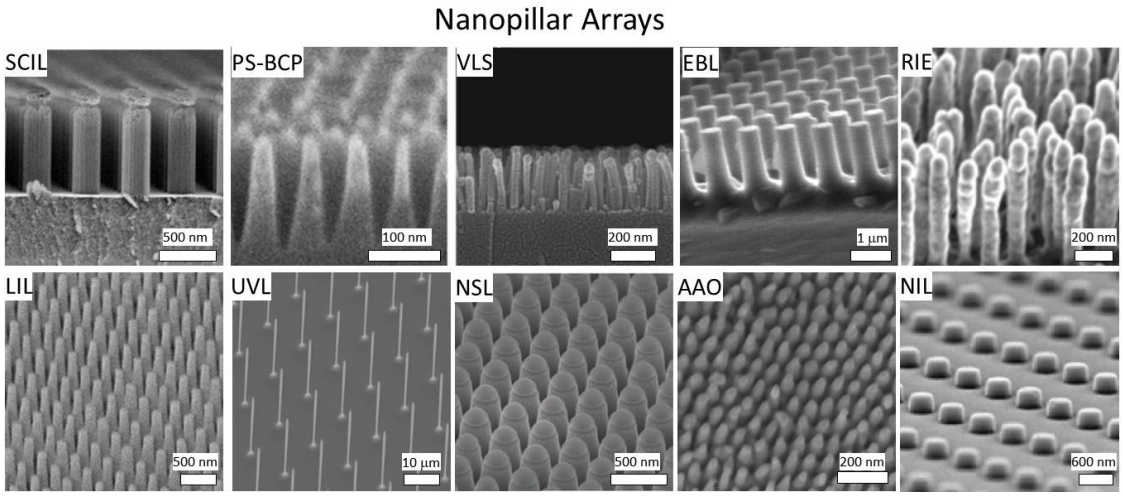

Figure 2.15. Nanopillar geometries are obtained from different nanofabrication techniques. SCIL: Substrate Conformal Imprint Lithography,[350] PS-BCP: Phase separated BCP,[306] VLS: Vapor-Liquid Solid,[351] EBL: E-beam lithography,[352] RIE: Reactive ion etching,[353] LIL: Laser inductive lithography,[354] UVL: UV lithography,[355] NSL: Nanosphere lithography,[356] AAO: Alumina-Anode Oxide,[357] NIL: Nanoimprint lithography.[358]

Nanopillar shapes offer a unique opportunity to control and enhance EM field profiles and enhancements.[359] Nanopillar arrays for plasmonic sensing have been reported previously in the literature, for detection of disease markers and identification of bacteria as well as environmental pollutants.[267,316,360,361] Such configurations can be obtained by metal deposition of optimal thickness on top of high aspect ratio dielectric pillars that can be produced by different approaches, namely, VLS growth,[351] pulsed laser deposition,[362]

black Si production by RIE with gas plasmas,[363] and patterned wet or dry etching with templates produced by other means, for example, photolithography, soft-lithography, EBL, NIL, NSL, and molecular self-assembly.[174,364–368] Nanopattern of pillars offers an advantage over stochastically arranged counterparts due to a better definition of the spatial relationship between the pillars that help rational enhancement to sensing performance. The stochastic arrangements, despite promising results, rely largely on empirical optimization and suffer from difficulty in identifying issues when they arise. Another aspect to consider is the stability of the pillar arrays, which is especially a concern for high aspect ratio structures.[188,266,369,370] High aspect ratio pillars can capture analyte between the pillars when they collapse by drying that may offer interesting means to trap analyte potentially at EM hot spots,[201,371] the approach, however, gives less control over the collapse nor the concentration of analyte that is trapped, thus offering a limited opportunity for rational design. The irreversible nature of such collapse would make it difficult to subject the pillars to solvent-based washing and drying steps, limiting them to a single time or single-step usage. Pillars of smaller aspect ratios would solve many of these issues, however, it will need to be produced with high spatial resolutions to ensure a large number of EM hot spots and preferably with good geometric definition allowing rational optimization toward both enhancing EM hot spots and analyte capture on the surface. An approach based on colloids of amphiphilic copolymers allows the possibility to generate nanopillars that are stable and reusable while allowing significant opportunities to rationally engineer the optical properties toward high plasmonic sensing performance.

Organic reverse micelle templates can be transferred into the underlying Si by adopting nanolithography processes based on reactive ion etching with halogen gas plasmas. Given the low template thickness (typically less than 30nm), and small widths (sub-100nm), nanolithography using these templates requires significant process optimization to ensure high selectivity to the underlying substrate, minimum undercut, and high anisotropy. It is possible to substitute the organic templates with a harder inorganic template to improve the selectivity and durability. This is achieved by transferring the organic template pattern into a thin dielectric film to generate harder dielectric masks for the next step of pattern-transfer into Si. We had earlier shown a high degree of control over the incorporation of the organometallic precursor by using atomic layer deposition, with the resulting oxide nanostructures enabling nanolithography down to sub-10nm regime.[243]

This was followed by several other investigations in literature focusing on vapor phase incorporation of metal-organic precursors within different BCP domains using ALD processes.[304,372–375] The nanolithography process must be optimized to not widen standard deviations between the features or across the wafer. The optimization processes across the full-wafer level should take into account the "loading effects", which impacts the outcome of the reactive ion etching process depending on the proportion of exposed surface area available for etching.

2.3.4. Gold Coated Silicon Nanopillar Arrays

❖ Silicon Nanopillar Arrays:

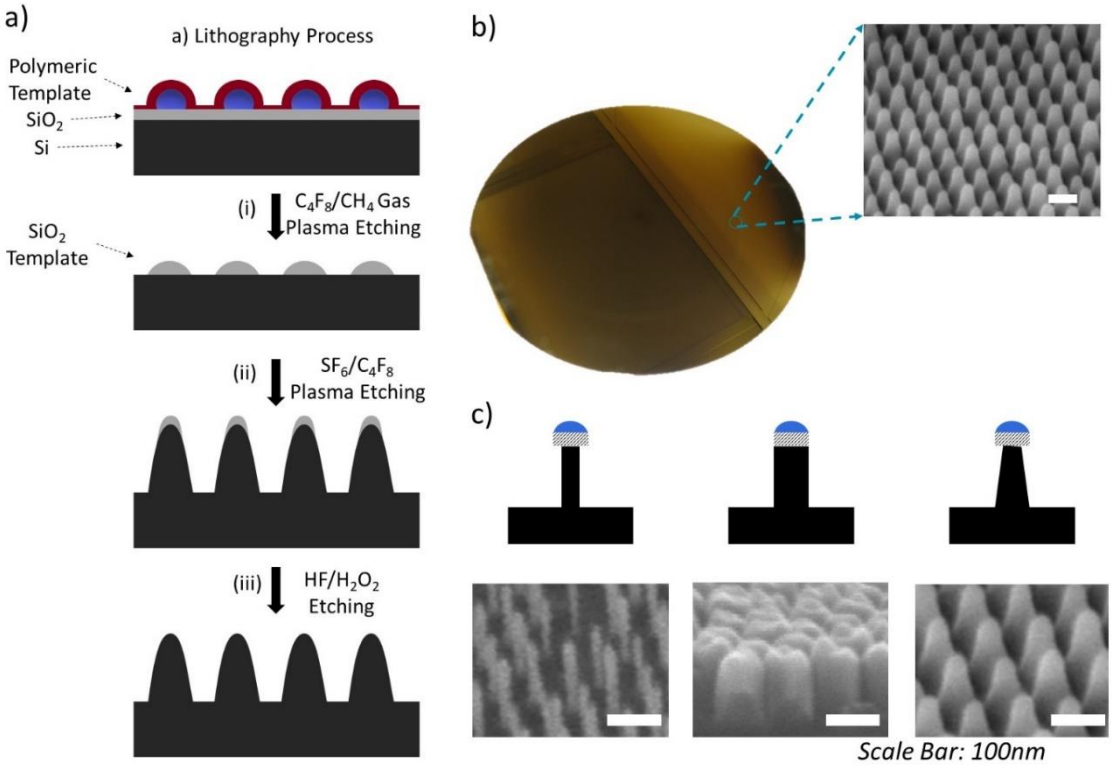

Figure 2.16. a) SEM image is taken from a random position on the wafer with nanopillar arrays. (c) SEM images of different shapes of nanopillars obtained by varying etching conditions.[243]

In a specific example, organic templates prepared using PS-b-PVP with a molecular weight of 80.5 kDa was spin-coated on a 100 mm Si wafer consisting of a 25 nm film of thermally grown SiO_2 layer. The coating is exposed to brief O_2 plasma to remove the thin residual layer between the template features and expose the substrate beneath. The resulting

organic template is then transferred into an underlying SiO_2 thin film using C_4F_8/CH_4 gas plasma. The resulting SiO_2 islands provide high selectivity in etching underlying Si using SF_6/C_4F_8 plasma to yield Si nanopillars and the remaining SiO_2 was removed using HF/H_2O_2 solution **(Figure 2.16a)**. The RIE conditions employed resulted in silicon pillars with a positively tapered profile with a feature size of 40nm (at half-width), and a pitch of 78nm and height of 120nm, as measured by SEM **(Figure 2.16b)**. The RIE process conditions can be varied to obtain pillars with other shapes as well **(Figure 2.16c)**. The pillar arrays were found to be uniform throughout the wafer, as qualified by uniform color, with a variation of < 10% as measured by reflectance spectroscopy.[243]

❖ Metal Coating On Silicon Nanopillars

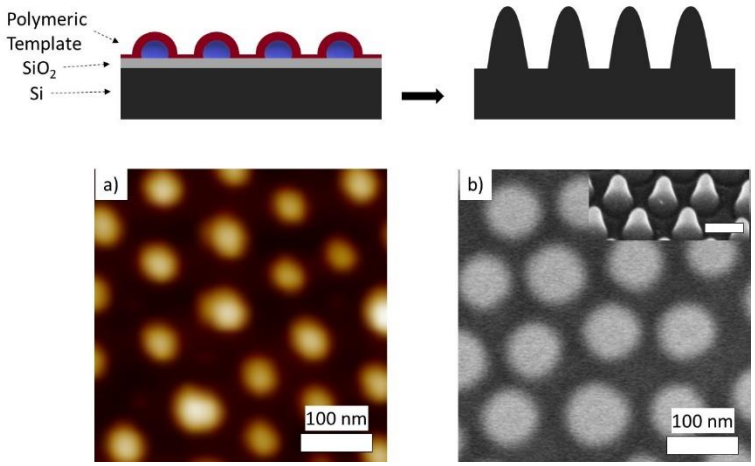

Figure 2.17. a) Fabrication process involved in pattern transfer from polymer template to fabricate silicon nanopillar arrays, b) AFM image of the polymeric template, Top view SEM image of the c) Si-NPA (inset: tilt view), and d) Au coated silicon Si-NPA (inset: tilt view).

Nanopillar arrays that are shorter and closer allows all advantages of the other reported approaches, while also conserving the metal to be deposited. Nanopillar arrays of silicon obtained by the molecular self-assembly approach **(Figure 2.17)** can subsequently be coated with gold or silver to prepare plasmonic nanopillar arrays. The conditions of the coating, including the choice of evaporation versus sputtering, the respective deposition parameters are critical to the structure and property of the resulting plasmonic arrays. The thickness of the films deposited in relation to the geometry of the underlying silicon pillars would be a key process parameter that determines the aspect ratio and the separation between the metal pillars. Both aspect ratio and the feature diameters increase, while the

feature separations decrease systematically as a function of the thickness of metal deposited. The observed film growth is strongly anisotropic with slow growth laterally as compared to vertically. The growth on top of the silicon pillars correlates well with the thickness of the metal deposited, while, the increase in diameter occurs much slower. The challenge in the processing includes the conformal deposition of metal, with good step edge coverage, especially when the deposition is made on top of closely separated high aspect ratio nanopillars.

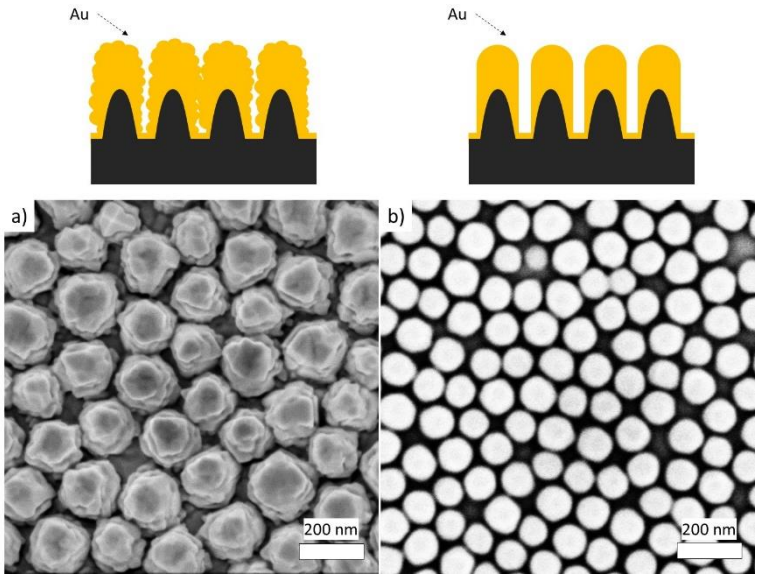

Figure 2.18. Gold metal-coated silicon nanopillars using a) E-beam evaporator, and b) Sputter coater.

In a specific example, silicon nanopillars were prepared using the method described above on a whole wafer **Figure 2.17**, and were diced into pieces to test for conformal coating of gold metal. The e-beam evaporation of gold metal on the pillar resulted in a flower-like coating of metal layers on the top of the pillars. On the other hand, sputtered films under specific conditions (described in **chapter 6**), as shown in **Figure 2.18a-b**.

2.4. Nanoscale Characterization Methods

2.4.1. Structural Analysis

Structural characterization tools, allow us to relate the changes in the fabrication process to the changes resulting in the geometric features. The process ⇔ structural

correlations were monitored at every step to validate the process and ensure the homogeneity between batches. The commonly used tools such as SEM and AFM were most frequently used during the project due to their simplicity and ability in providing physical interpretation of geometries.

❖ Dynamic Light Scattering (DLS)

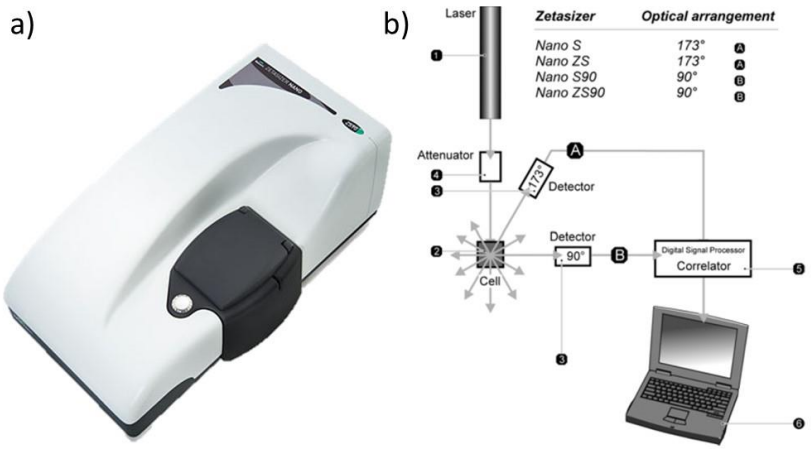

Figure 2.19. a) Dynamic Light Scattering Instrument, and b) Optical configurations of the Zetasizer Nano series for DLS measurement.[376]

DLS provides a statistical analysis of the average hydrodynamic size distribution of the NP in the suspension by intensity. This technique measures the Brownian motion of the particles in the solution and then relates the information to their to size. The velocity of the Brownian motion is higher for small particles and the knowledge of viscosity and the particular temperature of the solution is very important for the correct interpretation. The velocity of the Brownian motion is defined by the property called translational diffusion coefficient, D. The hydrodynamic diameter, $d(H)$, of the particle is determined by D using Stokes-Einstein Equation,

$$d(H) = \frac{k_B T}{3\pi\eta D} \qquad \text{Eq. 2.3}$$

where η is the viscosity, k_B, the Boltzman constant, and T, the temperature. It is important to note that the diameter values measured by DLS refer to how particle diffuses within a fluid, hence called as hydrodynamic diameter. It is a diameter that is obtained from D, which depends not only on the diameter of the core (particle) but also on the surface

structure, concentration, and type of ions surrounding in the medium. The polydispersity and the size distribution of the gold NP synthesized in the house were characterized using Zetasizer Nano Z (Malvern Panalytical, Malvern, UK).

❖ Atomic Force Microscopy (AFM)

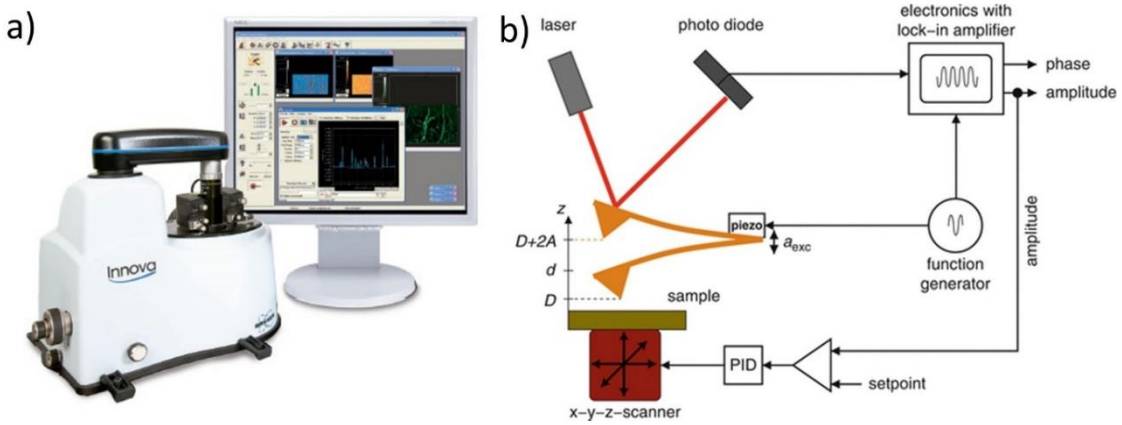

Figure 2.20. Atomic Force Microscopy Instrument. b) Schematic diagram of AFM. [377]

AFM (Innova, Bruker, USA) is an important feedback tool that enables to probe surface morphology based on the physical interaction of the AFM probe with the nanoscale structures on the surface at a very high resolution. The scans were performed using peak-force tapping mode in AFM, where the probe periodically taps the surface and measures changes in the force caused by the deflection of the cantilever when it comes in contact with the surface. The AFM tip is mounted on the reflective cantilever (together known as probe) and the interaction takes place between the tip and the sample surface. The tip material and type need to be compatible with the sample surface to avoid artifacts or misinterpretation in the surface morphologies.

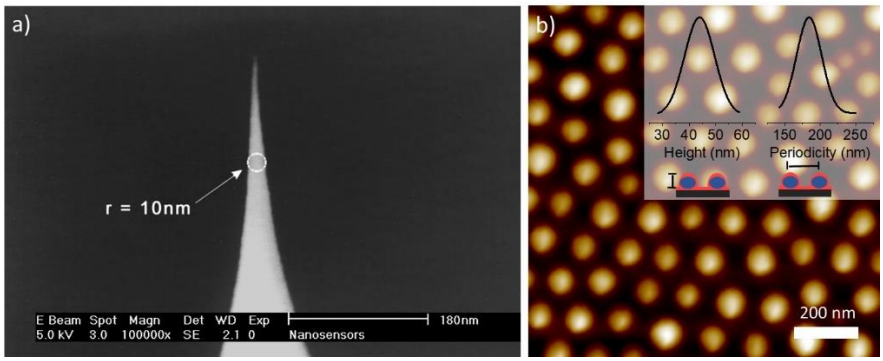

Figure 2.21. a) SEM image of the super sharp silicon – Non-Contact/Tapping mode - High Resonance Frequency - Reflex Coating (SSS-NCHR) AFM tip (Nanoandmore, Germany), and b) AFM image of the polymer template (inset – periodicity and height distribution of the organic template features)

With the help of AFM, we followed the impact of the fabrication process that was tailored to vary morphological dimensions of the self-assembled polymeric features on the surface. The high resolution scanned image of the template (soft/hard) was obtained using super sharp silicon tips and the processing of the image was performed using Nanoscope Analysis (Bruker, USA) software. The power spectral density function (2D-PSD) function was used to analyze the distribution of the mean distances between spherical features from the center to center, known as pitch (called here as periodicity). The height distributions were estimated using particle analysis function taking into account the shape of the tip and features, where necessary (for example in closely packed features, where the diameter of the tip is comparable to the separations between them). Additionally, step measurement function to analyze the scratched template (in case of a soft mask) were made as validation.

❖ Scanning Electron Microscopy (SEM)

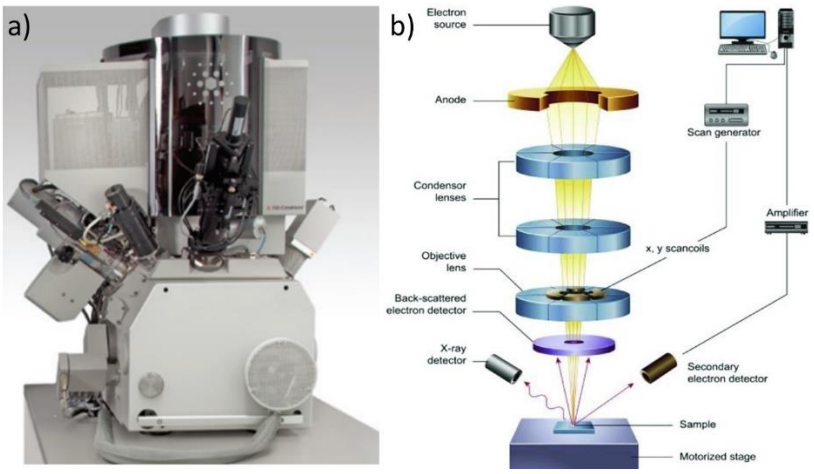

Figure 2.22. a) Scanning Electron Microscope Instrument, b) Schematic of the components that are needed to focus e-beam and the components of SEM instruments.[378]

SEM is an imaging technique, that can visualize the surface morphology or topography with high quality and spatial resolution using high energy focussed beam of electrons. Upon interaction of the incident electrons with the surface, they emit secondary

electrons and the backscattered electrons, which are then used to create a visual image corresponding to the exposed area on the sample.

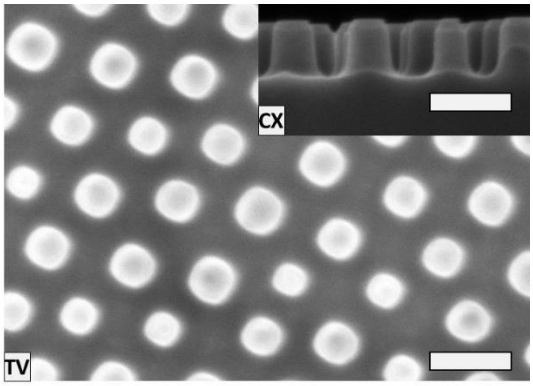

Figure 2.23. Exemplary SEM image of silicon nanopillars in top-view (TV) and a cross-sectional view (CX).

Helios Nanolab 600i (FEI, Oregan, US) was used to acquire images of the surface topography for the polymeric templates or nanoscale geometries after the pattern transfer step. Using ultra-high resolution images, structures were visualized and analyzed for statistical information of the geometric feature dimensions to validate tailored fabrication processes and ensure homogeneity over large areas. The SEM images further supported the rationally designed geometric models.

2.4.2. Optical/Spectroscopic Analysis

The use of optics to characterize nanostructured surfaces is common. Due to sub-wavelength geometric dimensions, the interaction of nanostructures with the light is distinctive. The optical characterization techniques that measure the ability of the nanostructures to absorb or reflect light are often used for comparative studies.

❖ Far-field Optical Measurements

Absorbance Measurement: Absorbance is measured for the attenuation of monochromatic light when transmitted through the sample. Absorbance A is expressed as,

$$\mathrm{A} = \log_{10} \frac{I_0}{I_{sample}} \qquad \text{Eq. 2.4}$$

where, I_0 is the intensity of light from the reference sample, and I_{sample} is the intensity of light from the sample. The light attenuated due to localized surface plasmon resonance at the surface of nanoparticle results in increase absorbance at resonance wavelength. This absorbance spectra can provide information about the absorbance modes, and thus the tendency of the shape and arrangements of the NP.

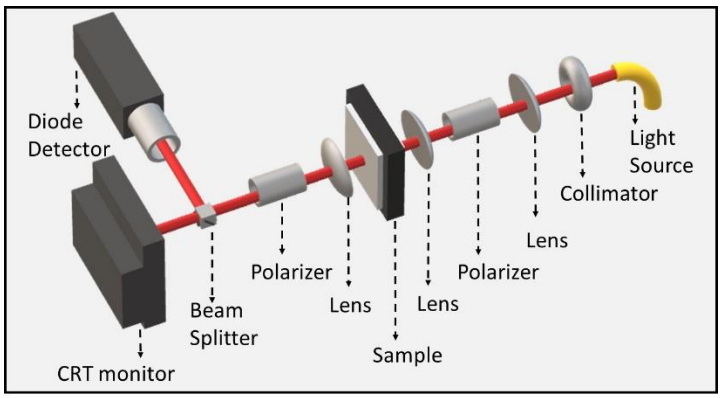

Figure 2.24. a) Extinction Measurement - Optics bench-top setup

Optical measurement for NCA on glass sutrates was performed in extinction mode in a homemade set-up on an optical table. The sample was illuminated with a white light source and polarized through a 50x/0.42 NA objective. The transmitted light was collected using a 20x/0.28NA objective which was followed by the beam splitter to direct 8% of the collected light to a CCD camera to visualize the area under investigation and the remaining part of the light is sent to the spectrophotometer via multimode optical fiber.

Reflectance Measurement: The absolute reflection measurements for NPA were taken from UV/Visible spectrometer (Perkin Elmer L1050) in an integrated sphere configuration using reflectance diffusive Teflon reference standard (WS-1, Ocean Optics). The resulting reflectance was automatically corrected with respect to the reference standard.

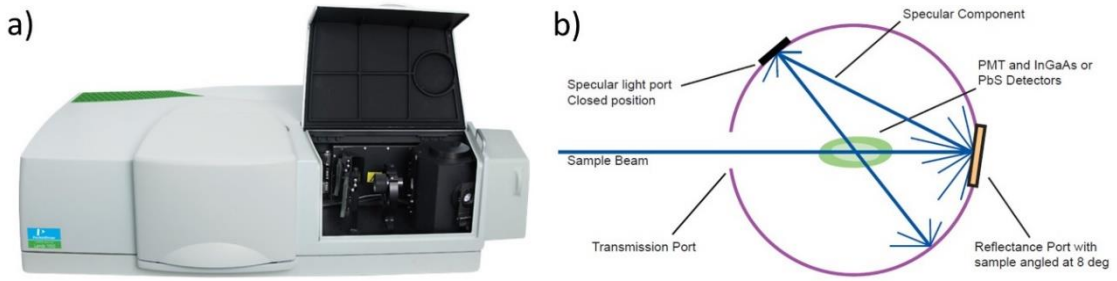

Figure 2.25. a) Integrating Sphere Ultra-Violet/Visible Spectrometer, and b) Lightpath for Reflectance Measurement in an Integrating Sphere set-up.

UV/Visible spectroscopy is a type of absorption or reflectance spectroscopy, that rely on the interaction of light with the matter (sample). The spectrophotometer measures the extent of light absorbed or reflected by the sample upon interaction with the UV/visible range of the electromagnetic spectrum. The integrating sphere is used for samples that have diffuse reflectance components for example, 'roughened surface', powders, etc. unlike mirror or highly reflective surfaces. Samples are placed in one end of the sphere and the light that reflects from the sample upon illumination is collected by the sphere. Typically, it measures absolute % reflectance, which means it is in relation to the reference signal. The light and dark reference signals are obtained using reference materials (as 100 % R) and from the sphere (as 0 % R).

The UV/visible spectrometer was used to measure absolute % reflectance (%R) of the nanopillar arrays and planar silicon substrates (with and without gold coating) using calibrated Spectralon standard (from Ocean Optics) as the reference. The calibration sheet (known reflectance values) of the reference sample allows us to calculate the absolute reflectance of the sample. The reflectance measurement is crucial in assessing the surface for optical, optoelectronic, and electro-optical applications. Nanostructures arrays are often judged based on their anti-reflective properties, due to their high aspect-ratio they tend to absorb a large portion of light from wide range incident angles.[379] The loss of light within the anti-reflective part of the surface occurs due to change or gradience in the refractive index in the environment within the nanostructured surface. The behavior of the light can be explained using the thin-film interference effect **(Figure 2.26)**.

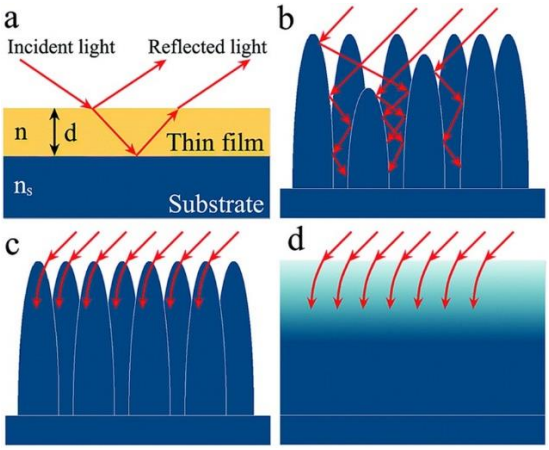

Figure 2.26. a) Propagation of incident light through a single layer film on a substrate (ns > n). (b) Multiple internal reflections of incident light in a microstructure array. (c) Interaction of incident light with the sub-wavelength-size nanoarray. (d) Schematic illustration of the refractive index change corresponding to (c).[379]

❖ Vibrational Spectroscopy

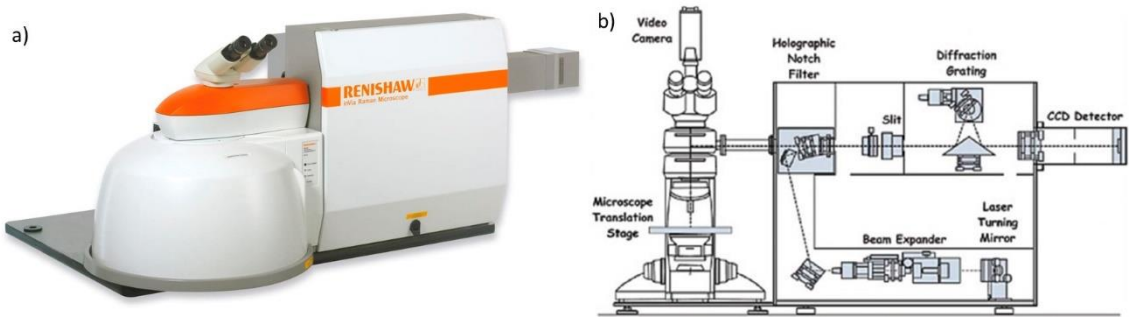

Figure 2.27. Micro-Raman Instrument, b) Schematic diagram of a Renishaw Raman Microscope.[380]

In principle, Raman signals are generated from inelastically scattered incident photons when they interact with Raman active molecule. The incident photon loses energy to the molecule, to shift the molecule from the ground state to its excited vibrational state (Stokes Raman Shift) or vice — versa (anti-stokes Raman Shift). The Raman signal intensity is proportional to the Raman cross-section of the molecule. The scattered photon consists of the information related to vibrational modes of the molecules they interact with, which are their unique energy signatures, allowing easier identification. Raman signal generated from analyte can be written as:

$$P_{Raman} = KN\sigma_R I \qquad \text{Eq. 2.5}$$

Here, P_{Raman} (photon/s) is the Raman signal power measured by the detector, K accounts for a fraction of the photons scattered from the molecule (stokes shifted) converted to electrons by the detector, N is the number of molecules illuminated, σ_R (cm^2/sterade.molecule) is the Raman-cross section of the molecule. The Raman set up **(Figure 2.27)** is similar to an optical microscope where the incoming wavelength is focussed on the sample and the scattered light is captured by the detector passing through Rayleigh filters. The setup is completely automated for laser wavelengths, gratings, as well as filters.

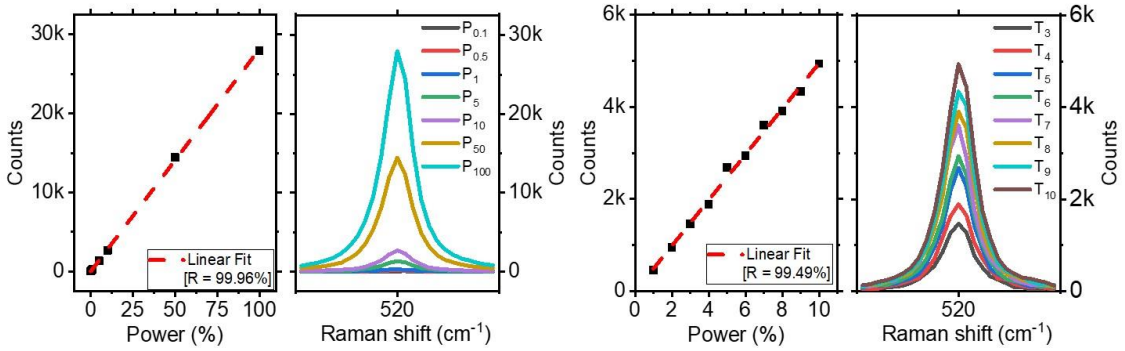

Figure 2.28. Calibration curve to check the linear increase in counts with systematically increasing a) power, and b) time.

The instrument is maintained by internal calibration using internal silicon and periodic automated alignment procedures. However, validation of power vs counts and time vs counts from internal silicon as calibrations were performed to validate their linear behavior. Also, the power of the incident laser was determined to consider the actual incident powers when calculating intensity (counts mW^{-1} s^{-1}) from counts.

SES measurements were carried out using a micro-Raman system (Renishaw InVia, UK) attached with the microscope, a peltier cooled CCD, and an excitation LASER of 633 nm. The system was preattached to a microscope (Leica), and the Laser was coupled through an objective lens of 50x with 0.5 N.A. Before each experiment, internal Silicon calibration was performed with a peak centered at 520 cm^{-1}. Data processing was performed using WIRE 5.0 software provided by the manufacturer of the system. Default

parameters were used for baseline subtraction to remove background noise from the signals. The measurements were acquired in an autofocus mode at 10 different positions at the same sample for observing standard deviations. After importing spectra into the OriginPro, all the spectral signals were then normalized with respect to exposure time and incident powers, to be able to follow the dependency of the signal intensities over analyte concentration. The spectral ranges were chosen according to the most intense peak, marking the presence of the analyte molecules.

2.4.3. Biomolecular Interaction Analysis

Biomolecular interactions involve a combination of multiple species with each other to form functional complexes. To follow their interaction kinetics with each other or surface, two techniques have been widely utilized commercially due to their sensitivity and dynamic interrogation capabilities. Although, both the techniques, namely quartz crystal microbalance (QCM) and surface plasmon resonance (SPR) use similar sensor surfaces to detect mass changes, they differ in their mode of interrogation.

❖ Quartz Crystal Microbalance – Dissipation (QCM-D)

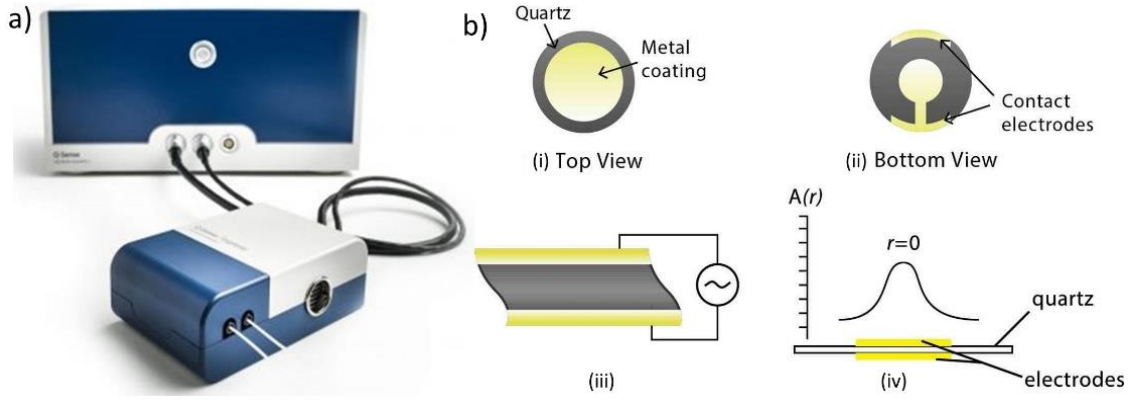

Figure 2.29. a) Quartz Crystal Microbalance Instrument, and b) Design of quartz crystal (grey) with electrodes (yellow); (i) top view (ii) bottom view. (iii) A schematic illustration of the strain-induced in an AT-cut crystal on the application of AC voltage. (iv A schematic illustration of how the amplitude of vibration (A(r)) varies with the distance (r) from the center of the sensor. The area of vibration is called the active surface area and is sensitive to mass changes.[381]

A QCM-D instrument is a mass balance that monitors the change in mass at the molecular level in real-time based on the piezoelectric response of the quartz which acts as a sensor. The quartz sensor is often coated with gold on both sides of the sensor, which works as electrodes. The quartz sensor is then excited from the bottom electrodes to oscillate at its resonance frequency by applying an alternating voltage. The top gold surface is then exposed to the analyte solution or sample which can adsorb on the surface either electrostatically or covalently to induce mass change on the surface of the sensor. The resonance frequency depends upon the total mass of the sensor and the adsorbed layers. Hence the small increase (due to adsorption) or decrease (desorption) in mass can result in the decrease or increase in the frequency, respectively. However, depending on the nature or the thickness of the adsorbed layer, the shift in the frequency can be governed by either the Sauerbrey model equation or a viscoelastic model (such as the Voigt model) **(Figure 2.30)**.

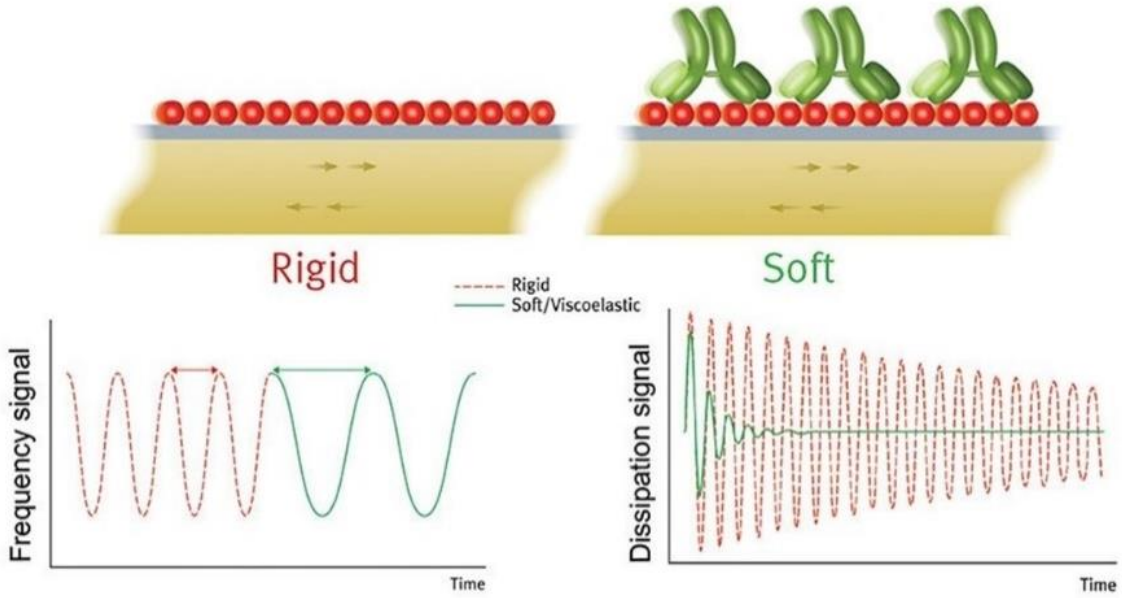

Figure 2.30. (Left) Rigid layers that follow Sauerbrey Equation for mass calculations, and (right) soft layers that follow the viscoelastic model for mass calculations.

When the adsorbed layer is thin and rigid, the change in the frequency, Δf, is proportional to the change in mass, Δm, at the surface of the sensor. Therefore, following a simple Suerbrey equation which is expressed as,

$$\Delta m = {}^{-(C * \Delta f)}/_{n} \qquad \text{Eq. 2.6}$$

here, C = 17.7 ng Hz^{-1} cm^{-2} for a 5 MHz quartz crystal, and n is the overtone number.

On the other hand, if the layers are soft and do not adhere to the surface strongly they do not couple with the oscillating frequency of the sensor. Consequently, the change in mass changes frequency as well as the amplitude of the oscillations. The damping can be observed with the change in energy dissipation, D. This is where the Sauerbrey equation becomes invalid and the viscoelastic model (such as Voigt Model) is used.

❖ Surface Plasmon Resonance (SPR)

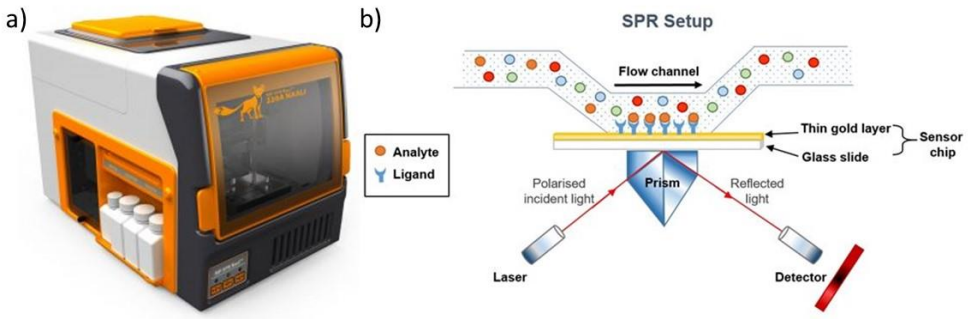

Figure 2.31. Surface Plasmon Resonance Instrument, and b) Illustration of the basic principle of an SPR measurement.

SPR instrument is an optical biosensor that enables sensitive detection of molecular interactions in real-time. SPR technique relies on free oscillating electron knows as surface plasmon (SP) at the interface of the metal and dielectric (negative and positive permittivity material) stimulated by incident light. Under specific conditions of irradiation angle (SPR angle) and wavelength, these surface plasmons resonate, hence are known as SPR.[102] Under SPR conditions, surface plasmons propagate parallel to the metal surface and generate exponentially decaying electromagnetic field (decay length ~ 400 nm) above and below the metal surface, known as an evanescent wave. Therefore, making this technique sensitive to changes in the refractive index at the vicinity of the metal surface.

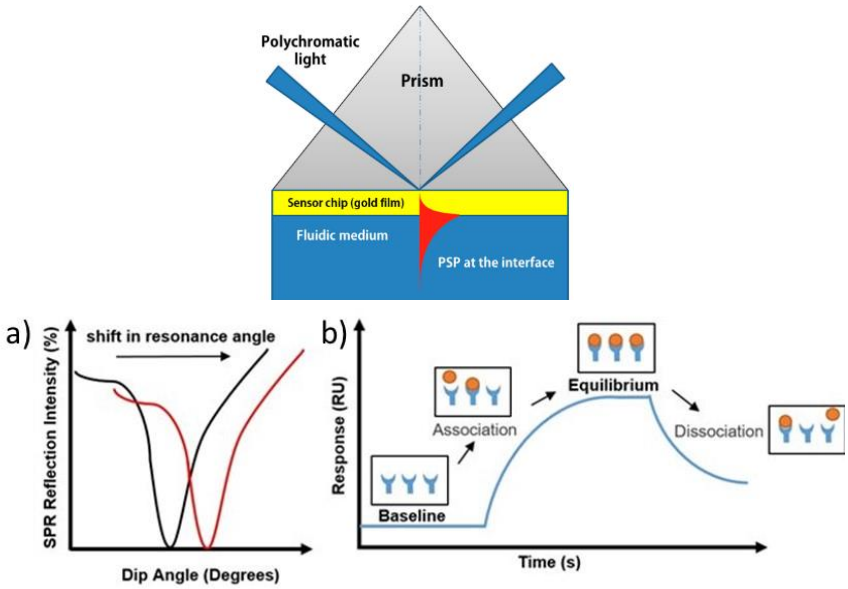

Figure 2.32. Kretschmann configuration[103,382] Surface Plasmon Resonance.

SPR sensor is a gold-coated glass chip that is placed in contact with the prism of the high refractive index corresponding to the Kretschmann configuration, as described in **Figure 2.31b**. Prism coupling in Kretschmann configuration represents the most commonly used method to optically excite the surface plasmons**Figure 2.32a**. In this configuration, a polarized light wave passes through the prism and is reflected at the base of the prism, where the SPR sensor is positioned. At the SPR angle, the absorption of light is maximum, therefore the reflected light intensity is significantly reduced. However, changes in the refractive index of the environment due to the presence or absence of molecules (association or dissociation) near the metal surface within the range of evanescent waves, causes a shift in the SPR angle. The SPR instrument measures this shift of the SPR angle at which the reflected light is minimum and is recorded as a sensogram **(Figure 2.32b)**.

2.5. Summary

Molecular self-assembly using amphiphilic copolymers and colloids derived thereof can deliver nanoplasmonic interfaces with high spatial resolutions, with control over geometric variables in steps of only a few nanometers. The approach enables metal nanoarrays with spatial coherence between features, orthogonal control over the different geometric attributes, and standard deviations below 10%. These characteristics can be leveraged to better understand and predict the optical properties of these arrays, allowing

rational routes to maximize plasmonic sensing performance. The self-assembly parameters at both the template production and pattern transfer stages could be rigorously controlled to ensure high uniformity, reproducibility, and scalability of the resulting plasmonic arrays on full wafers. The homogeneously distributed hot spots over large areas present an opportunity to not only detect but also quantify the concentration of analytes, with large dynamic range with promisingly low limits of detection.

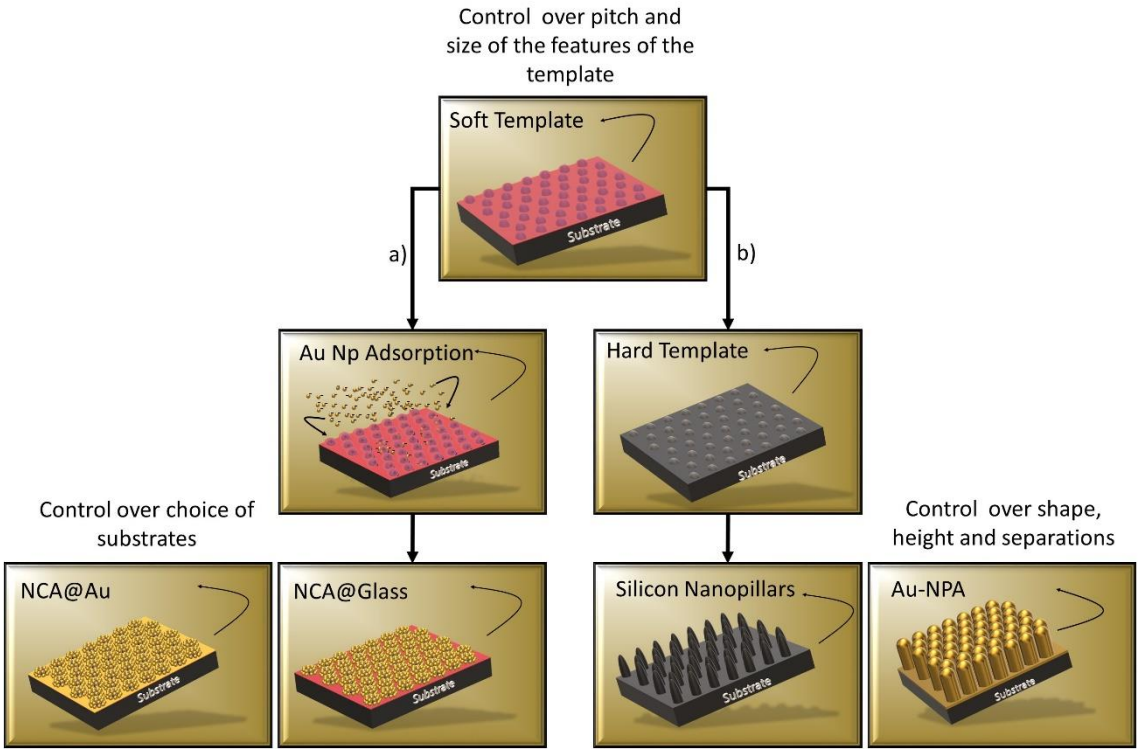

Figure 2.33. Schematic representation of process involved in fabrication of a) nanocluster arrays and b) nanopillar arrays from soft organic template.

Benefiting from such spatially resolved nanofabrication methods, plasmonic nanoarrays were rationally designed to achieve EM hot-spots corresponding to different geometric attributes. Plasmonic nanoarrays presenting a large number of gap hot spots, with gap distances down to sub-10 nm length scale, were studied in the case of nanoparticle cluster arrays and nanopillar arrays. Systematic variations in spatially resolved EM hot-spots were investigated to correlate their sensitivities in detecting molecules with small and large dimensions. Analyte molecules that are smaller in size, are well aligned with the spatial requirements for the gap between adjacent metal nanostructures presenting strong EM fields. However, to exploit these confined EM fields for biomolecular sensing, it is

essential to take into account the spatial requirement of the biomolecule, which can range from few nanometers to a few tens of nanometers.

The nanocharacterization tools such as SEM, AFM plays important roles in probing morphologies of the resulting nanoscale geometries with high resolution and assessing their optical properties using absorbance and reflectance properties. SPR and QCM based analysis gave an insight into understanding the biomolecular behavior while interacting with surfaces that are engineered at the nanoscale. Biomolecular interaction kinetics along with the surface densities were then correlated to the spectroscopic response of the sensor surface. Therefore, in the following chapters, the correlation of the geometry ⇔ optical ⇔ SES performance is demonstrated with a combination of experiments and numerical simulations.

Left Blank Intentionally!

Chapter 3. Nanoparticle Cluster Arrays

This chapter is based on the published paper in [Journal Name] "Gold Nanoparticle Cluster Arrays with Engineered Nanoscale Geometries for Quantitative Plasmonic Bioassays", R. Rastogi, E. A. Dogbe-Foli, R. Vincent, S. Poovathingal, P. Michel-Adam, S. Krishnamoorthy. [DOI].

High sensitivity in plasmonic biosensors results from non-linear enhancement of electromagnetic (EM) fields at the vicinity of nanostructured metal surfaces as well as the ability to leverage on these enhancements via optimal attachment of analyte to the EM hot-spots. However, EM hot-spots such as nanogaps are spatially restrictive for adsorption of larger analytes such as proteins. This ensures a trade-off between the geometric requirements to drive high EM enhancements and to accommodate analyte binding. We investigate nanoparticle cluster arrays (NCA) presenting dual length scale electromagnetic hot-spots, viz. interparticle (<1 nm) and inter-cluster hot-spots (sub-10 nm), on the sensitivity of plasmonic bioassay based on surface-enhanced Raman and Fluorescence spectroscopies. The sensitivity of the bioassays was found to be dependent on the size of the analyte in relation to the gap distance at the interparticle and intercluster EM hot-spots. With an accurate measure of the surface concentrations of NP and analyte molecules using a quartz crystal microbalance, it was possible to attribute a higher sensitivity of plasmonic assays to the ability to leverage on, inter-cluster EM hot-spots in case of proteins, and both interparticle and intercluster EM hot-spots in case of small organic analytes. The investigation demonstrates the need to factor in the size of the analyte into the design of the plasmonic nanoarrays to better leverage the EM hot-spots. Further, the ability to decouple the signal contributions due to EM field enhancements from the analyte surface concentrations allows significant opportunities for the rational design of the plasmonic sensors.

3.1. Introduction

Reliable and quantitative detection of bio-analytes with high sensitivity down to few molecules, response times within few minutes and miniaturized volumes is key to advancing a range of diagnostic goals including detection of diseases at an early stage, predicting disease risk, identification of infections for the point of care and delivering therapies tailored to the individual patients.[34] Nanoplasmonic sensors that control and enhance EM fields at length scales of the order of biomolecules provide a clear edge over other techniques due to high surface selectivity, ultra-low detection limits, response times of few seconds, and miniaturized form factors.[285] Plasmonic sensors have been used to detect analytes either by monitoring the variation in the localized refractive index or by their spectroscopic fingerprint. Spectroscopic detection relying on EM fields allows unique identification of analytes using plasmon-enhanced Raman or Fluorescence, with competitively low limits of detection compared to other techniques.[55] These EM fields on a nanostructured metal surface are heterogeneously distributed and are concentrated in nanogaps or sharp corners of metal nanostructures that act as EM hot-spots.[147] Gap hot-spots are known to be stronger than curvature hot-spots, [143,151,383] and several studies have shown an exponential rise in the enhancement as the function of the closing gap between the metal nanostructures. [137,151,152,384] To attain the best sensitivities, the analyte needs to be co-localized within the EM hot-spots where these EM fields are concentrated.[169] However, these gaps are typically in the order of few nanometers and can permit only those analytes with dimensions smaller than the gap themselves. This is a challenge for bioassays as the length scale of typical biological interactions including hybridization of oligonucleotides, or immunosandwich assays extends up to few tens of nanometers. To address the inevitable trade-off between the geometric requirements for highly enhancing EM hot-spots, and spatial needs for biomolecular adsorption, it would be necessary to design plasmonic arrays to drive co-localization of larger analytes such as proteins, within the EM hot-spots.

Different approaches have been explored to date to co-localize analytes within EM hot-spots. They include sandwiching the analyte at the hot-spot formed between a nanoparticle and an underlying planar or nanostructured metal surface,[148,385] trapping analytes at the inter-pillar hot-spots formed upon collapsing of high-aspect-ratio metal nanopillars under the influence of capillary forces,[371] and selective polymerization at EM

gap hot-spots.[386,387] The sandwich configurations with analyte located at the EM hot-spot between a nanoparticle and an underlying metal film is limited by the gap distances determined by the thickness of the sandwich, is favorable for smaller molecules, but less interesting for bioassay configurations like immunoassays or nucleic acid assays that have dimensions of 20-40 nm. Mechanical trapping of analyte at inter-pillar hot-spots suffers from an inability to support washing-drying steps as used in standard wet (bio)chemical functionalization, thus of limited support in multi-step sequences in bioassays. Further, the random collapsing of the pillars offer less to support rational engineering of the resulting EM hot-spots. The strategies for efficient analyte co-localization at EM hot-spots thus, continue to be an unsolved challenge especially when it concerns bioassays.

The molecules present at EM hot-spots can disproportionately dominate the signal contribution as compared to those present in other sites.[169] This makes it particularly difficult to rationally engineer nanoplasmonic surfaces containing EM hot-spots to perform reliably for quantitative assays. Thus, for the rational optimization of plasmonic bioassays, it would be necessary to know the actual analyte surface concentrations that contribute to the final plasmonic signal. This would enable the rational design of metal nanoarray geometries that offer the analyte better leverage of EM enhancements. To accurately measure the analyte concentrations on a plasmonic surface is however a non-trivial challenge. Sensors that are capable of such measurements, e.g. quartz crystal microbalance (QCM) or surface plasmon resonance (SPR) require that the plasmonic arrays be reproduced on the QCM or SPR sensor surface, spanning uniformly across the entire sensor footprint (~1 cm^2). Very few processes can deliver plasmonic nanoarrays with highly resolved EM hot-spots, in areas spanning square centimeters, with a reproducibility across batches. In the current investigation, we employ such a process, to produce periodic nanoparticle cluster arrays of gold,presenting dual-lengthscale EM gap hot-spots with gap distances in the sub-10 nm regime **(Figure 3.1a-b)**. The dual lengthscale hot-spots offer the advantage of high sensitivity towards small (<1 nm) as well as larger (bio) analytes. Quantitative plasmonic assays of proteins based on surface-enhanced Raman spectroscopy and metal-enhanced Fluorescence (MEF) are obtained. Accurate measurement of the protein surface density by QCM served to rationalize highly sensitive nanoparticle cluster arrays configurations as those that offered bio-analytes to better leverage over EM hot-spots.

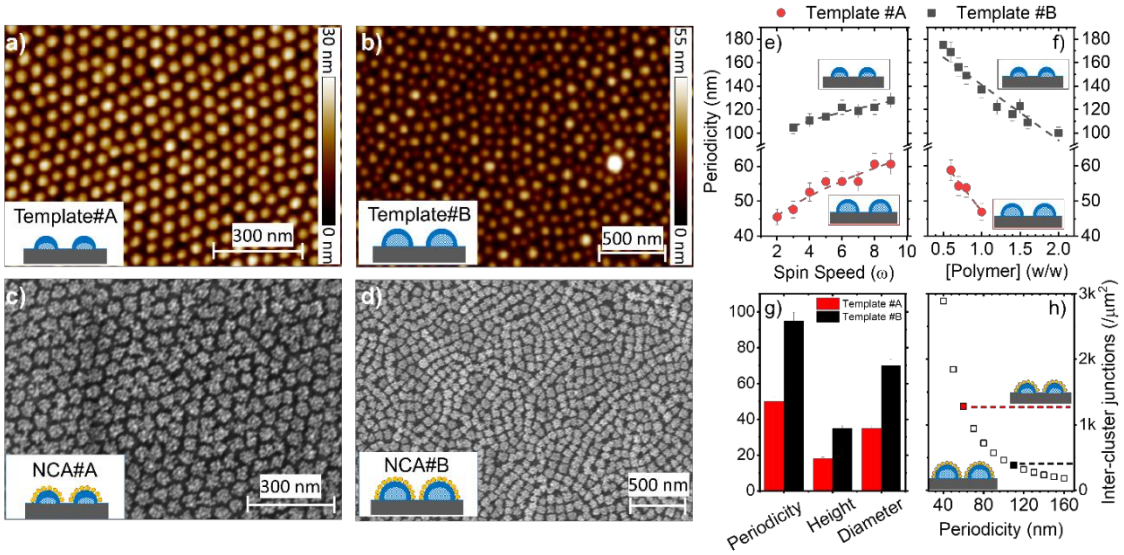

Figure 3.1. (a,b) Templates with smaller (Template#A) and larger size (Template#B) used to define (c,d) gold nanoparticle cluster arrays, NCA#A and NCA#B respectively. High degree of control over the periodicity of the templates with e) quadratic dependence on spin-speeds or f) linear dependence on polymer solution concentrations. g) comparative view of the geometric attributes of Template#A and Template#B. h) comparison of the number of inter-cluster junctions in NCA#A over NCA#B as function of periodicity.

3.1. Experimental Methods

Materials: Polystyrene-block-poly(2-vinylpyridine) (PS-*b*-PVP) (40500-b-41000 *g/mol and* 248-*b*-195 *g/mol*) was purchased from Polymer Source Inc. (Montreal, Canada). Quartz substrates were purchased from Siegert Wafer (Aachen, Germany). 1-napthalenethiol (≥99%), m-Xylene (≥99%), sodium citrate dihydrate (≥99%), Hydrogen tetrachloroaurate(III) trihydrate ($HAuCl_4.3H_2O$) (≥99.9%) were purchased from Sigma-Aldrich. Biotin-PEG-Thiol (400 *g/mol*) was purchased from Nanocs, New York, USA. Phosphate Buffer Saline (PBS) and Bovine Serum Albumin (*BSA*) solution (10x) was purchased from R&D Systems, Abingdon, UK. Streptavidin Conjugated with Cyanine-5 dye (60 kDa) was purchased from Rockland, Limerick, PA. Gold-coated QCM-D sensors (5 MHz, AT-cut Gold electrode) were purchased from LOT Quantum Design, Darmstadt, Germany. Supersharp, AFM tips (SSS-NCHR-50) were purchased from Nano and more (Paris, France).

3.1.1. Fabrication Of Nanoparticle Clusters

NCAs were fabricated on the chosen substrates (glass and QCM sensor chips) with identical geometric characteristics as confirmed by the AFM and FESEM measurements. The substrates were cleaned by ultrasonicating them in acetone followed by rinsing with Ethanol and 2-propanol and then subjecting them to Oxygen plasma in the Reactive Ion Etching chamber (Plasmatherm 790 RIE) for 3 minutes. Freshly cleaned substrates were immediately spin-coated of PS-b-PVP solutions in m-Xylene at 5000 and 3000 rpm for Template A and B, respectively. Template#A was coated from 0.75% (w/w) solution of PS-*b*-PVP with a molecular weight of 81.5 kDa. Template#B was coated using a 2% (w/w) solution PS-*b*-PVP with a molecular weight of 443 kDa. The coated layer was subjected to controlled exposure of oxygen plasma for 0 s for polymer A and 30 s for polymer B to avoid non-specific adsorption and increasing the gap between nanoclusters. These coated chips were immersed in a citrate-stabilized gold nanoparticle solution (pH 5.8) for 2 h followed by rinsing with deionized water. The 10.3 nm ±0.5 nm gold NP were prepared according to the method reported previously.[388] The AFM images of the templates were measured in tapping mode using super sharp AFM tips. Gaussian fit to the height and the periodicity histogram were used to determine the mean and standard deviations. In-built particle analysis functions in Nanoscope Analysis software was used for this purpose.

3.1.2. Spectroscopic Measurements

For NT Raman probe detection, an average of 10 scans per spot was acquired and an average of 10 different spots on each sample, to calculate the standard deviations. Each scan was taken with a total exposure of 9s with a 633 nm He-Ne LASER at a power of 1.9 mW under 50x/0.5 N.A. objective. For bio-molecular detection using fluorescent-dye Cy5 conjugated to Streptavidin, each measurement was recorded at 10 different places throughout the functionalized surface, with 15 s of total exposure time at 50% power to prevent the saturation of the CCD due to Fluorescence background.

3.1.3. Molecular Assays

For functionalization with NT, the NCAs were immersed into an ethanolic solution of systematically varying concentrations (μM to pM range) of NT overnight, and

subsequently washed with ethanol and dried before SERS measurements. For protein assays on NCAs supported on glass substrates, a PDMS well of 5 mm diameter, and an aspect ratio of 1 was prepared allowing a volume of 20 µL used for the experiments performed in the well. NCAs were exposed for 2 hours in a 1mM solution of Biotin PEG thiol, followed by 1% BSA in PBS solution was used as a blocking agent to avoid non-specific adsorption, and subsequently exposed to freshly prepared solutions of SA-Cy5 of different solution concentrations through PDMS wells. The substrate was rinsed with PBS between each step to remove loosely bound molecules. The calculation of the limit of detection (LOD = LOB + 1.645 [SD $_{\text{low concentration}}$]) was done considering limit of blank (LOB = [mean $_{\text{blank}}$] + 1.645 [SD $_{\text{blank}}$]) for each case.[389]

3.1.4. QCM-D Measurements

QSense Explorer (Biolin Scientific, Sweden) was employed to measure mass density of molecules adsorbed on the nanostructured surfaces by directly fabricating nanocluster arrays on to the QCM-D sensor (5 MHz quartz crystal with gold coating). Modified sensors were functionalized with BPT followed by BSA and SA-Cy5 at high concentrations of 800nM to assure saturated densities. The solution were injected at 10 µl/min until stable baseline was observed, with the steps separated by rinsing with PBS. Flow module with a minimum sample volume of 40 µl, mounted with sensor chip was connected to a bubble trap through tubings and a four-channel peristaltic pump (IPC Ismatec, Germany) for controlling flow rates, precisely. The validity of Sauerbrey approximation was confirmed through the low observed dissipation and invariance of the response of the frequency overtones. The 5th overtone was followed to calculate mass density values using Sauerbrey equation.[390]

3.1.5. Numerical Simulations

Numerical simulations were performed using the finite-difference time-domain method using a commercial software package from Lumericals Solution, Inc (Vancouver, Canada). A perfectly matched substrate layers were considered and then a periodic boundary condition is considered at the sides. Measurements were recorded with a mesh size of dx = 0.1 nm, dy = 0.1 nm, dz = 0.4 nm were chosen during the convergence analysis in order to guarantee the stability of the calculations of near field and absorbance. An

unpolarized excitation wavelength of 633 nm is used to incident normally through the air medium. The simulated models were constructed by matching the best possible arrangements as measured from AFM and SEM images. NCAs were modeled by distributing 12 or 48 NP (taken as gold nanospheres with material data from Robert L.Olmon et al.)[391] with a diameter of 11.5 nm distributed in layers (2 layers for A and 4 layers for B) around the features of the template A and B **(Table 3.1 and Figure 3.2)**. Template#A was modeled periodic array of organic features with the diameter of 25.5 nm, the height of 15 nm and pitch of 50 nm. Template#B was modeled with a diameter of 59 nm, a height of 37 nm, and a pitch of 90 nm. The NP were considered submerged to a depth of 1 nm into the polymer templates. The plane wave excitation in the excitation range 600 nm - 800 nm was considered.

Table 3.1. Geometrical Values obtained experimentally for the model in FDTD Simulation.

Parameters	**NCA#A [Model]**	**NCA#A [Experimental]**	**NCA#B [Model]**	**NCA#B [Experimental]**
Wavelength Incident	633	633	633	633
*Micelle Height (h)	15	19.6 ±1.9	37	38.3 ±3.8
NCA Height, H	23		47 [8r+1 from script]	-
*Micelle Width, w	25.5	38.4 ±3.8	59	69 ±6.9
Nanoparticle Radius (r)	5.75	5.15 ±0.5	5.75	5.15 ±0.5
NCA Diameter, D	48	46.5 ±5	80	85.6
Periodicity, P	50	57 ±5	90	92.9 ±19
*Inter-cluster distance (P – NCA Diameter)	~9	10.5	10	7.3
Inter-particle distance	0.75		0.75	
*No. of nanoparticle/cluster	12	11	48	42
*Overlapping of Nanoparticle inside polymer micelle, L	~1.5	-	~1.5	-
Absorbance Peak	635	648	641	653

*Adjusted values to make a structure model with low randomness and defined arrangements.

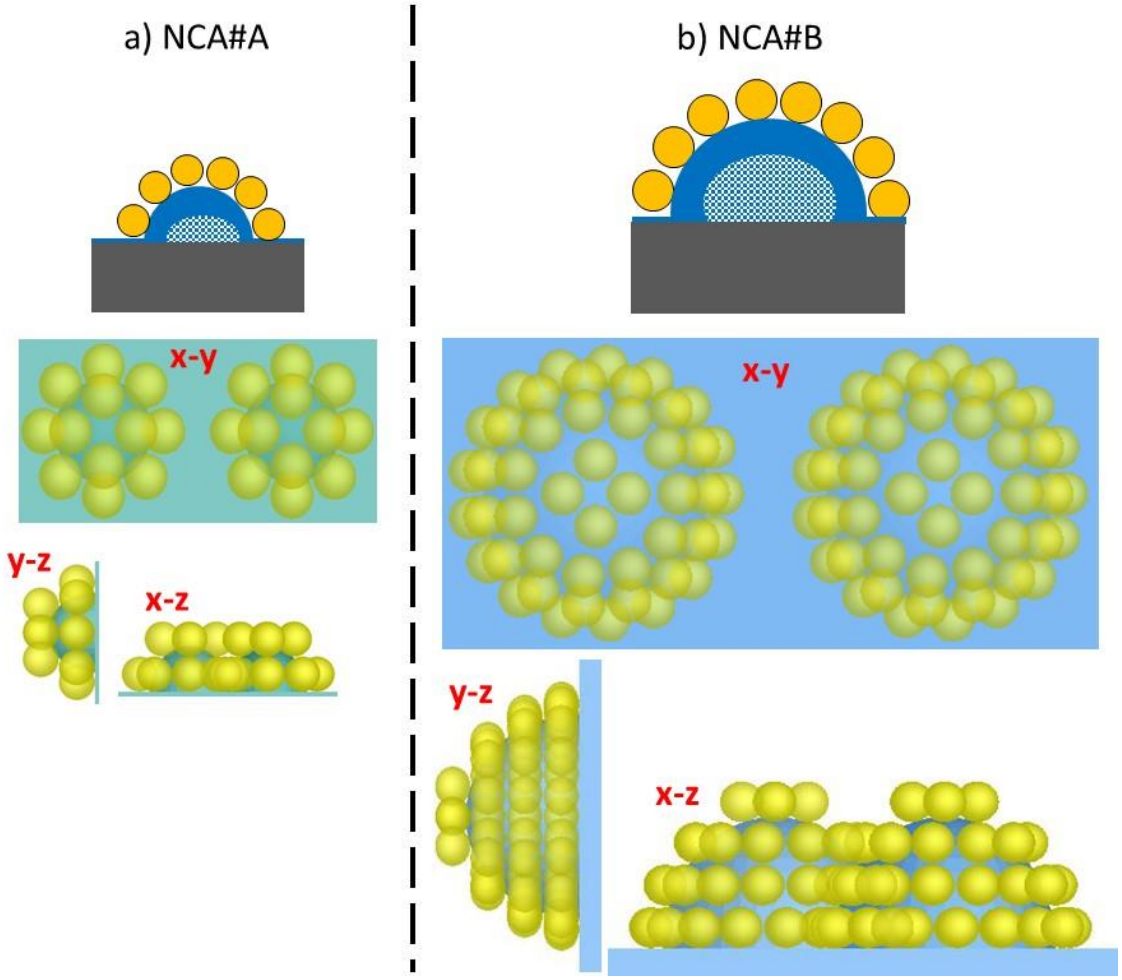

Figure 3.2. Layered crown arrangement of the NP used to model the optical response of NCAs.

3.2. Results and Discussions

3.2.1. Dual-Lengthscale EM hot-spots

Gold nanoparticle cluster arrays (NCA) exhibiting periodic arrays of the gold nanoparticle clusters giving rise to dual length scale EM hot-spots were obtained by molecular self-assembly approach, we reported earlier.[315] The approach involves self-assembly reverse micelles of polystyrene-block-polyvinylpyridine deposited under controlled conditions to produce periodic arrays of nanoscale templates **(Figure 3.1)**. The reverse micelle features acquire a positive charge in neutral or acidic aqueous media due to the basicity of the pyridyl group of the core-forming PVP blocks. This transforms the

template into arrays of polyelectrolyte features that enable spatially selective attachment of negatively charged gold NP to form an array of gold nanoparticle clusters. The nanoparticle cluster arrays conserve the periodicity (or pitch) of the original templates, while their feature width increases by a distance equivalent to the diameter of two NP.[315] The control over coating conditions is used to fine-tune the periodicity of the array, or in other words, the separation between the adjacent nanoparticle clusters **(Figure 3.1)**.

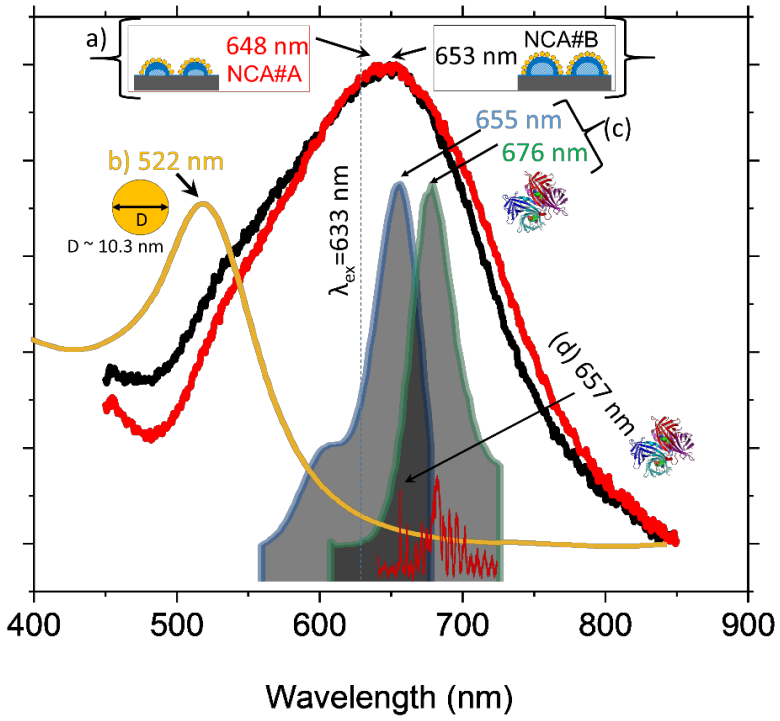

Figure 3.3. A comparative view of (a) Plasmon resonance peak positions of NCA#A (red), NCA#B (black) and (b) Gold nanoparticle, (c) Fluorescence excitation (blue) and emission (green) peaks of SA-Cy5 and (d) the characteristic Raman peak of Cy5 used for assays. The dotted line indicates the excitation wavelength of 633 nm used for SERS and Fluorescence measurements.

By nature of the formation, the NCAs present EM hot-spots between NP within a cluster (or, inter-particle hot-spots), and between adjacent clusters (or, inter-cluster hot-spots). NCAs with two different dimensions were optimized for the current study, with difference only in the size of the cluster, while ensuring a fixed inter-cluster separation distance **(Figure 3.1)**. To assure these geometric requirements, the NCAs were derived out of spherical reverse micelle templates produced from polystyrene-block-polyvinylpyridine copolymers of two different molecular weights, namely, 81.5 kDa (for NCA#A) and 443 kDa (for NCA#B).

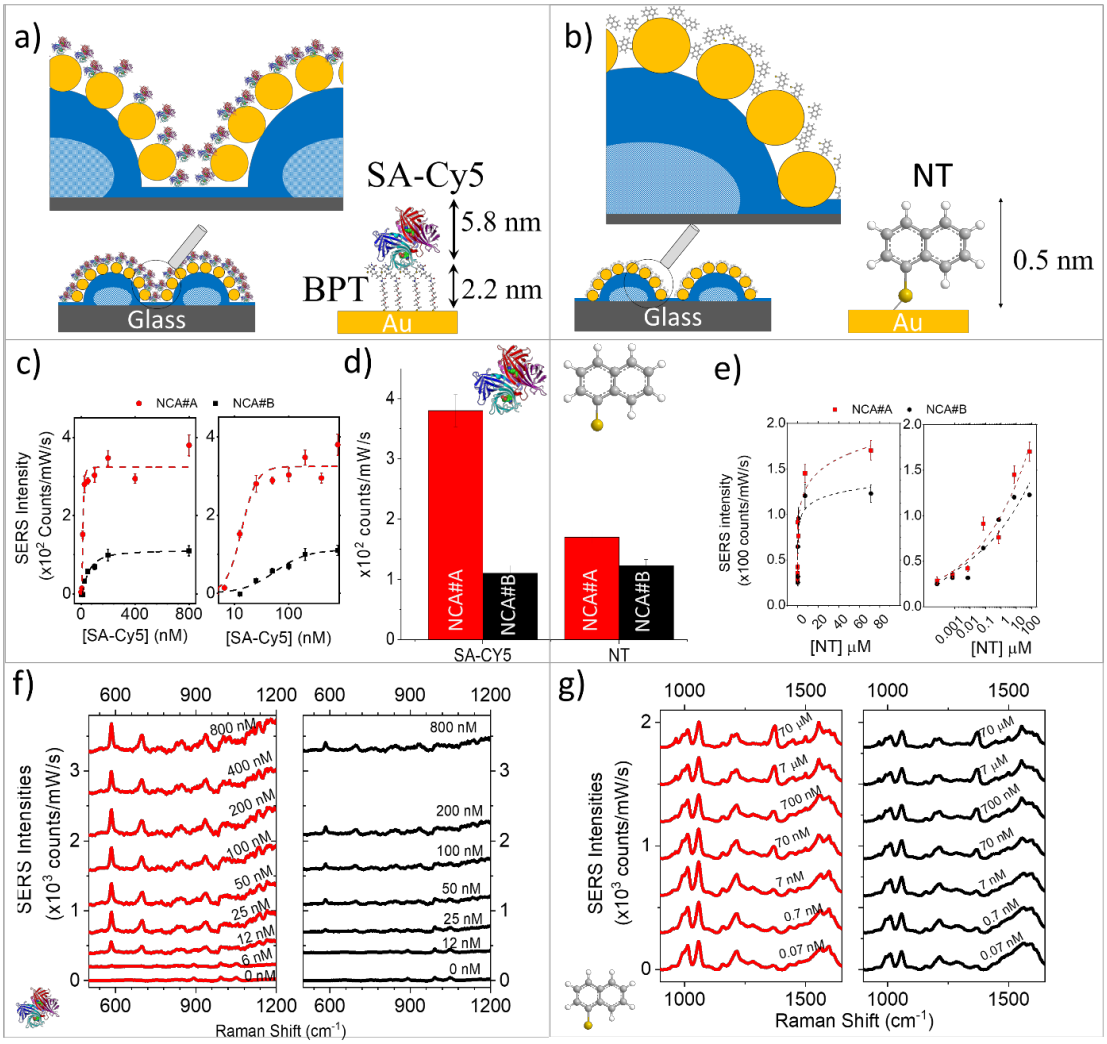

Figure 3.4. (a,b) Schematic illustration showing better leverage of (a) SA-Cy5 over inter-cluster hot-spots and (b) NT over inter-particle and inter-cluster hot-spots. The relative molecular dimensions are shown. (c,e) SERS Assay (c) SA-Cy5 and (e) 1-NT showing evolution of characteristic peak intensities at 583 cm^{-1} and 1371 cm^{-1} respectively. (d) SERS intensities corresponding to the saturated densities of SA-Cy5 and NT on NCA#A and NCA#B. (f, g) SERS spectral evolution on the NCAs at different concentrations of SA-Cy5 and NT.

The feature separations in the templates were systematically varied in steps of few nanometers at a time by varying spin-coating speeds and concentration. Template#A and template#B with equivalent feature separations of ~30 nm were subsequently chosen for preparation of NCA#A and NCA#B respectively. The chosen templates were subsequently exposed to an aqueous suspension of citrate-stabilized gold NP with ~10.3 nm diameter to produce NCAs. The feature separation (inter-cluster gaps) in NCAs reduced further by ~20 nm, corresponding to the diameter of two gold NP from adjacent clusters. Thus, the

optimization of the template spacing allowed producing both the NCAs (NCA#A and NCA#B) with the same inter-cluster gap of 10 nm ± 2 nm. However, the inter-particle distances in both NCAs are in the sub-5 nm length scales and exhibit variability which is characteristic of random sequential adsorption of particles.[392,393] Thus, the two NCAs exhibit inter-particle and inter-cluster distances that are equivalent, with the only difference being the size (width and height) of the NCAs, which is larger for NCA#B as compared to NCA#A. As a result of this, NCA#A has a greater density of features compared to NCA#B (Figure 1g-h). The highly resolved inter-particle and inter-cluster separations set the expectations for strong plasmonic coupling between particles within the clusters and between adjacent clusters. This is confirmed by the appearance of plasmon resonance peaks for NCA#A and NCA#B at ~648 nm and ~653 nm respectively, both of which considerably red-shifted from the plasmon resonance at ~522 nm for isolated gold NP **(Figure 3.3)**. It can be seen that the tools offered by the self-assembly approach enabling variation of the array pitch in steps of only a few nanometers, without affecting the size of the templates, was critical to deriving NCAs with desired geometric attributes.

3.2.2. Plasmonic Bio-Assays

The performance of NCAs towards plasmonic bioassays based on surface-enhanced Raman **(Figure 3.4)** and metal-enhanced Fluorescence **(Figure 3.5)** spectroscopies towards the quantitative measurement of Biotin-Streptavidin interactions were investigated. The interaction between biotin and streptavidin is amongst the strongest of non-covalent biological interactions known with dissociation constants in the femtomolar range.[394,395] The interaction is also widely used to tag biotinylated antibodies or oligonucleotides to streptavidin conjugates of enzyme, fluorophores, or NP in different bioassay schemes.[396,397] The pair also exhibits good resistance against denaturation and proves beneficial as model interaction for evaluating the performance of plasmonic assays.[394,395,398] The NCAs were first functionalized using PEG biotin thiol (0.4 kDa) (BPT) followed by Bovine Serum Albumin (BSA) to block non-specific binding sites, and subsequently to Streptavidin (SA) conjugated to Cyanin-5 (Cy5). Cy5 can be excited at 633 nm, which corresponds to its excitation wavelength **(Figure 3.3)** and serves as a useful reporter to follow the concentration of SA-Cy5 by both Raman and Fluorescence spectroscopies.[399] Each NCA is exposed to SA-Cy5 for 2 hours at different concentrations in the range of 1 - 800 nM.

This was followed by several cycles of washing with the buffer solution and drying with nitrogen before the acquisition of SERS and MEF spectra. SERS spectra show a good match with peak positions of Cy5 reported in the literature.[399] The intensity of the characteristic peak of Cy5 at 583 cm^{-1} was followed to quantify SERS spectral dependence as a function of the concentration of SA-Cy5. The SERS assay was found to be well-behaved and quantitative as revealed by an excellent fit to the Langmuir-Hill adsorption isotherm. The standard deviation in intensities obtained across multiple areas on-chip separated by several square millimeters was found to have variability below 10 %. An observable signal intensity was obtained down to 6.5 nM for NCA#A and 25 nM for NCA#B revealing higher sensitivity of NCA#A. The presence of a highly enhanced EM field from the underlying nanoparticle clusters together with the spacer layer from the biotin-streptavidin interaction pair provides a favorable situation to experience metal-enhanced fluorescence (MEF). Evolution of fluorescence intensities under 633 nm excitation show strong fluorescence enhancements on both NCAs. Comparison of the evolution of signal intensities with concentration of SA-Cy5 show higher intensities for NCA#A as compared to NCA#B, as observed in the SERS assays.

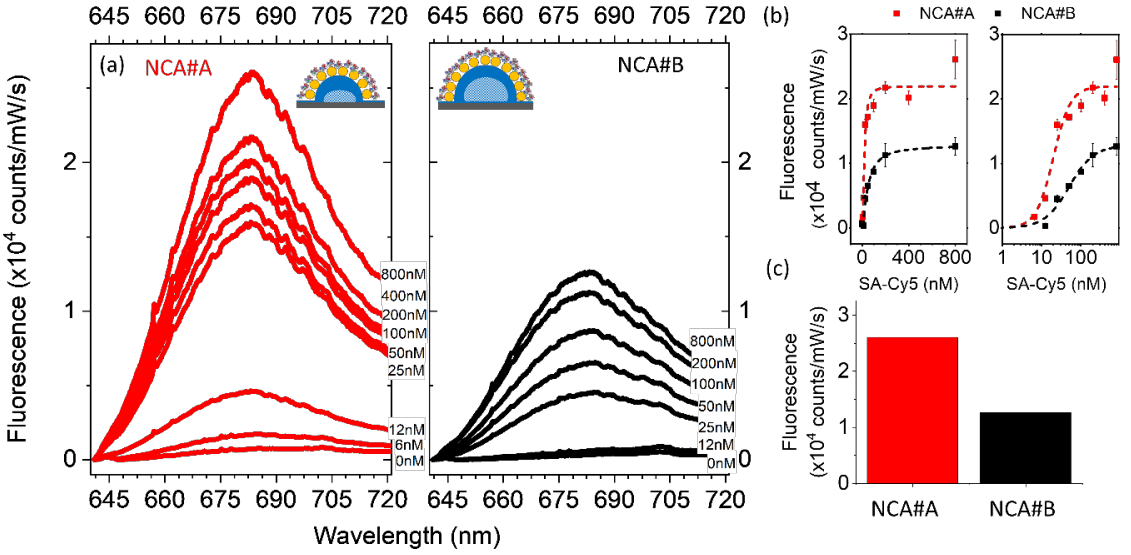

Figure 3.5. Comparison of (a) fluorescence spectral evolution as a function of the concentration of NCA#A and NCA#B. (b) Fluorescence assays of SA-Cy5 on NCA#A and NCA#B acquired with 633 nm excitation shown in (left) linear and (right) logarithmic scale, fitted with Langmuir-Hill isotherm. (c) comparison of the fluorescence intensities corresponding to a saturated density of SA-Cy5 on both NCAs.

3.1.1. Numerical Simulations

To rationalize the higher sensitivity of NCA#A compared to NCA#B, it is important to assess the local amplification of electromagnetic fields by the clusters. The EM profiles and the absorbance of the NCAs were simulated numerically using calculations in the time domain of finite differences (FDTD). The choice of geometries for the template and the nanoparticle dimensions were followed from the experimentally determined from AFM and SEM measurements. The number of NP per cluster was obtained following the distributions obtained from SEM. The inter-particle distance inside the cluster is considered as a variant between zero (contact) to a few nm for both configurations, in line with the observation of the random distribution of NP within the cluster. The NCAs are modeled as NP distributed in the layered crown **(**Error! Reference source not found.**Table 3.1 and Figure 3.2)** as shown by Zhang et al.[257] The inter-particle distance inside the cluster is fixed at S = 0.75 nm and that the micelles are arranged in a hexagonal periodic network with a period of 50 nm for NCA#A and 90 nm for NCA#B. The simulations were performed using a mesh of 0.1 nm in the x and y directions and 0.4 nm in the z-direction, adopting the Yu-Mitra method[400] to refine the mesh.

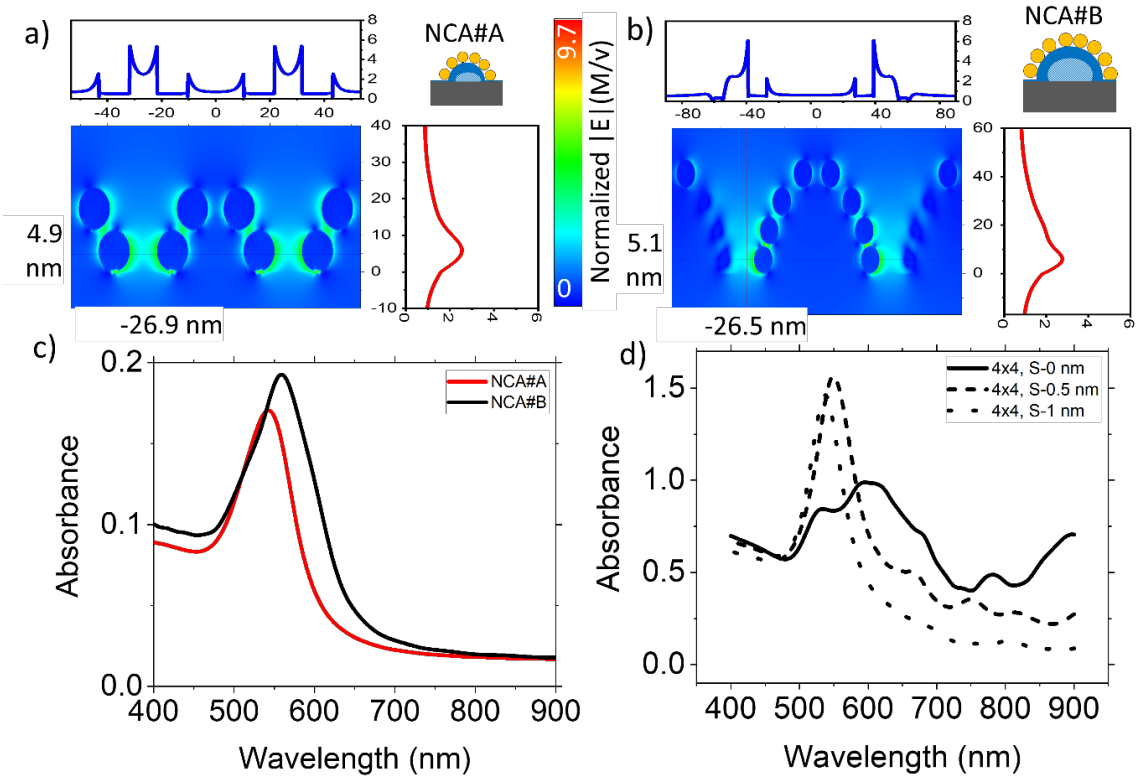

Figure 3.6. (a,b) Simulated electromagnetic field profiles on a) NCA#A and b) NCA#B at 633 nm excitation, and (c,d) simulated absorbance spectra of (c) the two NCAs and (d) comparison of response for 3 different interparticle separations (S) using 4x4 hexagonal nanoparticle network.

The near field simulations (**Figure 3.6**), confirm the presence of inter-particle and inter-cluster hot-spots with similar enhancement in the two NCAs. The normalized absorbance calculation is given in **Figure 3.6** and indicates plasmon resonance peak at 543 nm for NCA#A and 559 nm for NCA#B **(Figure 3.6b)**, which do not agree with the experimental spectra (**Figure 3.3**). However, a simulation-based on a cluster plan of 16 NP established in a 4x4 hexagonal nanoparticle network on substrate reproducing the study of Nadeyalkov[401] with our material and the size parameters offers further insights to rationalize the higher shifts in observed plasmonic peak wavelengths. **(Figure 3.6d)** The simulated absorbance for 4x4 configuration, and S = 0, shows broad resonance peak and a shift around 600 nm, which indicates the possibility of touching particles within the NCAs to contribute to the observed peak wavelengths. The gap distance is a critical parameter contributing to the amplification in dimers and nanoparticle-chain.[402–404] The observed experimental data for the nanoparticle cluster morphologies point to similar inter-particle and inter-cluster gaps in both the NCAs **(Figure 3.1).**

3.2.3. Leveraging Inter-Cluster EM Hot-Spots

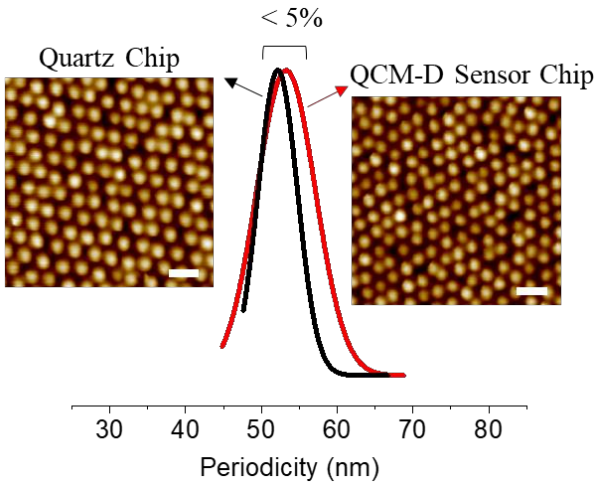

Figure 3.7. Comparison of the geometric attributes of the Template#A on fused silica chip and gold-coated QCM sensor, showing tapping mode AFM topography images, and the distribution in periodicities show variation below 5%.

The NCAs have two types of EM hot-spots, one at the junction between NP within the cluster (inter-particle hot-spots), with dimensions <1 nm, and other that is between the nanoparticle clusters (inter-cluster hot-spots) with dimensions <10 nm. Taking into account the dimensions of Biotin PEG thiol (2.2 nm long), and SA-Cy5 (4.2 nm x 4.2 nm x 5.8 nm),[405] the length of the interaction pair is expected to be around 6.6 – 8 nm. While the inter-cluster hot-spots are capable of accommodating the interaction, the inter-particle hot-spots cannot. Thus, it is reasonable to expect that the SA-Cy5 molecules would leverage only the inter-cluster EM hot-spots as illustrated in **Figure 3.4**. Given that the inter-cluster separations are maintained the same between the NCAs, **(Figure 3.1e)**, the smaller size of NCA#A (diameter 38 ±5 nm) compared to NCA#B (diameter 86 ±5 nm) manifests as lower values for lattice periodicity. The periodicity directly determines the feature density and the binary junctions between the features. Thus, smaller size in case of NCA#A (diameter ~38±5 nm) results in a larger density of features (density~350 /μm^2) as compared to NCA#B (diameter ~86±5 nm, density ~100 /μm^2) **(Figure 3.1g,h)**. This would result in a greater number of inter-cluster hot-spots in the case of NCA#A as compared to NCA#B. **(Figure 3.1g)** Since the SA-Cy5 can leverage only the inter-cluster hot-spots, which in turn occurs in greater numbers in NCA#A would explain the higher sensitivity of NCA#A.

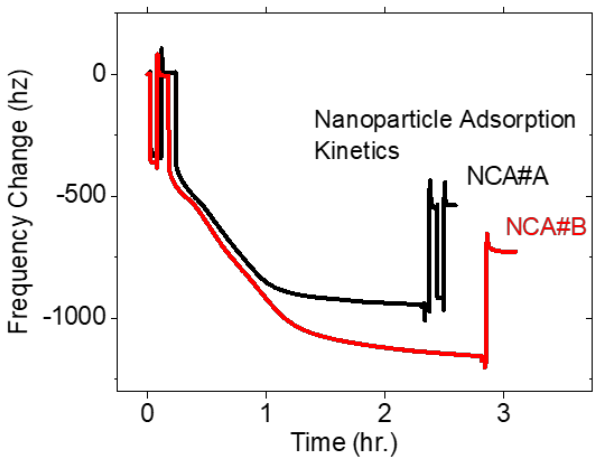

Figure 3.8. QCM-D measurement showing adsorption kinetics for NP on polymer template A (black) and B (red).

However, this hypothesis cannot be confirmed unless the concentration of the protein molecules in both the NCAs are known. To determine this, the templates A and B were coated on a QCM sensor, and the different steps including the deposition of the NP, and the bioassay was performed while monitoring the mass changes measured by the QCM.

The geometric characteristics of the templates on the QCM sensors were confirmed to be the same as those obtained on glass chips **(Figure 3.7)**. This allows extrapolating the QCM measurements of nanoparticle**.** QCM-D measurement showing adsorption kinetics for NP on polymer template A (black) and B (red) and SA-Cy5 **(Figure 3.8)** densities to those obtained on glass chips.

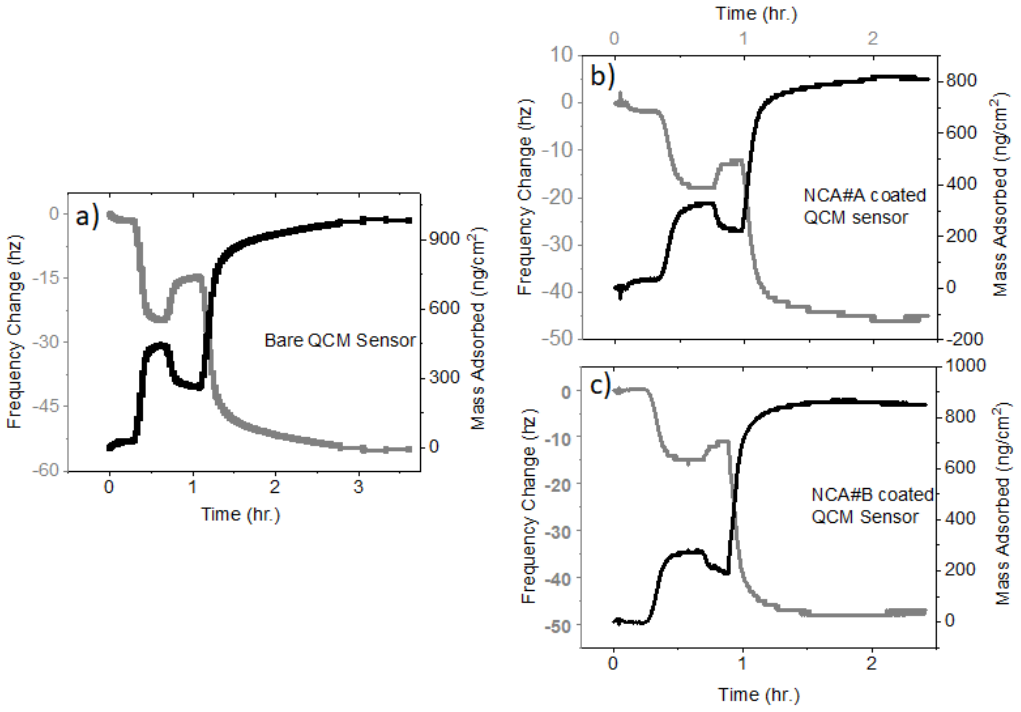

Figure 3.9. QCM-D measurement showing adsorption kinetics for a) Bare QCM-D sensor, b) NCA#A coated QCM-D sensor, and c) NCA#B coated QCM-D sensor.

The saturated density of NP, as well as the SA-Cy5 molecules after the bioassay completion, is plotted in **Figure 3.10a-b**. The saturated surface density of Au NP as well as SA-Cy5 is found to be higher for NCA#B as compared to NCA#A **(Figure 3.8 and Figure 3.9b-c)**. The SA-Cy5 concentrations are expected to follow the concentration of BPT attached to gold by thiol-gold interactions. However, an estimate of the surface sites available on the NCA rules out the possibility to account for the observed density of proteins. This strongly points to the adsorption of SA-Cy5 also in the polystyrene matrix between the features. A control experiment performed on polystyrene coated QCM sensors confirm the adsorption of biotin and Streptavidin with densities on par with those observed on the gold surface. We did not find prior work in literature explaining the strong adsorption of biotin to polystyrene, the origin of which needs further investigation and will be pursued

within a different study. The adsorption to PS confirms the distribution of SA-Cy5 in the space between the NCAs and thus co-localized with the inter-cluster EM hot-spots.

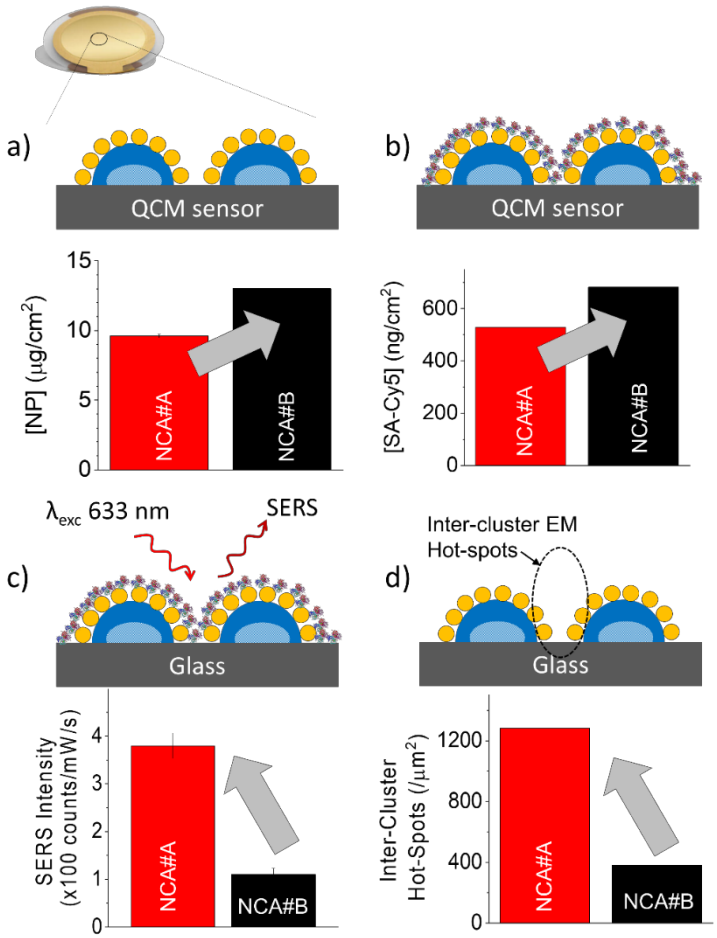

Figure 3.10. Saturated surface densities of (a) Au NP and (b) SA-Cy5 bound to biotinylated NCA show higher values for NCA#B compared to NCA#A. (c) Higher SERS intensities observed for NCA#A, aligned to trends for d) the density of inter-cluster EM hot-spots.

The observation of lower Au nanoparticle densities, as well as lower analyte surface concentration in the case of NCA#A, rules out the role of analyte concentrations towards its higher sensitivity. This supports well the hypothesis that the NCA#A derives its higher sensitivity from the greater number of inter-cluster hot-spots that the SA-Cy5 can leverage on. To further confirm the above arguments, the NCAs were compared for their SERS sensitivity towards the detection of 1-napthalenethiol (NT), which is a much smaller probe molecule. The dimension of a molecule of NT is only 0.3 nm, which unlike SA-Cy5, is expected to occupy not only inter-cluster EM hot-spots but also inter-particle hot-spots. Comparison of the SERS intensities of the concentrations of NT for NCA#A and NCA#B

shows a much-reduced difference in sensitivity for both. This aligns well with the expectation of outcome that would follow based on the assumption that the NT molecules would leverage both inter-particle and inter-cluster hot-spots. The reason for marginally higher SERS intensities for NCA#A over NCA#B despite the higher density of NP in NCA#B remains unclear at the moment. Yet, the higher sensitivity of NCA#A regardless of the lower analyte surface densities together with the dependence of the assay sensitivity on the dimension of analyte strongly highlights the opportunity to design plasmonic arrays taking into account the distribution of analyte in relation to the EM hot-spots.

3.3. Conclusions

Nanoparticle cluster arrays (NCA) of gold, exhibiting dual-lengthscale EM hot-spots were fabricated by hierarchical self-assembly based on block copolymer colloids. The dual-lengthscale EM hot-spots provided a unique opportunity to accommodate both small organic molecules, as well as large biomolecular analyte such as proteins. The NCA geometry that presented a greater number of inter-cluster junctions provided greater opportunities for co-localization of the larger protein analytes with the (inter-cluster) EM hot-spots. This was found to deliver higher sensitivity in SERS and MEF based plasmonic bioassays, delivering sensitivity down to 1 nM in highly sensitive assays. The convenient handles from the self-assembly approach, to control size and separation between the nanoparticle clusters was critical to identifying high performing geometry for plasmonic biosensing. The use of quartz crystal microbalance to measure the surface density of analytes on the NCAs was important to de-correlate the relative contributions due to the electromagnetic enhancements and analyte surface concentration towards the sensitivity of plasmonic assays. The findings open new opportunities to the rational design of plasmonic sensors by factoring in the dimensions of analyte molecules into the geometry of nanoplasmonic assemblies.

Chapter 4. Nanoparticle Cluster Arrays On Gold Substrate

This chapter is based on the published paper in [Journal Name] "Engineering Electromagnetic Enhancements in Gold Nanoparticle Cluster Arrays on Reflective substrates for High Sensitivity in (Bio)molecular detection", R. Rastogi, E. A. Dogbe-Foli, R. Vincent, P. Michel-Adam, S. Krishnamoorthy. [DOI].

Nanoplasmonic sensors based on surface-enhanced spectroscopies are capable of delivering sensitivity down to few molecules. Harnessing their potential for sensing requires producing highly electromagnetic (EM) hot-spots with high EM fields with configurations that encourage analyte co-localization with EM hot-spots. Here we report nanoparticle cluster arrays supported on gold substrates as capable of delivering high sensitivity in detection of large and small molecular analytes with limits of detection down to picomolar concentrations. Numerical simulations reveal both inter-particle and inter-cluster EM hot-spots, with such enhancements strongly dependent on the size of the clusters and the presence of gold film. Presence of gold film increased inter-cluster enhancements resulting in over 2 orders of magnitude for NCAs on gold as compared to NCAs on glass substrates. Sensitivity towards molecular detection was found to be higher for the larger NCAs (define, by NP numbers) on gold, and smaller NCAs on glass. The results show the rational design of plasmonic nanoarrays to play an important role in enabling analyte co-localization at EM hot-spots, suitable for biomolecular detection, and NCAs on gold to be a favourable configuration in this direction.

4.1. Introduction

Noble metal nanostructures have been used to harness light-matter interactions in different contexts including photovoltaics,[132] optoelectronics,[131] catalysis and molecular detection.[55,130,134] The high EM field enhancements in hot-spots, whose spatial dimensions are typically of the order of the molecules themselves, provide unique opportunity to enhance sensitivity in molecular detection by plasmon-enhanced spectroscopies. High EM

enhancements at the hot-spots are known to disproportionately dominate the signal contributions from analyte that are strategically located within the hot-spots.[169] EM enhancements at the hot-spots are dependent on the geometry of the nanoplasmonic interface, and are often strongly pronounced at the junctions between adjacent metal nanostructures. The EM enhancements at the junctions have shown non-linear decrease with increasing gap distance at the junction. This makes it necessary to produce ultra-low separations of the order of a nanometer to realize EM enhancement factors over 10^8.[60,61] Attaining large number of highly enhancing EM hot-spots within areas easily addressable by spectroscopic tools are amongst significant objectives in the fabrication of nanoplasmonic sensors for plasmon-enhanced spectroscopies. While most of such approaches have shown plasmonic arrays presenting hot-spots that can be leveraged for small molecules, they are inherently incompatible for large molecular analytes such as biomolecules. Engineering highly enhancing EM hot-spots in a configuration that can be readily leveraged by larger analytes, spanning few nanometers to few tens of nanometers remains a hard challenge to address.

Different configurations are explored in literature to achieve analyte co-localization at EM hot-spots, including responsive structures,[264,265,273,406] configuration with mechanical instabilities,[266,271,272] and NP separated from metal thin films.[259,261] Nanoparticles (NP) on metal thin films (MTF) are particularly interesting considering the ease of production without using complex lithographic tools. The optical response from NP-dielectric-MTF interfaces can be tuned by controlling the distance between the dielectric thickness,[149,407–412] interparticle distance,[413] polarisation and the incident angle,[414] or the choice of metal.[415] The hybridization between localized surface plasmons of NP and delocalized surface plasmons from the metal thin film can result in EM enhancements at NP-MTF gap, and the inter-NP gaps.[416] The localized EM fields at the NP-MTF gaps can be used to enhance sensitivity in detection of analyte that can be accommodated at the gap.[414,417] In NP assemblies, strong inter-NP plasmonic coupling at high NP density, and thus low inter-particle distances was found to result in decrease in EM field at NP-MTF gaps.[411] This was attributed to the increased scattering and absorption of incident light by the dense array of NP. The intense EM fields were achieved in any case at ultra-low separations close to a nanometer, which is impractical to leverage for large bio-molecular analytes.

While the studies of inter-particle coupling has focused so far on isolated NP and nanoparticle assemblies on MTF, they do not investigate the EM field distribution in nanoparticle clusters supported on MTF. Nanoparticle clusters have shown to exhibit specific EM field enhancement characteristics of high advantage compared to stochastic nanoparticle assemblies, viz. control over EM field profiles through the size and separation between nanoparticle clusters, and the possibility of two different types of EM hot-spots, one between NP within the cluster, and those between adjacent clusters. We have earlier shown periodic nanoparticle cluster arrays (NCA) by self-assembled molecular templates, with capability to produce controlled inter-cluster separations that are large enough to accommodate larger analytes. Enhancing EM enhancements at the inter-cluster space would thus result in higher sensitivity in detection of larger molecular analytes such as biomolecules. Here we demonstrate strong dependence of the EM fields on the presence of gold substrate and the size of the nanoparticle clusters, delivering configurations show picomolar sensitivity in detection of proteins **(Figure 4.1)**.

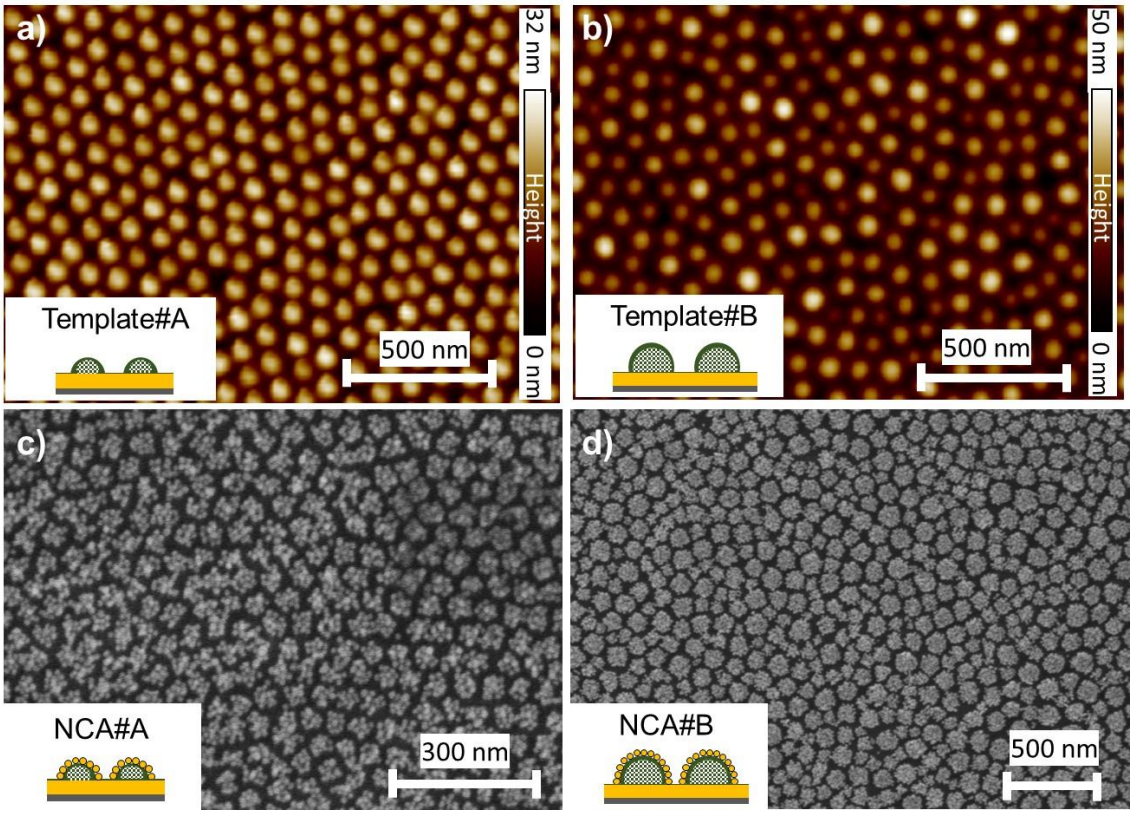

Figure 4.1. (a,b) Nanoscale templates, a) Template#A and b) Template#B that direct the formation of nanoparticle cluster arrays c) NCA#A and d) NCA#B. The insets show the illustration of the cross-section of the templates and the NCA.

4.2. Experimental Methods

Materials: Polystyrene-block-poly(2-vinylpyridine) (PS-*b*-PVP) (81.5 *kDa and* 443 *kDa*) was purchased from Polymer Source Inc. (Montreal, Canada). Quartz substrates were purchased from Siegert Wafer (Aachen, Germany). 1-napthalenethiol (≥99%), m-Xylene (≥99%), sodium citrate dihydrate (≥99%), Hydrogen tetrachloroaurate(III) trihydrate ($HAuCl_4.3H_2O$) (≥99.9%) were purchased from Sigma- Aldrich. Biotin-PEG-Thiol (400 *g/mol*) was purchased from Nanocs, New York, USA. Phosphate Buffer Saline (PBS) and Bovine Serum Albumin (*BSA*) solution (10x) was purchased from R&D Systems, Abingdon, UK. Streptavidin Conjugated with Cyanine-5 dye (60 kDa) was purchased from Rockland, Limerick, PA. Supersharp, AFM tips (SSS-NCHR-50) were purchased from Nano and more (Paris, France).

4.2.1. Fabrication of Nanoparticle Clusters

Polymer templates were fabricated as described in chapter 3, using 81.5 *kDa* and 443 *kDa* PS-b-P2VP polymer for NCA#A and NCA#B, respectively. Substrate were pre-coated with 100 nm gold coated quartz substrates with 5 nm chromium adhesive coating and bare quartz substrate. Freshly cleaned substrates were spin coated at 5000 rpm with 0.75 *% w/w* of polymer#A and 3000 rpm with 2 *% w/w* of polymer#B in m-xylene. After 30 s of oxygen plasma exposure (RIE Plasmatherm 790 RIE) for polymer#B coated sample only, both the samples were immersed in gold nanoparticle (diameter = 10.3 ±0.5 nm) solution synthesized in house using method reported earlier,[388] for 2 hours. Then the samples were rinsed thoroughly and dried to perform molecular assays. Topographical images were acquired through AFM (in tapping mode) and SEM. Gausian fit to diameters, heights and periodicities from Nanoscope analysis for AFM images and ImageJ analysis for SEM images were peformed to validate geometrical features used for modelling.

4.2.1. Spectroscopic Measurements

For NT Raman probe detection, an average of 10 scans per spot was acquired and an average of 10 different spots on each sample, to calculate the standard deviations. Each scan was taken with a total exposure of 9 s with a 633 nm He-Ne LASER at a power of 1.9 mW under 50x/0.5 N.A. objective. For bio-molecular detection using fluorescent-dye Cy5

conjugated to Streptavidin, each measurement was recorded at 10 different places throughout the functionalized surface, with 3 s of total exposure time at 1% power to prevent the saturation of the CCD due to Fluorescence background.

4.3. Results and Discussion:

4.3.1. Nanoparticle Cluster Arrays (NCA) On Gold Films

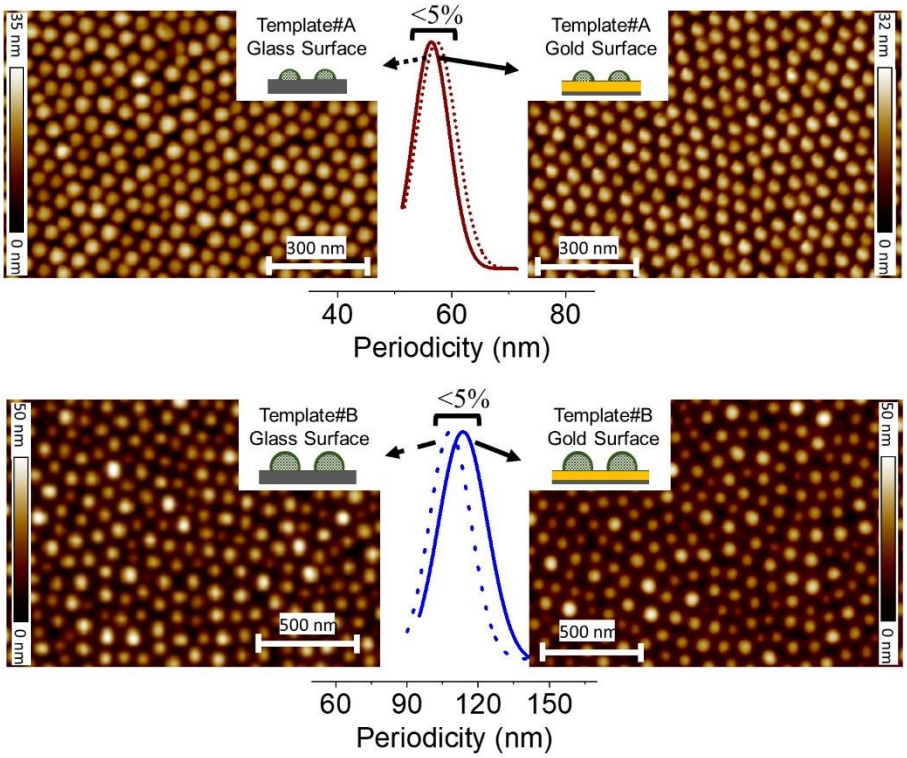

Figure 4.2. Comparison of atomic force microscopy images of the (above) template#A and (below) template#B fabricated on (left) glass and (right) gold.

NCAs were fabricated on gold thin films using electrostatic attachment of negatively charged gold NP on self-assembled block copolymer colloids containing polycationic blocks as reported earlier.[315] Solutions of polystyrene-block-polyvinylpyridine (PS-b-PVP) in xylene were spin-coated on the gold-coated quartz (fused silica) substrates to obtain quasi-periodic arrays of semi-ellipsoidal features of reverse micelles on surface. The features contain polystyrene exposed outside and the polyvinylpyridine buried within it. When exposed to aqueous solution of gold NP with acidic or neutral pH renders the PVP groups polycationic, resulting in the spatially selective electrostatic attachment of NP The

resulting NCA retain periodic organization of the original templates, with the size of the NCA (or, the number of NP per cluster) defined by the surface area available on the templates.

NCA of two different dimensions, NCA#A and NCA#B were fabricated using templates#A and B formed out of PS-b-P2VP with molecular weight of 81.5 and 443 kDa respectively. The resulting NCA#A and NCA#B exhibit a constant feature separation, albeit lower than that of the templates, due to presence of gold NP. The constant average inter-cluster separations of NCA#A and NCA#B assures attributing the optical and spectroscopic response to only the size, and free from impact of the feature separations.

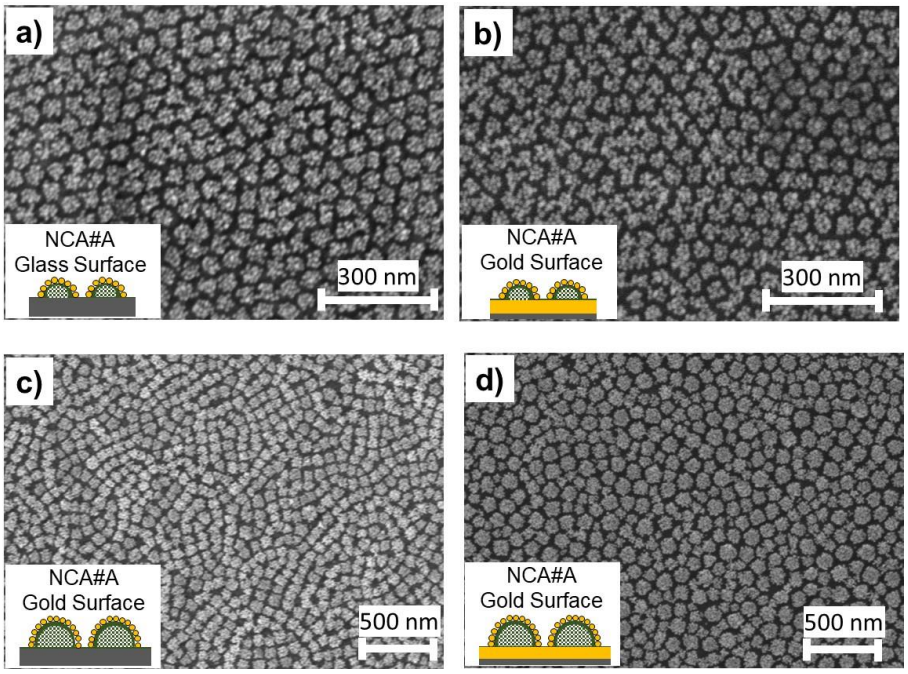

Figure 4.3. Comparison of scanning electron microscopy images of the NCAs fabricated on (a,c) glass and (b,d) gold.

The NCAs exhibit height, diameter and periodicity of 23 nm, 46.5 and 57 nm for NCA#A and 47 nm, 85.6 nm, 92.9 nm for NCA#B. The feature separations were manually obtained by histograms obtained out of 50 features, from high resolution scanning electron microscopy images with a magnification of at least 100kx. Control substrates with the NCA#A and NCA#B on fused silica substrates were made in order to compare the effect of the underlying substrate. The geometric attributes of the templates A and B, and that of the resulting NCAs were characterized using AFM and SEM, and were found to exhibit

variation below 5% **(Figure 4.2** and **Figure 4.3)**. Attaining geometrically equivalent NCA on glass (NCA@Glass) and gold substrates (NCA@Au) assures the investigation to attribute the observed differences solely to the effect of the substrate, and independent of the geometry of the NCAs.

4.3.2. Optical properties

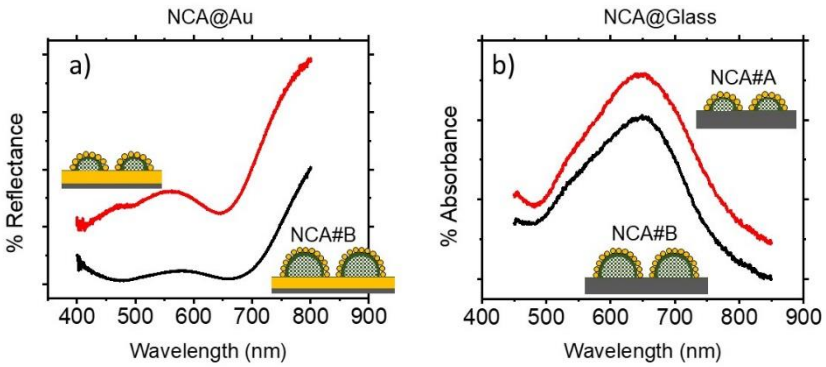

Figure 4.4. (a) Reflectance spectra w.r.t. planar gold film and b) absorbance spectra of NCA supported on a) gold and b) glass substrates.

The optical properties of the NCA@Au substrates were investigated by their reflectance spectra that show a dip at wavelengths corresponding to 647 nm for NCA#A and 669 nm for NCA#B. respectively. The absorbance spectra of NCA@Glass substrates show absorbance peak 646 and 648 nm respectively. **(Figure 4.4)** The strongly red shifted plasmon resonance peaks for NCAs as compared to isolated gold NP (~520 nm) can be attributed in part to the strong inter-particle and inter-cluster plasmonic coupling in the NCAs supported on the substrates. This was further confirmed from EM field maps that were simulated using FDTD calculations.

Numerical simulations based on finite difference time domain (FDTD) were performed with the NCAs geometrically modelled with values supported by experimental observations (as also discussed in section 3.3.5). Numerical simulations on NCA@Au reveal EM field enhancements in the inter-particle gaps and inter-cluster gaps for both NCA#A and NCA#B **(Figure 4.5)**. However, the EM field profiles in the inter-cluster space was much more pronounced in NCA#B as compared to NCA#A. In comparison, the EM field profiles of NCA@Glass show lower enhancements than observed for NCA@Au for both NCAs.

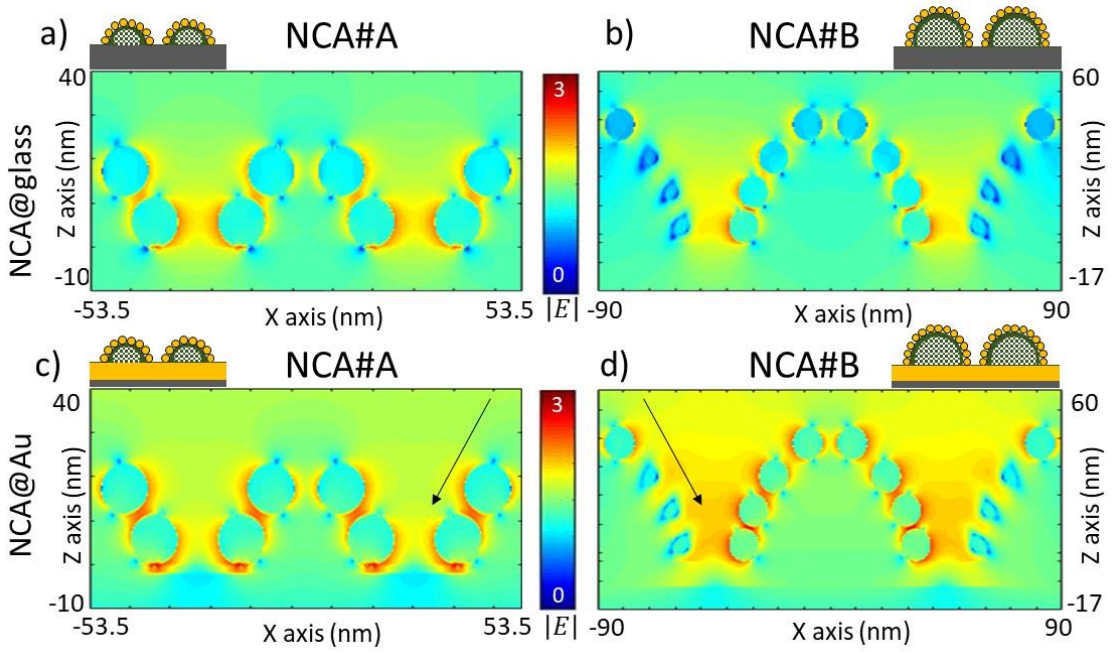

Figure 4.5. FDTD simulation of electromagnetic field profiles of (a,c) NCA#A and (b,d) NCA#B compared for (a,b) gold and (c,d) glass substrates.

The higher enhancements in NCA@Au can be attributed to role of underlying gold film in increasing field strength close to NCAs. The strong localized field strength close to the NCA observed in the EM field maps at 633 nm corroborate with dip in reflectance spectra at this wavelength. For NCA@gold, the field maps show greater inter-cluster enhancements for NCA#B than NCA#A, indicating strong inter-cluster plasmonic coupling in NCA#B. This field maps corroborates with the observation of the reflectance dip for NCA#B appearing at a higher wavelength as compared to that of NCA#A. In case of NCA@Glass, EM field maps show show similar inter-cluster EM enhancements for NCA#A and NCA#B. This shows a similar inter-cluster coupling irrespective of the cluster size. The simulated EM field maps corroborate with the similar absorbance peak position for both the clusters on glass substrate.

4.3.3. Plasmonic Assays

The sensitivity of NCA@gold towards molecular detection by surface-enhanced Raman spectroscopies was tested under 633nm excitation using two different molecules. One of the molecules is 1-naphthalenethiol, which was chosen on basis of its ultra-small size < 1 nm and the ease with which a conformal SAM layer can be obtained on gold

surface. The ultra-small dimensions of NT would allow it access inter-particle and inter-cluster EM hot-spots in the NCA. The second molecule tested is a protein, namely streptavidin labelled with Cy5 (SA-Cy5), interacting with biotinylated NCA surface. Biotin-Streptavidin interactions have been used as a model interaction due to its high affinity. NCA is easily biotinylated using self-assembled monolayers of biotin-PEG-thiols (BPT) to render them specific to binding with SA-Cy5. The dimensions of BPT (~2.2 nm) and SA-Cy5 (5.8 nm) would make the render the pair too large to be accommodated within inter-particle hot-spots, but easily enough accommodated in the inter-cluster gaps. Further, the choice of Cy5 as label can help enhance signal intensities due to resonance Raman effect due to alignment of the excitation wavelength with molecular absorbance of Cy5.

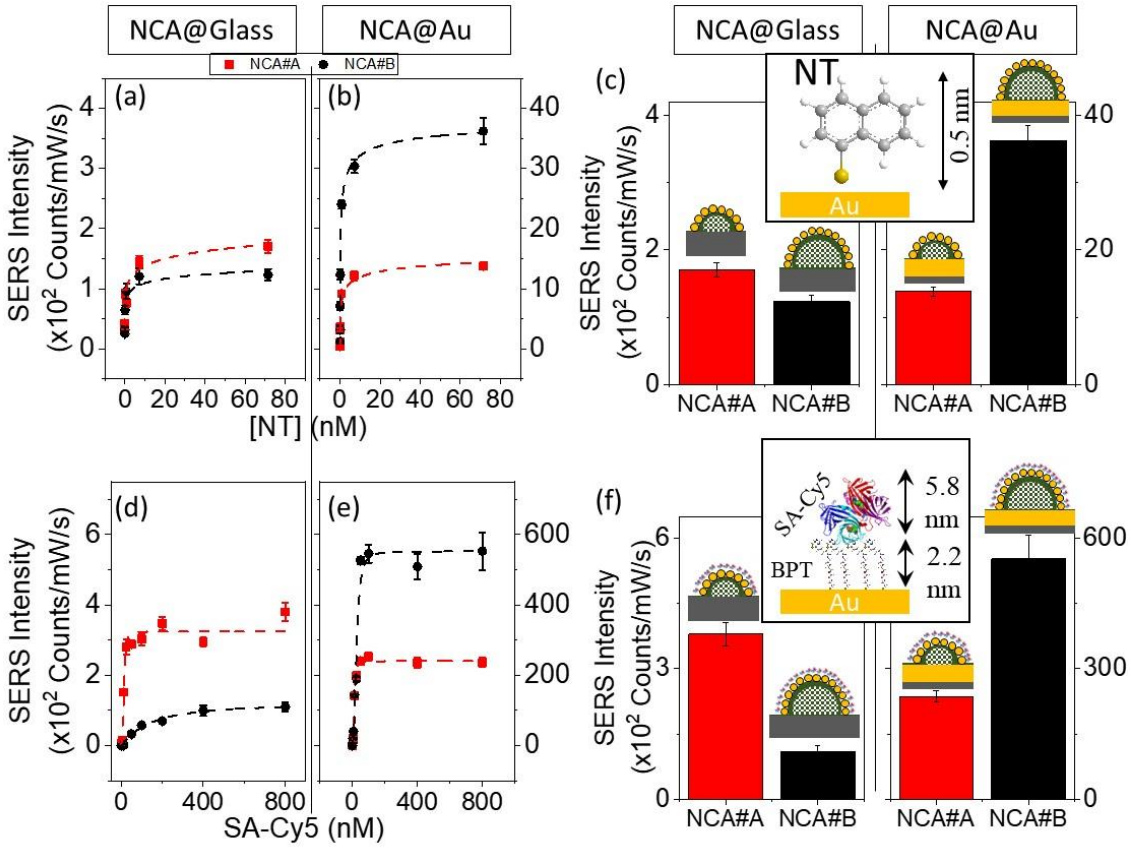

Figure 4.6. Assays of (a-c) NT on NCA and (d-f) SA-Cy5 on biotinylated NCA, compared for NCA#A and NCA#B on gold and glass substrates respectively. The illustration of molecular structure and dimensions for NT and SA-Cy5 are shown as inset.

The sensitivity of the NCA#A and NCA#B towards detection of NT was tested by following the intensity of characteristic vibrational Raman bands of NT at 1372 cm^{-1} as

function of their concentration between 0.07 nM - 71.5 μM **(Figure 4.6)**. The assays of SA-Cy5 were performed by biotinylated NCA, by following the intensity of characteristic Raman band of Cy5 at 583 cm^{-1} between 0.1 – 800 nM.[399] The assays were performed under identical conditions for both NCA@gold and NCA@glass samples. The NCA@gold show greater signal intensities as compared to NCA@glass counterparts by at least an order of magnitude in NT assays and at least 2 orders of magnitude in case of SA-Cy5 assays. The comparison of the NCA#A versus NCA#B also shows significant difference between the NCA@gold and NCA@glass samples. In case of NCA@gold, the NCA#B show higher sensitivity compared to NCA#A for both NT and SA-Cy5. However, the NCA@glass samples exhibited an inverse trend, with NCA#A exhibiting distinctly higher sensitivity for SA-Cy5, with reduced difference in sensitivity of NCA#A versus NCA#B for NT.

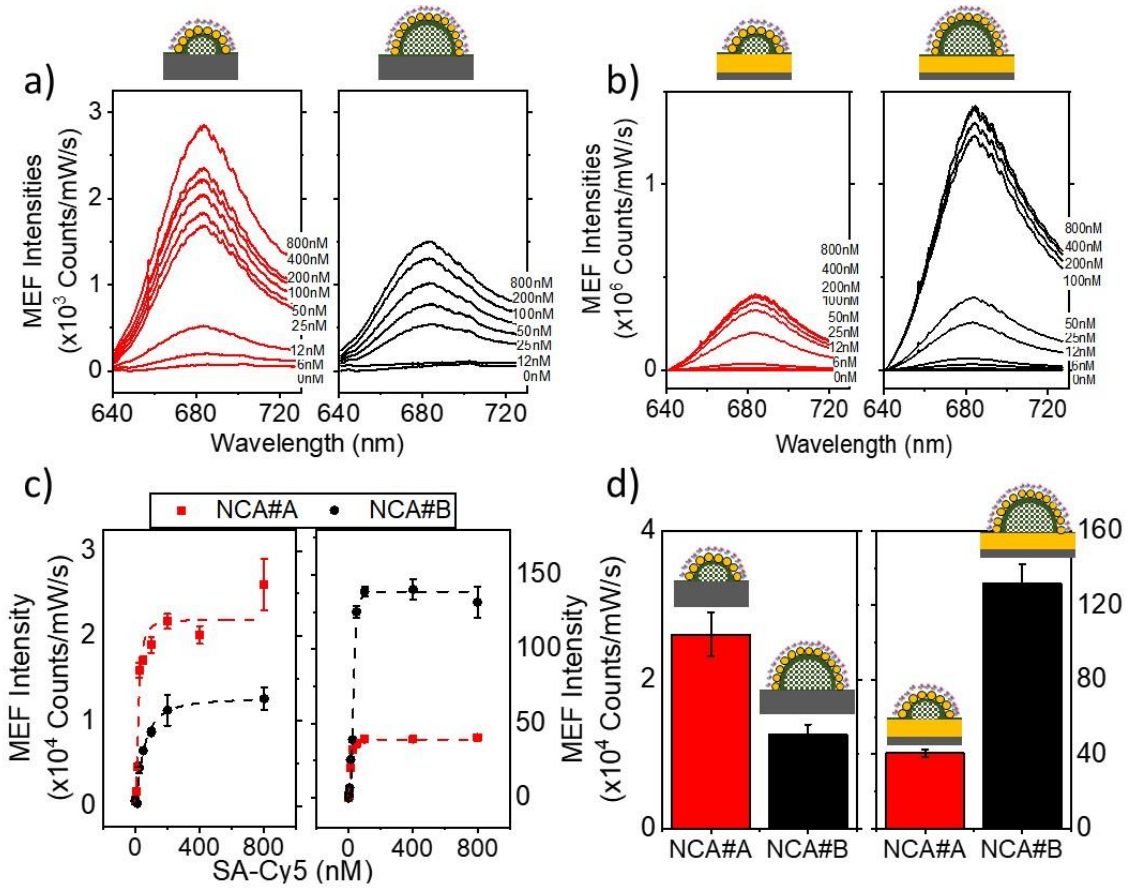

Figure 4.7. (a,b) MEF spectral evolution with concentration of SA-Cy5 on biotinylated NCAs for (c) plot of the peak intensity and (d) comparison of saturated NCA#A and NCA#B on gold and glass substrates.(d) bar plots comparing the saturated signal intensities for NCAs on gold and glass.

The binding of SA-Cy5 to biotinylated NCA can be monitored by the fluorescence signal from Cy5. The fluorescence assays show strong enhancement of fluorescence signals for the NCA@gold, with an enhancement 2 orders of magnitude greater than on NCA@glass controls **(Figure 4.7)**. Metal enhanced fluorescence (MEF) is expected to arise for fluorophores at an optimal distance from nanostructured metal surfaces. The presence of the biological interaction can serve as such spacer to positioning the fluorophore away from the surface and avoid fluorescence quenching due to direct fluorophore-metal contact. As observed with SERS, the MEF enhancements were found to be higher for the larger clusters, in case of NCA@gold samples, and smaller clusters for the NCA@glass samples.

The trends in sensitivity seen in the SERS and MEF assays for the NCA@gold as compared to NCA@glass are well aligned to expectations set by the EM field profiles obtained from numerical simulations. Overall, NCA@gold has clear increase in signal intensity enhancement compared to NCA@glass. The presence of gold film is found to result in greater EM enhancements on NCA#B as compared to NCA#A. In case of NCA@glass samples, the inter-cluster EM field enhancements were found to be similar for both NCA#A and NCA#B. However, NCA#A has a clear advantage due to higher density of inter-cluster hot-spots, which is over 3 times greater than that of NCA#B. Given that the SA-Cy5 could effectively leverage only the inter-cluster hot-spots, the greater number density of inter cluster hot-spots in NCA#A renders it more sensitive in protein detection (as discussed in previous chapter). However, for NT molecule that can leverage both inter-particle and inter-cluster hot-spots, the difference in SERS signal intensity between the clusters is considerably reduced. Thus, while the EM enhancements on NCA#B determines its higher sensitivity on gold substrates, the higher density of inter-cluster hot-spots determines higher sensitivity of NCA#A on glass.

Table 4.1. Comparison of LOD in detection of NT and SA-Cy5 on NCAs on glass and gold

	Substrate	**NCA@glass**		**NCA@gold**	
Nanospectroscopy	**Analyte**	**NCA#A**	**NCA#B**	**NCA#A**	**NCA#B**
SERS	NT	6.8	48.2	0.6	0.6
	SA-Cy5	2	9.6	0.4	0.4
MEF	SA-Cy5	6.2	12.9	0.3	0.4

The limit of detection (LOD), or the lowest concentrations at which the molecules could be detected, was found to be at least an order of magnitude lower in case of NCA@Au as compared to the best performing arrays in case of NCA@glass substrates **(Table 4.1)**. The NCA@gold substrates delivered a LOD of 400 pM in case of SA-Cy5 and 600 pM in case of NT for SERS based detection. The LOD for MEF assays were similar to those of SERS assays.

4.4. Conclusions

Periodic nanoparticle cluster arrays were fabricated on gold substrates were investigated for the differential advantages over glass substrates, for the resulting sensitivity towards detection of molecular analytes by surface enhanced Raman and Fluorescence spectroscopies. The presence of gold film under the NCAs was found to have a profound impact on the optical response and resulting spectroscopic enhancement during molecular sensing. Numerical simulations predict significant enhancement in electromagnetic field in the NCA@Au samples as compared to NCAs @ glass counterparts. This is well aligned to the observed higher sensitivity in case of NCA@Au samples. In addition, the larger clusters, namely NCA#B were found to exhibit greater EM enhancements in the inter-cluster region, over the NCA#A, which also explains the observation of greater signal enhancements observed for the larger clusters in SERS and MEF assay. The NCAs supported on glass substrates were found to have similar enhancements in both smaller and larger clusters. The observations based on the sensitivity of the NCA#A and NCA#B towards molecular analytes smaller and larger than the inter-particle hot-spots show how the larger protein analyte stands to benefit from the inter-cluster region. The NCA that provided the best advantage in terms of leveraging the inter-cluster enhancements by the protein was found to be greater number of inter-cluster junctions in case of NCA#A on glass, and greater electromagnetic enhancements in case of NCA#B on gold. The results strongly point to the significance of rational engineering of the geometry of plasmonic nanoarrays to best leverage EM hot-spots for larger bioanalytes. The unique geometry of NCA, the ease of production, and the different geometric variables to tune their optical behaviour provide unique opportunity for rationally engineering of EM hot-spots.

.

Chapter 5. In-Situ Quantification Of Surface-Concentration of Analyte In Plasmonic Bioassays

This chapter is based on the published paper in [Journal Name] "Combining Quartz Crystal Microbalance and Metal-Enhanced Fluorescence to Quantify Analyte Surface Concentration in Plasmon-Enhanced Spectroscopic Bioassays", R. Rastogi, M. Beggiato, C. Dupont-Gillain, P. Michel-Adam, S. Krishnamoorthy. [DOI].

Nanoplasmonic sensors based on surface-enhanced Raman or Fluorescence spectroscopies carry profound promise in the highly sensitive detection of molecular analytes within miniaturized measurement footprints. Despite decades of progress in the fabrication and investigation of plasmonic sensors, it remains a challenge to determine the surface concentration of molecules that contribute to the spectroscopic signal. This limits the ability to rationalize the observed plasmonic signal intensities by assessing the relative contributions due to analyte surface concentrations and electromagnetic enhancements presented by the surface. Lack of this information makes it difficult to rationally optimize plasmonic bioassays, through the design of plasmonic sensors that present highly enhancing electromagnetic hot-spots, while also favor analyte localization at these hot-spots. In this direction, we demonstrate a combination of metal enhanced fluorescence (MEF) detection of Streptavidin-dye conjugate on ordered gold nanoparticle cluster arrays fabricated on a Quartz crystal microbalance (QCM) sensor surface, enabling precise determination of the analyte surface densities responsible for given fluorescence intensity. The knowledge of analyte surface densities provides important insights into molecular distributions with respect to electromagnetic hot-spots. The combination is effectively leveraged to demonstrate the sensitivity of the in-situ MEF assays down to ~2 zeptomoles of protein within measurement footprints that are 8 orders of magnitude smaller than that of the QCM.

5.1. Introduction

Plasmonic sensors based on surface-enhanced spectroscopies (SES) relying on vibrational Raman or Fluorescence have proven capable of highly sensitive and rapid detection of molecular analytes within miniaturized footprints. The advantages can be leveraged in a range of sectors including food,[418,419] environment,[420,421] health,[422,423] and space.[424] In healthcare, SES sensors are especially valuable as their ultra-high sensitivity can be applied to early-stage detection of infectious or chronic diseases, or detect disease risk, that demand detection of molecular biomarkers down to few molecules. Signal enhancement in SES sensors results from a non-linear enhancement of the electromagnetic fields, which in turn are concentrated in EM hot-spots that are nanoscopic regions such as curvatures or junctions present in plasmonic nanoarrays. Analytes that sit at the EM-hot-spots make a disproportionately high contribution to the signal intensities, and enabling detection limits down to a few molecules.[169] Thus, the SES sensors present often a large heterogeneity in the signal contributions from molecule to molecule, depending on its location in relation to the EM hot-spots. Currently, SES assays relate Raman or Fluorescence signal intensities as a function of solution concentrations, while remaining blind to information of surface concentrations. The lack of information on surface concentrations makes it particularly difficult to separate the relative impact of the molecular surface concentrations and EM enhancements towards the sensor signals. This limits capability to rationally engineer the sensitivity of plasmonic bioassays, taking into account not only the EM enhancements, but also the molecular characteristics of analyte and their binding behavior. The latter determines the density and spatial distributions of analyte on the nanoplasmonic interface, which often presents heterogeneity in topography and surface chemistry down to the length scales of the analyte. In this direction, we demonstrate a combination of SES based on metal-enhanced fluorescence (MEF) with real-time monitoring via Quartz crystal microbalance (QCM) as means to enable correlation between MEF signals and the analyte surface concentrations. The MEF derives its sensitivity from plasmonic enhancement to the fluorescence signals from the fluorophores that are separated at an optimal distance from the plasmonic interface.[88,425–427] In combination with QCM, MEF assays would have information to rationally design the sensor interface to maximize

its leverage over plasmonic enhancements and consequently drive greater sensitivity **(Figure 5.1)**.

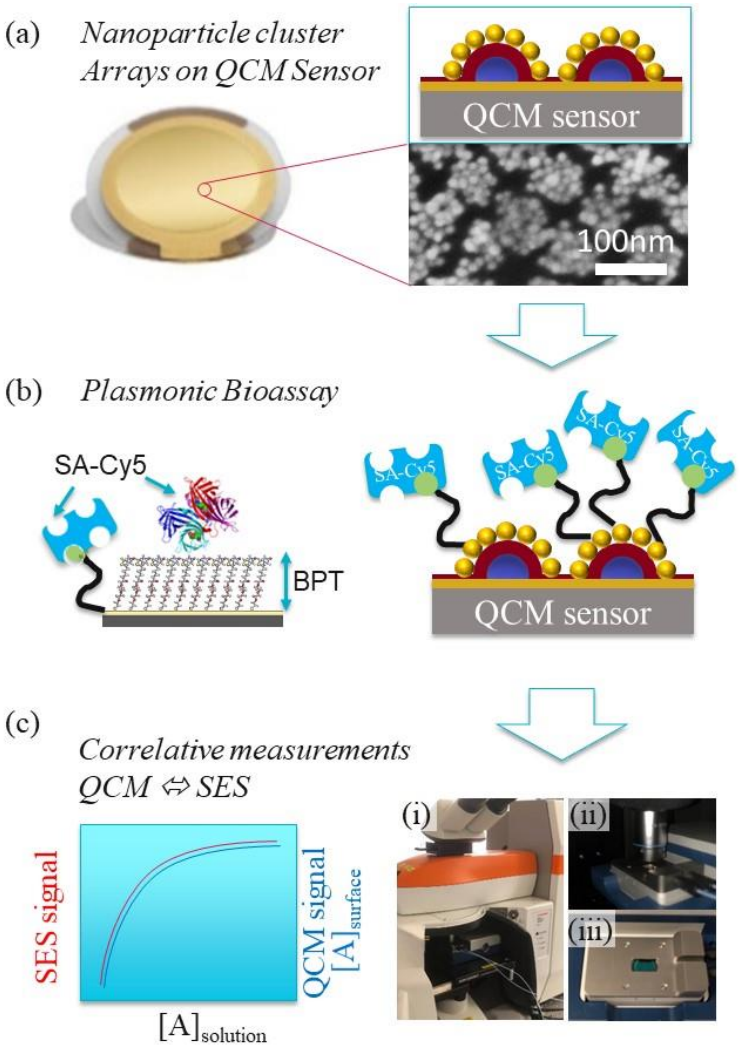

Figure 5.1. (a) Plasmonic arrays composed of gold nanoparticle cluster arrays fabricated on the QCM sensor. The picture of 5MHz QCM sensor chip and the SEM top-view measurements are shown along with an illustration of the cross-section; (b) Configuration of bio interaction configuration used for plasmonic bioassays based on biotin PEG thiol (BPT) functionalized nanoparticle cluster arrays interacting with SA-Cy5; (c) (left) illustration of correlative QCM-SES sensing, (right) (i) picture of the set up with QCM sensor placed under the objective of a confocal microscope; (ii, iii) close up of QCM microfluidic module with optical window enabling optical access during QCM measurements.

The information of surface concentrations of the analyte can be obtained by surface-sensitive chemical analysis tools such as X-ray photoelectron spectroscopy (XPS) and mass

spectrometry (MS). However, they do not allow correlative measurements in real-time and require extrapolating information a large number of separate measurements. The samples further require drying before being probed, which makes it difficult to investigate the outcome of complex multi-step bioassays. Correlative measurements that combine two label-free sensing approaches, most commonly, an optical with acoustic transduction has been shown in the literature,[428] with examples that include QCM-surface plasmon resonance (SPR),[429,430] QCM- localized surface plasmon resonance (LSPR),[431–434] and QCM-Electrochemical impedance (EIS),[435] QCM-Ellipsometry,[436] SPR-Surface acoustic wave (SAW) devices.[437–440] These combinations allow multimodal real-time information of the binding of biomolecules, yet, essentially combine information from two label-free techniques, thus do not carry analyte-specific information. A combination with SES would provide differential capabilities including spectroscopic information specific to the analyte or its reporter, with sensitivity down to sub-nanomolar detection limits, within miniaturized microscopic footprints. QCM is particularly attractive in the direction, as the QCM transduction remains complementary to the spectroscopic transduction by SES. Further, QCM as a tool is quite versatile by the virtue of flexibility it offers in terms of sensor dimensions, surface functionality (bare gold, or with different dielectric layers) and potential for portability and lowering costs.[441,442] In combination with SES, QCM would gain from an orthogonal validation of its label-free response through the spectral signature of the analyte. Spectral multiplexing by SES can further enable parallel detection of multiple reporters and pave way to constructing hybrid QCM-SES assays of greater complexity. However, fabricating a plasmonic sensor based on SES directly on a QCM sensor is not straightforward, as it requires uniform high-quality fabrication on a large area (several mm^2) of a rather fragile sensor chip. The process should further take into account the measures to achieve high sensitivity in SES, which often requires pushing spatial resolutions of EM hot-spots down to sub-10 nm lengthscales, and maximizing the density of such hot-spots. In this direction, we show highly resolved plasmonic nanoparticle cluster arrays realized on QCM sensor chips enabling hybrid QCM-SES assays that correlate highly sensitive metal–enhanced fluorescence with a mass density of proteins derived from QCM.

5.2. Experimental Methods

Materials: Amphiphilic block copolymers (polystyrene-*block*-2-vinyl pyridine, M_w = 443kDa) used to create gold nanoparticle cluster arrays were obtained from Polymer Source Inc (Montreal, Canada). Gold-coated quartz crystals (5MHz, AT-cut) were obtained from Quartzpro (Järfälla, Sweden). Biotin-PEG-thiol (BPT, M_w = 400Da) was purchased from Nanocs Inc. (New York, US). Phosphate Buffer Saline (PBS), and Bovine Serum Albumin (BSA) solution 10x was purchased from R&D System (Abingdon, UK). Polystyrene (PS, M_w = 280kDa) was purchased from Sigma Aldrich (Overijse, Belgium). The Streptavidin-Cy5 conjugate was purchased from Rockland (Limerick, PA). Sodium citrate dihydrate (≥99%), Hydrogen tetrachloroaurate(III) trihydrate ($HAuCl_4.3H_2O$) (≥99.9%), the spectroscopic grade of isopropanol, ethanol, and m-xylene were obtained from Sigma Aldrich (Overijse, Belgium). Water was filtered before any usage through a purification system (Milli-Q®, Merck) and used within the same day.

5.2.1. Fabrication of QCM Sensor Chips

Nanoparticle cluster arrays (NCA) of gold were prepared using the procedure we had reported earlier on silicon [443] and glass surfaces [444]. Briefly, the gold surface of the QCM crystal was first cleaned with organic solvents (ethanol and isopropanol) and air-dried. The sensors were exposed to Oxygen plasma in the Reactive Ion Etching Chamber (Plasmatherm 790 RIE) for 3 minutes and spin-coated with a 2%w/w solution of PS-b-P2VP (443kDa) in m-Xylene. The substrate as obtained was then again briefly treated with Oxygen plasma for 30 seconds and immersed in a suspension of citrate stabilized gold NP having an average diameter of 10.3nm at pH of 6.8 (prepared according to Turkevich's method [388]) for 2 hours for the nanoparticle to form nanoparticle cluster arrays (diameter ~102±10nm, density ~100/μm^2) due electrostatic attraction from positively charged polymeric templates (**Figure 5.2**). Polystyrene thin films used for the control experiments were spin-coated from 1% solution of the polymer in m-Xylene. The film was subsequently treated with O_2 plasma RIE for 30 seconds, resulting in a final thickness of 4 nm, as confirmed by AFM.

5.2.2. QCM Measurement

The Quartz Crystal Microbalance with Dissipation monitoring (QCM-D) from Biolin Scientific (QSense Explorer E1 system, Gothenburg, Sweden) was used for the QCM assays. QCM mass per unit area data was obtained from the conversion of the fifth overtone frequency following Sauerbrey's equation: $\Delta m = -C \, {\Delta f}/{n}$ where C = 17.7 ng/(cm^2 Hz) for the employed sensors and n is the odd overtone. The linear frequency-mass function was employed for mass calculation, since the additional layer over the specified quartz sensor is thin, rigid and firmly attached to the sensor surface, fulfilling the basic requirement to follow Sauerbrey's equation [390]. Also, the validity of the Sauerbrey's model was assured by low dissipation and invariance of the response as a function of the overtones.

5.2.3. Metal-Enhanced Fluorescence Measurement

A QCM microfluidic module with an optical window was used to acquire fluorescence spectra.[445] The module was injected with the reagents with flow speed controlled via a peristaltic pump (Ismatec, Germany). Fluorescence measurements were acquired by placing the QCM module on the microscope stage of a confocal micro-Raman system using the Invia Raman system. The fluorescence spectra were obtained at 633nm excitation at 1.9mW (P_{max}) for varying durations to prevent saturation of the CCD (1.5s - 25s) averaging 5 times for each scan using long working distance objective (50X, NA 0.55).

5.2.4. Molecular Bioassays

The NCA coated QCM sensor was functionalized with biotin-PEG-thiol (1mM in milli-Q) for 2 h, followed by thorough rinsing with Milli-Q water to remove all the loosely bound molecules, blow-dried and used immediately afterward. In the next step, the sensor chip was exposed to BSA as a blocking agent at high concentration (1% in PBS) for 30 minutes to block any remaining un-functionalized surface, to prevent non-specific adsorption of SA-Cy5 molecule. The biotin coated sensor chip is exposed to PBS buffer followed by sequential injections of 600µl of SA-Cy5 at progressively increasing solution concentration in the range of 1.5nM - 400nM in PBS. At each concentration, the QCM response was allowed to reach equilibrium, followed by injection of 300µl of buffer to get rid of loosely bound SA-Cy5 molecules. A stable frequency was reached before the

fluorescence measurements were acquired. The flow rate is maintained constant throughout the experiments at 10 µL/min.

5.3. Results and Discussions

5.3.1. Fabrication of Plasmonic QCM Sensor

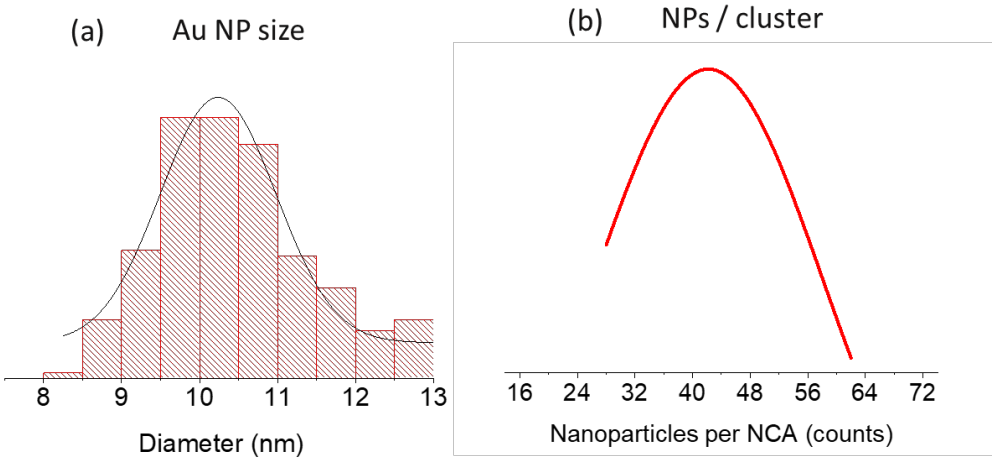

Figure 5.2. The distribution in the (a) size of gold NP (~10.3 nm) used and (b) number of NP (~42) per cluster determined from the peak of Gaussian fit to the histogram obtained by hand counting NP from SEM images of ~40 NCAs.

Table 5.1. Geometric attributes of the templates used.

Polymeric Template Geometry	Dimension
Template Period (nm)	110 ±19
Template Radius (nm)	34.5 ±3.2
Template Height (nm)	38.3 ±1.8
Template Density (/mm2)	100
NCA Diameter (nm)	102 ±8.5

Nanoparticle cluster arrays (NCA) were fabricated directly on 5 MHz QCM sensor with its bare gold surface using approaches we had demonstrated earlier.[443,444,446] Colloidal particles with pyridyl containing core and polystyrene exterior were prepared using amphiphilic copolymer based on polystyrene-block-polyvinylpyridine, with a molecular

weight of 443 kDa from m-Xylene. The technique has been extensively investigated in prior literature to prepare well-defined geometries suitable as a template for creating nanopatterns.[243,244,446,447] The pyridyl groups acquire a positive charge in neutral aqueous medium enabling electrostatic self-assembly of negatively charged citrate stabilized gold NP. The resulting gold nanoparticle clusters exhibit well-defined geometries, in terms of the number of NP per cluster, and their periodicity **(Figure 5.2 and Table 5.1)**. The tools of molecular self-assembly allow control over the periodicity in steps of few nanometers enabling the possibility to push the inter-cluster separations down to the sub-10nm regime. The inter-particle gaps (<5 nm) within the clusters and the inter-cluster gaps are capable of supporting and enhancing electromagnetic fields (EM) through the coupling of localized surface plasmon resonances from the adjacent metal nanostructures. The EM field enhancements can be advantageous within detection schemes that could leverage the vibration Raman or fluorescence enhancement of the analyte or its reporter down to trace levels. The clusters were demonstrated earlier for highly sensitive detection of small organic molecules, down to sub-nanomolar detection limits.[444] Their use was not so far explored for assays based on metal enhanced fluorescence (MEF). MEF assays are particularly at an advantage while exploring assays directly in solution, without having to dry the films before analysis. Performing plasmonic bioassays in solution are especially helpful while combining with real-time analysis using QCM, as the process remains seamlessly correlated, without interruption in the assay. This assures retaining the biological activity of the receptors on the surface, and that there is no adverse evolution of conditions on the surface, e.g. denatured receptors, increase in non-specific binding pockets, which can contribute to lowering the sensing performance.

5.3.2. Acquisition Of Correlative QCM-MEF Measurements

In this direction, the NCA coated QCM sensor was used to perform hybrid QCM-MEF bioassays based on streptavidin-biotin interactions. Streptavidin is a tetrameric protein, known to exhibit a strong interaction with biotin,[448] and is quite promising as a model interaction to mimic protein-ligand interactions on the surface.[394] The system has been studied in-depth in literature and is well-suited to demonstrate the value of combining the QCM with SES. The QCM measurements were performed using a flow cell that allowed optical interrogation through a transparent optical Sapphire window (7.1mm x 13.9 mm).

The NCA coated QCM sensors were coated with self-assembled monolayers of biotin-PEG-thiol to define the receptor layers for the subsequent interaction with Streptavidin. The surface was flown with BSA at high concentrations to block any non-specific binding sites in the BPT SAM layer. BSA has a high affinity for the gold surface and is small enough to occupy any non-specific binding pockets.[449] In the subsequent step, the QCM sensor with the BPT layer is exposed to different concentrations of streptavidin. The Streptavidin was labeled with Cy5 dye, to enable fluorimetric detection by MEF. The QCM sensor was sequentially injected with Streptavidin-Cy5 conjugate (SA-Cy5) of progressively increasing concentration in the range of 1.5 - 400nM. At each concentration, the evolution in the surface density of SA-Cy5 was monitored in real-time using QCM. **(Figure 5.3a**) Upon saturation of the frequency response, the sensor was flown with PBS to remove the SA-Cy5 solution and any loosely bound SA-Cy5 on the surface prior to performing fluorescence measurements. Following this, the sequence was repeated with the next higher concentration of SA-Cy5. The Fluorescence spectra were acquired without interruption to the QCM interrogation, with the buffer in place at the time points corresponding to the saturated response of the isotherms at each solution concentration. **(Figure 5.3a)** The Fluorescence spectra show progressive increase in intensities with increase in SA-Cy5 concentrations, as expected. **(Figure 5.3b)** The match of excitation wavelength (633 nm), the absorbance peak of Cy5 (650 nm), as well as the plasmonic resonance of the nanoparticle clusters[317] provides favorable conditions to enhance MEF intensities.[450,451]

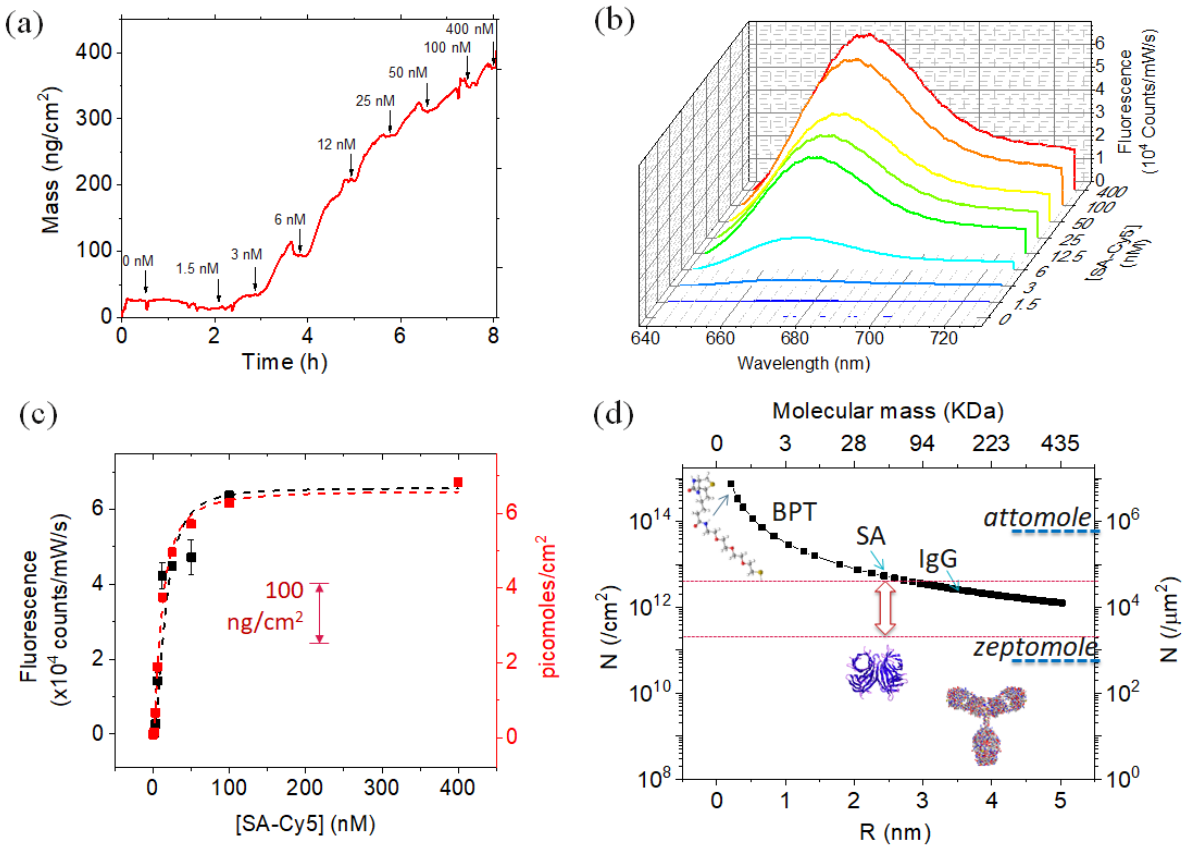

Figure 5.3. (a) Evolution in mass density as observed in QCM as a function of sequential injection of increasing concentrations of SA-Cy5 on biotinylated nanoparticle cluster arrays. The solution concentration values are indicated at the saturated response of respective isotherms; (b) Fluorescence spectral evolution as a function of SA-Cy5 concentration; (c) plot correlating Fluorescence (black) and QCM (red) assays, with fit to Langmuir-Hill function shown in dotted lines (d) plot of the estimated saturated surface density of molecules as a function of their molecular dimensions, expressed (left-Y) per cm2 and (right-Y) per μm2. The top-X axis shows the molecular mass of protein with an equivalent radius as in bottom-X. The vertical block arrow indicates the equivalent surface densities of SA-Cy5 as measured in the QCM assay in (c). Cartoon representations of BPT, SA-Cy5, and an antibody (immunoglobulin, IgG) molecule is shown for reference.

5.3.3. Quantifying Analyte Surface Concentrations Contributing to MEF

The Fluorescence and the QCM assays on the NCA when plotted together, enable quantifying surface densities of SA-Cy5 that contribute to a given MEF intensity **(Figure**

5.3b). The surface density enables useful insights into the analyte surface distribution on the plasmonic sensors. To rationalize the observed surface density, on the NCA coated QCM sensor surface was modeled to estimate the surface sites available for adsorption. The BPT is expected to form a self-assembled monolayer on the gold surface guided by thiol-gold interactions, subsequently directing the attachment of SA-Cy5 through biospecific interactions. The portion of the nanoparticle surface available for adsorption of SA-Cy5 (A) can be modelled as a spheroidal cap, taking into account the radius of the nanoparticle together with the thickness of the BPT layer and height (h) of the cap, as calculated using Eq. 5.1. **(Figure 5.5a)** The h can be obtained from the nanoparticle radius (R) and inter-particle separations (s) from Eq. 5.2. The radius of the spheroid (R') also takes into account the radius of gyration of SA-Cy5, to account for the limited ability of the molecule to access the areas that are closest to point of contact between the particles.

$$A = 2\pi(R + L_{BPT})h \qquad \text{Eq. 5.1}$$

$$h = (R + L_{BPT}) - a = (R + L_{BPT}) - \sqrt{(R + L_{BPT})^2 - R'^2} \qquad \text{Eq. 5.2}$$

where $R' = R + \frac{s}{2} - R_g$

$$\Delta M_{NCA} = \left(\frac{A}{A_{SA-Cy5}}\right) \times N \times M_{SA-Cy5} \qquad \text{Eq. 5.3}$$

The mass density of SA-Cy5 on NCA (ΔM_{NCA}) can be estimated from Eq. 5.3, taking into account the area per SA-Cy5 molecule (A_{SA-Cy5}), number of molecules per nanoparticle, the number density of NP (N) and the mass per molecule of SA-Cy5 (M_{SA-Cy5}). Given the high density of NP per cluster, the Au NP are expected to be in close proximity and separated by distances that are a fraction of the dimensions of SA-Cy5. Given the radius of gyration of SA of ~2.5 nm,[452] and mass density of a typical SA monolayer on the biotinylated surface to be 450-550 ng/cm^2,[453,454] the maximum possible adsorption onto the NCAs can be estimated to be ~71-87 ng/cm^2. This however is less than the observed mass density at the saturation of 414 ng/cm^2, strongly pointing to adsorption of the SA-Cy5 also occurring between the NCA features **(Figure 5.5b).**

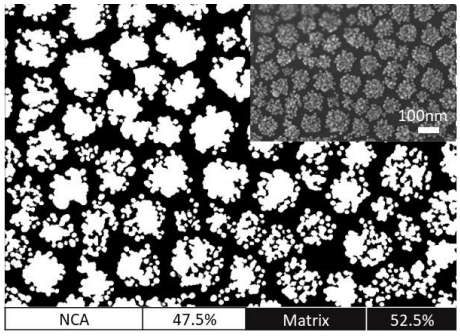

Figure 5.4. Pixel percent analysis of an SEM image of the NCA fabricated on QCM-D sensor chip.

The area around the NCA features (or the matrix) corresponds to ~ 52.5% of the surface, as obtained from the analysis of the electron microscopy images of the NCA coated QCM sensor **(Figure 5.4)**. The matrix has a thin layer of polystyrene formed by the fusion of the coronal blocks of the reverse micelles when they are deposited on the surface. The BPT or SA-Cy5 are not expected to adsorb to the matrix under the conditions of the experiment. To clarify the possibility, a control experiment was set up to repeat the assay on the QCM sensor coated with a thin film of polystyrene. The results show the BPT to adsorb well onto the polystyrene (PS) surface, with densities of ~400 ng/cm^2, followed by a negligible quantity of BSA and 690 ng/cm^2 of SA-Cy5. Based on the exposed PS area, this would correspond to a density of 362 ng/cm^2 between the NCA. The strong affinity of biotin-streptavidin interactions on PS supports well the contribution from the matrix towards the observed mass densities of SA-Cy5. This brings the total mass density from the model to be 433 - 449 ng/cm^2, which agrees closely with the observed value of 414 ng/cm^2. The geometric model however can deviate from the experimental scenario due to standard deviations in nanoparticle size, separations, NP/NCA, and the density of NCA on the QCM sensor, which can certainly vary the relative distributions of molecular densities on and between the NCAs. Nevertheless, these standard deviations were experimentally found to be < 15% of the mean values, allowing the construction of a model that closely represents the experimental scenario. While the results support the conclusion of the presence of SA-Cy5 on both the NCA and in the matrix, the relative proportions are still indicative. The consequences of the availability of the SA-Cy5 between the NCAs would allow them to benefit from inter-cluster electromagnetic hot-spots, enabling high sensitivity in MEF assays.

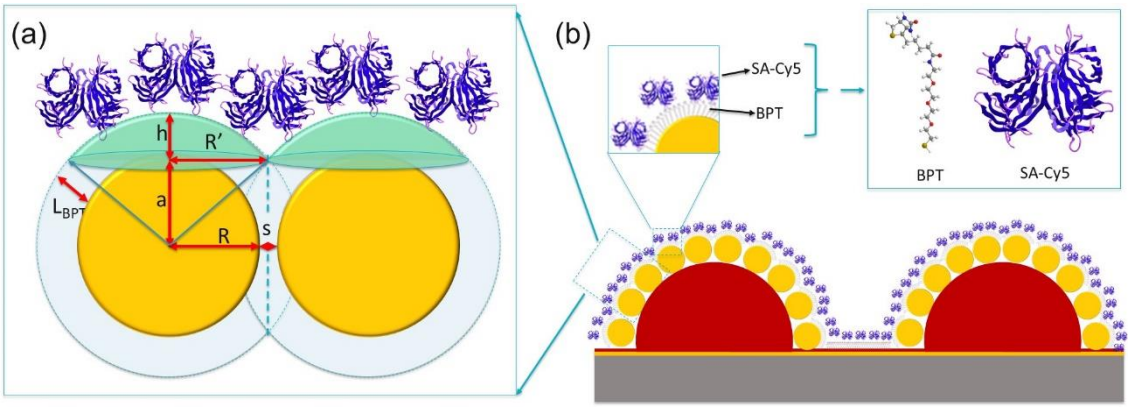

Figure 5.5. Illustration of the (a) geometric model used to estimate the molecular densities on NCAs, and (b) molecular distributions of SA-Cy5 on the NCAs. The polystyrene block of the template is shown in red. The molecular structure of BPTand the cartoon representation of the SA-Cy5 is shown in the inset.

5.3.4. Relative Sensitivities Of QCM Versus MEF

The MEF assays were performed using streptavidin concentrations down to 1.5 nM. The lowest detection limits (LOD) for MEF assays can be estimated to be 800 pM, taking into account the limit of blank and the standard deviation of the intensities of the blank, and at the lowest concentration.[389] The equivalent mass density corresponding to the solution concentration of 800 pM can be extrapolated from the Langmuir-Hill fit the QCM response to be ~0.13 pmol/cm^2, which corresponds to 7.9 ng/cm^2 or ~780 molecules/µm^2. Considering the footprint of 1.55 µm^2 (laser spot size under 50x objective with NA of 0.55 for 633 nm excitation) this would correspond to a signal from approximately 1209 molecules. The mass sensitivity of the QCM sensor with 5 MHz crystal under liquid is ~1.8 ng/cm^2, which however is not always met during practical measurements in liquid. [455] Under conditions of measurement, LOD of ~4.6 ng/cm^2 was obtained taking into account a value corresponding to 3 times the standard deviation of the response under buffer. This mass density corresponds to 6.4 x 10^{10} molecules of SA-Cy5 within the QCM footprint of 1.4 cm^2. Although the lowest detection limits from MEF is close to that of the QCM, the MEF signals are acquired from the absolute molecular concentration on the surface that is 8 orders of magnitude lower than that of the QCM. The ability to detect low concentration of molecular analytes is critical to realizing diagnostic platforms of practical utility, e.g. analytical sensitivity as low as few hundrd copies of viral RNA is necessary to detect an

asymptomatic patient infected with SARS-CoV-2 during earliest phase of infection.[456] Typical concentrations of antibodies marking acquired immunity in patients exposed to the viral infection, or biomarkers for early-stage detection of life-threatening diseases lie in the pico-femtomolar regime.[457]

Figure 5.3a shows a plot of the estimated number of molecules per unit area of the surface at their maximum density, as a function of the molecular dimensions (radius of gyration, molecular mass).[452] The number of molecules per square centimeters (left-Y) is typically the order encountered for macroscopic sensors (as in case of the QCM sensor), while micro spectrometry (as in case of SES) would probe molecular concentrations that are 8 orders (a factor arising out of conversion from cm^2 to μm^2) of magnitude lower (right-Y). For most proteins, the upper limit of a monolayer of molecules within the footprint of the SES measurement would be ~10^4 - 10^6 molecules (~16.6 zeptomole – 1.7 attomole) [452] This highlights the advantage for microscopic sensors as compared with their macroscopic counterparts. Thus, MEF, as a microspectroscopic solution would be a particularly promising route to miniaturizing sensor footprints to areas equivalent to the measurement footprints and with associated opportunity to further improve the detection sensitivity. Combination with QCM enables rational understanding of the plasmonic enhancements, and to rationally arrive at measures to maximize EM enhancements.

5.4. Conclusions

Plasmonic nanoparticle cluster arrays with well-defined geometries, and presenting high densities of inter-particle and inter-cluster hot-spots were fabricated directly on the surface of a QCM sensor. Quantitative in-situ measurements of the binding of fluorescently labelled streptavidin to biotinylated plasmonic arrays could be simultaneously performed with MEF and QCM modalities. The combination allowed quantitative measurement of the surface density of proteins that contributed to the MEF intensity. The molecular densities taken together with the available surface sites predicted by geometric modelling proved instrumental in confirming the presence of the proteins on and between the nanoparticle clusters. The mass densities predicted by the geometric model show excellent agreement with experimental values obtained from QCM. The agreement can be attributed to the low standard deviation of the geometric attributes of the NCAs that serves to minimize the

deviation of the model from the experimental scenario. The determination of surface density of molecules contributing to MEF serves to express its sensitivity in terms of the actual number of molecules detected. This makes it particularly interesting to evaluate the relative sensitivities of MEF and QCM using surface concentration of molecules as the common scale of comparison. While both modalities showed comparable limits of detection in terms of the surface densities of proteins, QCM requires a measurement footprint that is 8 orders of magnitude larger as compared to MEF. The measurements show that the MEF assays to be sensitive to protein concentration in the range of 1209 – 4 x 10^4 molecules (in 1.55 μm^2 probed area) while the QCM sensor would detect in the proteins in the range of 6.4 x 10^{10} – 5.7 x 10^{12} molecules (in 1.4 cm^2 probed area). The comparison presents a convincing case for MEF in driving miniaturization and sensitivity goals for future sensors. The approach opens interesting avenues for rational optimization of nanoplasmonic interfaces to drive high sensitivity in plasmon-enhanced spectroscopic biosensors.

Left Blank Intentionally

Chapter 6. Metal Nanopillar Arrays With Inter-Pillar EM hot-spots

This chapter is based on the published paper in [Journal Name] "Investigating Analyte Co-Localization at Electromagnetic Gap Hot-Spots For Highly Sensitive Biomolecular Detection by Plasmon Enhanced Spectroscopies", R. Rastogi, H. Arianfard, S. Juodkazis, D. Moss, P. Michel-Adam, S. Krishnamoorthy [DOI].

Colossal enhancement of electromagnetic (EM) field within ultranarrow gaps at the junctions of plasmonic nanostructures is capable of driving limits of detection by plasmon-enhanced spectroscopies down to few molecules. However, leveraging the EM enhancements requires access to the gaps, which in turn depends on the size of the analyte in relation to gap distances. Herein we leverage a well-calibrated process based on molecular self-assembly to deliver large number of uniform nanogaps with gap distances systematically varied down to sub-10nm regime. The results show compelling trends of the impact of analyte dimensions with respect to the gap distances towards leveraging EM enhancements at the inter-pillar hot-spots in surface-enhanced spectroscopic assays. Comparing the detection of labelled proteins in surface-enhanced Raman and metal-enhanced fluorescence configurations further reveal the relative advantage of the two configurations while encountering the spatial limitations imposed by the gaps. Quantitative assays with limits of detection down to picomolar concentrations is realized for both the small organic molecules and the proteins by rational choices over EM hot-spot geometry and assay configuration. The findings emphasize the need for the rational design of EM hot-spots that take into account the analyte dimensions to drive ultra-high sensitivity in plasmon-enhanced spectroscopies.

6.1. Introduction

Optical sensors that employ plasmonic transducers have gained significant attention in the last decade, especially due to their ability to detect analytes at ultra-low concentrations, in miniaturized volumes, with application to a range of sectors including

medical diagnostics,[458,459] environmental monitoring,[378,460] food safety,[461,462] defense,[463,464] and forensics.[465,466] Plasmon-enhanced spectroscopies sensors such as those relying on electromagnetic enhancement to Raman or Fluorescence intensities of analyte were shown to be particularly promising in driving analytical detection down to single-molecule level.[467–470] However, despite over four decades of work in the direction, their adoption into practical technologies remains limited, especially due to the inability to assure high sensitivity without compromising reliability in performance and scalability in production.[285] Sensitivity in plasmon-enhanced spectroscopy results from a disproportionately high enhancement of electromagnetic (EM) field at the vicinity of optically excited metal nanostructures, e.g. metal nanogaps, sharp metal ends with high curvatures (lightning rod effect).[471–473] Fang et al showed that only 63 molecules per million were required to achieve a sizeable signal (24% of signal contribution) when present within EM hot-spots presenting enhancement factors $>10^9$.[169] Such high EM enhancements are achievable at ultra-narrow gaps or junctions between adjacent metal nanostructures typically for gap distances approaching sub-10nm regime.[151,162,474,475] While such gaps can accommodate analytes smaller than the gap size, they would be incapable of accommodating large molecules, e.g. proteins, or oligonucleotides. The ensuing spatial constraints towards leveraging the highly enhanced EM hot-spots for biosensing negatively impacts the sensitivity of plasmonic bioassays. While there has been intensive research in the past decade on approaches to achieve highly enhancing EM hot-spots, their performance has often been validated using small molecules, typically with sub-nanometric dimensions. While such validation helps to understand the enhancement at the EM hot-spots, they do not address the challenge of the inability to accommodate larger biomolecular analytes.

Different approaches were adopted in literature to achieve analyte co-localization at EM hot-spots. In one of the studies, the irreversible collapse of high-aspect-ratio metal nanopillars was used to mechanically trap molecular analytes at the inter-pillar EM hot-spots.[371] However, the mechanical flexibility of the pillars also risks adversely impacting their stability, as they cannot be subjected to multiple washing-drying steps, requires storage in scrupulously moisture-free conditions, and cannot be subjected to classical multi-step adsorption sequence typical of most biological assays. Further, the approach is devoid of opportunities for the rational design of the geometry of the EM hot-spots. Another

approach includes the formation of vertical 3D hot-spots defined by the analyte sandwiched between a metal nanoparticle and a plasmonic substrate.[148] The width of the vertical EM hot-spots is defined by the size of the sandwiched analyte, and thus is sensitive only for small molecules but not large biomolecules whose detection relies on receptor-ligand complexes with dimensions spanning several tens of nanometers.[476] In an instance that resembles this strategy, plasmonic sensing of a cancer biomarker was demonstrated by sandwiching an antibody-antigen complex (~30-40 nm) between detection antibody labeled with gold nanostars and gold nanotriangle array.[477] The approach, however, gains largely from a high concentration of highly sensitive dye reporters trapped within the gold nanostars, rather than the EM enhancements between the nanostars and the metal nanoarray. Alternative configurations have been shown using dynamic plasmonic nanostructures that can swell and collapse in response to the presence of an analyte. These configurations have been typically demonstrated for the detection of physiological changes[478–481] such as temperature and pH, or small molecules such as water (moisture), or glucose, but not been exploited for sensing larger molecules.[265,479] These evidences reinforce the challenge of configuring EM hot-spots that take into account the large dimension of biomolecules. The advancement in this direction requires the ability to perform reliable investigations of the sensitivity of plasmonic transducer as a function of the geometry of the EM hot-spot while taking into account the molecular dimensions. This will however require producing well-defined EM hot-spots with geometries precisely controlled down to sub-molecular dimensions to serve as good models to derive robust correlations. Further, the EM hot-spots should be obtained on large enough numbers to allow systematic investigations, and over macroscopic areas that may permit use of alternative characterization tools with a macroscopic footprints (e.g. XPS, Ellipsometry) if so desired. Herein we show a clear impact of the molecular dimension of analytes in relation to that of EM hot-spots in the ability to leverage EM enhancements at inter-pillar hot-spots for SERS and MEF assays. The choice of geometry and assay configuration is shown to deliver analytical sensitivities down to picomolar concentration for analyte smaller and larger than the EM hot-spots.

6.2. Experimental Methods

Materials: Polystyrene-block-poly(2-vinylpyridine) (PS-*b*-PVP) (102000-b-95000 *g mol*$^{-1}$) was purchased from Polymer Source Inc. (Montreal, Canada). Silicon (Si) substrates with thick Silicon Oxide (SiO_2) coatings were purchased from Silicon Valley Microelectronics (Santa Clara, CA). 1-Napthalenethiol (≥99%), *m*-Xylene (≥99%) were purchased from Sigma- Aldrich. Biotin-PEG-Thiol (BPT) (400 *g mol*$^{-1}$) was purchased from Nanocs, New York, USA. Phosphate Buffer Saline (PBS) and Bovine Serum Albumin (BSA) solution (*10x*) was purchased from R&D Systems, Abingdon, UK. Streptavidin Conjugated with Cyanine-5 dye was purchased from Rockland, Limerick, PA. AFM Tips were purchased from Nanoandmore, Germany. Polydimethylsiloxane (PDMS) was purchased from Dow Corning along with the activator to form PDMS blocks.

6.2.1. Nanopillar Arrays

The pillar arrays were prepared using a protocol that was reported earlier. The coating solution was prepared using PS-b-PVP with a molecular weight of 197 kDa in a p-Xylene organic solvent (0.8% w w^{-1}). These organic templates were spin-coated at 6000 rpm over freshly cleaned 100 mm Si wafer consisting of 25 nm SiO_2 film. C_4F_8/CH_4 gas plasma to transfer the template pattern into the underlying SiO_2 layer. Resulting SiO_2 pattern behaves as a highly selective pattern for Si etching using SF_6/C_4F_8 plasma to obtain silicon nanopillars. The center-to-center periodicity of 105.8 nm (coefficient of variation below 10% from chips to chips) of the features was preserved from the polymeric template, confirmed using AFM and SEM images from the template and nanopillar arrays. Edge separations between the gold-coated pillars was determined by subjecting the SEM images of the Au-NPA to image analysis using ImageJ.[482] The silicon nanopillars were sputter-coated while rotating at 10 rpm continuously with a 5 nm ±1 nm adhesive layer of Chromium at 100 W (60 sccm) of Argon (Ar) Gas under 10^{-2} mbar pressure for 14 s (0.36 nm s^{-1}). The desired thickness of Gold was deposited under similar conditions at 0.86 nm s^{-1} rate with a standard deviation of 6%.

6.2.2. Spectroscopic Measurements

For NT Raman probe detection, an average of 10 scans per spot was acquired and an average of 10 different spots on each sample, to calculate the standard deviations. Each scan was taken with a total exposure of 10s with a 633 nm He-Ne LASER at a power of 1.9 mW under 50x/0.5 N.A. objective. For bio-molecular detection using fluorescent-dye Cy5 conjugated to Streptavidin, each measurement was recorded at 5 different places throughout the functionalized surface, with 3 s of total exposure time at varying power (0.0095 to 0.095 mW) to prevent the saturation of the CCD due to Fluorescence background.

6.2.3. Plasmonic Arrays

For NT assays, the Au-NPA were incubated overnight in the ethanolic solution of NT at a varying concentration from nM to µM range and were then rinsed thoroughly with absolute ethanol before drying and recording Raman spectra. Biotin-Streptavidin Interactions: Au-NPA was immersed in the 1 mM solution of Bi-functional PEG molecule (Biotin-PEG-Thiol, 0.4 kDa) for 2 hours. Then, the substrate was left for 30 minutes in BSA (1%) in PBS to block all the rest of the available sites on the gold-coated surface. These substrates are then covered with the freshly made PDMS block punched with "wells" of 5mm diameter. These "wells" were then filled with 30 µl of Streptavidin protein conjugated with Cy5 dye in varying concentrations and left for 2 hours. Later, these "wells" were rinsed properly with PBS and water before removing the PDMS block. PDMS block was prepared using the SYLGARD^{TM} 184 Silicone Elastomer (Dow Corning). The wells allowed selectively functionalizing the regions on the same substrate maintaining low reagent consumption and ease of washing. The LOD was determined from the mean and standard deviation of the blank and the standard deviation of the signal at the lowest concentration.[389]

6.3. Results and Discussions

6.3.1. Nano-engineered Inter-Pillar Gaps

The gold-coated nanopillar arrays exhibiting high density well resolved EM hot-spots were obtained by molecular self-assembly approach, reported earlier.[316,483] Ordered nanopillar arrays (NPA) were prepared by lithographic pattern-transfer of nanoscale

polymer template obtained from soft colloidal particles of polystyrene-block-polyvinylpyridine into underlying silicon surface. The self-assembly approach gives control over template separations down to sub-10 nm length scales with uniformity spanning full wafers, and produced at high throughput.[252,483]

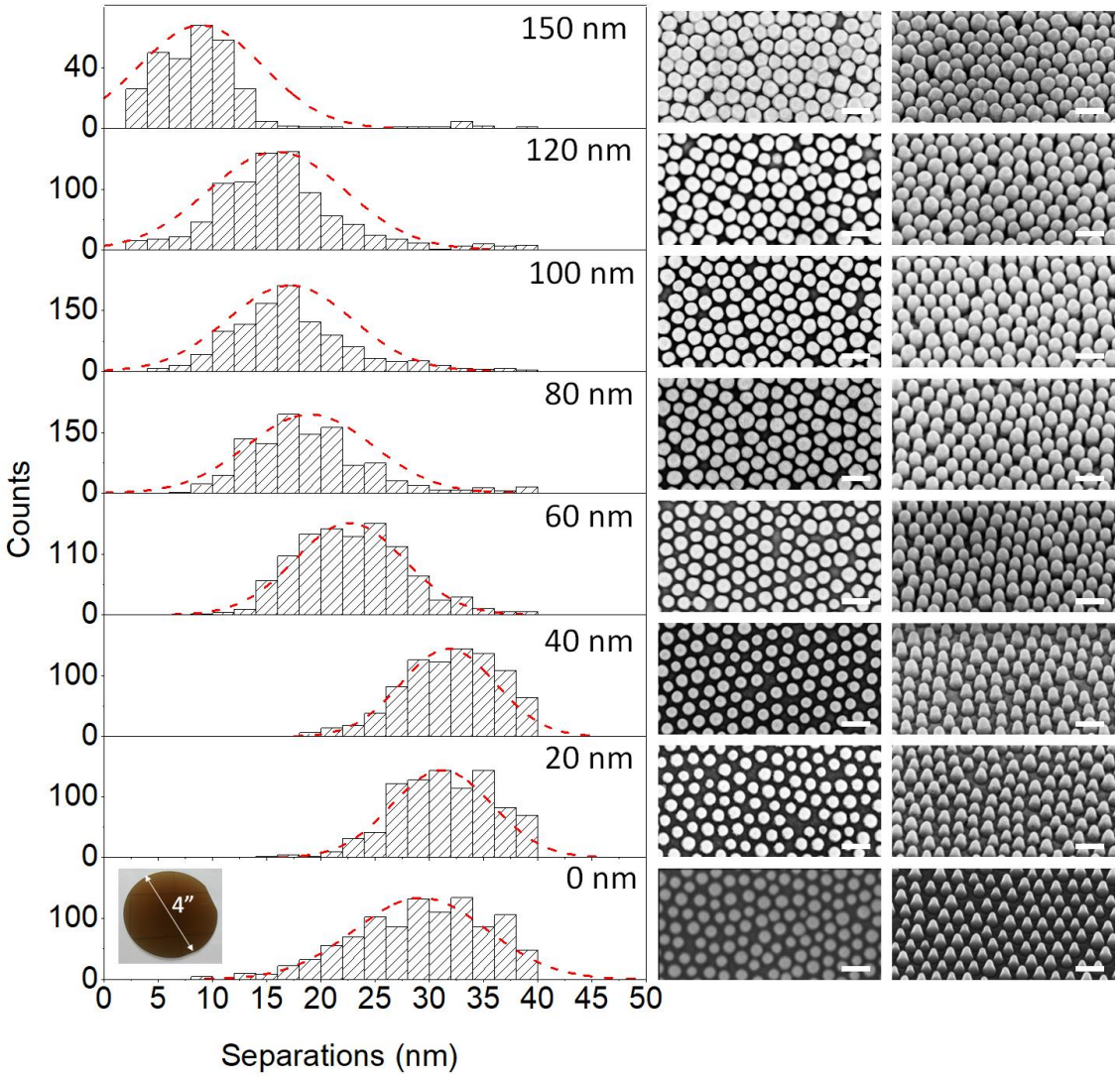

Figure 6.1. Histograms of inter-pillar gap distances as a function of the thickness of sputtered gold films, and the SEM images of the nanopillar arrays acquired in the top and tilt view (30° inclination). The scale bars indicate 200 nm. Picture of 4” uniform nanopillar arrays on 4” Si wafers is shown as an inset.

Nanopillars with a positively tapered profile with a height of 108 nm ± 5 nm, the diameter of 77.5 nm ± 9.8nm, and edge-to-edge separation of 30.6 nm ± 7.3 nm were obtained. 100 mm Silicon wafer with silicon nanopillars was diced into 1x1 cm chips for

further use. The silicon NPA is subsequently sputter-coated with an adhesive layer of chromium followed by gold (Au) with thickness ranging from 20-150 nm to obtain ordered Au nanopillar arrays (Au-NPA). Cross-sectional measurements in SEM show conformal coating of gold on the silicon nanopillars in all cases resulting in systematic increase of the height and diameter, and decreasing inter-pillar separations in the Au-NPA **(Figure 6.1)**. The periodicity of the Au-NPA however remained a constant, and in good agreement with those of the original self-assembled polymeric template. An asymmetric growth of gold is observed, with the preferential increase in feature heights over diameters in steps of ~1.0 nm and ~0.2 nm respectively for every nanometer increase in thickness of sputtered gold. **(Figure 6.2)** Until a thickness of 40 nm of sputtered gold, the diameter does not change, and consequently yielding similar inter-pillar separations. This can be attributed to the positively tapered silicon pillars which evolve into Au-NPA with a cylindrical side wall morphology with increase in Au thickness. For thickness above 40 nm, the Au-NPA separation was found to systematically decrease in steps of ~0.2 nm per nanometer of sputtered gold exhibiting values between 30.6 nm - 8.4 nm. **(Figure 6.2)**

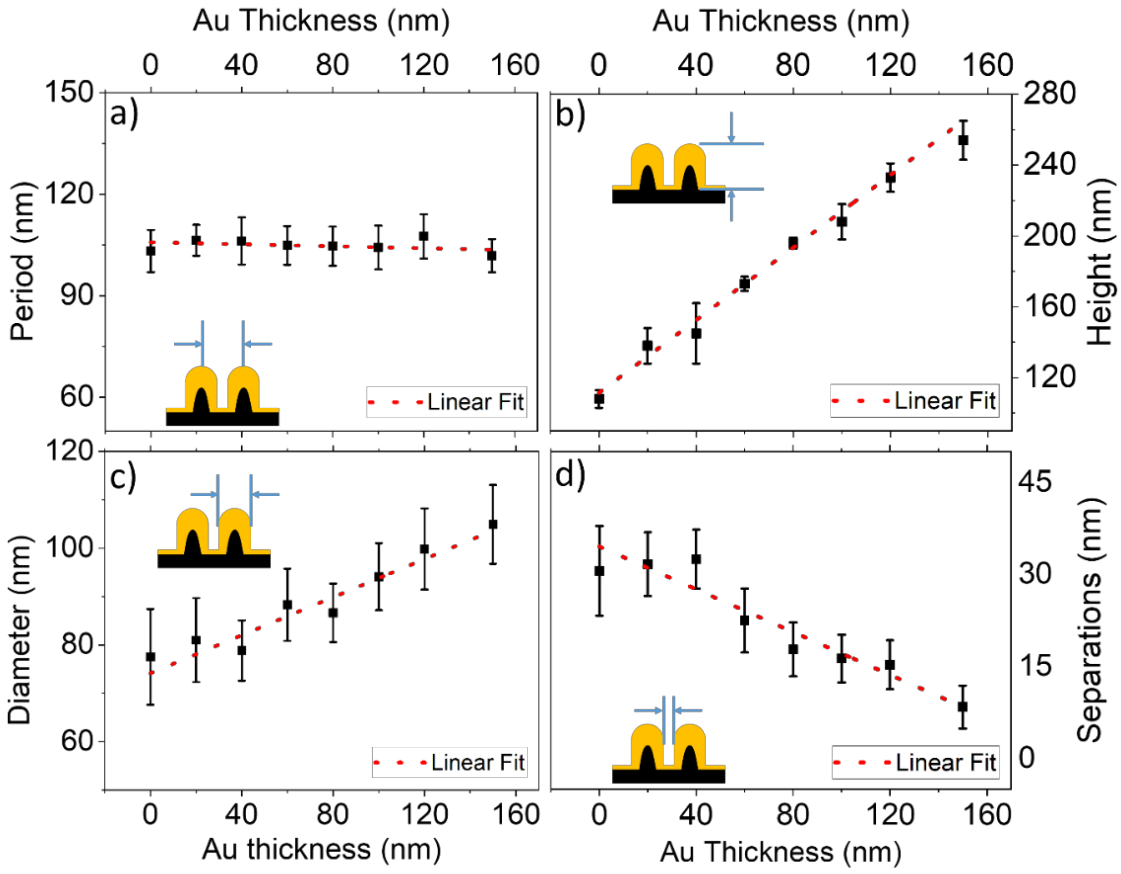

Figure 6.2. Plots show systematic variation in a) period, b) height, c) diameter and d) separations of Au-NPA as function of sputtered gold thickness.

The conservation of the characteristic periodicities and the standard deviations of the original polymer template into the Au-NPAs and the correlation between the gold film thickness and the resulting Au-NPA morphology allow the rational design of desired Au-NPA geometries, from the start. The well-callibrated changes to feature separations across macroscopic areas is critical to assure meaningful correlations in the subsequent investigations of analyte co-localization at EM hot-spots by surface enhanced spectroscopies. The low standard deviations of the Au-NPA geometry enables geometric models that closely resemble the experimental data, assuring better prediction of optical properties by numerical simulations

6.3.2. Inter-Pillar EM Hot-Spots

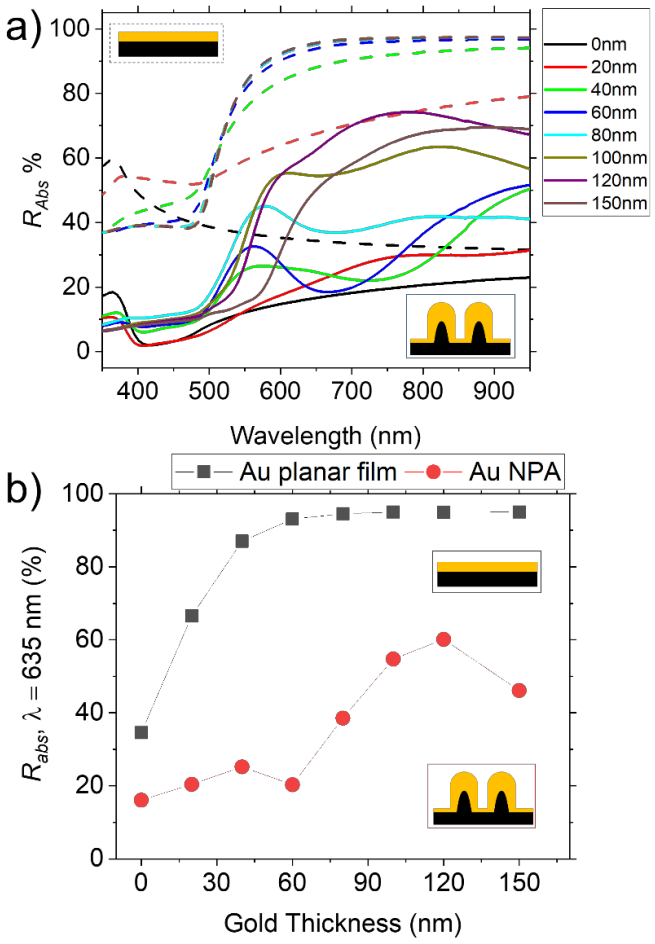

Figure 6.3. Comparison of (a) absolute reflectance spectra of the AU-NPAs (continuous line) versus planar gold films (dotted curves) on Si substrate, as a function of gold film thickness, and b) plot of absolute reflectance at 635 nm compared for AU-NPAs versus bare substrates.

The optical response of the metal nanopillars was investigated by experiments in feedback with numerical simulations. The Au-NPAs were found to reduce reflection compared to their planar counterparts for all thicknesses **(Figure 6.3)**. The nanopillar structure consists of inter-pillars gaps smaller than the incident wavelength. Therefore, the nanopillar arrays are a subwavelength structure that provides an effective refractive-index gradient between air and the substrate, which reduces the reflection of incident light from the nanopillar surface and improve the transmission of light through the interface.

6.3.3. Numerical Simulations

Table 6.1. Structural parameters value of the nanopillars based on the experimental data used for the simulation of the electric field distribution in hot-spots.

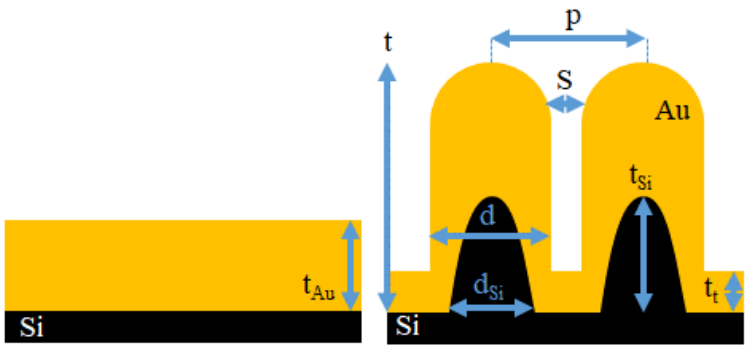

Au Deposition t_{Au} (nm)	Au-np Diameter d (nm)	Au-np Separation S (nm)	Au-np Pitch p (nm)	Au thickness at NP Base t_t (nm)	Au-np Height t (nm)
150	104	6	110	44	265
120	98	12	110	37	235
100	94	16	110	32	214
80	90	20	110	28	194
60	86	24	110	23	173
40	82	28	110	18	153
20	78	32	110	13	132

0 (SiNP)	74	36	110	0	111

*np = nanopillar

The Three-Dimensional (3D) Finite-Difference Time-Domain (FDTD) method is used to simulate the electric field distribution for different thicknesses of hexagonal nanopillar arrays. The structural parameters of the nanopillar arrays chosen for the models were guided by the experimental data from **Figure 6.2 (Figure 6.4, Table 6.1)**. As can be seen in **Figure 6.5a**, the NPAs formed by gold nanodomes on silicon nanocones. In the FDTD algorithm, the anisotropic perfectly matched layer as the absorbing boundary condition is set at z boundary and periodic boundary conditions are set at x and y boundaries of the simulation domain. The grid sizes of 0.5 nm in the x- and z-directions and 1 nm in the y-direction are chosen to ensure numerical convergence. Simulated electric field profiles in **Figure 6.5(b-c)** confirm expectations of EM hot-spots at the inter-pillar gaps, with increasing enhancements as a function of decreasing pillar separations. The electric field enhancements were found to be maximized at 150 nm gold film thickness, and corresponding to an average separation of 6.5 nm.

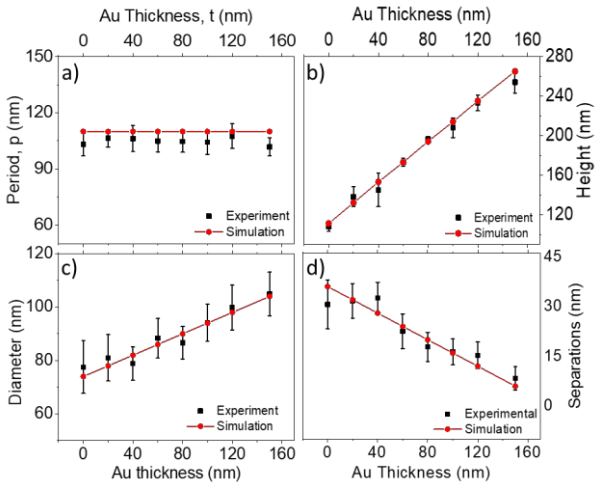

Figure 6.4. The plots show comparison of the experimental values for the different geometric parameters with those used in the models for FDTD simulations.

The Au-NPA present a two-fold advantage - First, the silicon nanocones reduce the incident light reflection by grading the refractive index mismatch between air and silicon **(Figure 6.3)**. Second, the Au-NPA provide high SERS enhancement in inter-pillar gaps due to the coupling of localized surface plasmon resonances and efficient light-trapping in inter-pillar gaps owing to the anti-reflective effect of the silicon pillars. The simulated

electric field distribution in **Figure 6.5** are in good agreement with the experimental optical measurements and highlight successful engineering of inter-pillar EM hot-spot geometries using the gold nanopillar arrays.

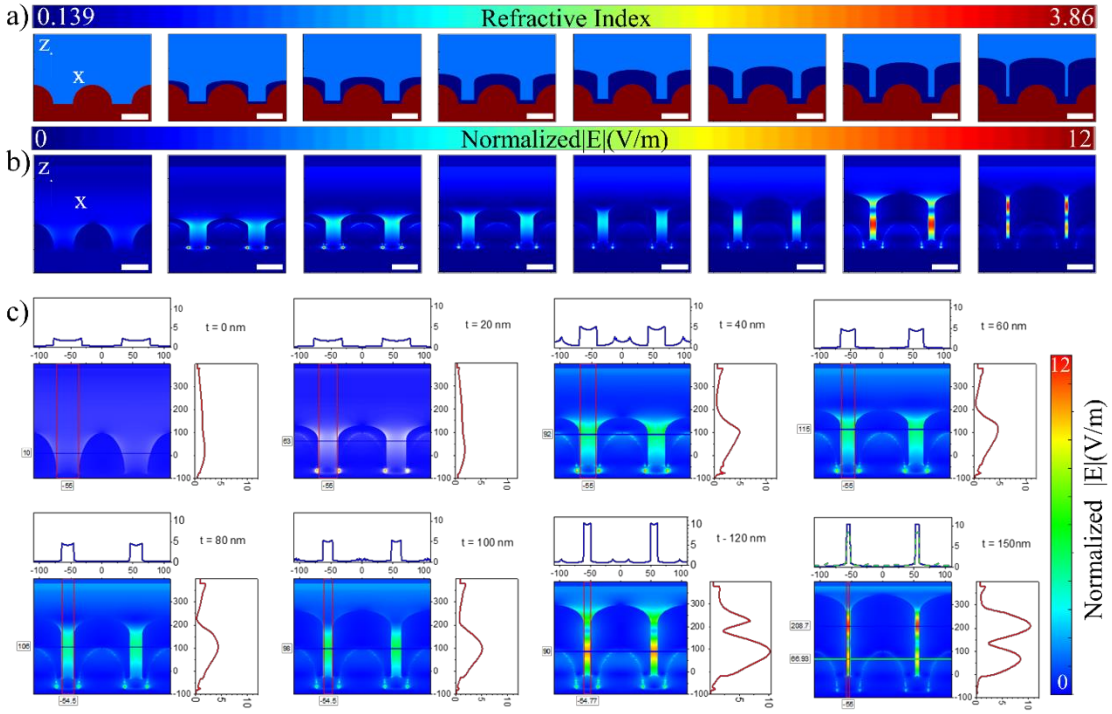

Figure 6.5. (a) Refractive index profile in the x-z cross-section of nanopillar structure. (b) Electric field profile in the x-z cross-section of nanopillar structure at an incident wavelength of 633 nm, and (c) Evolution of electric field profile with increasing gold layer thickness at an incident wavelength of 633 nm. The scale bars indicate 100 nm.

6.3.4. Molecular Size Dependence

The NPA were subsequently subjected to investigations probing the SERS signal intensity evolution as a function of separation for two different molecules with molecular dimensions that were an order of magnitude apart, viz. a small organic molecule and another, a protein. SERS spectra were recorded at 633 nm excitation using 50X objective with a numerical aperture of 0.55. 1-Naphthalene thiol (NT) was used as the small molecular probe, especially due to the well defined spectroscopic characteristics, sub-nanometric size, and its readiness to form self-assembled monolayers on gold surface. The signal intensity of the ring stretching mode of NT at 1377 cm^{-1} was followed to quantify the SERS enhancements as a function of the Au-NPA geometry, and molecular

concentrations. Investigations with a larger molecule were pursued with Streptavidin, a tetrameric protein with a molecular weight of 55 kDa, with a dimension of 4.2 nm x 4.2 nm x 5.8 nm.[405] Streptavidin exhibits strong interaction with biotin and exhibits a high binding affinity (dissociation constant of 10^{-15} M).[484] To detect Streptavidin, the NPA surface was immobilized with biotin-PEG-thiol (BPT), with biotin head groups to bind to Streptavidin (SA) in the solution. The Streptavidin conjugated to Cy5 dye (SA-Cy5) was used for the study, to enable the use of Cy5 as a Raman and Fluorescence reporter to follow the impact of Au-NPA geometry and molecular concentrations on the surface. The SA-Cy5 has an average value of dye to protein molar ratio of 10:1, indicating an on an average 10 Cy5 molecules conjugated to each SA molecule. The SERS intensities of the characteristic Raman peak of Cy5 at 583 cm^{-1} were followed to ascertain the impact of the Au-NPA geometry and the surface concentrations. The biotinylation of the surface was followed by a high concentration of BSA to block non-specific binding sites followed by exposure to Streptavidin with different concentrations. The Biotin-Streptavidin interaction under identical conditions was performed on the bare gold surface was followed using Quartz Crystal Microbalance (QCM). This confirmed the protein resistance of BSA, and to confirm that the binding response of the assay is as expected.

The impact of Au-NPA geometries, especially the inter-pillar gap EM hot-spots on the SERS intensity evolution of NT and SA-Cy5 was investigated at saturated surface densities of NT and SA-Cy5 obtained respectively at 1μM solution of ethanol and 400 nM solution in PBS. Under these conditions, the molecular concentrations are large enough in solution to assure complete coverage on surfaces. The use of saturated surface density is essential to ensure that the changes to the SERS signal intensities can be entirely attributed to the Au-NPA geometry. As confirmed by numerical simulations, the Au-NPA present EM gap hot-spots at the interpillar gaps with distances that vary from 30.6 nm – 8.4 nm. Given the molecular dimensions of NT (d_{NT} ~ 0.5 nm), and BPT – SA-Cy5 ($d_{BPT} + d_{SA\text{-}Cy5}$ ~ 7.7 nm), it is reasonable to expect that while NT could access the inter-pillar EM hotspots in all cases, the SA-Cy5 would be unable to access the EM hot-spots with gaps smaller than the interaction dimensions.

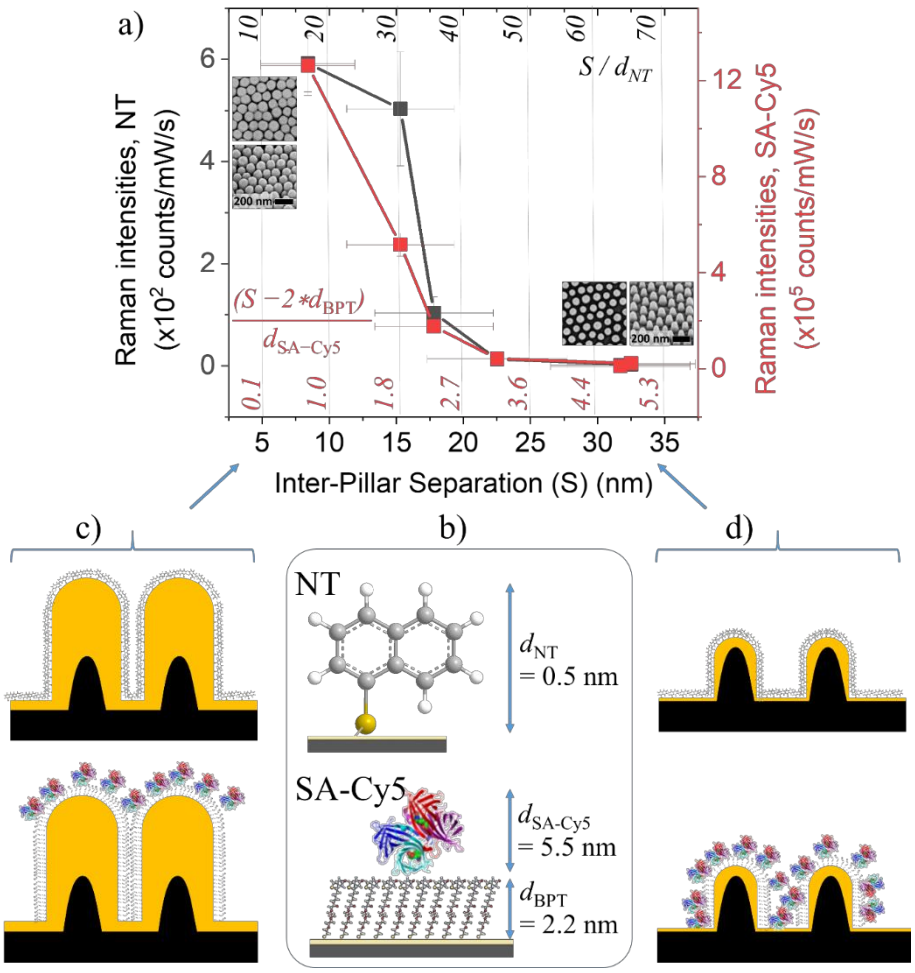

Figure 6.6. Comparison of SERS signal dependence on the inter-pillar separation in Au-NPA for the NT (black curve) and SA-Cy5 (red curve). The inter-pillar gaps are indicated in the units of NT(d_{NT}) and SA-Cy5 ($d_{SA\text{-}Cy5}$) interaction dimensions. The SEM images in top and tilt views of Au-NPA at lowest and highest separations are shown for reference. (b) schematic illustration of the relative dimensions of NT and (SA-Cy5)-BPT pair (c,d) and their expected distribution on Au-NPA at (c) low and (d) high separations.

The SERS intensity response of NT and SA-Cy5 as a function of the inter-pillar separations is shown in **Figure 6.6**. The SERS intensities for both molecules were matched at the minimum and maximum separations to follow only the evolution of the response as a function of the separation. The inter-pillar separations were further expressed in the units of respective molecular dimensions, thus, the experimental Au-NPA separations could be represented as 4.9 – 0.5 units of SA-Cy5, or 65.2 – 14 units of NT. **(Figure 6.6a)** The interpillar gaps in the case of SA-Cy5 detection take into account the reduced gap due to pre-adsorbed self-assembled monolayer of BPT ($d_{BPT} \sim 2.2$ nm), that reduces the separation

further by a distance of 4.4 nm. The response as a function of decreasing inter-pillar gaps shows a significant increase in signal intensities below 15.9 nm separations for both NT and SA-Cy5. The rise of the SERS signal intensities to the maximum intensity in the case of NT is steeper compared to that of SA-Cy5. **(Figure 6.6a)** The response of the NT continues to increase, but gets less steep between 16.3 nm to 8.4 nm, showing what appears to be signs of saturation. The apparent saturation can be attributed to partial fusion of some of the features at 150 nm thickness as seen in the electron microscopy images, which results from the standard deviation of the pillar periodicities. Despite the low standard deviations of the array periodicities, targeting inter-pillar gaps of the order of the standard deviations would risk closing gaps of a population of pillars corresponding to the lowest separations. The partial fusion reduces the feature densities from 120 μm^{-2} to 40 μm^{-2} with consequently the density of inter-pillar gaps from ~491 μm^{-2} to 161 μm^{-2}, which is almost 67% reduction in the density of hot-spots. The remaining inter-pillar gaps exhibit lower distances and thus greater EM enhancements, which would explain the continued increase in observed signal intensities. Unlike in the case of NT, the SA-Cy5 intensities were observed to rise less steeply at pillar separations below 15 nm, which, in other words at gap distances that are below twice the SA-Cy5 dimensions. The gradual increase of SA-Cy5 signal intensities in comparison to that of NT could result from the inability to leverage the inter-pillar EM hot-spots, due to the steric hindrance to entering the gaps. As the pillar gaps reduce further to 8.4 nm, spatial constraints rule out the possibility for any SA-Cy5 at the inter-pillar hot-spots as the gaps can no longer accommodate the molecule. This favors a transition to SA-Cy5 occupying entirely the top of the Au-NPA with the possibility to benefit to the extent of EM enhancements at sites closer to the EM hot-spots. If the arguments were true, the NT would leverage best from its co-localization with inter-pillar EM hot-spots, down to the smallest separations, and should consequently deliver higher analytical sensitivity over SA-Cy5. The SA-Cy5 in comparison would be unable to leverage the best performing EM hot-spots, due to its inability to enter the gaps, and thus should contribute to lower sensitivity in detection. To confirm this, the Au-NPA with lowest separations (labeled henceforth Au-NPA_150) was evaluated for their performance in quantitative assays of both NT and SA-Cy5. **(Figure 6.7)**

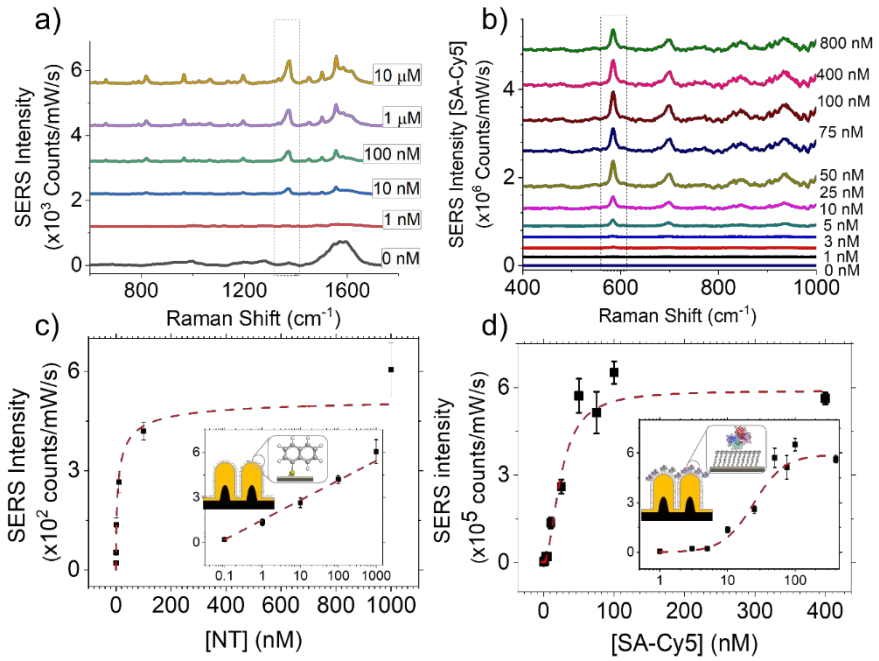

Figure 6.7. Comparison of the SERS assays of (a,c) NT and (b,d) SA-CY5 on biotinylated AU-NPA_150, showing Raman (a,b) spectral evolution and the (c,d) plot of intensity of characteristic peak of (c) NT (at 1377 cm^{-1}) and (d) SA-Cy5 (at 583 cm^{-1}) as function of concentration. Dotted lines show Hill-Langmuir fits. Insets show response with concentration represented in the logarithmic scale.

The SERS signal intensities of the characteristic peaks of NT and SA-Cy5 were followed as before as a function of increasing solution concentrations of the respective molecules. The assays show the excellent quantitative response of SERS signal intensities with low standard deviations, even with multiple repetitions of the assays with sensor chips from different batches. The signals for NT on the Au-NPA_150 was observed down to 1nM within the experimental range tested, while the lowest detection limits (LOD) taking into account the limit of blank was estimated to be 800 pM. In case of SA-Cy5, the signals were observed down to 1 nM concentrations, while the LOD was estimated to be 1.3 nM. Considering that each SA-Cy5 has ~10 Cy5 molecules, the LOD corresponds to signal contribution from the Cy5 concentrations that is effectively an order of magnitude higher. The LOD of SA-Cy5 is thus clearly lower as compared to the NT, which is despite the fact that the Cy5 absorption peak (655 nm) is close to that of the excitation wavelength of 633 nm, and thus is capable of resonance Raman excitation. Resonance Raman excitation has the potential to contribute to 3 orders of magnitude higher signal enhancements compared

to non-resonant counterparts.[399] The greater sensitivity in the detection of NT is consistent with the observations of the impact of molecular dimensions over gap size-dependent SERS enhancements.

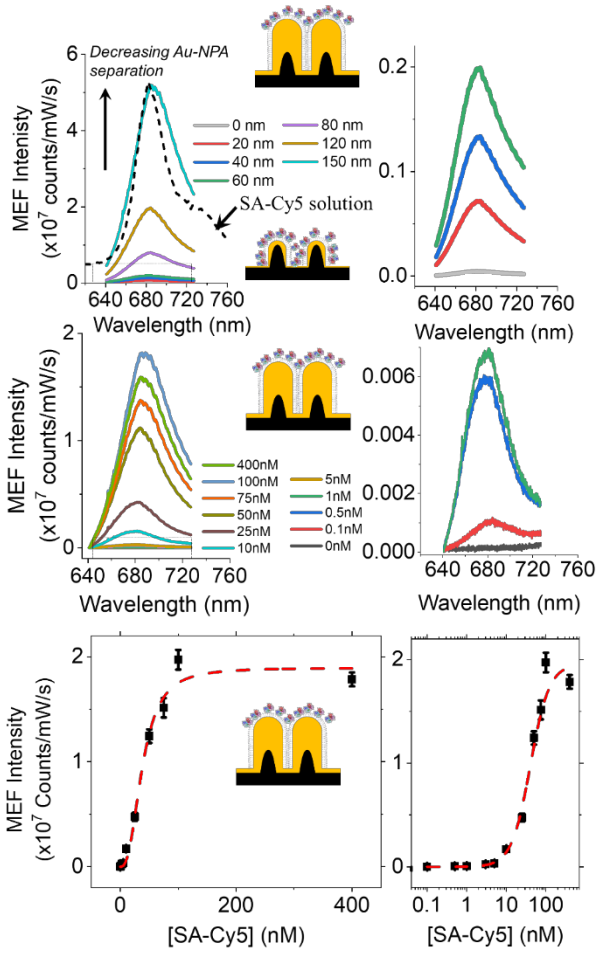

Figure 6.8. a) MEF spectral evolution of saturated coverage of SA-Cy5 on biotinylated AU-NPA as a function of gold thickness. The emission spectra of the SA-Cy5 molecule in solution is shown for comparison. b) MEF spectra acquired on AU-NPA_150 as a function of SA-Cy5 concentrations and d) MEF assay of SA-Cy5 on biotinylated AU-NPA_150. The dotted line indicates fit to Hill-Langmuir function.

A strategy to overcome the issue of steric limitation to position molecules at the hot-spots is to use metal-enhanced Fluorescence (MEF) in place of SERS. Unlike SERS, MEF requires the analyte to be positioned at an optimal distance away from the hot-spots to benefit from high enhancements.[425–427] This plays to the advantage of partially relieving the spatial constraints associated with SERS. To investigate this, the assays of SA-Cy5 shown in **Figure 6.6** and **Figure 6.7Figure 6.7.** were repeated while measuring the Fluorescence

emission intensities of SA-Cy5 as a function of concentrations. The Fluorescence spectra show strong enhancement in relation to the bare gold substrate controls and increased as a function of gold film thickness with the Au-NPA_150 still exhibiting the maximum signal enhancements amongst the Au-NPAs **(Figure 6.8a).** The plot of Fluorescence peak intensities of SA-Cy5 gave a well-behaved quantitative response as a function of the concentration of SA-Cy5, with the lowest observable signal at a concentration of 100 pM. An LOD of 120 pM was estimated taking into account the mean and standard deviation of the blank signal and the standard deviation of the signal intensities at the lowest concentration **(Figure 6.8b-c)**. The LOD observed in the MEF assays is an order of magnitude lower than that of the SERS assays, mainly benefitting from the compatibility of the spatial requirement to the dimension of the molecules. The high sensitivity of the Au-NPA_150 in MEF assays can also be seen from the enhancements by 4 orders of magnitude higher for the Au-NPA_150 as compared to the bare gold surface under identical conditions. The enhancements observed are greater than those reported in the literature, for MEF assays based on Cy5[427,485–487] or other dyes,[488,489] and can be attributed to the large number of highly enhancing EM hot-spots attained on the pillar arrays.

6.4. Conclusions

Plasmonic nanoarrays consisting of gold nanopillars (Au-NPA) with systematic control over inter-pillar electromagnetic (EM) gap hot-spots were achieved down to sub-10 nm separations. The rational control over the geometric attributes of the NPA, with separations, height, and standard deviations was determined at the early phases of fabrication, due to robust correlations between the process and structure for the different processes used, including self-assembly, pattern-transfer, metal deposition, and surface functionalization. The excellent geometric definition allowed modeling the nanopillar geometries with low deviation from experimental arrays. The numerical simulations show tight confinement of EM fields at the inter-pillar gaps, with maximum enhancements observed for the smallest gap distances. This sets expectations that are consistent with experimental observations of the impact of the molecular size on gap dependent spectral signal evolution. Consequently, the analytical sensitivity in the detection of NT by SERS was an order of magnitude better than the labelled protein analyte, despite the opportunity for resonance Raman excitation in the latter case. The spatial constraints requiring the

analyte co-localization at the EM hot-spots for the best leverage in SERS assays could be at least partially relieved by adopting MEF assays. The MEF assays delivered an analytical sensitivity that was over an order of magnitude better than the SERS assays pushing the lowest detection limits down to 120 pM. The findings provide convincing case for the need for rational design of nanoplasmonic interfaces to take into consideration, analyte dimensions in relation to EM hot-spots, in order to achieve the highest sensitivities.

Chapter 7. Conclusions and Outlook

The thesis dealt with the investigation of rationally designed plasmonic nanoarrays to enhance sensitivity for biomolecular detection using surface-enhanced spectroscopies (SES). The EM enhancements are strongly pronounced at junctions between adjacent nanostructures resulting in gap hot-spots. EM enhancements at these hot-spots increase non-linearly as a function of gap distance down to the sub-10 regime. Analyte molecules present at these gaps can leverage these EM enhancements, resulting in ultra-high sensitivity in detection by surface-enhanced Raman or Fluorescence spectroscopies. However, such confining gaps affect the ability of large analytes such as biomolecules to enter and thereby leverage EM fields within the gaps. This presents spatial needs to enhance EM fields at odds with those for accommodating biomolecular interactions. Therefore, to achieve high sensitivity in detecting biomolecules, the surface geometries are required that can provide large number of EM hot-spots that also takes into consideration the size of the target moelcules.

This brings in to focus of this thesis where, the EM hot-spots which offers high sensitivities and large densities on the surface are fabricated and their geometries were tailored in response to the target analyte dimensions to investigate the impact of biomolecular detection using molecular self-assembly approach. The work draws advantage from the capabilities offered by the molecular self-assembly approach based on amphiphilic copolymers. Plasmonic nanoarrays consisting of discontinuous metal nanostructures based on nanoparticle clusters and continuous, yet presenting three-dimensional topographies based on metal nanopillars were focussed to investigate the dependence of the sensitivities on the size of the target molecules in relation to the diminished gaps between metal nanostrucutres using surface-enhanced Raman Spectroscopy (SERS) and surface-enhanced fluorescence (SEF).

The approach enabled overcoming the challenge of fabricating large densities of EM hot-spots with low standard deviations of <15% for the key geometric variables, provided

orthogonal control over the size and spacing between the features, and potential options for the transfer of the pattern to realize different nanoplasmonic interfaces. Therefore, the definition of the resulting nanoplasmonic arrays contributed to the ease of geometric modeling to predict and understand optical and spectroscopic properties and estimate biomolecular densities based on surface area calcualtions.

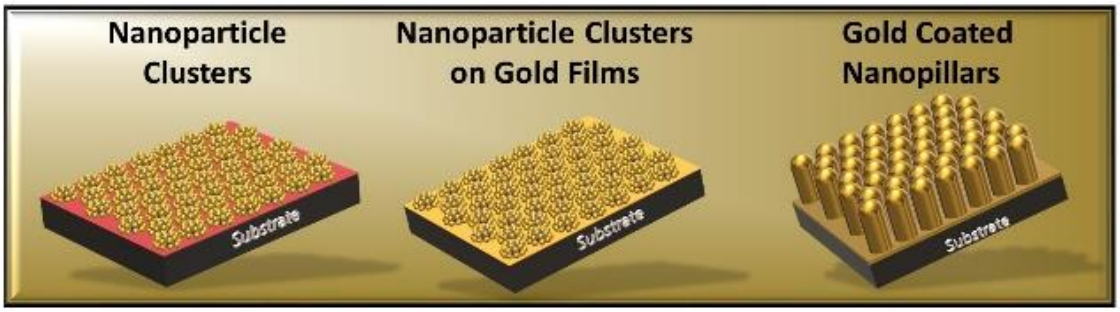

Figure 7.1. Cartoonistic representation of the types of nanoplsmonic arrays investigated in this thesis.

Nanoparticle cluster array (NCA) provided unique hybrid geometries allowing both EM hot-spots <1 nm between NP within the cluster and <10nm between the clusters. Such dual length scale EM hot-spots provided a unique opportunity to accommodate smaller (<1nm) analytes in inter-particle hot-spots, while the larger analytes could take advantage from the inter-cluster hot-spots. The NCA fabricated on glass substrates that presented a greater number of inter-cluster hot-spots provided greater opportunities for the co-localization of the larger protein analytes. Ensuing, higher sensitivity during the detection based on SES. Hence, configurations with higher densities of EM hot-spots can promote higher sensitivity.

Also, EM enhancements observed on NCA on glass substrates could be enhanced significantly upon fabrication on the reflective gold metal film. Based on the observations, the presence of metallic film (MF) on the substrate below the NCA improved the sensitivities. However, the impact of the presence of MF was found to favor more to the NCA that were larger in dimensions and presented lower densities of inter-cluster hot-spots. Therefore, the enhancement of the EM field at both inter-particle and inter-cluster hot-spots served to enhance the sensitivity in the detection of small analytes and larger biomolecules, with limits of detection lower by an order of magnitude better than glass. Detection of

Naphthalene thiol and Streptavidin-Cy5 was demonstrated with LOD down to picomolar concentrations in the case of NCAs on gold films for SERS as well as SEF.

The flexibility offered by the molecular self-assembly based nanofabrication approach enabled the fabrication of NCA over the choice of substrates. This enabled to deduce observations that are discussed above. The ability to physically quantify the exact surface densities of the NP and biomolecules enabled to correlate the signal contributions for each case. Therefore, knowledge of nanoparticle concentrations and the biomolecular densities on the NCA by quartz crystal microbalance (QCM) enabled understanding the configuration of NCA that contributed to the best sensitivities. For NCAs on glass, the smaller clusters that provided greater densities of inter-cluster EM hot-spots, and on gold, the larger clusters that provided greater EM enhancements in the inter-cluster hot-spots were found to dominate the relative sensitivities between the smaller and larger clusters.

QCM sensor being versatile in the sense that it can be modified as per requirement, the fabrication of NCA on the QCM sensor directly contributed significantly in identifying the best plasmonic configurations. The challenge in understanding the surface-concentration of molecules that contribute to the plasmonic signal was made possible by in-situ measurements of QCM together with metal-enhanced fluorescence. The use of MEF was particularly helpful for the high signal intensities observed even under the buffer environment. The surface concentrations together with geometric modeling enabled clarity of understanding of the biomolecular distribution with respect to the inter-cluster EM hot-spots. This makes it particularly interesting to evaluate MEF and QCM using the surface concentration of molecules as the common scale. While MEF was shown to achieve a detection range from ~1209 to $4x10^4$ molecules (in 1.55 μm^2 probed area) while the QCM sensor would detect in the proteins in the range of $6.4 \times 10^{10} – 5.7 \times 10^{12}$ molecules (in 1.4 cm^2 probed area). Therefore, this configuration presents a convincing case for MEF driving miniaturization and sensitivity goals. The approach also holds the potential to extend its application to perform real-time spectroscopic analysis and relate mass transport of the analyte on the surface in-situ. The extended approach was also employed during the work in the thesis to rationalize the configurations by identifying key contributing factors in the detection sensitivities and maintaining control over surface functionalizations to identify factors causing standard deviations or signal variations.

Continuous metal nanostructures presenting three-dimensional topographies were investigated to identify the impact of enhanced EM fields as a function of closing gaps between metal nanostructures on the ability of the target molecule to take advantage of emerging EM hot-spots. Well defined periodic nanopillar arrays (NPA) with anisotropically coated gold were demonstrated to provide spatially resolved sub-10 nm gap hot-spots. These gaps were controlled with sub-5 nm steps by systematically controlling the sputter-coated metal thickness and their detection sensitivities with decreasing gap distances between metal pillars were probed using target molecules of different sizes. The sensitivity in the detection of the target analyte shows a strong dependence on the size of the target molecule in relation to the inter-pillar gaps. Small and large analytes result in higher enhancements with decreasing gaps between the Au-NPA. However, the analytical sensitivity for SERS of the analyte molecule with a smaller size was found to be higher than that of the larger molecules. The spatial constraints experienced by the larger analyte molecule limited its ability to take advantage of the enhanced EM fields for SERS. However, this was observed to be a favorable configuration for SEF. Since, SEF phenomena benefit from the presence of spacer between the reporter and the metal surfaces, which is well-met by the biomolecular dimensions. The analytical sensitivities achieved using SEF for larger analyte was further pushed down to an order of magnitude as compared to SERS.

Therefore, this thesis identifies configurations that enhance leverage over EM hot-spots by configurations drive analyte co-localization with EM hot-spots driving sensitivity down to picomolar concentrations. Work demonstrates robust correlations between the geometry ó optical/spectroscopic properties ó sensitivity in molecular assays with experiments combined with numerically simulated field maps of plasmonic nanoarrays. The observations discussed above with engineered EM hot-spots were demonstrated while maintaining the ability to quantify analyte detection benefiting from nanofabrication technique that enabled homogeneously distributed EM hot-spots over large areas. The approaches shown in the thesis could be extended already for preliminary results showing high sensitivity in the detection of proteins by immunosandwich assays and oligonucleotides. The findings provide a convincing case for the need for the rational design of nanoplasmonic interfaces to take into consideration, analyte dimensions in relation to EM hot-spots, in order to achieve the highest sensitivities.

Further work would benefit from improving the logistics of the measurements with on-chip fluidics, and portable spectroscopic measurements. The interfaces need to be tested and optimized for functioning in complex media such as sputum, blood, and urine, which may pose different challenges. The issue of diffusion limitations arising at ultra-low concentrations resulting in the problem of the analyte finding the surface akin to ‘finding a needle in a haystack’. There is a need for independent approaches to improve analyte mass transport that remains compatible with the stability and performance of the nanoplasmonic transducers. While the plasmonic sensors have held high promise for highly sensitive, fast responding, and portable configurations, they need significant transversal developments cutting across topics beyond fabrication, physics, and photonics, to ensure reliable devices that address emerging analytical challenges.

Left Blank Intentionally

Publications List

Peer reviewed journal publications:

- **R. Rastogi**, E. A. Dogbe-Foli, R. Vincent, S. Poovathingal, P. Michel-Adam, S. Krishnamoorthy, "*Gold Nanoparticle Cluster Arrays with Engineered Nanoscale Geometries for Quantitative Plasmonic Bioassays*." (Under Review)
- **R. Rastogi**, E. A. Dogbe-Foli, R. Vincent, P. Michel-Adam, S. Krishnamoorthy, 'Engineering Electromagnetic Enhancements in Gold Nanoparticle Cluster Arrays on Reflective substrates for High Sensitivity in (Bio)molecular detection' (To be submitted)
- **R. Rastogi**, M. Beggiato, C. Dupont-Gillain, P. Michel-Adam, S. Krishnamoorthy, 'Combining Quartz Crystal Microbalance and Metal-Enhanced Fluorescence to Quantify Analyte Surface Concentration in Plasmon-Enhanced Spectroscopic Bioassays.' (Under Review)
- **R. Rastogi**, H. Arianfard, S. Juodkazis, D. Moss, P. Michel-Adam, S. Krishnamoorthy 'Investigating Analyte Co-Localisation at Electromagnetic Gap Hot-Spots for Highly Sensitive Biomolecular Detection by Plasmon-Enhanced Spectroscopy.' (Under Review)
- **R. Rastogi**, P. Michel-Adam, S. Krishnamoorthy 'Strategies and tools to rationally design nanoplasmonic biosensor: A Review.' (Under Preparation)
- C. Stoffels, P. Grysan, C. Sion, **R. Rastogi**, M. Beggiato, E. Olmos, S. Krishnamoorthy, '*Engineered Plasmonic Microcarriers for Sensing and Cell-Expansion.*' (Contributer)
- M. Beggiato, **R. Rastogi**, C. Dupont-Gillain, S. Krishnamoorthy, '*Nanopattern as a tool to control analyte mass transport.*' (Contributer)

Book Sections and Chapters:

- M. Beggiato, **R. Rastogi**, C. Dupont-Gillain, S. Krishnamoorthy, '*Nanopattern as a tool to control analyte mass transport.*' (Contributer) **R. Rastogi,** C. Pedrosa, S. Krishnamoorthy, Nanoimprint Lithography, Nanosphere Lithography, Directed Self-Assembly, and Pattern Transfer Optical Spectroscopy in book chapter 'Nanomaterials

for nano spectroscopy' (Chapter 6) Section 6.4.2 (Structure transfer by Lithography), published by DeGruyter.

- **R. Rastogi**, M. Beggiato, P. M. Adam, S. Juodkazis, S. Krishnamoorthy '*Nanoplasmonic arrays with high spatial resolutions, quality, and throughput for Quantitative Detection of Molecular Analytes*', in Plasmonics, published by Intechopen, 2019, DOI: 10.5772/intechopen.89064.

Filed Patents:

- S. Krishnamoorthy and **R. Rastogi**, Quartz crystal microbalance with higher sensitivity, patent application LU101354, filed on 19/08/2019. PCT application filed on 19/08/2020.

Contribution to conferences and Scientific Events:

- **R. Rastogi**, S. Poovanthingal, P. M. Adam, J. Starikov, S. Juodkazis, and S. Krishnamoorthy, '*Confined nanoscale geometries to enhance the sensitivity of plasmonic immunoassays*', 16th IUVSTA School: ISS on Physics at Nanoscale, 2017 – Poster Presentation
- **R. Rastogi**, S. Poovanthingal, P. M. Adam, J. Starikov, S. Juodkazis, and S. Krishnamoorthy, '*Engineering nanopattern geometry at the molecular resolution to enhance the sensitivity of nanoplasmonic biosensors*', SPIE Conference Proceedings, 2018 – Oral Talk
- **R. Rastogi**, P. M. Adam, S. Poovanthingal, S. Juodkazis, and S. Krishnamoorthy, 'Controlling Nanoscale Geometries and Biomolecular Interactions on Gold Nanoparticle Cluster arrays for High Performance Plasmonic Biosensing', Conference Poster, NFO 2018 – Poster Presentation
- **R. Rastogi**, P. M. Adam, S. Krishnamoorthy, '*Plasmonically active - Nanoscale geometries for detection of biomolecule*' –Pich (2 min) Presentation at MRT PhD. Day, Luxembourg, 2018 – Oral Talk
- **R. Rastogi**, P. M. Adam, S. Krishnamoorthy, '*Wafer Level Fabrication of sub-10 nm Gap Hot Spots for Reliable Quantification of Biomolecules by SES*', Conference Presentation, International Conference of Enhanced Spectroscopy, Ontario, Canada, 2019. – Oral Talk

- **R. Rastogi**, P. M. Adam, S. Krishnamoorthy, '*Nanoscale Geometries for Plasmonic Biosensing*' –Pich (5 min) Presentation at LIST PhD. Day, Luxembourg, 2019 – Oral Talk
- **R. Rastogi**, 'My journey as a yound researcher', event organized by FNR to promote career in science among teenagers – Chercheurs a l'ecole, --- March 2019, Luxembourg, Lycee Aline Mayrisch, Oral Talk

Left Blank Intentionally

Annexe A. Résumé Français

Introduction

Les professionnels de santé et des chercheurs du monde entier déploient une multitude d'efforts variés pour les soins de santé et les diagnostics, notamment pour éviter les maladies ou améliorer la technologie actuelle des biocapteurs disponibles pour détecter les biomarqueurs moléculaires présents dans le système vivant. Les biomarqueurs moléculaires désignent les espèces biologiques capables de rapporter avec précision des informations relatives à la santé du patient. Une seule goutte de sang contient des millions de cellules, de protéines et d'acides aminés renfermant une grande quantité d'informations sur la santé du patient qui peuvent tous être considérés comme des biomarqueurs.[15] Au stade initial de la progression de la maladie, les biomarqueurs présents dans des milieux complexes à une concentration *aussi faible que la concentration femtomolaire* dans le cas du cancer, posent des défis essentiels. La capacité de détecter rapidement ces biomarqueurs à des niveaux cliniquement pertinents,[21] est devenue l'un des objectifs principaux des technologies de bio-détection. Par conséquent, les biocapteurs qui présentent des sensibilités de détection pour des concentrations ultra-faibles (généralement nanomolaires et inférieures) avec des temps de réponse rapides sont essentiels aux besoins émergents en matière de diagnostic médical.

Les technologies populaires et les technologies émergentes alternatives pâtissent du compromis entre *une sensibilité élevée* et *des temps de réponse rapides* dans le cadre d'empreintes de détection miniaturisées.[30,38] Avec une sensibilité prouvée jusqu'à quelques molécules dans des empreintes microscopiques et un temps de réponse allant de quelques secondes à quelques minutes, seules, les spectroscopies exaltées de surface (SES) peuvent combler cette lacune.[41–44] Les biocapteurs basés sur

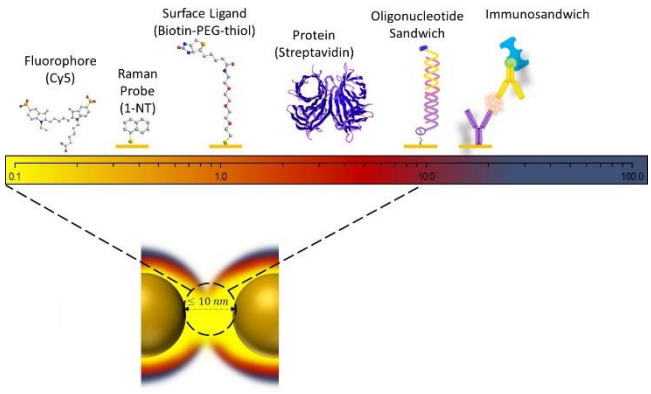

Illustration A.1. Représentation schématique des échelles de longueur biomoléculaire par rapport aux espaces géométriques confinés dans les points chauds EM.

les SES reposent sur des interactions lumière-matière qui se déroulent à proximité des formes nanométriques à la surface du capteur. Les champs électromagnétiques (EM) ainsi créé sont concentrés et leurs intensités accrues dans les espaces entre les surfaces métalliques. Les molécules positionnées à ces points chauds EM bénéficient d'exaltation électromagnétiques ou chimiques pour émettre des signaux spectroscopiques exaltation. Les molécules présentes dans les points chauds EM avec une intensité relativement plus élevée de champs EM contribuent de manière disproportionnée au signal spectroscopique global provenant de l'ensemble des molécules présentes sur la surface du capteur.[169]

En effet, les champs EM existant dans les intervalles nanométriques entre des nanostructures de métaux nobles sont connus pour présenter des exaltation de haute intensité qui augmentent exponentiellement avec la diminution des distances entre les intervalles. Ces intensités améliorées sont maximisées avec des intervalles distants de seulement quelques nanomètres, ce qui impose des contraintes spatiales importantes pour que l'analyte puisse pénétrer ces points chauds EM et en tirer parti. Cela représente un compromis entre des séparations fermées, nécessaires pour des exaltation spectroscopiques élevées, et les besoins spatiaux pour l'adsorption biomoléculaire, entraînant l'incapacité de la molécule cible à bénéficier de ces champs EM exaltés aux points chauds EM. Les recherches menées dans le cadre de cette thèse visent à la conception rationnelle de nanoréseaux plasmoniques qui présentent une haute densité de points chauds EM et à étudier leur structure et leurs fonctionnalités pour améliorer la sensibilité de détection des tests biomoléculaires à l'aide de spectroscopies à effet exalté.

Origine de l'exaltation des points chauds EM: Les spectroscopies exaltées de surface (SES) reposent sur l'exaltation des signaux spectroscopiques provenant des molécules de l'analyte fixées aux nanostructures métalliques ou à proximité immédiate de celles-ci. La présence de nanostructures métalliques capables de concentrer et exalter les champs EM entraîne une exaltation des signaux spectroscopiques de l'analyte. Avec des signaux fortement exaltés, la SES compense la section transversale au signal plus faible des molécules de l'analyte, permettant une utilité au-delà de la caractérisation spectroscopique dans un outil de détection moléculaire avec des limites de détection (LOD) réduites à quelques molécules. Parmi les différentes techniques d'exaltation de surface, la diffusion Raman exaltée en surface (SERS) et la fluorescence améliorée de surface (SEF) sont très prometteuses en raison de leur compatibilité avec les gammes de longueurs d'onde visibles,

de leur capacité à réduire l'empreinte des capteurs et de leur facilité d'utilisation en situation de mobilité. Dans le cas de la SERS ou de la SEF, lorsque l'analyte cible est intégré dans un environnement de champ EM exalté, il est soumis à des exaltation chimiques et électromagnétiques. Une exaltation des signaux de plus de 10^8 pour le SERS et de 10^3 pour la SEF a été rapportée dans plusieurs études lorsque l'environnement immédiat de la molécule cible est modifié en raison de la présence d'intenses champs EM.[80–83] Cela nécessite bien sûr de respecter un ensemble de conditions, notamment que la surface du capteur soit capable de présenter une forte localisation du champ EM au niveau des points chauds EM et que l'analyte soit à une distance optimale de la surface du métal. Pour la SERS, l'émetteur Raman doit être à proximité (généralement moins de ~ 10 nm) ou en contact avec la surface métallique pour tirer parti des champs EM localisés dans l'environnement où il est intégré et bénéficier, autant que possible, des exaltation chimiques **(Illustration A.2a)**.[68] Pour la SEF, cette distance devrait être supérieure à une certaine distance seuil (généralement inférieure à ~20 nm), ou le taux de décroissance radiative peut primer sur l'extinction, tout en étant capable de tirer parti des radiations EM exaltées dans l'environnement immédiat de la surface métallique **(Illustration A.2b)**.[86]

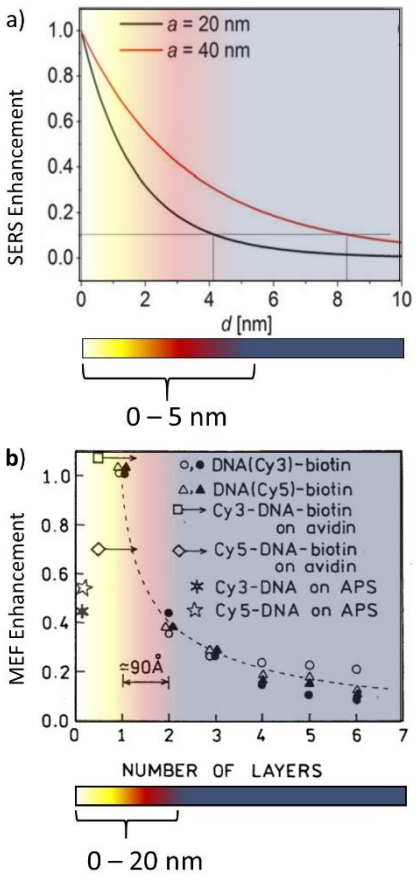

Illustration A.2 . a) G_{SERS} (GSERS), normalisé à la valeur de surface, est représenté en tant que fonction d*d* pour une sphère de rayon a = 20 nm (ligne noire) et pour une sphère de rayon a = 40 nm (ligne rouge). [Adapté avec la permission de Pilot et al. (2017) (réf. 14); Copyright © 2018 Springer International Publishing AG], b) Dépendance de la distance de l'intensité du signal MEF et la surface du métal. [Adapté avec la permission de Lakowicz et al. (2004) (réf. 15); Copyright © 2003 par Academic Press]

Couplage plasmonique aux points chauds des intervalles: Les intensités du champ sont généralement réparties de manière hétérogène autour de la surface des nanostructures et principalement concentrées dans de très petits volumes de points chauds.[144,145] De telles zones peuvent apparaître en raison de l'élaboration de caractéristiques nettes d'une nanostructure isolée, [146] ou d'intervalles nanométriques entre des nanostructures

adjacentes.[147–149] Cependant, les intensités du champ sont plus fortes dans les points chauds des intervalles. L'émergence d'un point chaud EM résulte de l'interaction optique entre deux nanostructures métalliques et le champ EM distribué sur leurs surfaces.[139–142] Les « points chauds » EM désignent les zones situées à proximité des substrats métalliques où l'intensité du champ local est supérieure à celle du champ incident. Malgré les règles de sélection basées sur la taille, la forme et les arrangements (dimères ou réseaux), l'équation de la résonnance plasmonique explique que le comportement de couplage entre deux ou plusieurs nanostructures est exponentiel par rapport à la distance qui les sépare. Par conséquent, il est crucial de noter que pour réaliser un couplage entre nanostructures, les séparations à l'échelle nanométrique sont fondamentales. Cependant, les intensités de couplage peuvent varier en dessous des distances correspondant à la longueur de décroissance du champ ℓ pour un type spécifique de nanostructure **(Illustration A.3)**.[151]

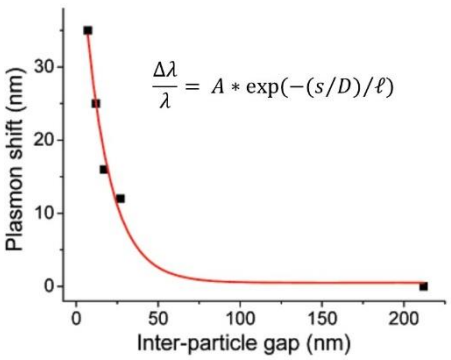

Illustration A.3. Relation entre le décalage de la longueur d'onde et la distance interparticulaire, où entrent en jeu le décalage fractionnaire de la longueur d'onde de résonance plasmonique, l'amplitude du couplage dipolaire, la séparation interparticulaire bord à bord, le diamètre de la nanoparticule sphérique, et la longueur de décroissance du champ électromagnétique à partir de la surface. [Adapté avec la permission de Jain et al. (2007) (réf. 117) ; Copyright © 2007 American Chemical Society]

Exaltation du signal spectroscopique suivant la taille de l'intervalle: Il est admis que le fait de combler les intervalles jusqu'à des distances extrêmes améliore la force du couplage entre les nanostructures métalliques et aboutit à renforcer les champs EM situés entre ces intervalles. [164] Cela a également été observé par Schuck et al. en 2005. [162] Ils ont étudié la relation entre la localisation du champ électromagnétique et la diminution des distances interparticulaires à l'aide d'un dimère de type nanostructure à nœud papillon en or. Les exaltations EM augmentaient de façon exponentielle lorsque les deux nanostructures se rapprochaient de ~20 nm, comme le montre l'**illustration A.4**.[162] Cependant, on observe que les intensités de champ EM sont distribuées de manière hétérogène dans et autour des points chauds de l'intervalle.[145,163] La forme de la nanostructure joue également un rôle essentiel dans la détermination de la force de ces interactions de champ EM,[163,165] ainsi que les modes plasmoniques qui apparaissent dans

leurs spectres d'extinction.[166] Par exemple, il a été démontré que les nanostructures sphériques présentent des facteurs d'exaltation plus faibles si, isolées, elles subissent un couplage plus fort au sein du réseau de longue distance organisé aléatoirement, ce qui entraîne des intensités EM très élevées aux points chauds EM.[167]

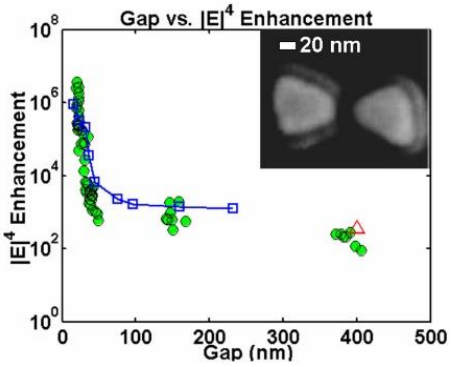

Illustration A.4 Dépendance non linéaire des exaltations de champ EM en fonction de la réduction des distances des intervalles montrant des exaltations EM élevées à des intervalles inférieurs à 10 nm. [Adapté avec la permission de Schuck et al. (2005) (Réf. 28). Copyright © 2005 American Physical Society]

Il est possible d'obtenir des facteurs d'exaltation élevés suffisants pour la détection d'une seule molécule, avec les points chauds des intervalles. Cependant, il manque actuellement des techniques pouvant offrir un contrôle précis pour créer efficacement des points chauds d'intervalles à haute résolution jusqu'à moins de 10 nm à des endroits prédéterminés, ou pour positionner stratégiquement une molécule donnée sur le point chaud.

Interactions Nano-Bio: Dans l'application de biodétection, l'objectif fondamental de l'utilisation d'un analyte est de trouver les réponses aux deux questions les plus importantes : A) *Qu'est-ce que c'est ?* et B) *Combien cela coûte-t-il ?* Répondre à la première question en utilisant la technique spectroscopique exaltée peut être très efficace. Cependant, quantifier la concentration de biomarqueurs moléculaires à l'aide de spectroscopies exaltées nécessite la capacité d'obtenir des signaux spectroscopiques directement liés aux concentrations de biomarqueurs et qui seront moins affectés par les écarts-types intrinsèques dus aux nanostructures artificielles de la plateforme de biodétection. Les biomolécules stratégiquement positionnées sur le substrat dans les géométries des points chauds EM jouent un rôle important dans la détermination des performances du biocapteur moléculaire basé sur la SES. Il s'agit de tirer parti, en parallèle, des outils biotechnologiques avancés pour capturer efficacement les bioanalytes. Cela comprendrait une variété de moyens physiques et chimiques permettant la fonctionnalisation de la surface du biocapteur afin d'améliorer la spécificité et le transport de masse des molécules de l'analyte à partir de la solution. Il devient nécessaire d'identifier un substrat qui permette un consensus sur la taille du point chaud de l'intervalle, afin qu'il

puisse accueillir de grandes biomolécules tout en concentrant des champs EM suffisamment forts pour présenter des sensibilités plus élevées dans la gamme de nM à fM.

Conception rationnelle des tests biologiques plasmoniques: De nombreux défis restent à relever – en commençant par le développement de biocapteurs efficaces et performants pour répondre aux besoins cliniques urgents.[38,285] L'objectif principal reste de capturer spécifiquement les molécules d'intérêt, puis d'en tirer des informations pertinentes grâce aux techniques de transduction offrant une rétroaction rapide avec des sensibilités ultra-élevées. L'examen de l'état actuel des connaissances met en évidence le besoin de points chauds EM fortement exaltés et uniformes sur la surface du capteur afin de pouvoir retranscrire de manière fiable les événements de liaison à de très faibles concentrations. Ces zones doivent ensuite être fonctionnalisées de manière optimale en utilisant des chimies de surface pour améliorer l'efficacité de capture de la cible de la surface du capteur. Pour regrouper de telles caractéristiques dans le capteur, il faudrait des approches rationnelles en fonction des objectifs clés suivants :

- ✓ La capacité de produire à des résolutions allant jusqu'à des échelles de longueur inférieures à 10 nm, associée à la qualité et à la cadence de production.
- ✓ Contrôle orthogonal des variables géométriques.
- ✓ Capacité à concevoir/modéliser les points chauds EM.
- ✓ Capacité à produire des signaux fiables et reproductibles.
- ✓ Quantification des concentrations moléculaires sur les nanoréseaux plasmoniques.

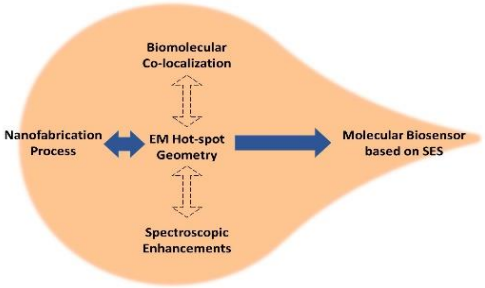

Illustration A.5. Corrélation entre le processus de nanofabrication ⇔ Les géométries des points chauds EM permettent d'étudier la corrélation entre les géométries des points chauds EM ⇔ colocalisation biomoléculaire et géométries des points chauds EM ⇔ Exaltations spectroscopiques, qui peuvent aider à construire un biocapteur moléculaire conçu rationnellement et basé sur la SES.

Réseaux nanoplasmoniques avec des résolutions spatiales inférieures à 10 nm

Le processus de nanofabrication des nanostructures plasmoniques a été réalisé dans la chambre stérile (classe 100) du département de recherche et de technologie des matériaux de l'Institut luxembourgeois des sciences et de la technologie, au Luxembourg. L'humidité ambiante a été maintenue entre 45 % et 55 %, surveillée par un hygromètre à l'intérieur de la chambre stérile. Les outils de caractérisation qui ont été utilisés au cours de ce travail comprennent la Microscopie à Force Atomique (AFM) et la Microscopie Électronique à Balayage (MEB) afin de suivre de près les caractéristiques géométriques grâce à différents contrôles de processus. Le diamètre hydrodynamique des nanoparticules a été observé en utilisant la Diffusion dynamique de la lumière (DLS). La réponse optique des géométries leur comportement de couplage plasmonique ont été analysées à l'aide d'un spectrophotomètre UV/visible et d'un système optique d'extinction artisanal au laboratoire Lumière, nanomatériaux et nanotechnologies (L2N) de l'Université de technologie de Troyes, en France. Les mesures spectroscopiques ont utilisé un spectromètre Raman microscopique pour les mesures de la SERS et de la MEF. La microbalance à cristal de quartz (QCM) et la résonance plasmonique de surface (SPR) ont été utilisées pour l'analyse des interactions (bio) moléculaires avec les nanostructures **(Illustration A.6)**.

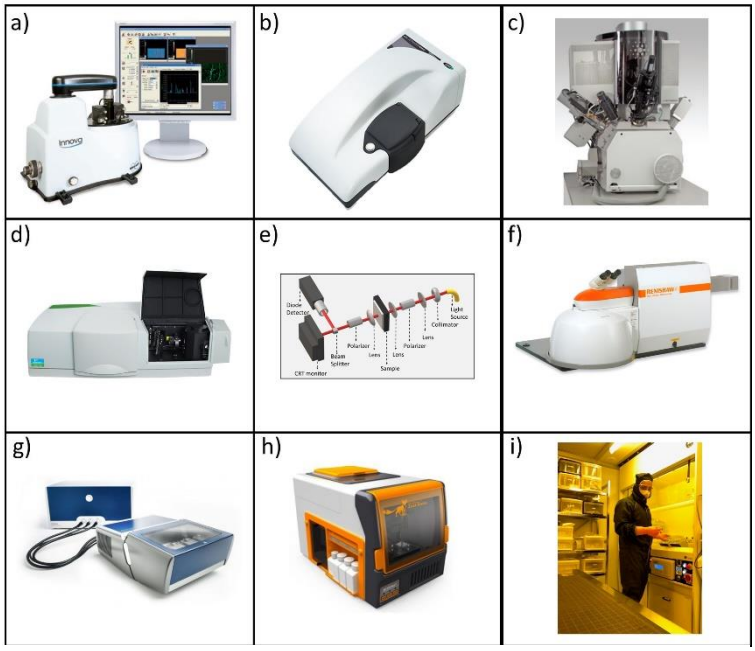

Illustration A.6. Outils de caractérisation utilisés pour analyser les topographies physiques : a) AFM, b) DLS, c) SEM) ; propriétés optiques : d) spectrophotomètre UV/visible, e) configuration de l'optique d'extinction, f) spectrophotomètre micro-Raman ; interactions bio-nano : g) QCM-D, h) SPR ; et i) L'auteur dans la chambre stérile lors du processus de nanofabrication.

Auto-assemblage moléculaire pour la nanolithographie à haute résolution : Cette section présente notre approche des nanoréseaux plasmoniques à haute résolution spatiale, qui repose sur l'auto-assemblage hiérarchique de copolymères amphiphiles diblocs en colloïdes mous, et leur organisation quasi périodique ultérieure lorsqu'ils sont déposés sur une surface plane.[243] Cette approche permet d'obtenir des modèles organiques bien définis sur la surface avec un contrôle nanométrique de la largeur, de la topographie et de la hauteur, réalisé par le contrôle des paramètres d'auto-assemblage moléculaire. En analysant l'impact des différents paramètres des procédés sur le résultat géométrique obtenu, il est possible de fournir des modèles hautement reproductibles et uniformes sur des plaquettes pleines, avec un rendement> 90 %.[245] Ces modèles sont matérialisés par des capteurs plasmoniques très sensibles basés sur la SERS, avec un contrôle des nano intervalles métalliques jusqu'à un niveau inférieur à 10 nm.

Modèles auto-assemblés : Les copolymères diblocs amphiphiles peuvent s'auto-assembler en micelles inverses lorsqu'ils sont dissous dans un solvant qui ne dissout sélectivement que le bloc apolaire du copolymère. Au cours du processus d'enduction par centrifugation, les micelles chargées de solvant en solution se déforment en surface pour prendre une forme ellipsoïdale, avec une fusion partielle de la couronne des micelles inverses adjacentes, ce qui donne un film organique globalement continu présentant topographie à contraste périodique avec un film ultrafin (<5 nm) en arrière-plan **(Illustration A.7)**. La forme du motif qui apparaît sur la surface peut être modifiée par étapes de <5 % de sa valeur moyenne, en contrôlant le taux d'évaporation ou la concentration des micelles en solution. Le taux d'évaporation peut être contrôlé en utilisant les vitesses de centrifugation ou d'immersion du revêtement.[245] Dans des conditions optimales de revêtement, des réseaux de micelles peuvent être produits avec un écart type de <10 % de leurs caractéristiques géométriques sur une plaquette complète.

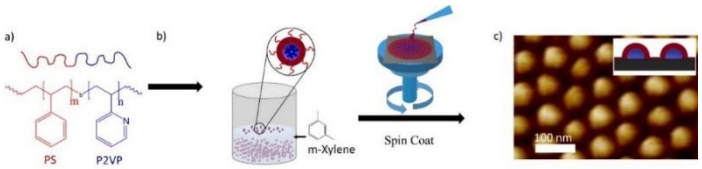

Illustration A.7 Représentation schématique de l'auto-assemblage du copolymère dibloc amphiphile en micelles inverses et de leur assemblage ultérieur pour former des réseaux bidimensionnels à la surface.

Nanoréseaux plasmoniques par transfert de motifs: La production de nanoréseaux plasmoniques à partir de modèles organiques repose sur des modes de transfert de motifs, par exemple la croissance, le dépôt ou la gravure guidés par un modèle, pour

définir des nanoréseaux de métaux nobles avec conservation du motif du gabarit original. Les méthodes de transfert de motifs offrent une grande liberté dans le choix de la géométrie des différentes composantes, ce qui permet de fabriquer des nanoréseaux plasmoniques de différents types, par exemple des réseaux de nanoparticules en clusters, des réseaux de nanopiliers, de nanobâtonnets ou de nanodisques.[316–318] Les paramètres de transfert du modèle permettent un contrôle indépendant du ratio taille, forme, aspect des caractéristiques et doivent être optimisés pour garantir qu'ils n'affectent pas l'agencement spatial, l'uniformité et la reproductibilité par rapport au modèle original. Dans le cadre de ce projet, des clusters de nanoparticules d'or et des réseaux de nanopiliers d'or ont été créés en utilisant l'auto-assemblage moléculaire de micelles de copolymères séquencés amphiphiles, comme indiqué précédemment.

Réseaux d'clusters de nanoparticules d'or (NCA) : Les NCA ont été obtenues sur des substrats sélectionnés qui ont été nettoyés par ultrasons dans de l'acétone, puis rincés à l'éthanol et au 2-propanol, avant d'être exposés pendant 3 minutes à du plasma d'oxygène dans la chambre de gravure par ions réactifs (Plasmatherm 790 RIE). Les substrats fraîchement nettoyés ont été immédiatement enduits par centrifugation de solutions de PS-b-PVP dans du m-xylène à 5 000 et 3 000 tr/min pour les modèles A et B, respectivement. Le modèle A a été revêtu d'une solution à 0,75 % (p/p) de PS - *b* -PVP avec un poids moléculaire de 81,5 kDa. Le modèle B a été revêtu d'une solution à 2 % (p/p) de PS - *b* -PVP avec un poids moléculaire de 443 kDa. La couche enduite a été soumise à une exposition contrôlée au plasma d'oxygène pendant 0 s pour le polymère A et 30 s pour le polymère B pour éviter une adsorption non spécifique et augmenter l'écart entre les nanoclusters. Ces puces enduites ont été immergées dans une solution de nanoparticules d'or stabilisées au citrate (pH 5,8) pendant 2 h, puis rincées à l'eau désionisée. Les nanoparticules d'or de

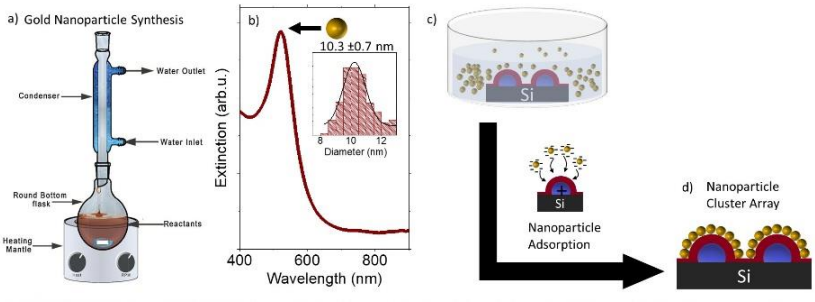

Illustration A. 8. a) Représentation schématique de la configuration utilisée pour la synthèse de Au np par voie chimique humide, b) Analyse statistique de la distribution de taille de Au np à partir d'images au SEM, c-d) Schéma de fabrication de réseaux de clusters de nanoparticules d'or par attraction électrostatique de Au np chargé négativement vers des modèles chargés positivement en surface.

10,3 nm ± 0,5 nm ont été préparées selon la méthode décrite précédemment **(Illustration A.8)**.[388] Les images AFM des modèles ont été mesurées en mode tapotement à l'aide de pointes AFM ultra nettes. L'ajustement gaussien à la hauteur et l'histogramme de périodicité ont été utilisés pour déterminer les écarts moyens et les écarts-types. Les fonctions d'analyse de particules intégrées dans le logiciel Nanoscope Analysis ont été utilisées à cette fin.

Réseaux de nanopiliers à revêtement d'or (NPA) : Les réseaux de piliers ont été préparés suivant un protocole décrit précédemment. La solution de revêtement a été préparée en utilisant du PS-b-PVP avec un poids moléculaire de 197 kDa dans un solvant organique de p-xylène (0,8 % p/p). Ces modèles organiques ont été enduits par centrifugation à 6000 tr/min sur une plaquette Si de 100 mm fraîchement nettoyée, constituée d'un film de SiO_2 de 25 nm. Le plasma gazeux C_4F_8/CH_4 transfère la forme du modèle dans la couche de SiO_2 sous-jacente. Le motif SiO_2 qui en résulte se comporte comme un motif hautement sélectif pour la gravure du Si en utilisant le plasma SF_6/C_4F_8 pour obtenir des nanopiliers de silicium **(Illustration A.9)**. La périodicité centre à centre de 105,8 nm (coefficient de variation inférieur à 10 % d'une puce à l'autre) des caractéristiques a été préservée à partir du modèle polymère puis confirmé par les images AFM et SEM du modèle et des réseaux de nanopiliers. Les séparations des bords entre les piliers enduits d'or ont été déterminées en soumettant les images SEM de l'Au-NPA à une analyse d'images à l'aide de ImageJ.[482] Les nanopiliers de silicium ont été enduits par pulvérisation cathodique à 10 tr/min en continu avec une couche adhésive de 5 nm ± 1 nm de chrome à 100 W (60 sccm) d'argon (Ar) sous une pression de 10^{-2} mbar pendant 14s ($0{,}36\ nm^{-1}$).

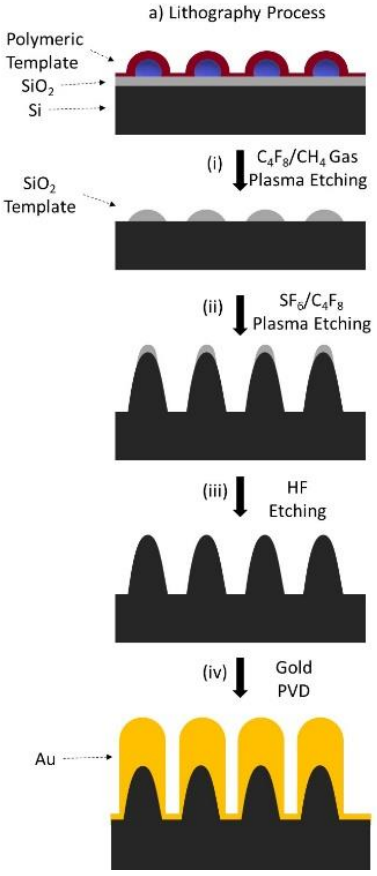

Illustration A.9. a) Procédé de nanofabrication pour la fabrication de réseaux de nanopiliers de silicium qui implique i) le transfert de motif d'un modèle organique mou vers un modèle inorganique dur, ii) une gravure au plasma sous le substrat de silicium pour obtenir des nanopiliers coniques de silicon, iii) l'élimination du masque résiduel de SiO_2, iv) une couche d'or appliquée par pulvérisation sur des nanopiliers de silicium.

L'épaisseur d'or souhaitée a été déposée dans des conditions similaires à un taux de 0,86 nm s^{-1} avec un écart type de 6 %.

Réseaux de clusters de nanoparticules avec points chauds EM conçus pour les essais biologiques quantitatifs

Dans le cadre de cette recherche, nous produisons des réseaux périodiques de cluster de nanoparticules d'or, présentant des points chauds aux intervalles EM à double échelle de longueur avec des intervalles dans le registre de distances inférieures à 10 nm. Les points chauds à double échelle de longueur offrent l'avantage d'une grande sensibilité aux petits (<1 nm) ainsi qu'aux grands (bio) analytes. On obtient des dosages plasmoniques quantitatifs de protéines basés sur la diffusion Raman exaltée en surface et la Fluorescence exaltée par le métal (MEF). La mesure précise de la densité de surface des protéines par QCM a permis de rationaliser les configurations de clusters de nanoparticules hautement sensibles, comme celles qui offraient des bio-analytes, pour mieux exploiter les points chauds EM.

Points chauds EM à double échelle de longueur : De par la nature de la formation, les NCA présentent des points chauds EM entre des nanoparticules au sein d'un cluster (ou, des points chauds interparticulaires), et entre les clusters adjacents (ou, des points chauds intercluster). Les NCA de deux dimensions différentes ont été optimisées pour l'étude actuelle, avec une différence uniquement dans la taille du cluster, tout en garantissant une distance de séparation fixe intercluster **(Figure A.10)**. Les deux NCA présentent des distances interparticulaires et intercluster équivalentes, la seule différence étant la taille (largeur et hauteur) des NCA, qui est plus grande pour NCA#B que pour NCA#A. En conséquence, NCA#A a une plus grande densité de caractéristiques que NCA#B. Les séparations à

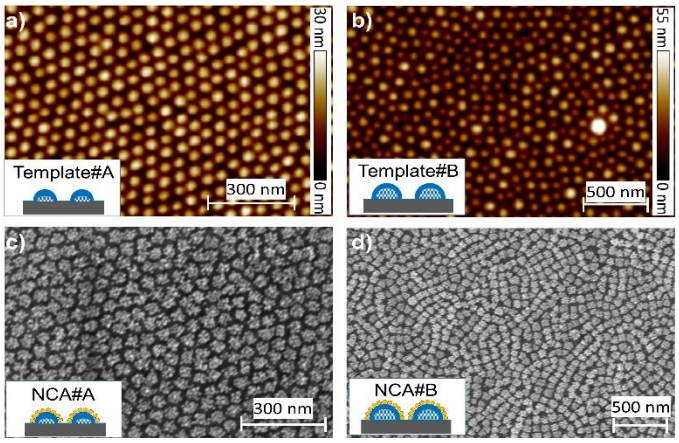

Illustration A.10. (a,b) Modèles avec une taille plus petite (modèle # A) et plus grande (modèle # B) utilisés pour définir (c, d) les réseaux d'clusters de nanoparticules d'or (NCA), NCA # A et NCA # B respectivement.

haute résolution interparticulaires et interclusters permettent d'espérer un fort couplage plasmonique entre les particules au sein des clusters et entre les clusters adjacents. Ceci est confirmé par l'apparition de pics de résonance plasmonique pour les NCA#A et #B, respectivement à ~648 nm et ~653 nm, tous deux ayant considérablement décalé vers le rouge par rapport à la résonance plasmonique à ~522 nm pour les nanoparticules d'or isolées.

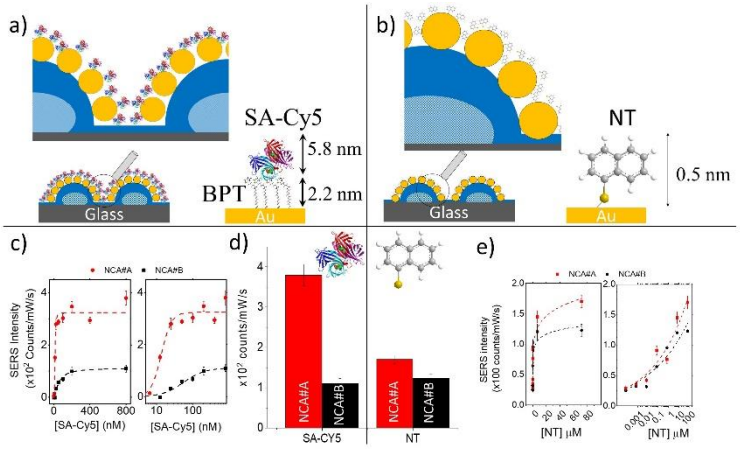

Illustration A.11 . (a, b) Schéma représentant un meilleur effet de levier de (a) SA-Cy5 sur les points chauds intercluster et (b) NT sur les points chauds interparticules et intercluster. Les dimensions moléculaires relatives sont indiquées. (c, e) Test SERS (c) SA-Cy5 et (e) 1 -NT montrant l'évolution des intensités caractéristiques des pics, respectivement à 583 cm^{-1} et 1371 cm^{-1}. (d) Intensités SERS correspondant aux densités saturées de SA-Cy5 et NT sur NCA#A NCA#B

Tests biologiques plasmoniques : Les performances des NCA pour les bioessais plasmoniques basés sur la diffusion Raman exaltée de surface **(Illustration A.11)** et la spectroscopie de fluorescence exaltée par le métal **(Illustration A.12)** pour la mesure quantitative des interactions biotine-streptavidine ont été étudiées. Les spectres SERS montrent une bonne correspondance avec les positions des pics de Cy5 rapportées dans la littérature. [399] L'intensité du pic caractéristique de Cy5 à 583 cm^{-1} a été suivie pour quantifier la dépendance spectrale de la SERS en fonction de la concentration de SA-Cy5. Le test SERS s'est avéré concluant et quantitatif, comme le révèle un excellent ajustement à l'isotherme d'adsorption de Langmuir-Hill. L'écart type des intensités obtenues sur plusieurs zones de la plaquette, à plusieurs millimètres carrés d'écart, a présenté une variabilité inférieure à 10 %. L'intensité du

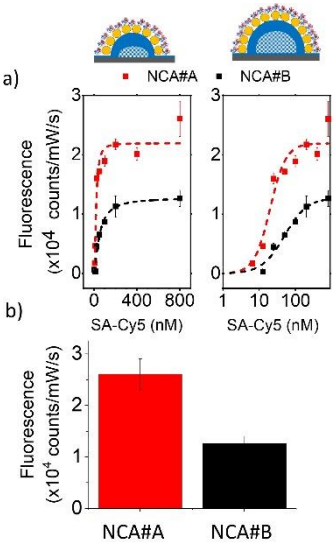

Illustration A.12. (a) Comparaison des tests de fluorescence de SA-Cy5 sur la NCA#A et la NCA#B obtenus avec une stimulation à 633 nm, présentés à l'échelle linéaire (à gauche) et logarithmique (à droite), équipés de l'isotherme de Langmuir-Hill. b) comparaison des intensités de fluorescence correspondant à une densité saturée de SA-Cy5 sur les deux NCA

signal observable a été obtenue jusqu'à 6,5 nM pour la NCA#A et 25 nM pour la NCA#B, révélant une sensibilité plus élevée de la NCA#A. La présence d'un champ EM fortement exalté, provenant des clusters sous-jacents de nanoparticules ainsi que de la couche d'espacement de la paire d'interaction biotine-streptavidine, offre une situation favorable pour expérimenter la fluorescence amplifiée par métal (MEF). L'évolution des intensités de fluorescence sous stimulation à 633 nm montre de fortes exaltation de la fluorescence sur les deux NCA. Une comparaison de l'évolution des intensités de signal avec la concentration de SA-Cy5 montre des intensités plus élevées pour NCA#A que pour NCA#B, comme observé dans les essais SERS.

Simulations numériques : Les profils EM et le taux d'absorbance des NCA ont été simulés numériquement à l'aide de calculs basés sur les différences finies dans le domaine temporel (FDTD). Le choix dela géométrie du modèle et les dimensions de las nanoparticule a été effectué à partir des mesures expérimentales de la AFM et du SEM. Les simulations en champ proche **(Illustration A.13)** confirment la présence de points chauds interparticulaires et intercluster avec une exaltation similaire dans les deux NCA.

Exploiter les points chauds EM intercluster : Les NCA ont deux types de points chauds EM, l'un à la jonction entre les nanoparticules au sein du cluster (points chauds interparticulaires), avec des dimensions <1 nm, et l'autre entre les clusters de nanoparticules (points chauds intercluster) avec des dimensions <10 nm. Compte tenu des dimensions du PEG thiol de la biotine (2,2 nm de long) et du SA-Cy5 (4,2 nm × 4.2 nm × 5,8 nm),[405] la longueur de la paire d'interaction devrait être d'environ 6,6 à 8 nm. Alors que les points chauds intercluster sont capables de s'adapter à l'interaction, les points chauds interparticulaires ne le peuvent pas. Il est donc raisonnable de penser que les molécules SA-Cy5 n'exploiteront les points chauds EM intercluster, comme indiqué dans l'**Illustration A.11**. Étant donné que les séparations intercluster sont maintenues identique entre les NCA, la dimension plus petite duNCA#A (diamètre de 38 ±5 nm) par rapport au NCA#B (diamètre de 86 ±5 nm) se manifeste par des valeurs inférieures pour la périodicité du réseau. La

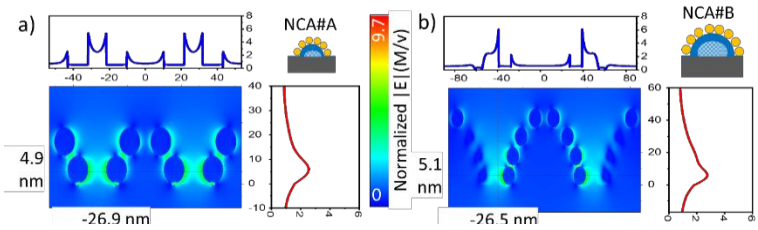

Illustration A. 13. (a, b) Profils de champs électromagnétiques simulés sur a) NCA#A et b) NCA#B avec une stimulation à 633 nm.

périodicité détermine directement la densité des caractéristiques et les jonctions binaires entre les caractéristiques. Ainsi, une taille réduite, dans le cas du NCA#A (diamètre~38 ±5 nm) se traduit par une plus grande densité de caractéristiques (densité~350/µm^2) par rapport au NCA#B (diamètre~86 ±5 nm, densité~100/µm^2). Cela se traduirait par un nombre plus élevé de points chauds intercluster dans le NCA#A que dans le NCA#B. Comme le SA-Cy5 ne peut exploiter que les points chauds intercluster, qui à leur tour se produisent en plus grand nombre dans le NCA#A, cela expliquerait la plus grande sensibilité du NCA#A.

Cependant, cette hypothèse ne peut être confirmée que si la concentration des molécules de protéine dans les deux NCA est connue. Pour la déterminer, les modèles A et B ont été enduits sur un capteur QCM, et les différentes étapes, y compris le dépôt des nanoparticules et le bioessai, ont été réalisées tout en surveillant les changements de masse mesurés par le QCM. La densité saturée des nanoparticules et des molécules SA-Cy5 à la fin du bioessai est représentée sur l'**illustration A.14a-b**. La densité de surface saturée des nanoparticules Au et SA-Cy5 s'avère plus élevée pour le NCA#B que pour le NCA#A. Les concentrations de SA-Cy5 devraient suivre la concentration de BPT liée à l'or par les interactions thiol-or.

Cependant, une estimation des zones de surface disponibles sur le NCA exclut la possibilité de tenir compte de la densité observée de protéines. Cela souligne fortement l'adsorption de SA-Cy5 également dans la matrice de polystyrène, entre les éléments. Une expérience témoin réalisée sur des capteurs QCM recouverts de polystyrène confirme l'adsorption de la biotine et de la streptavidine avec des densités comparables à celles observées sur la surface de l'or. Nous n'avons pas trouvé de travaux antérieurs dans la littérature expliquant la forte adsorption de la biotine sur le polystyrène, dont l'origine devra être étudiée par la suite dans le cadre d'une autre étude. L'adsorption sur le PS confirme la

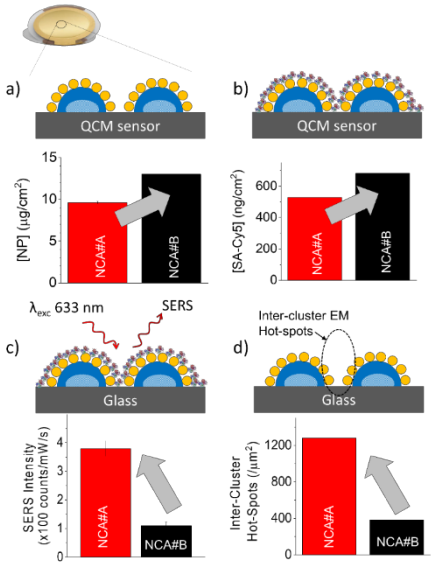

Illustration A.14. Les densités de surface saturées de (a) nanoparticules d'Au et (b) SA-Cy5, liées à des NCA# Biotinylés montrent des valeurs plus élevées pour les NCA#B que dans pour les NCA#A. (c) Des intensités de SERS plus élevées sont observées pour le NCA#A, conformément aux tendances pour d) la densité des points chauds EM intercluster.

distribution de SA-Cy5 dans l'espace entre les NCA, coïncidant ainsi avec les points chauds EM intercluster.

L'observation de densités plus faibles de nanoparticules d'Au, ainsi que d'une concentration réduite de la surface de l'analyte dans le cas du NCA#A, exclut que les concentrations de l'analyte jouent un rôle dans sa plus grande sensibilité.. Cela confirme bien l'hypothèse selon laquelle le NCA#A tire sa sensibilité plus élevée du plus grand nombre de points chauds intercluster exploitables par le SA-Cy5. Afin de corroborer les arguments ci-dessus, on a comparé la sensibilité SERS des NCA dans la détection du 1-naphthalenethiol (NT), qui est une molécule sonde beaucoup plus petite. La dimension d'une molécule de NT n'est que de 0,3 nm, contrairement à SA-Cy5, et pourrait occuper non seulement les points chauds EM intercluster, mais également les points chauds interparticulaires. La comparaison des intensités SERS dans les concentrations de NT pour le NCA#A et le NCA#B montre une différence de sensibilité très réduite pour les deux. Cela correspond bien au résultat attendu, en partant de l'hypothèse que les molécules NT exploiteront à la fois les points chauds interparticulaires et interclusters. La raison des intensités légèrement plus élevées de la SERS pour le NCA#A que pour le NCA#B, malgré la densité plus élevée de nanoparticules dans le NCA#B, reste pour l'instant incertaine. Toutefois, la plus grande sensibilité du NCA#A, indépendamment des densités de surface réduites de l'analyte ainsi que la corrélation entre la sensibilité du test et la dimension de l'analyte, mettent fortement en évidence la possibilité de concevoir des réseaux plasmoniques en tenant compte de la distribution de l'analyte par rapport aux points chauds EM.

Réseaux d'clusters de nanoparticules avec points chauds EM sur des surfaces métalliques

Dans ce cas, les champs EM dépendent fortement de la présence de substrat d'or et de la taille des clusters de nanoparticules, entraînant des configurations qui présentent une sensibilité picomolaire dans la détection des protéines. Les deux types de NCA, utilisés dans la section précédente sur des substrats de verre, ont été fabriqués sur un mince film d'or de 100 nm déposé sur des substrats de quartz. La AFM et le SEM ont révélé que les caractéristiques géométriques des modèles A et B, et celles des NCA, qui en découlent,

présentent une variation inférieure à 5 % entre les substrats. L'obtention d'un NCA géométriquement équivalent sur des substrats de verre (NCA@Glass) et d'or (NCA@Au) garantit que l'enquête attribue les différences observées uniquement à l'effet du substrat, indépendamment de la géométrie des NCA **(Illustration A.15)**.

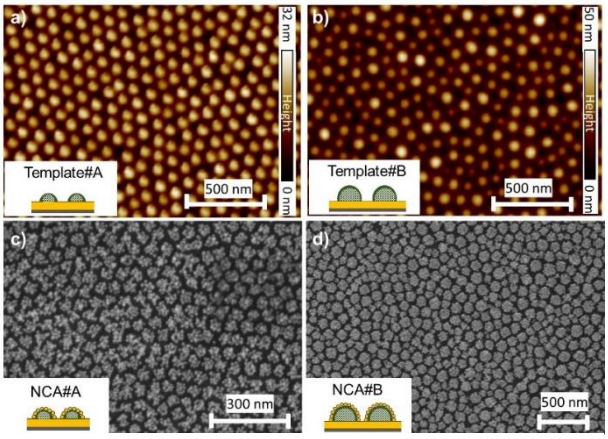

Illustration A.15. (a,b) Modèles à l'échelle nanométrique, a) Modèle#A et b) Modèle#B qui dirigent la formation de Réseaux d'clusters de nanoparticules (NCA) c) NCA#A et d) NCA#B. Les encadrés montrent les illustrations de la section transversale des modèles et des NCA.

Propriétés optiques : Les propriétés optiques des substrats NCA@Au ont été étudiées via leurs spectres de réflectance, qui affichent une baisse à des longueurs d'onde correspondant respectivement à 647 nm pour NCA#A et 669 nm pour NCA#B. Les spectres d'absorbance des substrats NCA@Glass montrent respectivement un pic d'absorbance de 646 et 648 nm. La position du pic de résonance plasmonique, tirant fortement vers le rouge pour les NCA, peut être en partie attribuée à un fort couplage plasmonique interparticulaire et intercluster dans les NCA.

Simulations numériques: Des simulations numériques basées sur les différences finies dans le domaine temporel (FDTD) ont été effectuées sur les NCA modélisées sous forme géométrique grâce à des valeurs basées sur des observations expérimentales. Des simulations numériques sur le NCA@Au révèlent des exaltations du champ EM dans les espaces interparticulaires et les espaces intercluster pour les NCA#A et NCA#B **(Illustration A.16)**. Cependant, les profils de champ EM dans l'espace intercluster étaient beaucoup plus prononcés dans le NCA#B que dans le NCA#A. Une comparaison des profils de champs EM obtenus sur des simulations numériques de NCA@Glass dévoile des observations intéressantes. Dans les deux NCA, les exaltations du champ EM se

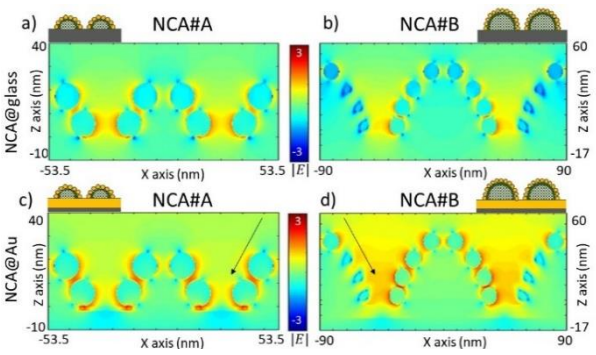

Illustration A.16. FDTD simulation des profils de champ électromagnétique de (a,c) NCA#A et (b,d) NCA#B par comparaison à (a,b) l'or et (c,d) aux substrats de verre.

sont avérées plus élevées dans le cas du NCA@Au que du NCA@Glass. Contrairement aux NCA@Au, dans le cas du NCA@Glass, les NCA#A et #B présentent des exaltations EM intercluster similaires.

Essais plasmoniques: La sensibilité du NCA@gold à la détection moléculaire par les diffusions Raman exaltées en surface a été testée avec une stimulation de 633 nm et deux molécules différentes. L'une des molécules est le 1-naphtalènethiol, choisie pour sa très petite taille <1 nm et de la facilité avec laquelle une couche SAM conforme peut être obtenue sur la surface de l'or. La très petite taille du NT lui permettrait d'accéder aux points chauds EM interparticulaires et intercluster dans le NCA. La deuxième molécule testée est une protéine, à savoir la streptavidine marquée au Cy5 (SA-Cy5), interagissant avec la surface biotinylée du NCA. Les interactions biotine-streptavidine ont été utilisées comme modèle d'interaction en raison de sa forte affinité. Les dimensions de la paire BPT (~ 2,2 nm) et SA-Cy5 (5,8 nm) la rendent trop grande pour se loger dans des points chauds interparticulaires, mais favorisent sa présence dans les intervalles intercluster.

La sensibilité des NCA#A et #B à la détection des NT a été testée en suivant l'intensité des fréquences vibratoires Raman caractéristiques de NT à 1372 cm^{-1} en fonction de leur concentration entre 0,07 nM — 71,5 µM. Les essais de SA-Cy5 ont été réalisés par NCA biotinylé, en suivant l'intensité de la fréquence Raman caractéristique de Cy5 à 583 cm^{-1} entre 0,1 - 800 nM **(Illustration A.17)**.[399] Les tests ont été effectués dans des conditions identiques pour les échantillons de NCA@gold et NCA@glass. Les NCA@gold présentent des intensités de signal supérieures à celles de leurs équivalents NCA@glass, au moins une fois supérieurs dans les tests NT et deux fois dans le cas des essais SA-Cy5. La comparaison des NCA#A et #B révèle également une différence significative entre les échantillons de NCA@gold et NCA@glass. Dans le cas du NCA@gold, le NCA#B montre une sensibilité plus

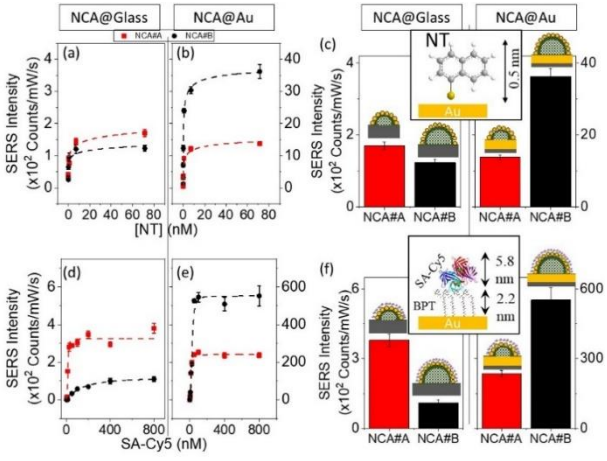

Illustration A.17 Essais de (a-c) NT sur NCA et (d-f) SA-Cy5 sur NCA biotinylé, comparés à NCA#A et NCA#B sur des substrats d'or et de verre respectivement. L'illustration de la structure moléculaire et des dimensions pour NT et SA-Cy5 est présentée dans l'encadré.

élevée que le NCA#A pour le NT et le SA-Cy5. Toutefois, les échantillons de NCA@glass présentent une tendance inverse, puisque dans tous les cas de figure le NCA#A a une sensibilité plus élevée.

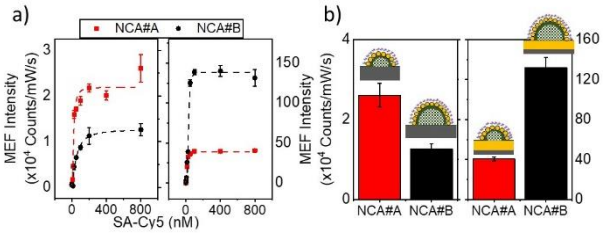

Illustration A.18. Évolution spectrale du MEF avec concentration de SA-Cy5 sur des NCA biotinylés pour (a) tracer le pic d'intensité et (b) comparer les NCA#A et NCA#B saturés sur des substrats d'or et de verre.

La combinaison du SA-Cy5 et du NCA biotinylé peut être contrôlée par le signal de fluorescence du Cy5. Les essais de fluorescence montrent une forte exaltation des signaux de fluorescence pour le NCA@gold, deux fois supérieure à ceux du NCA@glass. Pour les fluophores, la fluorescence exaltée par métal (MEF) devrait se produire à une distance optimale des surfaces métalliques nanostructurées **(Illustration A.18)**. La présence de l'interaction biologique peut servir à éloigner le fluorophore de la surface et ainsi éviter l'extinction de la fluorescence due au contact direct entre le fluorophore et le métal. Comme observé avec la SERS, les amplifications de la MEF se sont avérées plus élevées pour les grands clusters, dans le cas des échantillons NCA@gold, et les petits clusters pour les échantillons NCA@glass.

La comparaison des tendances de sensibilité du NCA@glass et du NCA@gold observées dans les essais SERS et MEF est bien conforme aux attentes définies par les profils de champ EM obtenus à partir de simulations numériques. Le NCA#B@gold présente à la fois de plus fortes exaltations EM inter-cluster et un plus grand nombre de points chauds EM interparticulaires que les échantillons du NCA#A@gold. Cela permet à la fois d'améliorer la sensibilité du NT, qui peut occuper des points chauds interparticulaires et interclusters, et du SA-Cy5, qui peut principalement exploiter les points chauds inter-cluster. Dans le cas des échantillons du NCA@glass, les exaltations de champ EM se sont avérées similaires pour le NCA#A et #B, même si le NCA#A a trois fois plus de points chauds inter-cluster que le NCA#B. Cela est principalement dû à une plus grande densité de caractéristiques dans le NCA#A que dans le NCA#B, ce qui augmente le nombre de points chauds inter-cluster. Étant donné que le SA-Cy5 pourrait efficacement et uniquement exploiter les points chauds inter-cluster, la plus grande densité de nombre de points chauds inter-cluster dans le NCA#A le rend plus sensible à la détection des protéines. Il est possible de supposer que ces densités jouent un rôle clé, étant donné l'absence de

différence significative dans les exaltations EM inter-cluster entre les deux groupes sur les substrats en verre. Cela explique également la différence limitée entre le NCA#A et #B dans la sensibilité à la détection de NT sur du verre. Le NT peut exploiter peut également exploiter les points chauds interparticulaires, plus nombreux dans le NCA#B. La limite de détection (LOD) du NCA@Au, soit les plus faibles concentrations moléculaires permettant une détection, s'est avérée être au moins une fois inférieure aux essais les plus concluants dans le cas des substrats du NCA@glass. Les substrats du NCA@gold ont une LOD de 400 pM dans le cas de SA-cy5 et de 600 pM dans le cas de NT pour la détection basée sur la SERS. Les LOD des essais de MEF étaient similaires à ceux des essais de la SERS.

Détection piézoélectrique et spectroscopique de biomolécules dans leur milieu naturel

Un capteur QCM couvert de NCA a été utilisé pour effectuer des bioessais hybrides QCM-MEF basés sur les interactions streptavidine-biotine. Les mesures par QCM ont été effectuées à l'aide d'une cellule de mesure permettant l'interrogation optique au travers d'une plaque transparente en saphir optique (7,1 mm x 13,9 mm) **(Illustration A.19)**. Les capteurs QCM couverts de NCA ont été enrobés de monocouches auto-assemblées de biotine-PEG-thiol pour définir les couches de récepteur allant servir à l'interaction avec la streptavidine. La surface a été traitée avec de fortes concentrations de BSA afin de bloquer toute zone de liaison non spécifique dans la couche de BPT SAM. Dans l'étape suivante, le capteur QCM avec la couche de BPT est exposé à différentes concentrations de streptavidine. La streptavidine est marquée avec un colorant Cy5 pour

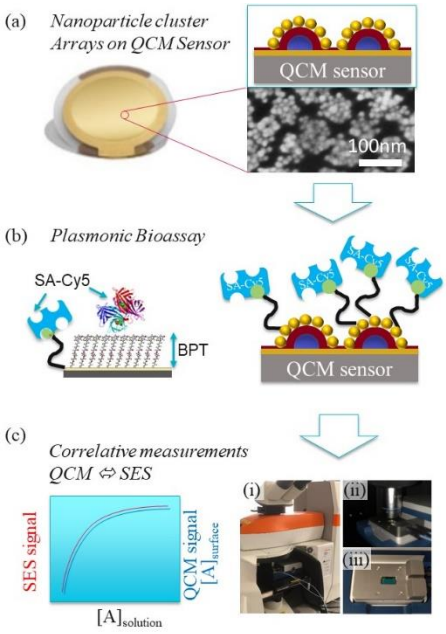

Illustration A. 19. (a) Réseaux plasmoniques composés de réseaux d'clusters de nanoparticules d'or fabriqués sur le capteur QCM. L'image de la plaquette du capteur QCM à 5 MHz et les mesures de la vue de dessus par SEM sont présentées avec une illustration de la coupe transversale ; (b) Configuration de la structure de bio-interaction utilisée pour les bioessais plasmoniques basés sur des réseaux d'clusters de nanoparticules fonctionnalisées au PEG thiol de biotine (BPT) interagissant avec le SA-Cy5 ; (c) (à gauche) la détection corrélative du QCM-SES, (à droite) (i) le capteur QCM placé sous l'objectif d'un microscope confocal ; (ii, iii) gros plan du module microfluidique du QCM avec fenêtre optique permettant un accès optique pendant les mesures du QCM.

permettre la détection fluorimétrique par MEF. Le capteur QCM a séquentiellement reçu une injection de streptavidine-Cy5 (SA-Cy5) avec une concentration progressivement croissante dans une fourchette de 1,5 à 400 nM. Pour chaque concentration, l'évolution de la densité de surface de SA-Cy5 a été suivie en temps réel à l'aide du capteur QCM **(Illustration A.20a)**. Lors de la saturation de la réponse en fréquence, le capteur est traité au PBS pour éliminer la solution de SA-Cy5 et toute trace de SA-Cy5 non fixée à la surface avant d'effectuer les mesures de fluorescence. Puis, la séquence est répétée avec la concentration suivante plus élevée de SA-Cy5. Les spectres de fluorescence ont été obtenus sans rupture par le capteur QCM, le tampon étant en place aux temps correspondants à la réponse saturée des isothermes à chaque concentration de solution. Comme escompté, les spectres de fluorescence montrent une augmentation progressive des intensités avec une augmentation des concentrations de SA-Cy5 **(Illustration A.20b).** La concordance de la longueur d'onde d'excitation (633 nm), du pic d'absorbance de Cy5 (650 nm) et de la résonance plasmonique des clusters de nanoparticules, [317] offre des conditions favorables pour augmenter les intensités de la MEF. [450,451]

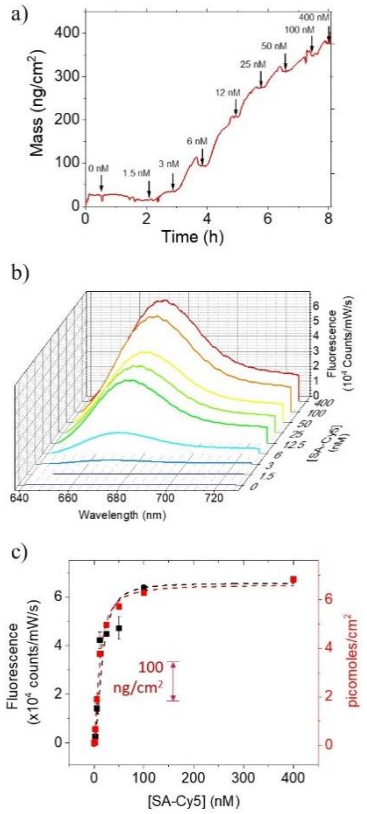

Illustration A.20. (a) Évolution de la densité de masse observée dans la MQC en fonction de l'injection séquentielle de concentrations croissantes de SA-Cy5 sur des réseaux d'clusters de nanoparticules biotinylés. Les valeurs de concentration de la solution sont indiquées par la réaction de saturation des isothermes respectives ; (b) évolution du spectre de fluorescence en fonction de la concentration de SA-Cy5 ; (c) tracé de la corrélation entre les essais de fluorescence (noir) et de QCM (rouge), l'ajustement à la fonction de Langmuir-Hill étant représenté par des lignes en pointillés. La flèche verticale du bloc indique les densités de surface équivalentes de SA-Cy5 telles que mesurées dans l'essai QCM au point (c).

Sensibilités relatives du QCM par rapport à la MEF: Les essais MEF ont été réalisés en utilisant des concentrations de streptavidine jusqu'à 1,5 nM. Les limites de détection (LOD) les plus basses pour les essais MEF peuvent être estimées à 800 pM, pour la plus faible concentration, en tenant compte de la limite de l'essai témoin et de l'écart type d'intensité de l'essai témoin. [389] La densité de masse équivalente correspondant à une concentration à 800 pM de la solution peut être extrapolée à partir de l'ajustement de Langmuir-Hill, qui équivaudrait

à une réponse du QCM d'environ 0,13 pmol/cm ^{2}, soit 7,9 ng/cm^2 ou ~780 molécules/µm^2. Compte tenu de l'empreinte de 1,55 µm^2 (taille du spot laser sous objectif 50x avec NA de 0,55 pour une excitation de 633 nm) cela correspondrait à un signal provenant d'environ 1209 molécules. La sensibilité à la masse du capteur QCM avec cristal de 5 MHz sous liquide est d'environ 1,8 ng/cm^2, ce qui n'est toutefois pas toujours respecté lors de mesures pratiques dans un liquide. [455] Dans les conditions de mesure, une LOD de ~4,6 ng/cm^2 est obtenue en prenant en compte une valeur correspondant à trois fois l'écart type de la réponse sous tampon. Cette masse volumique correspond à 6,4 x 10^{10} molécules de SA-Cy5 dans une empreinte du QCM de 1,4 cm^2. Bien que les limites de détection les plus basses de la MEF soient proches de celles du QCM, les signaux de la MEF sont obtenus à partir de la concentration moléculaire absolue sur la surface qui est huit fois inférieure à celle du QCM.

Réseaux de nanopiliers - Nanostructures à fort ratio d'aspect

Dans cette partie, nous démontrons l'impact manifeste de la dimension moléculaire des analytes sur celle des points chauds EM dans la capacité à tirer parti des exaltations EM aux points chauds interpiliers pour les essais de SERS et MEF. Il est démontré que le choix de la géométrie et de la configuration de l'essai permet d'obtenir des sensibilités analytiques allant jusqu'à une concentration picomolaire pour les petites et plus grandes analytes aux points chauds EM.

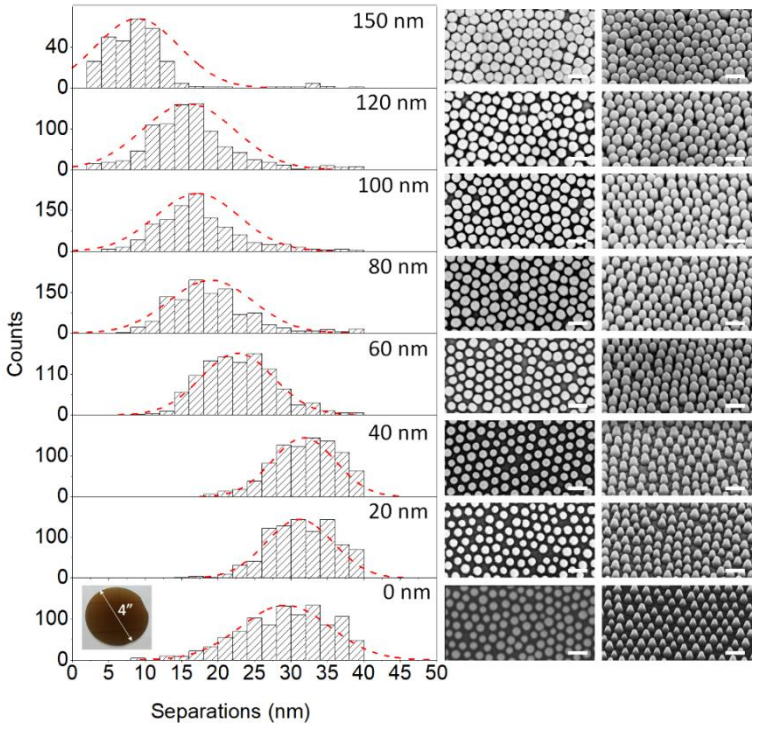

Illustration A.21. Histogrammes des distances entre les piliers en fonction de l'épaisseur des films d'or pulvérisés, et les images SEM des réseaux de nanopiliers acquis, vue de haut et inclinée (inclinaison de 30°). Les barres de mesure indiquent 200 nm. L'image des réseaux de nanopiliers uniformes de 4" sur des plaquettes de 4"Si est présentée dans l'encadré.

Nano-conception des espaces interpiliers : Des

nanopiliers coniques de 108 nm ± 5 nm de hauteur, 77,5 nm ± 9,8 nm de diamètre et avec une séparation bord à bord de 30,6 nm ± 7,3 nm ont été obtenus. Une tranche de silicium de 100 mm avec des nanopiliers de silicium a été découpée en plaquettes de 1x1cm pour une utilisation ultérieure. Le silicium NPA est ensuite enduit par pulvérisation d'une couche adhésive de chrome puis d'or (Au) avec une épaisseur allant de 20 à 150 nm pour obtenir des réseaux ordonnés de nanopiliers Au (Au-NPA) **(Illustration A.21)**. Les mesures en coupe transversale au SEM montrent dans tous les cas un revêtement conforme d'or sur les nanopiliers de silicium, ce qui entraîne une augmentation systématique de la hauteur et du diamètre, et une diminution des séparations interpiliers dans l'Au-NPA. On observe une croissance asymétrique et par étapes de l'or, avec d'abord une augmentation de la hauteur des éléments suivie d'un accroissement du diamètre, respectivement de ~1,0 nm et ~0,2 nm pour chaque nanomètre de gain de diamètre pour l'or pulvérisé **(Illustration A.22)**. Jusqu'à une épaisseur de 40 nm d'or pulvérisé, le diamètre ne change pas et par conséquent les séparations interpiliers restent similaires. Cela peut être dû aux piliers de silicium coniques qui évoluent en Au-NPA avec une paroi latérale cylindrique suite à une plus grande épaisseur d'Au. Pour une épaisseur supérieure à 40 nm, la séparation Au-NPA a systématiquement diminué par étapes de ~0,2 nm par nanomètre d'or pulvérisé, avec des valeurs comprises entre 30,6 nm et 8,4 nm **(Illustration A.22d)**.

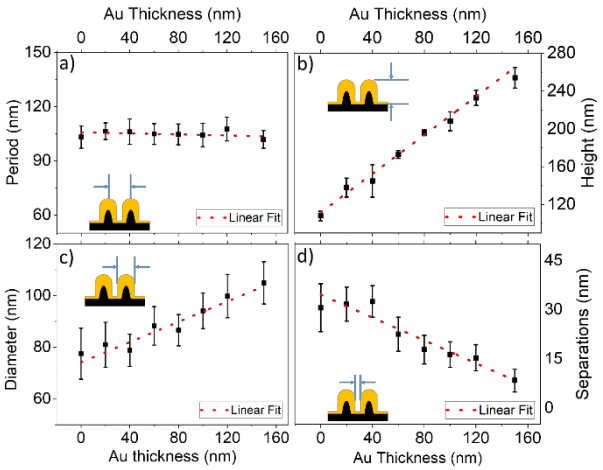

Illustration A.22 Schéma de l'évolution géométrique des nanopiliers d'or a) Période, b) Rayon des nanopiliers, c) Séparations bord à bord entre les nanopiliers suivant l'épaisseur d'Au déposée par pulvérisation cathodique d) Schéma des différents paramètres géométriques pris en compte.

Points chauds EM interpiliers : La réponse optique des nanopiliers métalliques a été étudiée via des expériences de rétroaction avec simulations numériques. Il a été constaté que les Au-NPAs réduisent davantage la réflexion que leurs équivalents planaires, et ce pour toutes les épaisseurs. La structure des nanopiliers est composée d'espaces interpiliers inférieurs à la longueur d'onde incidente. Par conséquent, les réseaux de nanopiliers sont une structure de sous-longueurs d'onde qui fournit un gradient d'indice de réfraction

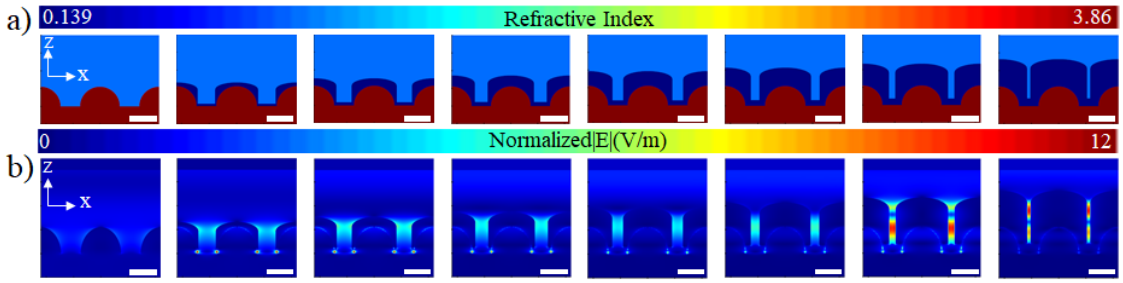

Illustration A.23. (a) Profil d'indice de réfraction dans la section transversale x-z de la structure des nanopiliers, (b) Profil de champ électrique dans la section transversale x-z de la structure des nanopilliers avec une longueur d'onde incidente de 633 nm.

efficace entre l'air et le substrat, ce qui réduit la réflexion de la lumière incidente de la surface des nanopiliers et améliore la transmission de la lumière à travers l'interface.

Simulations numériques : La méthode FDTD (Finite-Difference Time-Domain, ou de la différence finie dans le domaine temporel) tridimensionnelle (3D) est utilisée pour simuler la distribution du champ électrique pour des réseaux de nanopiliers hexagonaux d'épaisseurs différentes. Les exaltation de champ électrique sont maximisées lorsque le film d'or a une épaisseur de 150 nm, et correspond à une séparation moyenne de 6,5 nm. L'Au-NPA présente un double avantage — Premièrement, les nanocônes de silicium réduisent la réflexion de la lumière incidente en évaluant le décalage d'indice de réfraction entre l'air et le silicium. Deuxièmement, l'Au-NPA fournit une exaltation élevée de la SERS dans les espaces interpiliers en raison du couplage des *résonances plasmoniques de surface localisées* et de la *capture efficace de la lumière* dans les espaces interpiliers grâce à l'effet antireflet des piliers en silicium. La distribution simulée du champ électrique sur l'**Illustration 23** s'aligne avec les mesures optiques expérimentales et met en évidence la conception réussie de géométries de points chauds EM interpiliers en se basant sur les réseaux de nanopiliers d'or.

Dépendance à la taille moléculaire : Le NPA a par la suite été soumis à des examens portant sur l'évolution de l'intensité du signal SERS en fonction de la séparation de deux molécules différentes dont les dimensions moléculaires étaient distantes d'un ordre de grandeur, à savoir. une petite molécule organique et une autre, une protéine. Une excitation de 633 nm a été enregistrée en utilisant un objectif 50x avec une ouverture numérique de 0,55 pour les spectres SERS. Le 1-naphtalène thiol (NT) a été utilisé comme petite sonde moléculaire, surtout en raison de ses caractéristiques spectroscopiques bien définies, de sa taille sous-nanométrique et de sa capacité à former des monocouches auto-

assemblées sur la surface de l'or. L'intensité du signal du mode étiré de la plaque de NT à 1377 cm^{-1} a été suivie pour quantifier les exaltations SERS en fonction des géométries Au-NPA et des concentrations moléculaires. Des recherches avec une molécule plus grande ont été menées avec la streptavidine, une protéine tétramère avec un poids moléculaire de 55 kDa, et une dimension de 4,2 nm x 4,2 nm x 5,8 nm.[405] Pour détecter la streptavidine, la surface du NPA a été immobilisée avec de la biotine-PEG-thiol (BPT), avec des groupes de tête de biotine se liant dans la solution à la streptavidine (SA). L'étude a utilisée de la streptavidine conjuguée à un colorant Cy5 (SA-Cy5) pour employer le Cy5 comme rapporteur Raman et de fluorescence et suivre l'impact de la géométrie Au-NPA et des concentrations moléculaires sur la surface. Les intensités SERS du pic Raman caractéristique de Cy5 à 583 cm^{-1} ont été suivies pour déterminer l'impact de la géométrie Au-NPA et les concentrations de surface. La biotinylation de la surface a été suivie d'une concentration élevée de BSA pour bloquer les zones de liaison non spécifiques, puis d'une exposition à la streptavidine à différentes concentrations. L'interaction biotine-streptavidine dans des conditions similaires a été réalisée à même la surface de l'or et contrôlée grâce à une microbalance à quartz (QCM). Cela valide la résistance aux protéines du BPT, puisque l'essai a obtenu le résultat attendu.

L'impact des formes Au-NPA, en particulier des points chauds EM interpiliers sur l'évolution de l'intensité SERS de NT et SA-Cy5 a été étudié à des densités de surface saturées de NT et SA-Cy5 obtenues respectivement à 1µM de solution d'éthanol et 400nM de solution dans le PBS. Dans ces conditions, les concentrations moléculaires sont suffisamment importantes dans la solution pour assurer une couverture complète sur les surfaces. L'utilisation d'une densité de surface saturée est essentielle pour garantir que les modifications de l'intensité du signal SERS soient entièrement attribuables à la forme Au-NPA. Comme le confirment les simulations numériques, l'Au-NPA présente des points chauds d'intervalle EM au niveau des espaces interpiliers avec des intervalles variant de 30,6 nm à 8,4 nm. Étant donné les dimensions moléculaires de NT ($d_{NT} \sim 0,5$ nm) et BPT — SA-Cy5 ($d_{BPT} + d_{SA\text{-}Cy5} \sim 7,7$ nm), il faut s'attendre à ce que NT puisse accéder aux points chauds EM interpiliers. Quoi qu'il en soit, le SA-Cy5 ne pourrait accéder aux points chauds EM avec des intervalles inférieurs aux dimensions d'interaction.

La réponse en intensité SERS de NT et SA-Cy5 en fonction des séparations interpiliers est indiquée dans l'**illustration A.24**. Les intensités SERS pour les deux molécules étaient adaptées aux séparations minimales et maximales pour uniquement suivre l'évolution de la réponse en fonction de la séparation. Les séparations interpiliers ont été exprimées en unités de dimensions moléculaires respectives, ainsi, les séparations expérimentales Au-NPA pourraient être représentées comme 4,9 - 0,5 unité de SA-Cy5 ou 65,2 - 14 unités de NT. **(Illustration A.24a)** Dans le cas de la détection SA-Cy5, les espaces interpiliers prennent en compte la réduction de l'intervalle due à la monocouche auto-assemblée et pré-adsorbée de BPT (d_{BPT} ~ 2,2 nm), ce qui réduit encore la séparation de 4,4 nm. La

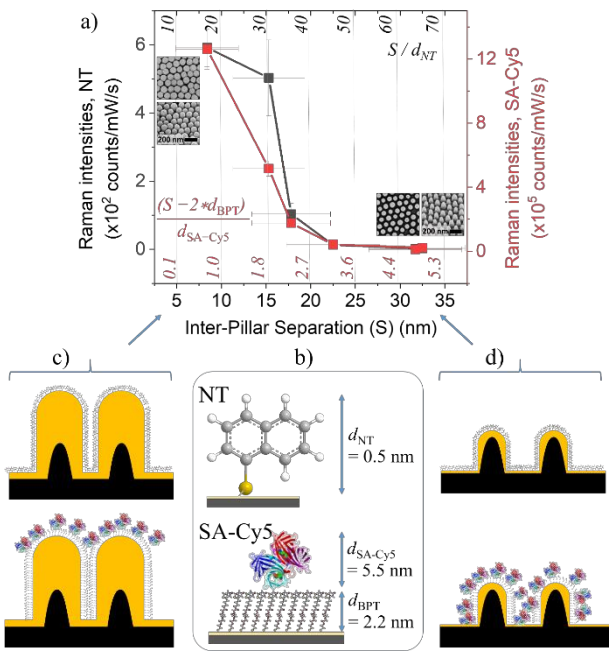

Illustration A.24. Comparaison de la dépendance du signal SERS sur la séparation interpiliers dans Au-NPA pour le NT (courbe noire) et SA-Cy5 (courbe rouge). Les espaces interpiliers sont indiqués dans les unités de dimensions d'interaction NT (d_{NT}) et SA-Cy5 (d_{SA-Cy5}). Les images du SEM représentant les vues de dessus et inclinée de Au-NPA aux séparations les plus faibles et les plus importantes servent de référence. (b) Schéma des dimensions relatives de la paire NT et (SA-Cy5) — BPT (c, d) et de leur répartition attendue sur Au-NPA avec (c) des séparations faibles et (d) des séparations importantes.

réponse suivant la diminution des écarts interpiliers montre une augmentation significative des intensités de signal en deçà de séparations de 15,9 nm pour NT et SA-Cy5. La montée des intensités du signal SERS jusqu'à l'intensité maximale est plus forte dans le cas de NT que de SA-Cy5. **(Illustration A.24a)** La réponse du NT continue d'augmenter, mais est moins accentuée entre 16,3 nm et 8,4 nm, ce qui semble indiquer la saturation. La saturation apparente peut être liée à la fusion partielle de certaines des caractéristiques à 150 nm d'épaisseur dans l'écart type des périodicités des piliers, comme le montrent ces images obtenues au microscope électronique. Malgré les faibles écarts-types de périodicités des

réseaux, cibler des écarts interpiliers comme les écarts-types risquerait de combler les intervalles minimes d'une série de piliers. La fusion partielle réduit les densités des caractéristiques de 120 µ m^{-2} à 40 $\mu m^{-2,}$ faisant passer la densité des espaces interpiliers de ~491 µ m^{-2} à 161 μm^{-2}, soit une réduction de près de 67 % de la densité des points chauds. Les espaces interpiliers restants sont plus faibles, ce qui entraîne des exaltations EM plus importantes, et expliquerait l'augmentation continue des intensités de signal observées. Contrairement au cas de NT, les intensités avec SA-Cy5 ont été observées pour augmenter moins fortement à des séparations de piliers inférieures à 15 nm, ce qui revient en d'autres termes à des intervalles de dimensions deux fois inférieures à celles de SA-Cy5. L'augmentation progressive des intensités de signal SA-Cy5, par rapport à celle de NT, pourrait résulter de l'impossibilité à exploiter les points chauds EM interpiliers à cause de l'encombrement stérique empêchant de pénétrer dans les intervalles. Lorsque les espaces interpiliers se réduisent encore, atteignant 8,4 nm, les contraintes spatiales excluent la possibilité de tout SA-Cy5 aux points chauds inter-piliers, car les intervalles sont alors dans l'incapacité d'accueillir la molécule. Cela favorise une transition vers la SA-Cy5 occupant entièrement le sommet de l'Au-NPA avec la possibilité de se développer à la mesure des exaltations EM dans des zones plus proches des points chauds EM. Si les arguments s'avéraient justes, le NT tirerait le meilleur parti de sa co-localisation avec les points chauds EM interpiliers, et ce jusqu'aux plus petites intervalles, et par conséquent aurait une sensibilité analytique plus élevée que SA-Cy5. En comparaison, le SA-Cy5, incapable de pénétrer dans les intervalles, ne pourrait pas exploiter les points chauds EM les plus performants, contribuant à la détection d'une sensibilité limitée. Afin de confirmer cette hypothèse, une évaluation de l'Au-NPA aux séparations les plus réduites (désormais nommé A-NPA_150) a été effectuée pour ses performances dans les essais quantitatifs de NT et SA-Cy5. **(Illustration A.25)**

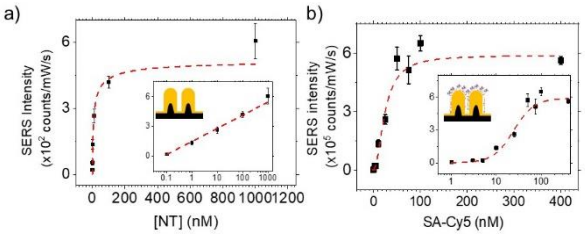

Illustration A.25. Comparaison des tests SERS de (a,c) NT et (b,d) SA-CY5 sur AU-NPA_150 biotinylé, montrant l'évolution spectrale Raman (a,b) et la courbe d'intensité du pic caractéristique de (c) NT (à 1377 cm-1) et (d) SA-Cy5 (à 583 cm-1) en fonction de la concentration. Les lignes en pointillés montrent les ajustements de Hill-Langmuir. Les ajustements montrent la réaction en fonction de la concentration représentée sur l'échelle logarithmique.

Les intensités du signal SERS des pics caractéristiques de NT et SA-Cy5 ont été suivies comme précédemment en fonction de l'augmentation des

concentrations de solution des molécules respectives. Les tests montrent l'excellente réponse quantitative des intensités du signal SERS avec de faibles écarts types, même en répétant les tests en utilisant des puces de capteur provenant de lots différents. Les signaux pour NT sur l'Au-NPA_150 ont été observés jusqu'à 1 nM dans la fourchette d'expérimentation, tandis que les limites de détection les plus basses (LOD), prenant en compte la limite du test témoin, ont été estimées à 800 pM. Dans le cas de SA-Cy5, les signaux ont atteint des concentrations de 1nM, tandis que la LOD était estimée à 1,3 nM. En considérant que chaque SA-Cy5 a ~10 molécules de Cy5, la LOD correspond à la transmission du signal par les concentrations de Cy5, qui est effectivement supérieure. La LOD du SA-Cy5 est donc nettement inférieure à celle du NT, malgré le fait que le pic d'absorption de Cy5 (655 nm) soit proche de celui de la longueur d'onde d'excitation de 633 nm, et est donc capable d'excitation Raman par résonance. L'excitation Raman par résonance peut contribuer à obtenir des amplifications de signal 3 fois supérieures à ces équivalents non résonnants.[399] La plus grande sensibilité dans la détection de NT est en lien avec les observations de l'impact des dimensions moléculaires sur les exaltations de la SERS basées sur la taille de l'intervalle.

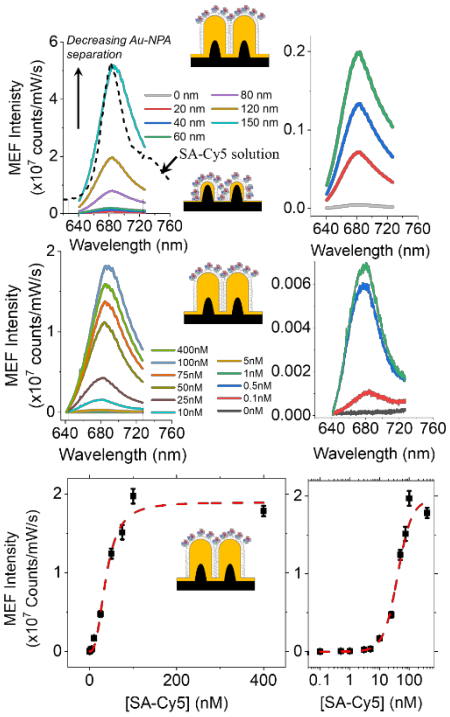

Illustration A.26. Évolution spectrale du MEF de la couverture saturée de SA-Cy5 sur l'AU-NPA biotinylé en fonction de l'épaisseur de l'or. Les spectres d'émission de la molécule de SA-Cy5 en solution sont présentés à titre de comparaison. b) Spectres MEF acquis sur AU-NPA_150 en fonction des concentrations de SA-Cy5 et d) Dosage MEF de SA-Cy5 sur AU-NPA_150 biotinylé. La ligne en pointillés indique l'ajustement à la fonction de Hill-Langmuir.

Une stratégie pour surmonter le problème de la limitation stérique au positionnement des molécules sur points chauds consiste à utiliser la fluorescence exaltée par métal (MEF) à la place du SERS. Contrairement à la SERS, la MEF nécessite que l'analyte soit positionné à distance optimale des points chauds pour exploiter les fortes exaltation. [425–427] Cela présente l'avantage d'alléger partiellement les contraintes spatiales liées à la SERS. Pour étudier la question, les analyses de SA-Cy5 représentées dans les **illustrations A.24** et **A.25** ont été répétées tout en mesurant les intensités d'émission de fluorescence de SA-

Cy5 en fonction des concentrations. Les spectres de fluorescence présentent une forte exaltation par rapport aux contrôles du substrat d'or brut et se sont amplifiés à mesure de l'épaississement de la couche d'or, l'Au-NPA_150 présentant toujours l'exaltation maximale du signal parmi les Au-NPA. **(Illustration A.26)** Le tracé des intensités de pic de fluorescence de SA-Cy5 a donné une réponse quantitative concluante liée à la concentration de SA-Cy5, avec le signal observable le plus faible à une concentration de 100 pM. Une LOD de 120 pM a été estimée en tenant compte de la moyenne et de l'écart type du signal témoin, ainsi que de l'écart type des intensités du signal à la concentration la plus faible. La LOD observée dans les tests MEF est inférieure à celle des tests de SERS, notamment grâce à la compatibilité de l'exigence spatiale avec la dimension des molécules. On constate également la sensibilité élevée de l'Au-NPA_150 dans les test MEF par les exaltation 4 fois plus élevées pour l'Au-NPA_150 comparé à la surface d'or brut dans des conditions identiques. Les exaltation observées sont supérieures à celles rapportées dans la littérature, pour les tests MEF basés sur Cy5 [427,485–487] ou d'autres colorants, [488,489] et peuvent être attribuées à un grand nombre de points chauds EM fortement exaltés sur les réseaux de piliers.

Conclusions et perspectives

La thèse décrit les travaux réalisés dans le cadre du projet PLASENS, financé par le Fonds National de la Recherche du Luxembourg. Elle traite de l'étude de nanoréseaux plasmoniques conçus de manière rationnelle pour relever les défis de la détection bioanalytique grâce à des spectroscopies exaltées de surface (SES). Cette thèse identifie les configurations qui renforcent l'effet de levier sur les points chauds électromagnétiques (EM). Grâce à la co-localisation de l'analyte, les points chauds EM réduisent la sensibilité à des concentrations picomolaires. La thèse établit d'importantes corrélations entre la géométrie ⇔ les propriétés optiques/spectroscopiques ⇔ la sensibilité dans les essais moléculaires avec des expériences combinées à des simulations numériques. Les résultats ouvrent de nouvelles opportunités pour une conception rationnelle de capteurs plasmoniques prenant en compte les dimensions des molécules d'analyte dans la géométrie des assemblages nanoplasmoniques.

Le projet tire parti des possibilités offertes par la méthode d'auto-assemblage moléculaire basée sur les copolymères amphiphiles et les colloïdes qui en sont dérivés.

Cette méthode a permis d'obtenir des écarts types spécifiques et faibles de <15 % pour les principales variables géométriques, un contrôle orthogonal de la taille et de l'espacement entre les caractéristiques, et des options de transfert du modèle pour réaliser différentes interfaces nanoplasmoniques. La définition des réseaux nanoplasmoniques ainsi obtenus a contribué à la facilité de la modélisation géométrique pour la prédiction et la compréhension des propriétés optiques et spectroscopiques. Les paramètres d'auto-assemblage, à la fois au stade de la production du modèle et du transfert du modèle, pourraient être rigoureusement contrôlés pour assurer une uniformité, reproductibilité et évolutivité élevées des réseaux plasmoniques ainsi obtenus sur des plaquettes entières de 4".

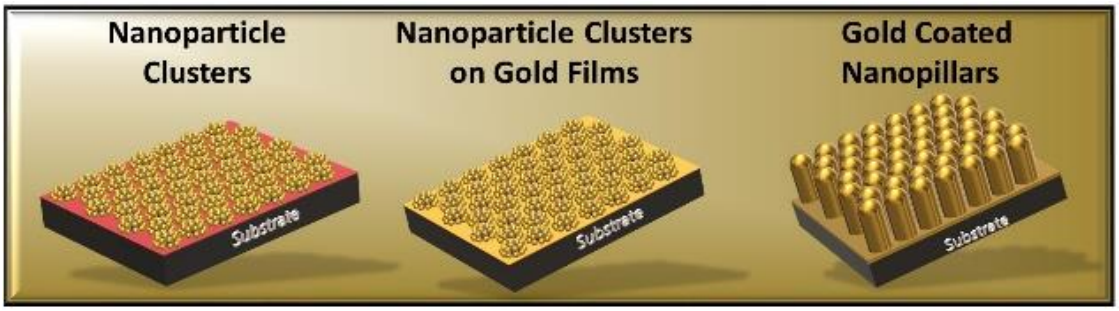

Les points chauds électromagnétiques (EM) à haute résolution spatiale ont été fabriqués avec la méthode d'auto-assemblage moléculaire. Les nanoréseaux plasmoniques constitués de nanostructures métalliques discontinues, basés sur des clusters de nanoparticules et des topographies continues bien que tridimensionnelles, et reposant sur des nanopiliers métalliques, ont été mis au point pour étudier la dépendance des sensibilités à la taille des molécules cibles en utilisant la spectroscopie Raman exaltée par effet de surface (SERS) et la fluorescence exaltée en surface en (SEF).

Des réseaux de clusters de nanoparticules (NCA) aux formes hybrides uniques, permettant à la fois des points chauds EM <1 nm entre les nanoparticules du cluster et <10 nm entre les clusters, ont été étudiés. La contribution des points chauds interparticulaires et des points chauds inter-cluster dans les sensibilités de détection liées la taille des molécules d'analyte est étudiée. Les stratégies pour améliorer les sensibilités identifiées et les détections quantitatives très sensibles ont été démontrées en utilisant une petite sonde organique et un modèle de test sandwich. En outre, les capacités du QCM-SEF en milieu naturel ont été démontrées, ce qui permet de corréler les signaux spectroscopiques

avec la concentration de surface des molécules cibles. La méthode peut étendre son potentiel d'application à une analyse spectroscopique en temps réel et faire le lien avec le transport de masse de l'analyte sur la surface en milieu naturel. La méthode étendue a également été utilisée pendant ces travaux afin de rationaliser les configurations par l'identification des facteurs clés contribuant aux sensibilités de détection et le maintien du contrôle des fonctionnalisations de surface pour identifier les facteurs provoquant des écarts types ou des variations de signal. Des réseaux de nanopiliers recouverts d'or (NPA) sous forme de nanostructures tridimensionnelles continues et rigides de moins de 10 nm ont également été étudiés. Leurs écarts interpiliers ont été contrôlés par tranches de moins de 5 nm et l'impact de la fermeture de la séparation sur la sensibilité de détection des molécules de taille différente a été observé. Outre la démonstration des concentrations picomolaires et d'intensités de signal fortement exalté pour la SERS et la SEF, les contributeurs aux sensibilités de détection ont été évalués.

Les recherches présentées dans la thèse pourraient déjà être prolongées pour des résultats préliminaires montrant une grande sensibilité dans la détection des protéines via des tests immunologiques et des oligonucléotides. Les recherches à venir gagneraient à améliorer la logistique des mesures grâce à des fluides intégrés aux plaquettes et aux mesures spectroscopiques portables. Les interfaces doivent être testées et optimisées pour fonctionner dans des milieux complexes tels que les crachats, le sang et l'urine, qui peuvent poser différents problèmes. La question des limitations de la diffusion se pose à des concentrations ultra-faibles, ce qui entraîne le problème de l'analyte qui doit trouver la surface comme on « trouve une aiguille dans une botte de foin ». Il est nécessaire d'adopter des approches indépendantes pour améliorer le transport de masse de l'analyte afin qu'il reste compatible avec la stabilité et les performances des transducteurs nanoplasmoniques.

References

1. Sarangadharan, I. *et al.* Risk stratification of heart failure from one drop of blood using hand-held biosensor for BNP detection. *Biosens. Bioelectron.* **107**, 259–265 (2018).
2. Zhou, S.-F. & Zhong, W.-Z. Drug Design and Discovery: Principles and Applications. *Molecules* **22**, 279 (2017).
3. Bengsch, B., Thimme, R. & Blum, H. E. Individualisierte Medizin 2011. *Gastroenterologe* **6**, 106–111 (2011).
4. Bell, J. Predicting disease using genomics. *Nature* **429**, 453–456 (2004).
5. Paterson, S. J. Cognitive Modularity and Genetic Disorders. *Science (80-.).* **286**, 2355–2358 (1999).
6. Cohen, M. L. Changing patterns of infectious disease. *Nature* **406**, 762–767 (2000).
7. Bernell, S. & Howard, S. W. Use Your Words Carefully: What Is a Chronic Disease? *Front. Public Heal.* **4**, 2–4 (2016).
8. Roussel, A. (USAID/Benin). Disease Threats, Global killers - The National Academies. *The National Academy of Sciences* (2020).
9. Coleman, W. B. & Tsongalis, G. J. Basic Concepts in Molecular Pathology—Introduction to Molecular Testing in Human Disease. in *Diagnostic Molecular Pathology* **2**, 3–14 (Elsevier, 2017).
10. Lurie, N., Saville, M., Hatchett, R. & Halton, J. Developing Covid-19 Vaccines at Pandemic Speed. *N. Engl. J. Med.* **382**, 1969–1973 (2020).
11. Dincer, C., Bruch, R., Kling, A., Dittrich, P. S. & Urban, G. A. Multiplexed Point-of-Care Testing – xPOCT. *Trends Biotechnol.* **35**, 728–742 (2017).
12. Haeberle, S. & Zengerle, R. Microfluidic platforms for lab-on-a-chip applications. *Lab Chip* **7**, 1094–1110 (2007).
13. Mathur, S. & Sutton, J. Personalized medicine could transform healthcare (Review). *Biomed. Reports* **7**, 3–5 (2017).
14. Seeree, P., Pearngam, P., Kumkate, S. & Janvilisri, T. An omics perspective on molecular biomarkers for diagnosis, prognosis, and therapeutics of cholangiocarcinoma. *Int. J. Genomics* **2015**, (2015).
15. Molecular Biology of the Cell: Second Edition. in (Garland Publishing, Inc., 1989).
16. Dorcely, B. *et al.* Novel biomarkers for prediabetes, diabetes, and associated complications. *Diabetes, Metab. Syndr. Obes. Targets Ther.* **10**, 345–361 (2017).
17. Barnhart, K. T. *et al.* Symptomatic Patients With an Early Viable Intrauterine Pregnancy. *Obstet. Gynecol.* **104**, 50–55 (2004).
18. Polanski, M. & Anderson, N. L. A List of Candidate Cancer Biomarkers for Targeted Proteomics. *Biomark. Insights* **1**, 117727190600100 (2006).
19. Kim, J. J., Han, B. G., Lee, H. I., Yoo, H. W. & Lee, J. K. Development of SNP-based human identification system. *Int. J. Legal Med.* **124**, 125–131 (2010).
20. Kauwe, J. S. K. *et al.* Validating predicted biological effects of Alzheimer's disease associated SNPs using CSF biomarker levels. *J. Alzheimer's Dis.* **21**, 833–842 (2010).
21. Kelley, S. O. What Are Clinically Relevant Levels of Cellular and Biomolecular Analytes? *ACS Sensors* **2**, 193–197 (2017).
22. Pelt-Verkuil, E. van, Leeuwen, W. B. van & Witt, R. te. *Molecular Diagnostics*. (Springer Singapore, 2019). doi:10.1007/978-981-13-1604-3
23. Tsongalis, G. J. & Silverman, L. M. Molecular diagnostics: A historical perspective. *Clin. Chim. Acta* **369**, 188–192 (2006).
24. Hughes, M. D. Molecular Diagnostics Market Trends and Outlook. *Enterp. Anal. Corp.* 2013 (2013).
25. Diagnostics: Investment Banking & M&A Industry Trends & Performance - InvestmentBank.com.
26. Liu, Y., Matharu, Z., Howland, M. C., Revzin, A. & Simonian, A. L. Affinity and enzyme-based biosensors: Recent advances and emerging applications in cell analysis and point-of-care testing. *Anal. Bioanal. Chem.* **404**, 1181–1196 (2012).
27. WHO. Systematic review of needs for medical devices for ageing populations. 116 (2015).
28. Snyderman, R. Personalized health care: From theory to practice. *Biotechnol. J.* **7**, 973–979 (2012).
29. Giljohann, D. A. & Mirkin, C. A. Drivers of biodiagnostic development. *Nature* **462**, 461–464 (2009).
30. Shen, J., Li, Y., Gu, H., Xia, F. & Zuo, X. Recent development of sandwich assay based on the nanobiotechnologies for proteins, nucleic acids, small molecules, and ions. *Chem. Rev.* **114**, 7631–7677 (2014).
31. Nong, R. Y., Gu, J., Darmanis, S., Kamali-Moghaddam, M. & Landegren, U. DNA-assisted protein detection technologies. *Expert Rev. Proteomics* **9**, 21–32 (2012).

32. Peña-Bahamonde, J., Nguyen, H. N., Fanourakis, S. K. & Rodrigues, D. F. Recent advances in graphene-based biosensor technology with applications in life sciences. *J. Nanobiotechnology* **16**, 1–17 (2018).
33. Chan, A. I., McGregor, L. M. & Liu, D. R. Novel selection methods for DNA-encoded chemical libraries. *Curr. Opin. Chem. Biol.* **26**, 55–61 (2015).
34. Krishnamoorthy, S. Nanostructured sensors for biomedical applications — a current perspective. *Curr. Opin. Biotechnol.* **34**, 118–124 (2015).
35. Maltez-Da Costa, M. *et al.* Simple monitoring of cancer cells using nanoparticles. *Nano Lett.* **12**, 4164–4171 (2012).
36. Zhang, J., Atay, T. & Nurmikko, A. V. Optical Detection of Brain Cell Activity Using Plasmonic Gold Nanoparticles. *Nano Lett.* **9**, 519–524 (2009).
37. Biological and technological scales compared-en.
38. Arlett, J. L., Myers, E. B. & Roukes, M. L. Comparative advantages of mechanical biosensors. *Nat. Nanotechnol.* **6**, 203–215 (2011).
39. Waggoner, P. S., Varshney, M. & Craighead, H. G. Detection of prostate specific antigen with nanomechanical resonators. *Lab Chip* **9**, 3095–3099 (2009).
40. Rich, R. L. & Myszka, D. G. Advances in surface plasmon resonance biosensor analysis. *Curr. Opin. Biotechnol.* **11**, 54–61 (2000).
41. Hering, K. *et al.* SERS: A versatile tool in chemical and biochemical diagnostics. *Anal. Bioanal. Chem.* **390**, 113–124 (2008).
42. Constantino, C. J. L., Lemma, T., Antunes, P. A. & Aroca, R. Single-molecule detection using surface-enhanced resonance raman scattering and Langmuir-Blodgett monolayers. *Anal. Chem.* **73**, 3674–3678 (2001).
43. Subaihi, A. *et al.* Rapid, accurate, and quantitative detection of propranolol in multiple human biofluids via surface-enhanced raman scattering. *Anal. Chem.* **88**, 10884–10892 (2016).
44. Eryilmaz, M., Zengin, A., Boyaci, I. H. & Tamer, U. Rapid quantification of total protein with surface-enhanced Raman spectroscopy using o-phthalaldehyde. *J. Raman Spectrosc.* **48**, 653–658 (2017).
45. Ataka, K. & Heberle, J. Biochemical applications of surface-enhanced infrared absorption spectroscopy. *Anal. Bioanal. Chem.* **388**, 47–54 (2007).
46. Ataka, K., Stripp, S. T. & Heberle, J. Surface-enhanced infrared absorption spectroscopy (SEIRAS) to probe monolayers of membrane proteins. *Biochim. Biophys. Acta - Biomembr.* **1828**, 2283–2293 (2013).
47. Pellegrini, G., Finazzi, M., Celebrano, M., Duò, L. & Biagioni, P. Surface-enhanced chiroptical spectroscopy with superchiral surface waves. *Chirality* **30**, 883–889 (2018).
48. Abdali, S. Observation of SERS effect in Raman optical activity, a new tool for chiral vibrational spectroscopy. *J. Raman Spectrosc.* **37**, 1341–1345 (2006).
49. Abdali, S. & Blanch, E. W. Surface enhanced Raman optical activity (SEROA). *Chem. Soc. Rev.* **37**, 980–992 (2008).
50. Pour, S. O., Bell, S. E. J. & Blanch, E. W. Use of a hydrogel polymer for reproducible surface enhanced Raman optical activity (SEROA). *Chem. Commun.* **47**, 4754–4756 (2011).
51. Vosgröne, T. & Meixner, A. J. Surface and resonance enhanced micro-Raman spectroscopy of xanthene dyes at the single-molecule level. *J. Lumin.* **107**, 13–20 (2004).
52. Balčytis, A. *et al.* From Fundamental toward Applied SERS: Shared Principles and Divergent Approaches. *Adv. Opt. Mater.* **6**, 1–29 (2018).
53. Geddes, C. D. *Metal-Enhanced Fluorescence*. *John Wiley and Sons* **53**, (2010).
54. Aslan, K. *et al.* Metal-enhanced fluorescence: An emerging tool in biotechnology. *Curr. Opin. Biotechnol.* **16**, 55–62 (2005).
55. Mun, J., Lee, D., So, S., Badloe, T. & Rho, J. Surface-enhanced spectroscopy: Toward practical analysis probe. *Appl. Spectrosc. Rev.* **54**, 142–175 (2019).
56. What is Stokes Shift? *Edinburgh Instruments*
57. Ru, E. Le & Etchegoin, P. *Principles of Surface Enhanced Raman Spectroscopy and related plasmonic effects*. *Elsevier* (2008).
58. Bantz, K. C. *et al.* Recent progress in SERS biosensing. *Phys. Chem. Chem. Phys.* **13**, 11551–11567 (2011).
59. Aroca, R. *Surface-Enhanced Vibrational Spectroscopy*. *Surface-Enhanced Vibrational Spectroscopy* (John Wiley & Sons, Ltd, 2006).
60. Nie, S. & Emory, S. R. Probing single molecules and single nanoparticles by surface-enhanced Raman scattering. *Science (80-.).* **275**, 1102–1106 (1997).

61. Le Ru, E. C., Blackie, E., Meyer, M. & Etchegoin, P. G. Surface Enhanced Raman Scattering Enhancement Factors: A Comprehensive Study. *J. Phys. Chem. C* **111**, 13794–13803 (2007).
62. Le Ru, E. C. & Etchegoin, P. G. Single-molecule surface-enhanced raman spectroscopy. *Annu. Rev. Phys. Chem.* **63**, 65–87 (2012).
63. Moskovits, M. Surface roughness and the enhanced intensity of Raman scattering by molecules adsorbed on metals. *J. Chem. Phys.* **69**, 4159–4161 (1978).
64. Pilot, R. *et al.* A review on surface-enhanced Raman scattering. *Biosensors* **9**, (2019).
65. Ausman, L. K. & Schatz, G. C. On the importance of incorporating dipole reradiation in the modeling of surface enhanced Raman scattering from spheres. *J. Chem. Phys.* **131**, (2009).
66. Schatz, G. C., Young, M. A. & Van Duyne, R. P. Electromagnetic mechanism of SERS. *Top. Appl. Phys.* **103**, 19–46 (2006).
67. Langer, J. *et al.* Present and future of surface-enhanced Raman scattering. *ACS Nano* **14**, 28–117 (2020).
68. Pilot, R., Signorini, R. & Fabris, L. *Surface-enhanced Raman spectroscopy: Principles, substrates, and applications*. *Metal Nanoparticles and Clusters: Advances in Synthesis, Properties and Applications* (2017). doi:10.1007/978-3-319-68053-8_4
69. Muniz-Miranda, M., Muniz-Miranda, F. & Pedone, A. Spectroscopic and Computational Studies on Ligand-Capped Metal Nanoparticles and Clusters. in *Metal Nanoparticles and Clusters* 55–87 (Springer International Publishing, 2018). doi:10.1007/978-3-319-68053-8_3
70. Otto, A. The 'chemical' (electronic) contribution to surface-enhanced Raman scattering. *J. Raman Spectrosc.* **36**, 497–509 (2005).
71. Long, D. A. *The Raman effect: a unified treatment of the theory of Raman scattering by molecules. 2002*. *West Sussex, England: John Wiley & Sons Ltd* **8**, (2002).
72. Eberhardt, K., Stiebing, C., Matthaüs, C., Schmitt, M. & Popp, J. Advantages and limitations of Raman spectroscopy for molecular diagnostics: An update. *Expert Rev. Mol. Diagn.* **15**, 773–787 (2015).
73. Kleinman, S. L. *et al.* Single-molecule surface-enhanced raman spectroscopy of crystal violet isotopologues: Theory and experiment. *J. Am. Chem. Soc.* **133**, 4115–4122 (2011).
74. Marcu, L. Fluorescence Lifetime Techniques in Medical Applications. *Ann. Biomed. Eng.* **40**, 304–331 (2012).
75. Gakamsky, D. M. Fluorescence-based applications for Life Science , Biotechnology and Clinical Diagnostics. **0**, (2005).
76. Prabhakar, U., Eirikis, E., Miller, B. E. & Davis, H. M. Multiplexed cytokine sandwich immunoassays: clinical applications. *Methods Mol. Med.* **114**, 223–232 (2005).
77. Dini, C. *et al.* Fluorescence Detection-Based Functional Assay for High-Throughput Screening for MraY. *Antimicrob. Agents Chemother.* **48**, 897–902 (2004).
78. Yazgan, N. N., Boyaci, I. H., Topcu, A. & Tamer, U. Detection of melamine in milk by surface-enhanced Raman spectroscopy coupled with magnetic and Raman-labeled nanoparticles. *Anal. Bioanal. Chem.* **403**, 2009–2017 (2012).
79. Jeong, Y., Kook, Y. M., Lee, K. & Koh, W. G. Metal enhanced fluorescence (MEF) for biosensors: General approaches and a review of recent developments. *Biosens. Bioelectron.* **111**, 102–116 (2018).
80. Lakowicz, J. R. Radiative decay engineering: Biophysical and biomedical applications. *Anal. Biochem.* **298**, 1–24 (2001).
81. Gersten, J. & Nitzan, A. Spectroscopic properties of molecules interacting with small dielectric particles. *J. Chem. Phys.* **75**, 1139–1152 (1981).
82. Gill, R. & Le Ru, E. C. Fluorescence enhancement at hot-spots: The case of Ag nanoparticle aggregates. *Phys. Chem. Chem. Phys.* **13**, 16366–16372 (2011).
83. Kinkhabwala, A. *et al.* Large single-molecule fluorescence enhancements produced by a bowtie nanoantenna. *Nat. Photonics* **3**, 654–657 (2009).
84. Geddes, C. D., Gryczynski, I., Malicka, J., Gryczynski, Z. & Lakowicz, J. R. Metal-enhanced fluorescence: potential applications in HTS. *Comb. Chem. High Throughput Screen.* **6**, 109–117 (2003).
85. Strickler, S. J. & Berg, R. A. Relationship between absorption intensity and fluorescence lifetime of molecules. *J. Chem. Phys.* **37**, 814–822 (1962).
86. Malicka, J., Gryczynski, I., Gryczynski, Z. & Lakowicz, J. R. Effects of fluorophore-to-silver distance on the emission of cyanine–dye-labeled oligonucleotides. *Anal. Biochem.* **315**, 57–66 (2003).
87. Bauch, M., Toma, K., Toma, M., Zhang, Q. & Dostalek, J. Plasmon-Enhanced Fluorescence Biosensors: A Review. *Plasmonics* **9**, 781–799 (2014).
88. Mishra, H., Mali, B. L., Karolin, J., Dragan, A. I. & Geddes, C. D. Experimental and theoretical study

of the distance dependence of metal-enhanced fluorescence, phosphorescence and delayed fluorescence in a single system. *Phys. Chem. Chem. Phys.* **15**, 19538–19544 (2013).
89. Chen, Y., Munechika, K. & Ginger, D. S. Dependence of fluorescence intensity on the spectral overlap between fluorophores and plasmon resonant single silver nanoparticles. *Nano Lett.* **7**, 690–696 (2007).
90. Anger, P., Bharadwaj, P. & Novotny, L. Enhancement and quenching of single-molecule fluorescence. *Phys. Rev. Lett.* **96**, (2006).
91. Geddes, C. D. & Lakowicz, J. R. Metal-Enhanced Fluorescence. *J. Fluoresc.* **12**, 121–129 (2002).
92. Maier, S. A. *Plasmonics - Fundamentals and Applications*. (Springer Science+Business Media LLC, 2007).
93. Klimov, V. *Nanoplasmonics*. (CRC Press, 2014).
94. Maier, Stefan Alexander (Centre forPhotonicsandPhotonic Materials DepartmentofPhysics, University ofBath, U. *Plasmonics - Fundamentals and Applications*. (Springer). doi:10.1007/978-0-387-37825-1
95. Agrawal, A. *et al.* Localized Surface Plasmon Resonance in Semiconductor Nanocrystals. *Chem. Rev.* **118**, 3121–3207 (2018).
96. Zayats, A. V., Smolyaninov, I. I. & Maradudin, A. A. Nano-optics of surface plasmon polaritons. *Phys. Rep.* **408**, 131–314 (2005).
97. Koppens, F. H. L., Chang, D. E. & García De Abajo, F. J. Graphene plasmonics: A platform for strong light-matter interactions. *Nano Lett.* **11**, 3370–3377 (2011).
98. Krauter, C. M., Schirmer, J., Jacob, C. R., Pernpointner, M. & Dreuw, A. Plasmons in molecules: Microscopic characterization based on orbital transitions and momentum conservation. *J. Chem. Phys.* **141**, 1–11 (2014).
99. PB Johnson, R. C. Optical Contstants of Noble Metal. *Physical Review B* (1972).
100. Han, Y. *et al.* Effect of oxidation on surface-enhanced raman scattering activity of silver nanoparticles: A quantitative correlation. *Anal. Chem.* (2011). doi:10.1021/ac2005839
101. Ravi Shukla, † *et al.* Biocompatibility of Gold Nanoparticles and Their Endocytotic Fate Inside the Cellular Compartment: A Microscopic Overview. *Langmuir* (2005).
102. Nguyen, H. H., Park, J., Kang, S. & Kim, M. Surface plasmon resonance: A versatile technique for biosensor applications. *Sensors (Switzerland)* **15**, 10481–10510 (2015).
103. Willets, K. A. & Van Duyne, R. P. Localized Surface Plasmon Resonance Spectroscopy and Sensing. *Annu. Rev. Phys. Chem.* **58**, 267–297 (2007).
104. Haes, A. J., Zou, S., Schatz, G. C. & Van Duyne, R. P. A nanoscale optical biosensor: The long range distance dependence of the localized surface plasmon resonance of noble metal nanoparticles. *J. Phys. Chem. B* **108**, 109–116 (2004).
105. Li, M., Cushing, S. K. & Wu, N. Plasmon-enhanced optical sensors: a review. *Analyst* **140**, 386–406 (2015).
106. Jatschka, J., Dathe, A., Csáki, A., Fritzsche, W. & Stranik, O. Propagating and localized surface plasmon resonance sensing - A critical comparison based on measurements and theory. *Sens. Bio-Sensing Res.* **7**, 62–70 (2016).
107. Haes, A. J. & Van Duyne, R. P. A unified view of propagating and localized surface plasmon resonance biosensors. *Anal. Bioanal. Chem.* **379**, 920–930 (2004).
108. Pérez-Luna, V. H. *et al.* Molecular Recognition between Genetically Engineered Streptavidin and Surface-Bound Biotin. *J. Am. Chem. Soc.* **121**, 6469–6478 (1999).
109. Jung, L. S. & Campbell, C. T. Sticking Probabilities in Adsorption from Liquid Solutions: Alkylthiols on Gold. *Phys. Rev. Lett.* **84**, 5164–5167 (2000).
110. Georgiadis, R., Peterlinz, K. P. & Peterson, A. W. Quantitative Measurements and Modeling of Kinetics in Nucleic Acid Monolayer Films Using SPR Spectroscopy. *J. Am. Chem. Soc.* **122**, 3166–3173 (2000).
111. Haake, H.-M., Schütz, A. & Gauglitz, G. Label-free detection of biomolecular interaction by optical sensors. *Fresenius. J. Anal. Chem.* **366**, 576–585 (2000).
112. Haes, A. J. & Van Duyne, R. P. A nanoscale optical biosensor: Sensitivity and selectivity of an approach based on the localized surface plasmon resonance spectroscopy of triangular silver nanoparticles. *J. Am. Chem. Soc.* **124**, 10596–10604 (2002).
113. McFarland, A. D. & Van Duyne, R. P. Single Silver Nanoparticles as Real-Time Optical Sensors with Zeptomole Sensitivity. *Nano Lett.* **3**, 1057–1062 (2003).
114. Malinsky, M. D., Kelly, K. L., Schatz, G. C. & Van Duyne, R. P. Chain Length Dependence and Sensing Capabilities of the Localized Surface Plasmon Resonance of Silver Nanoparticles Chemically Modified with Alkanethiol Self-Assembled Monolayers. *J. Am. Chem. Soc.* **123**, 1471–

1482 (2001).
115. Jonathan C. Riboh, †, Amanda J. Haes, †, Adam D. McFarland, Chanda Ranjit Yonzon, and & Duyne*, R. P. Van. A Nanoscale Optical Biosensor: Real-Time Immunoassay in Physiological Buffer Enabled by Improved Nanoparticle Adhesion. 1772–1780 (2003). doi:10.1021/JP022130V
116. Jung, L. S., Campbell, C. T., Chinowsky, T. M., Mar, M. N. & Yee, S. S. Quantitative interpretation of the response of surface plasmon resonance sensors to adsorbed films. *Langmuir* **14**, 5636–5648 (1998).
117. Haes, A. J., Zou, S., Schatz, G. C. & Van Duyne, R. P. Nanoscale Optical Biosensor: Short Range Distance Dependence of the Localized Surface Plasmon Resonance of Noble Metal Nanoparticles. *J. Phys. Chem. B* **108**, 109–116 (2004).
118. Brockman, J. M., Nelson, B. P. & Corn, R. M. Surface Plasmon Resonance Imaging Measurements of Ultrathin Organic Films. *Annu. Rev. Phys. Chem.* **51**, 41–63 (2000).
119. Van Duyne, R. P., Haes, A. J. & McFarland, A. D. <title>Nanoparticle optics: fabrication, surface-enhanced spectroscopy, and sensing</title>. in (eds. Lian, T. & Dai, H.-L.) 197–207 (2003). doi:10.1117/12.509862
120. Shumaker-Parry, J. S., Zareie, M. H., Aebersold, R. & Campbell, C. T. Microspotting Streptavidin and Double-Stranded DNA Arrays on Gold for High-Throughput Studies of Protein−DNA Interactions by Surface Plasmon Resonance Microscopy. *Anal. Chem.* **76**, 918–929 (2004).
121. Mock, J. J., Smith, D. R. & Schultz, S. Local Refractive Index Dependence of Plasmon Resonance Spectra from Individual Nanoparticles. *Nano Lett.* **3**, 485–491 (2003).
122. Hall, D. Use of Optical Biosensors for the Study of Mechanistically Concerted Surface Adsorption Processes. *Anal. Biochem.* **288**, 109–125 (2001).
123. Schuck, P. USE OF SURFACE PLASMON RESONANCE TO PROBE THE EQUILIBRIUM AND DYNAMIC ASPECTS OF INTERACTIONS BETWEEN BIOLOGICAL MACROMOLECULES. *Annu. Rev. Biophys. Biomol. Struct.* **26**, 541–566 (1997).
124. Garland, P. B. Optical evanescent wave methods for the study of biomolecular interactions. *Q. Rev. Biophys.* **29**, 91–117 (1996).
125. Jung, L. S. & Campbell, C. T. Sticking Probabilities in Adsorption of Alkanethiols from Liquid Ethanol Solution onto Gold. *J. Phys. Chem. B* **104**, 11168–11178 (2000).
126. Knoll, W. INTERFACES AND THIN FILMS AS SEEN BY BOUND ELECTROMAGNETIC WAVES. *Annu. Rev. Phys. Chem.* **49**, 569–638 (1998).
127. Shumaker-Parry, J. S. & Campbell, C. T. Quantitative Methods for Spatially Resolved Adsorption/Desorption Measurements in Real Time by Surface Plasmon Resonance Microscopy. *Anal. Chem.* **76**, 907–917 (2004).
128. Karlsson, R. & Stahlberg, R. Surface Plasmon Resonance Detection and Multispot Sensing for Direct Monitoring of Interactions Involving Low-Molecular-Weight Analytes and for Determination of Low Affinities. *Anal. Biochem.* **228**, 274–280 (1995).
129. Sjoelander, S. & Urbaniczky, C. Integrated fluid handling system for biomolecular interaction analysis. *Anal. Chem.* **63**, 2338–2345 (1991).
130. Devasenathipathy, R., Wu, D.-Y. & Tian, Z.-Q. Surface Plasmon Enhanced Chemical Reactions on Metal Nanostructures. in *Nanoplasmonics* (IntechOpen, 2020). doi:10.5772/intechopen.89606
131. Shanker, G. S., Tandon, B., Shibata, T., Chattopadhyay, S. & Nag, A. Doping controls plasmonics, electrical conductivity, and carrier-mediated magnetic coupling in Fe and Sn codoped In2O3 nanocrystals: Local structure is the key. *Chem. Mater.* **27**, 892–900 (2015).
132. Yang, J. *et al.* Plasmonic polymer tandem solar cell. *ACS Nano* **5**, 6210–6217 (2011).
133. O'Connor, D. & Zayats, A. V. Data storage: The third plasmonic revolution. *Nat. Nanotechnol.* **5**, 482–483 (2010).
134. Jahn, M. *et al.* Plasmonic nanostructures for surface enhanced spectroscopic methods. *Analyst* **141**, 756–793 (2016).
135. Fesenko, O. & Yatsenko, L. *Nanoplasmonics, Nano-Optics, Nanocomposites, and Surface Studies*. **167**, (Springer International Publishing, 2015).
136. Stockman, M. I. Nanoplasmonics: The physics behind the applications. *Phys. Today* **64**, 39–44 (2011).
137. Jain, P. K. & El-Sayed, M. A. Plasmonic coupling in noble metal nanostructures. *Chem. Phys. Lett.* **487**, 153–164 (2010).
138. Kelly, K. L., Coronado, E., Zhao, L. L. & Schatz, G. C. The Optical Properties of Metal Nanoparticles: The Influence of Size, Shape, and Dielectric Environment. *J. Phys. Chem. B* **107**, 668–677 (2003).
139. Nordlander, P., Oubre, C., Prodan, E., Li, K. & Stockman, M. I. Plasmon hybridization in nanoparticle

dimers. *Nano Lett.* **4**, 899–903 (2004).
140. Gunnarsson, L. *et al.* Confined plasmons in nanofabricated single silver particle pairs: Experimental observations of strong interparticle interactions. *J. Phys. Chem. B* **109**, 1079–1087 (2005).
141. Wei, X. Z. & Mulvaney, P. *Optical properties of strongly coupled plasmonic nanoparticle clusters*. *Handbook of Surface Science* **4**, (Elsevier B.V., 2014).
142. Rechberger, W. *et al.* Optical properties of two interacting gold nanoparticles. *Opt. Commun.* **220**, 137–141 (2003).
143. Kleinman, S. L., Frontiera, R. R., Henry, A. I., Dieringer, J. A. & Van Duyne, R. P. Creating, characterizing, and controlling chemistry with SERS hot spots. *Phys. Chem. Chem. Phys.* **15**, 21–36 (2013).
144. Le Ru, E. C., Etchegoin, P. G. & Meyer, M. Enhancement factor distribution around a single surface-enhanced Raman scattering hot spot and its relation to single molecule detection. *J. Chem. Phys.* **125**, (2006).
145. Cang, H. *et al.* Probing the electromagnetic field of a 15-nanometre hotspot by single molecule imaging. *Nature* **469**, 385–388 (2011).
146. Fathi, F., Rashidi, M. R. & Omidi, Y. Ultra-sensitive detection by metal nanoparticles-mediated enhanced SPR biosensors. *Talanta* **192**, 118–127 (2019).
147. Lee, D. & Yoon, S. Effect of Nanogap Curvature on SERS: A Finite-Difference Time-Domain Study. *J. Phys. Chem. C* **120**, 20642–20650 (2016).
148. Sergiienko, S., Moor, K., Gudun, K., Yelemessova, Z. & Bukasov, R. Nanoparticle-nanoparticle vs. Nanoparticle-substrate hot spot contributions to the SERS signal: Studying Raman labelled monomers, dimers and trimers. *Phys. Chem. Chem. Phys.* **19**, 4478–4487 (2017).
149. Ciracì, C. *et al.* Probing the ultimate limits of plasmonic enhancement. *Science (80-.).* **337**, 1072–1074 (2012).
150. Su, K. H. *et al.* Interparticle coupling effects on plasmon resonances of nanogold particles. *Nano Lett.* **3**, 1087–1090 (2003).
151. Jain, P. K., Huang, W. & El-Sayed, M. A. On the Universal Scaling Behavior of the Distance Decay of Plasmon Coupling in Metal Nanoparticle Pairs: A Plasmon Ruler Equation. *Nano Lett.* **7**, 2080–2088 (2007).
152. Tabor, C., Murali, R., Mahmoud & El-Sayed, M. A. On the use of plasmonic nanoparticle pairs as a plasmon ruler: The dependence of the near-field dipole plasmon coupling on nanoparticle size and shape. *J. Phys. Chem. A* **113**, 1946–1953 (2009).
153. Jain, P. K., Huang, W. & El-Sayed, M. A. On the universal scaling behavior of the distance decay of plasmon coupling in metal nanoparticle pairs: A plasmon ruler equation. *Nano Lett.* **7**, 2080–2088 (2007).
154. Kottmann, J. P. & Martin, O. J. F. Plasmon resonant coupling in metallic nanowires. *Opt. Express* **8**, 655 (2001).
155. Zhang, W., Li, Q. & Qiu, M. A plasmon ruler based on nanoscale photothermal effect. *Opt. Express* **21**, 172 (2013).
156. Sönnichsen, C., Reinhard, B. M., Liphardt, J. & Alivisatos, A. P. A molecular ruler based on plasmon coupling of single gold and silver nanoparticles. *Nat. Biotechnol.* **23**, 741–745 (2005).
157. Reinhard, B. M., Siu, M., Agarwal, H., Alivisatos, A. P. & Liphardt, J. Calibration of dynamic molecular rulers based on plasmon coupling between gold nanoparticles. *Nano Lett.* **5**, 2246–2252 (2005).
158. Ray, P. C., Fan, Z., Crouch, R. A., Sinha, S. S. & Pramanik, A. Nanoscopic optical rulers beyond the FRET distance limit: Fundamentals and applications. *Chem. Soc. Rev.* **43**, 6370–6404 (2014).
159. Ben, X. & Park, H. S. Size dependence of the plasmon ruler equation for two-dimensional metal nanosphere arrays. *J. Phys. Chem. C* **115**, 15915–15926 (2011).
160. Hill, R. T. *et al.* Plasmon Ruler with Angstrom Length Resolution. *ACS Nano* **6**, 9237–9246 (2012).
161. Zhu, W. *et al.* Quantum mechanical effects in plasmonic structures with subnanometre gaps. *Nat. Commun.* **7**, 1–14 (2016).
162. Schuck, P. J., Fromm, D. P., Sundaramurthy, A., Kino, G. S. & Moerner, W. E. Improving the mismatch between light and nanoscale objects with gold bowtie nanoantennas. *Phys. Rev. Lett.* **94**, 14–17 (2005).
163. Etchegoin, P. G. & Le Ru, E. C. A perspective on single molecule SERS: Current status and future challenges. *Phys. Chem. Chem. Phys.* **10**, 6079–6089 (2008).
164. Halas, N. J., Lal, S., Chang, W. S., Link, S. & Nordlander, P. Plasmons in strongly coupled metallic nanostructures. *Chem. Rev.* **111**, 3913–3961 (2011).
165. Marhaba, S. Effect of Size, Shape and Environment on the Optical Response of Metallic

Nanoparticles. *Noble Precious Met. - Prop. Nanoscale Eff. Appl.* (2018). doi:10.5772/intechopen.71574
166. Zhan, C. *et al.* From plasmon-enhanced molecular spectroscopy to plasmon-mediated chemical reactions. *Nat. Rev. Chem.* **2**, 216–230 (2018).
167. Solís, D. M., Taboada, J. M., Obelleiro, F., Liz-Marzán, L. M. & García De Abajo, F. J. Optimization of Nanoparticle-Based SERS Substrates through Large-Scale Realistic Simulations. *ACS Photonics* **4**, 329–337 (2017).
168. Lin, K. Q. *et al.* Size Effect on SERS of Gold Nanorods Demonstrated via Single Nanoparticle Spectroscopy. *J. Phys. Chem. C* **120**, 20806–20813 (2016).
169. Fang, Y., Seong, N. H. & Dlott, D. D. Measurement of the distribution of site enhancements in surface-enhanced raman scattering. *Science (80-.).* **321**, 388–392 (2008).
170. Camden, J. P. *et al.* Probing the structure of single-molecule surface-enhanced Raman scattering hot spots. *J. Am. Chem. Soc.* **130**, 12616–12617 (2008).
171. Zou, S. & Schatz, G. C. Silver nanoparticle array structures that produce giant enhancements in electromagnetic fields. *Chem. Phys. Lett.* **403**, 62–67 (2005).
172. Wustholz, K. L., Brosseau, C. L., Casadio, F. & Van Duyne, R. P. Surface-enhanced Raman spectroscopy of dyes: from single molecules to the artists' canvas. *Phys. Chem. Chem. Phys.* **11**, 7350 (2009).
173. Xu, H., Aizpurua, J., Käll, M. & Apell, P. Electromagnetic contributions to single-molecule sensitivity in surface-enhanced Raman scattering. *Phys. Rev. E - Stat. Physics, Plasmas, Fluids, Relat. Interdiscip. Top.* **62**, 4318–4324 (2000).
174. Dieringer, J. A. *et al.* Surface enhanced Raman spectroscopy : new materials , concepts , characterization tools , and applications. 9–26 (2006). doi:10.1039/b513431p
175. Duyne, R. P. Van, Hulteen, J. C. & Treichel, D. A. Atomic force microscopy and surface - enhanced Raman spectroscopy . I . Ag island films and Ag film over polymer nanosphere surfaces supported on glass Atomic force microscopy and surface-enhanced Raman spectroscopy . I . Ag island films and Ag film over . **2101**, 2101–2115 (2006).
176. Lemma, T. & Aroca, R. F. Single molecule surface-enhanced resonance Raman scattering on colloidal silver and Langmuir-Blodgett monolayers coated with silver overlayers. *J. Raman Spectrosc.* **33**, 197–201 (2002).
177. Stiles, P. L., Dieringer, J. A., Shah, N. C. & Van Duyne, R. P. Surface-Enhanced Raman Spectroscopy. *Annu. Rev. Anal. Chem.* **1**, 601–626 (2008).
178. Hulteen, J. C. *et al.* Nanosphere lithography: Size-tunable silver nanoparticle and surface cluster arrays. *J. Phys. Chem. B* **103**, 3854–3863 (1999).
179. Orendorff, C. J., Gearheart, L., Jana, N. R. & Murphy, C. J. Aspect ratio dependence on surface enhanced Raman scattering using silver and gold nanorod substrates. *Phys. Chem. Chem. Phys.* **8**, 165–170 (2006).
180. Halas, N. Playing with plasmons: Tuning the optical resonant properties of metallic nanoshells. *MRS Bull.* **30**, 362–367 (2005).
181. Camden, J. P., Dieringer, J. A., Zhao, J. & Van Duyne, R. P. Controlled plasmonic nanostructures for surface-enhanced spectroscopy and sensing. *Acc. Chem. Res.* **41**, 1653–1661 (2008).
182. Yang, M. *et al.* SERS-active gold lace nanoshells with built-in hotspots. *Nano Lett.* **10**, 4013–4019 (2010).
183. Diebold, E. D., Mack, N. H., Doom, S. K. & Mazur, E. Femtosecond Laser-Nanostructured substrates for Surface-Enhanced raman scattering. *Langmuir* **25**, 1790–1794 (2009).
184. Diebold, E. D., Peng, P. & Mazur, E. Isolating surface-enhanced Raman scattering hot spots using multiphoton lithography. *J. Am. Chem. Soc.* **131**, 16356–16357 (2009).
185. Gunnarsson, L. *et al.* Interparticle coupling effects in nanofabricated substrates for surface-enhanced Raman scattering. **78**, 802–804 (2001).
186. Atay, T., Song, J. H. & Nurmikko, A. V. Strongly interacting plasmon nanoparticle pairs: From dipole-dipole interaction to conductively coupled regime. *Nano Lett.* **4**, 1627–1631 (2004).
187. Yu, Q., Guan, P., Qin, D., Golden, G. & Wallace, P. M. Inverted size-dependence of surface-enhanced Raman scattering on gold nanohole and nanodisk arrays. *Nano Lett.* **8**, 1923–1928 (2008).
188. Lee, S. J., Morrill, A. R. & Moskovits, M. Hot spots in silver nanowire bundles for surface-enhanced Raman spectroscopy. *J. Am. Chem. Soc.* **128**, 2200–2201 (2006).
189. Qin, L., Park, S., Huang, L. & Mirkin, C. A. On-Wire Lithography. **309**, 113–116 (2005).
190. Qin, L. *et al.* Designing, fabricating, and imaging Raman hot spots. *Proc. Natl. Acad. Sci. U. S. A.* **103**, 13300–13303 (2006).
191. Ward, D. R. *et al.* Electromigrated nanoscale gaps for surface-enhanced Raman spectroscopy. *Nano*

Lett. **7**, 1396–1400 (2007).
192. Gopinath, A. *et al.* Plasmonic nanogalaxies: Multiscale aperiodic arrays for surface-enhanced Raman sensing. *Nano Lett.* **9**, 3922–3929 (2009).
193. Lim, D. K., Jeon, K. S., Kim, H. M., Nam, J. M. & Suh, Y. D. Nanogap-engineerable raman-active nanodumbbells for single-molecule detection. *Nat. Mater.* **9**, 60–67 (2010).
194. Lim, D. K. *et al.* Highly uniform and reproducible surface-enhanced Raman scattering from DNA-tailorable nanoparticles with 1-nm interior gap. *Nat. Nanotechnol.* **6**, 452–460 (2011).
195. Gehan, H. *et al.* Thermo-induced electromagnetic coupling in gold/polymer hybrid plasmonic structures probed by surface-enhanced raman scattering. *ACS Nano* **4**, 6491–6500 (2010).
196. Álvarez-Puebla, R. A., Contreras-Cáceres, R., Pastoriza-Santos, I., Pérez-Juste, J. & Liz-Marzán, L. M. Au@pNIPAM colloids as molecular traps for surface-enhanced, spectroscopic, ultra-sensitive analysis. *Angew. Chemie - Int. Ed.* **48**, 138–143 (2009).
197. Kim, N. H., Lee, S. J. & Moskovits, M. Reversible Tuning of SERS Hot Spots with Aptamers. *Adv. Mater.* **23**, 4152–4156 (2011).
198. Doering, W. E., Piotti, M. E., Natan, M. J. & Freeman, R. G. SERS as a Foundation for Nanoscale, Optically Detected Biological Labels. *Adv. Mater.* **19**, 3100–3108 (2007).
199. Gratton, S. E. A. *et al.* The pursuit of a scalable nanofabrication platform for use in material and life science applications. *Acc. Chem. Res.* **41**, 1685–1695 (2008).
200. Alexander, K. D. *et al.* A high-throughput method for controlled hot-spot fabrication in SERS-active gold nanoparticle dimer arrays. *J. Raman Spectrosc.* **40**, 2171–2175 (2009).
201. Hu, M. *et al.* Gold Nanofingers for Molecule Trapping and Detection. *J. Am. Chem. Soc.* **132**, 12820–12822 (2010).
202. Ou, F. S. *et al.* Hot-spot engineering in polygonal nanofinger assemblies for surface enhanced Raman spectroscopy. *Nano Lett.* **11**, 2538–2542 (2011).
203. Domke, K. F., Zhang, D. & Pettinger, B. Toward Raman fingerprints of single dye molecules at atomically smooth Au(111). *J. Am. Chem. Soc.* **128**, 14721–14727 (2006).
204. Neacsu, C. C., Dreyer, J., Behr, N. & Raschke, M. B. Scanning-probe Raman spectroscopy with single-molecule sensitivity. *Phys. Rev. B - Condens. Matter Mater. Phys.* **73**, 1–4 (2006).
205. Sonntag, M. D. *et al.* Single-molecule tip-enhanced Raman spectroscopy. *J. Phys. Chem. C* **116**, 478–483 (2012).
206. Li, J. F. *et al.* Shell-isolated nanoparticle-enhanced Raman spectroscopy. *Nature* **464**, 392–395 (2010).
207. Anema, J. R., Li, J. F., Yang, Z. L., Ren, B. & Tian, Z. Q. Shell-isolated nanoparticle-enhanced raman spectroscopy: Expanding the versatility of surface-enhanced raman scattering. *Annu. Rev. Anal. Chem.* **4**, 129–150 (2011).
208. Liu, L. *et al.* A high-performance and low cost SERS substrate of plasmonic nanopillars on plastic film fabricated by nanoimprint lithography with AAO template. *AIP Adv.* **7**, (2017).
209. Ye, X. *et al.* Improved size-tunable synthesis of monodisperse gold nanorods through the use of aromatic additives. *ACS Nano* **6**, 2804–2817 (2012).
210. Lim, I. I. S. *et al.* Adsorption of cyanine dyes on gold nanoparticles and formation of J-aggregates in the nanoparticle assembly. *J. Phys. Chem. B* **110**, 6673–6682 (2006).
211. Fraire, J. C., Pérez, L. A. & Coronado, E. A. Cluster size effects in the surface-enhanced raman scattering response of ag and Au nanoparticle aggregates: Experimental and theoretical insight. *J. Phys. Chem. C* **117**, 23090–23107 (2013).
212. Chan, S., Kwon, S., Koo, T. W., Lee, L. P. & Berlin, A. A. Surface-Enhanced Raman Scattering of Small Molecules from Silver-Coated Silicon Nanopores. *Adv. Mater.* **15**, 1595–1598 (2003).
213. Demirel, M. C. *et al.* Bio-organism sensing via surface enhanced Raman spectroscopy on controlled metal/polymer nanostructured substrates. *Biointerphases* **4**, 35–41 (2009).
214. Kudelski, A. Raman studies of rhodamine 6G and crystal violet sub-monolayers on electrochemically roughened silver substrates: Do dye molecules adsorb preferentially on highly SERS-active sites? *Chem. Phys. Lett.* **414**, 271–275 (2005).
215. Zeman, E. J. & Schatz, G. C. J100287a028. 1–10 (2001).
216. Hildebrandt, P. & Stockhurger, M. Surface-Enhanced Resonance Raman Spectroscopy of Rhodamine 6G adsorbed on colloidal silver. *J. Phys. Chem.* **88**, 5935–5944 (1984).
217. Cintra, S. *et al.* Sculpted substrates for SERS. *Faraday Discuss.* **132**, 191–199 (2006).
218. Choi, S. S. *et al.* Fabrication of pyramidal probes with various periodic patterns and a single nanopore. *J. Vac. Sci. Technol. B, Nanotechnol. Microelectron. Mater. Process. Meas. Phenom.* **33**, 06F203 (2015).
219. Gaddis, A. L. Geometrical Effects on Electromagnetic Enhancement to SERS from Metal

Nanoparticle Dimer Arrays. (2009).
220. Şendur, K. & Baran, E. Near-field optical power transmission of dipole nano-antennas. *Appl. Phys. B Lasers Opt.* **96**, 325–335 (2009).
221. Huebner, U., Boucher, R., Schneidewind, H., Cialla, D. & Popp, J. Microfabricated SERS-arrays with sharp-edged metallic nanostructures. *Microelectron. Eng.* **85**, 1792–1794 (2008).
222. Grand, J. *et al.* Optimization of SERS-active substrates for near-field Raman spectroscopy. *Synth. Met.* **139**, 621–624 (2003).
223. Walsh, G. F., Forestiere, C. & Dal Negro, L. Plasmon-enhanced depolarization of reflected light from arrays of nanoparticle dimers. *Opt. Express* **19**, 21081 (2011).
224. Brolo, A. G., Gordon, R., Leathem, B. & Kavanagh, K. L. Surface plasmon sensor based on the enhanced light transmission through arrays of nanoholes in gold films. *Langmuir* **20**, 4813–4815 (2004).
225. Heyderman, L. J. *et al.* Arrays of nanoscale magnetic dots: Fabrication by x-ray interference lithography and characterization. *Appl. Phys. Lett.* **85**, 4989–4991 (2004).
226. Haynes, C. L. & Van Duyne, R. P. Nanosphere lithography: A versatile nanofabrication tool for studies of size-dependent nanoparticle optics. *J. Phys. Chem. B* **105**, 5599–5611 (2001).
227. Alvarez-Puebla, R. A., Ross, D. J., Nazri, G. A. & Aroca, R. F. Surface-enhanced Raman scattering on nanoshells with tunable surface plasmon resonance. *Langmuir* **21**, 10504–10508 (2005).
228. Murphy, C. J. *et al.* Anisotropic metal nanoparticles: Synthesis, assembly, and optical applications. *J. Phys. Chem. B* **109**, 13857–13870 (2005).
229. Aizpurua, J. *et al.* Optical Properties of Gold Nanorings. *Phys. Rev. Lett.* **90**, 4 (2003).
230. Huang, W., Yu, X., Liu, Y., Qiao, W. & Chen, L. A review of the scalable nano-manufacturing technology for flexible devices. *Front. Mech. Eng.* **12**, 99–109 (2017).
231. Krishnamoorthy, S. Nanostructured sensors for biomedical applications-a current perspective. *Curr. Opin. Biotechnol.* **34**, 118–124 (2015).
232. Park, S. *et al.* Macroscopic 10 Terabit/in2 Arrays from Block Copolymers with Lateral Order Supplemental Information. *Science (80-.).* **323**, 1030 (2009).
233. Cheng, J. Y., Ross, C. A., Thomas, E. L., Smith, H. I. & Vancso, G. J. Fabrication of nanostructures with long-range order using block copolymer lithography. *Appl. Phys. Lett.* **81**, 3657–3659 (2002).
234. Stoykovich, M. P. *et al.* Directed self-assembly of block copolymers for nanolithography: Fabrication of isolated features and essential integrated circuit geometries. *ACS Nano* **1**, 168–175 (2007).
235. Yang, J. K. W. *et al.* Complex self-assembled patterns using sparse commensurate templates with locally varying motifs. *Nat. Nanotechnol.* **5**, 256–260 (2010).
236. Cetin, A. E. *et al.* Handheld high-throughput plasmonic biosensor using computational on-chip imaging. *Light Sci. Appl.* **3**, e122 (2014).
237. Aksu, S. *et al.* High-throughput nanofabrication of infrared plasmonic nanoantenna arrays for vibrational nanospectroscopy. *Nano Lett.* **10**, 2511–2518 (2010).
238. Vazquez-Mena, O. *et al.* High-resolution resistless nanopatterning on polymer and flexible substrates for plasmonic biosensing using stencil masks. *ACS Nano* **6**, 5474–5481 (2012).
239. Chou, S. Y., Krauss, P. R. & Renstrom, P. J. Imprint Lithography with 25-Nanometer Resolution. *Science (80-.).* **272**, 85–87 (1996).
240. McNay, G., Eustace, D., Smith, W. E., Faulds, K. & Graham, D. Surface-enhanced Raman scattering (SERS) and surface-enhanced resonance raman scattering (SERRS): A review of applications. *Appl. Spectrosc.* **65**, 825–837 (2011).
241. Sánchez-Iglesias, A. *et al.* Chemical seeded growth of Ag nanoparticle arrays and their application as reproducible SERS substrates. *Nano Today* **5**, 21–27 (2010).
242. Rekha, C. R., Sameera, S., Nayar, V. U. & Gopchandran, K. G. Simultaneous detection of different probe molecules using silver nanowires as SERS substrates. *Spectrochim. Acta - Part A Mol. Biomol. Spectrosc.* **213**, 150–158 (2019).
243. Krishnamoorthy, S., Manipaddy, K. K. & Yap, F. L. Wafer-level self-organized copolymer templates for nanolithography with sub-50 nm feature and spatial resolutions. *Adv. Funct. Mater.* **21**, 1102–1112 (2011).
244. Rastogi, R., Beggiato, M., Adam, P. M., Juodkazis, S. & Krishnamoorthy, S. Nanoplasmonic Arrays with High Spatial Resolutions, Quality, and Throughput for Quantitative Detection of Molecular Analytes. *Nanoplasmonic* (2019). doi:10.5772/intechopen.89064
245. Krishnamoorthy, S., Pugin, R., Brugger, J., Heinzelmann, H. & Hinderling, C. Tuning the dimensions and periodicities of nanostructures starting from the same polystyrene-block-poly(2-vinylpyridine) diblock copolymer. *Adv. Funct. Mater.* **16**, 1469–1475 (2006).
246. Scopelliti, P. E. *et al.* The effect of surface nanometre-scale morphology on protein adsorption. *PLoS*

One **5**, 1–9 (2010).
247. Raffaini, G. & Ganazzoli, F. Surface topography effects in protein adsorption on nanostructured carbon allotropes. *Langmuir* **29**, 4883–4893 (2013).
248. De, M., Miranda, O. R., Rana, S. & Rotello, V. M. Size and geometry dependent protein–nanoparticle self-assembly. *Chem. Commun.* 2157 (2009). doi:10.1039/b900552h
249. Roach, P., Farrar, D. & Perry, C. C. Surface tailoring for controlled protein adsorption: Effect of topography at the nanometer scale and chemistry. *J. Am. Chem. Soc.* **128**, 3939–3945 (2006).
250. Pino, P. Del *et al.* Protein corona formation around nanoparticles - From the past to the future. *Mater. Horizons* **1**, 301–313 (2014).
251. Rechendorff, K., Hovgaard, M. B., Foss, M., Zhdanov, V. P. & Besenbacher, F. Enhancement of protein adsorption induced by surface roughness. *Langmuir* **22**, 10885–10888 (2006).
252. Pedrosa, C. R. *et al.* Controlled Nanoscale Topographies for Osteogenic Differentiation of Mesenchymal Stem Cells. *ACS Appl. Mater. Interfaces* **11**, 8858–8866 (2019).
253. Biggs, M. J. P., Richards, R. G. & Dalby, M. J. Nanotopographical modification: a regulator of cellular function through focal adhesions. *Nanomedicine Nanotechnology, Biol. Med.* **6**, 619–633 (2010).
254. Li, S. S. *et al.* Simultaneous quantification of multiple endogenous biothiols in single living cells by plasmonic Raman probes. *Chem. Sci.* **8**, 7582–7587 (2017).
255. Ming, T. *et al.* Strong polarization dependence of plasmon-enhanced fluorescence on single gold nanorods. *Nano Lett.* **9**, 3896–3903 (2009).
256. Chaabani, W., Chehaidar, A., Proust, J. & Plain, J. Theoretical Analysis of the Optical Response of Silicon/Silica/Gold Multishell Nanoparticles in Biological Tissue. *Adv. Mater. Sci. Eng.* **2019**, (2019).
257. Zhang, L. *et al.* Highly active Au NP microarray films for direct SERS detection. *J. Mater. Chem. C* **7**, 15259–15268 (2019).
258. Driskell, J. D. *et al.* Low-level detection of viral pathogens by a surface-enhanced Raman scattering based immunoassay. *Anal. Chem.* **77**, 6147–6154 (2005).
259. Chikkaraddy, R. *et al.* Mapping Nanoscale Hotspots with Single-Molecule Emitters Assembled into Plasmonic Nanocavities Using DNA Origami. *Nano Lett.* **18**, 405–411 (2018).
260. Kim, M. *et al.* Hierarchic Interfacial Nanocube Assembly for Sensitive, Selective, and Quantitative DNA Detection with Surface-Enhanced Raman Scattering. *Anal. Chem.* **91**, 10467–10476 (2019).
261. Li, A., Isaacs, S., Abdulhalim, I. & Li, S. Ultrahigh Enhancement of Electromagnetic Fields by Exciting Localized with Extended Surface Plasmons. *J. Phys. Chem. C* **119**, 19382–19389 (2015).
262. Li, M. *et al.* Three-Dimensional Hierarchical Plasmonic Nano-Architecture Enhanced Surface-Enhanced Raman Scattering Immunosensor for Cancer Biomarker Detection in Blood Plasma. *ACS Nano* **7**, 4967–4976 (2013).
263. Li, M. *et al.* Plasmonic nanorice antenna on triangle nanoarray for surface-enhanced Raman scattering detection of hepatitis B virus DNA. *Anal. Chem.* **85**, 2072–2078 (2013).
264. Zheng, Y. *et al.* Reversible gating of smart plasmonic molecular traps using thermoresponsive polymers for single-molecule detection. *Nat. Commun.* **6**, 1–8 (2015).
265. Wang, T. *et al.* Naked eye plasmonic indicator with multi-responsive polymer brush as signal transducer and amplifier. *Nanoscale* **9**, 1925–1933 (2017).
266. Chandra, D. & Yang, S. Capillary-force-induced clustering of micropillar arrays: Is it caused by isolated capillary bridges or by the lateral capillary meniscus interaction force? *Langmuir* **25**, 10430–10434 (2009).
267. Oh, Y.-J., Kang, M., Park, M. & Jeong, K.-H. Engineering hot spots on plasmonic nanopillar arrays for SERS: A review. *BioChip J.* **10**, 297–309 (2016).
268. Hao, E. & Schatz, G. C. Electromagnetic fields around silver nanoparticles and dimers. *J. Chem. Phys.* **120**, 357–366 (2004).
269. Ding, S. Y. *et al.* Nanostructure-based plasmon-enhanced Raman spectroscopy for surface analysis of materials. *Nat. Rev. Mater.* **1**, (2016).
270. Fang, C. *et al.* Metallization of silicon nanowires and SERS response from a single metallized nanowire. *Chem. Mater.* **21**, 3542–3548 (2009).
271. Wu, K. Engineering Plasmonic Nanopillar Arrays for Surface-enhanced Raman Spectroscopy. (2016).
272. Kim, A. *et al.* Study of molecular trapping inside gold nanofinger arrays on surface-enhanced raman substrates. *J. Am. Chem. Soc.* **133**, 8234–8239 (2011).
273. Drachev, V. P. *et al.* Adaptive silver films for surface-enhanced Raman spectroscopy of biomolecules. *J. Raman Spectrosc.* **36**, 648–656 (2005).

274. Goodacre, R., Graham, D. & Faulds, K. Recent developments in quantitative SERS: Moving towards absolute quantification. *TrAC - Trends Anal. Chem.* **102**, 359–368 (2018).
275. Hu, Y. & Lu, X. Rapid Detection of Melamine in Tap Water and Milk Using Conjugated 'One-Step' Molecularly Imprinted Polymers-Surface Enhanced Raman Spectroscopic Sensor. *J. Food Sci.* **81**, N1272–N1280 (2016).
276. Álvarez-Puebla, R. A. & Liz-Marzán, L. M. Environmental applications of plasmon assisted Raman scattering. *Energy Environ. Sci.* **3**, 1011–1017 (2010).
277. Qiao, X. *et al.* Selective Surface Enhanced Raman Scattering for Quantitative Detection of Lung Cancer Biomarkers in Superparticle@MOF Structure. *Adv. Mater.* **30**, 1–8 (2018).
278. Borisov, I. A., Lobanov, A. V., Reshetilov, A. N. & Kurganov, B. I. Quantitative Analysis of the Calibration Dependences for Biosensors. *Prikl. Biokhimiya i Mikrobiol.* **36**, 259–260 (2000).
279. Davies, C. Immunoassay Performance Measures. in *The Immunoassay Handbook* 11–26 (Elsevier, 2013). doi:10.1016/B978-0-08-097037-0.00003-8
280. Gillet, P., Mori, M., Van Esbroeck, M., Van Den Ende, J. & Jacobs, J. Assessment of the prozone effect in malaria rapid diagnostic tests. *Malar. J.* **8**, 1–7 (2009).
281. Amarasiri Fernando, S. & Wilson, G. S. Studies of the 'hook' effect in the one-step sandwich immunoassay. *J. Immunol. Methods* **151**, 47–66 (1992).
282. Bell, S. E. J. *et al.* Towards Reliable and Quantitative Surface-Enhanced Raman Scattering (SERS): From Key Parameters to Good Analytical Practice. *Angew. Chemie - Int. Ed.* **59**, 5454–5462 (2020).
283. Szlag, V. M. *et al.* Molecular Affinity Agents for Intrinsic Surface-Enhanced Raman Scattering (SERS) Sensors. *ACS Appl. Mater. Interfaces* **10**, 31825–31844 (2018).
284. Hassibi, A., Vikalo, H. & Hajimiri, A. On noise processes and limits of performance in biosensors. *J. Appl. Phys.* **102**, 1–12 (2007).
285. Wu, Y., Tilley, R. D. & Gooding, J. J. Challenges and Solutions in Developing Ultrasensitive Biosensors. *J. Am. Chem. Soc.* **141**, 1162–1170 (2019).
286. Gooding, J. J. & Gaus, K. Single-Molecule Sensors: Challenges and Opportunities for Quantitative Analysis. *Angew. Chemie - Int. Ed.* **55**, 11354–11366 (2016).
287. Jonsson, M. Nanoplasmonic Biosensing Exploring Unique Possibilities. (2010). doi:10.1017/CBO9781107415324.004
288. Wayment, J. R. & Harris, J. M. Biotin-avidin binding kinetics measured by single-molecule imaging. *Anal. Chem.* **81**, 336–342 (2009).
289. Jung, L. S., Nelson, K. E., Stayton, P. S. & Campbell, C. T. Binding and dissociation kinetics of wild-type and mutant streptavidins on mixed biotin-containing alkylthiolate monolayers. *Langmuir* **16**, 9421–9432 (2000).
290. Cussler, E. L. *Diffusion: mass transfer in fluid systemsitle*. (Cambridge university press, 2009).
291. Singh, N., Karim, A., Bates, F. S., Tirrell, M. & Furusawa, K. Adsorption of End-Functionalized Polystyrene on Model Textured Surfaces. *Macromolecules* **27**, 2586–2594 (1994).
292. Nair, P. R. & Alam, M. A. Theory of 'selectivity' of label-free nanobiosensors: A geometro-physical perspective. *J. Appl. Phys.* **107**, 1–6 (2010).
293. Stone, H. A., Stroock, A. D. & Ajdari, A. Engineering Flows in Small Devices. *Annu. Rev. Fluid Mech.* **36**, 381–411 (2004).
294. O'Kane, D. F. & Mittal, K. L. Plasma Cleaning of Metal Surfaces. *J Vac Sci Technol* **11**, 567–569 (1974).
295. Sowell, R. R., Cuthrell, R. E., Mattox, D. M. & Bland, R. D. Surface cleaning by ultraviolet radiation. *J. Vac. Sci. Technol.* **11**, 474–475 (2002).
296. Boyd, D. A. *Block Copolymer Lithography*. *New and Future Developments in Catalysis: Catalysis by Nanoparticles* (Elsevier B.V., 2013). doi:10.1016/B978-0-444-53874-1.00013-5
297. Krishnamoorthy, S., Hinderling, C. & Heinzelmann, H. Nanoscale patterning with block copolymers. *Mater. Today* **9**, 40–47 (2006).
298. Hawker, C. J. & Russell, T. P. Block Copolymer Lithography: Merging "Bottom-Up" with "Top-Down" Processes. *MRS Bull.* **30**, 952–966 (2005).
299. Swann, J. M. G. & Topham, P. D. Design and application of nanoscale actuators using block-copolymers. *Polymers (Basel).* **2**, 454–469 (2010).
300. Lynd, N. A., Meuler, A. J. & Hillmyer, M. A. Polydispersity and block copolymer self-assembly. *Prog. Polym. Sci.* **33**, 875–893 (2008).
301. Gromadzki, D. Engineering soft nanostructured functional materials via orthogonal chemistry. *Rev. Environ. Sci. Biotechnol.* **9**, 301–306 (2010).
302. Douglas, J. F. Polymeric Liquids and Networks: Structure and Properties Polymeric Liquids and Networks: Structure and Properties William W. Graessley Garland Science, New York, 2004. $84.95

(559 pp.). ISBN 0-8153-4169-5. *Phys. Today* **58**, 64–65 (2005).
303. Bates, F. S. & Fredrickson, G. H. Block copolymer thermodynamics: Theory and experiment. *Annu. Rev. Phys. Chem.* **41**, 525–557 (1990).
304. Ku, S. J. *et al.* Highly ordered freestanding titanium oxide nanotube arrays using Si-containing block copolymer lithography and atomic layer deposition. *Nanotechnology* **24**, 085301 (2013).
305. Wang, Y. *et al.* Nanostructured gold films for SERS by block copolymer-templated galvanic displacement reactions. *Nano Lett.* **9**, 2384–2389 (2009).
306. Li, T. *et al.* Wafer-Scale Nanopillars Derived from Block Copolymer Lithography for Surface-Enhanced Raman Spectroscopy. *ACS Appl. Mater. Interfaces* **8**, 15668–15675 (2016).
307. Hillmyer, M. A. Nanoporous materials from block copolymer precursors. *Adv. Polym. Sci.* **190**, 137–181 (2005).
308. Kim, S. H., Misner, M. J. & Russell, T. P. Solvent-induced ordering in thin film diblock copolymer/homopolymer mixtures. *Adv. Mater.* **16**, 2119–2123 (2004).
309. Atanase, L. I. & Riess, G. Self-assembly of block and graft copolymers in organic solvents: An overview of recent advances. *Polymers (Basel).* **10**, (2018).
310. Li, W. *et al.* Nano polymeric carrier fabrication technologies for advanced antitumor therapy. *Biomed Res. Int.* **2013**, (2013).
311. Mansky, P., haikin, P. & Thomas, E. L. Monolayer films of diblock copolymer microdomains for nanolithographic applications. *J. Mater. Sci.* **30**, 1987–1992 (1995).
312. Lu, J. *et al.* Using a ferrocenylsilane-based block copolymer as a template to produce nanotextured Ag surfaces: Uniformly enhanced surface enhanced Raman scattering active substrates. *Nanotechnology* **17**, 5792–5797 (2006).
313. Spatz, J. P., Sheiko, S. & Möller, M. Substrate-induced lateral micro-phase separation of a diblock copolymer. *Adv. Mater.* **8**, 513–517 (1996).
314. Letchford, K. & Burt, H. A review of the formation and classification of amphiphilic block copolymer nanoparticulate structures: micelles, nanospheres, nanocapsules and polymersomes. *Eur. J. Pharm. Biopharm.* **65**, 259–269 (2007).
315. Yap, F. L., Thoniyot, P., Krishnan, S. & Krishnamoorthy, S. Nanoparticle cluster arrays for high-performance SERS through directed self-assembly on flat substrates and on optical fibers. *ACS Nano* **6**, 2056–2070 (2012).
316. Dinda, S. *et al.* Engineering 3D Nanoplasmonic Assemblies for High Performance Spectroscopic Sensing. *ACS Appl. Mater. Interfaces* **7**, 27661–27666 (2015).
317. Yap, F. L., Thoniyot, P., Krishnan, S. & Krishnamoorthy, S. Nanoparticle Cluster Arrays for High-Performance SERS through Directed Self-Assembly on Flat Substrates and on Optical Fibers. *ACS Nano* **6**, 2056–2070 (2012).
318. Krishnamoorthy, S., Krishnan, S., Thoniyot, P. & Low, H. Y. Inherently reproducible fabrication of plasmonic nanoparticle arrays for SERS by combining nanoimprint and copolymer lithography. *ACS Appl. Mater. Interfaces* **3**, 1033–1040 (2011).
319. Yang, Y. *et al.* A facile method of removing several common surface-enhanced Raman scattering probe molecules adsorbed on Ag with sodium borohydride solution. *J. Opt. (United Kingdom)* **17**, (2015).
320. Yang, C. *et al.* Large-scale controlled fabrication of highly roughened flower-like silver nanostructures in liquid crystalline phase. *Sci. Rep.* **5**, 1–8 (2015).
321. Lu, Y., Liu, G. L. & Lee, L. P. High-density silver nanoparticle film with temperature-controllable interparticle spacing for a tunable surface enhanced Raman scattering substrate. *Nano Lett.* **5**, 5–9 (2005).
322. Yang, L. *et al.* Engineering nanoparticle cluster arrays for bacterial biosensing: The role of the building block in multiscale SERS substrates. *Adv. Funct. Mater.* **20**, 2619–2628 (2010).
323. Wang, P., Yu, X., Zhu, Y., Yu, Y. & Yuan, W. Batch fabrication of broadband metallic planar microlenses and their arrays combining nanosphere self-assembly with conventional photolithography. *Nanoscale Res. Lett.* **12**, (2017).
324. Yang, B. *et al.* Tuning the intensity of metal-enhanced fluorescence by engineering silver nanoparticle arrays. *Small* **6**, 1038–1043 (2010).
325. Nordlander, P. & Prodan, E. Plasmon hybridization in nanoparticles near metallic surfaces. *Nano Lett.* **4**, 2209–2213 (2004).
326. Brandl, D. W., Mirin, N. A. & Nordlander, P. Plasmon modes of nanosphere trimers and quadrumers. *J. Phys. Chem. B* **110**, 12302–12310 (2006).
327. Hentschel, M. *et al.* Transition from Isolated to Collective Modes in Plasmonic Oligomers. *Nano Lett.* **10**, 2721–2726 (2010).

328. Quinten, M. & Kreibig, U. Optical properties of aggregates of small metal particles. *Surf. Sci.* **172**, 557–577 (1986).
329. Mirin, N. A., Bao, K. & Nordlander, P. Fano Resonances in plasmonic nanoparticle aggregates. *J. Phys. Chem. A* **113**, 4028–4034 (2009).
330. Natan, M. J. Concluding Remarks : Surface enhanced Raman scattering. *Faraday Discuss.* **132**, 321 (2006).
331. Ueno, K., Juodkazis, S., Mizeikis, V., Sasaki, K. & Misawa, H. Clusters of closely spaced gold nanoparticles as a source of two-photon photoluminescence at visible wavelengths. *Adv. Mater.* **20**, 26–30 (2008).
332. Fan, J. A. *et al.* Fano-like interference in self-assembled plasmonic quadrumer clusters. *Nano Lett.* **10**, 4680–4685 (2010).
333. Jin, R. Nanoparticle clusters light Up in SERS. *Angew. Chemie - Int. Ed.* **49**, 2826–2829 (2010).
334. Le, F. *et al.* Metallic Nanoparticle Arrays : A Common Substrate for Both Surface-Enhanced Raman Scattering and Surface-Enhanced Infrared Absorption. *ACS Nano* **2**, 707–718 (2008).
335. Lee, J. S., Ulmann, P. A., Han, M. S. & Mirkin, C. A. A DNA - Gold nanoparticle-based colorimetric competition assay for the detection of cysteine. *Nano Lett.* **8**, 529–533 (2008).
336. Harpster, M. H. *et al.* SERS detection of indirect viral DNA capture using colloidal gold and methylene blue as a Raman label. *Biosens. Bioelectron.* **25**, 674–681 (2009).
337. Talley, C. E. *et al.* Surface-enhanced Raman scattering from individual Au nanoparticles and nanoparticle dimer substrates. *Nano Lett.* **5**, 1569–1574 (2005).
338. Lassiter, J. B. *et al.* Fano resonances in plasmonic nanoclusters: Geometrical and chemical tunability. *Nano Lett.* **10**, 3184–3189 (2010).
339. Ap, A. *et al.* Organization Of Nanocrystal Molecules Using DNA. *Nature* **382**, 609–611 (1996).
340. Qiu, P., Jensen, C., Charity, N., Towner, R. & Mao, C. Oil phase evaporation-induced self-assembly of hydrophobic nanoparticles into spherical clusters with controlled surface chemistry in an oil-in-water dispersion and comparison of behaviors of individual and clustered iron oxide nanoparticles. *J. Am. Chem. Soc.* **132**, 17724–17732 (2010).
341. Correa-Duarte, M. A. & Liz-Marzán, L. M. Carbon nanotubes as templates for one-dimensional nanoparticle assemblies. *J. Mater. Chem.* **16**, 22–25 (2006).
342. Wang, H. *et al.* Cylindrical block co-micelles with spatially selective functionalization by nanoparticles. *J. Am. Chem. Soc.* **129**, 12924–12925 (2007).
343. Blum, A. S. *et al.* Cowpea mosaic virus as a scaffold for 3-D patterning of gold nanoparticles. *Nano Lett.* **4**, 867–870 (2004).
344. Lee, W., Lee, S. Y., Briber, R. M. & Rabin, O. Self-assembled SERS substrates with tunable surface plasmon resonances. *Adv. Funct. Mater.* **21**, 3424–3429 (2011).
345. Misner, M. J., Skaff, H., Emrick, T. & Russell, T. P. Directed Deposition of Nanoparticles Using Diblock Copolymer Templates. *Adv. Mater.* **15**, 221–224 (2003).
346. Wang, L., Montagne, F., Hoffmann, P., Heinzelmann, H. & Pugin, R. Hierarchical positioning of gold nanoparticles into periodic arrays using block copolymer nanoring templates. *J. Colloid Interface Sci.* **356**, 496–504 (2011).
347. Förster, S. & Antonietti, M. Amphiphilic block copolymers in structure-controlled nanomaterial hybrids. *Adv. Mater.* **10**, 195–217 (1998).
348. Turkevich, J., Stevenson, P. C. & Hillier, J. A study of the nucleation and growth processes in the synthesis of colloidal gold. *Discuss. Faraday Soc.* **11**, 55–75 (1951).
349. Frens, G. Controlled nucleation for the regulation of the particle size in monodisperse gold suspensions. *Nat. Phys. Sci.* **241**, 20 (1973).
350. Wang, D., Ji, R., Du, S., Albrecht, A. & Schaaf, P. Ordered arrays of nanoporous silicon nanopillars and silicon nanopillars with nanoporous shells. *Nanoscale Res. Lett.* **8**, 1–9 (2013).
351. Diedenhofen, S. L. *et al.* Broad-band and omnidirectional antireflection coatings based on semiconductor nanorods. *Adv. Mater.* **21**, 973–978 (2009).
352. Mujeeb-U-Rahman, M., Adalian, D. & Scherer, A. Fabrication of Patterned Integrated Electrochemical Sensors. *J. Nanotechnol.* **2015**, (2015).
353. Yang, J. *et al.* Surface-enhanced Raman spectroscopy based quantitative bioassay on aptamer-functionalized nanopillars using large-area Raman mapping. *ACS Nano* **7**, 5350–5359 (2013).
354. Gartia, M. R. *et al.* Rigorous surface enhanced Raman spectral characterization of large-area high-uniformity silver-coated tapered silica nanopillar arrays. *Nanotechnology* **21**, (2010).
355. Wasistoa, H. S. *et al.* Femtogram mass measurement of airborne engineered nanoparticles using silicon nanopillar resonators. *Procedia Eng.* **47**, 289–292 (2012).
356. Park, H. *et al.* Broadband optical antireflection enhancement by integrating antireflective nanoislands

with silicon nanoconical-frustum arrays. *Adv. Mater.* **23**, 5796–5800 (2011).
357. Ruan, C., Eres, G., Wang, W., Zhang, Z. & Gu, B. Controlled fabrication of nanopillar arrays as active substrates for surface-enhanced Raman spectroscopy. *Langmuir* **23**, 5757–5760 (2007).
358. Kubo, W. & Fujikawa, S. Au double nanopillars with nanogap for plasmonic sensor. *Nano Lett.* **11**, 8–15 (2011).
359. Kugel, V. & Ji, H.-F. Nanopillars for Sensing. *J. Nanosci. Nanotechnol.* **14**, 6469–6477 (2014).
360. Karadan, P., Aggarwal, S., Anappara, A. A., Narayana, C. & Barshilia, H. C. Tailored periodic Si nanopillar based architectures as highly sensitive universal SERS biosensing platform. *Sensors Actuators, B Chem.* **254**, 264–271 (2018).
361. Gudur, A. & Ji, H.-F. Bio-Applications of Nanopillars. *Front. Nanosci. Nanotechnol.* **2**, 1–10 (2017).
362. Zavaliche, F. *et al.* Electrically assisted magnetic recording in multiferroic nanostructures. *Nano Lett.* **7**, 1586–1590 (2007).
363. Schneider, L., Feidenhans'L, N. A., Telecka, A. & Taboryski, R. J. One-step Maskless Fabrication and Optical Characterization of Silicon Surfaces with Antireflective Properties and a White Color Appearance. *Sci. Rep.* **6**, 1–6 (2016).
364. Fujikawa, S., Takaki, R. & Kunitake, T. Fabrication of arrays of sub-20-nm silica walls via photolithography and solution-based molecular coating. *Langmuir* **22**, 9057–9061 (2006).
365. Cheung, C. L., Nikolić, R. J., Reinhardt, C. E. & Wang, T. F. Fabrication of nanopillars by nanosphere lithography. *Nanotechnology* **17**, 1339–1343 (2006).
366. Wang, Y., Lee, K. & Irudayaraj, J. Silver nanosphere SERS probes for sensitive identification of pathogens. *J. Phys. Chem. C* **114**, 16122–16128 (2010).
367. Shiohara, A., Wang, Y. & Liz-Marzán, L. M. Recent approaches toward creation of hot spots for SERS detection. *J. Photochem. Photobiol. C Photochem. Rev.* **21**, 2–25 (2014).
368. Kim, J. H. *et al.* A well-ordered flower-like gold nanostructure for integrated sensors via surface-enhanced Raman scattering. *Nanotechnology* **20**, (2009).
369. Duan, H., Yang, J. K. W. & Berggren, K. K. Controlled collapse of high-aspect-ratio nanostructures. *Small* **7**, 2661–2668 (2011).
370. Gates, B. D. *et al.* Shear patterning of microdominos: A new class of procedures for making micro- and nanostructures. *Angew. Chemie - Int. Ed.* **43**, 2780–2783 (2004).
371. Schmidt, M. S., Hübner, J. & Boisen, A. Large area fabrication of leaning silicon nanopillars for Surface Enhanced Raman Spectroscopy. *Adv. Mater.* **24**, 11–18 (2012).
372. Singh, A. *et al.* Impact of sequential infiltration synthesis on pattern fidelity of DSA lines. in *Advances in Patterning Materials and Processes XXXII* (eds. Wallow, T. I. & Hohle, C. K.) **9425**, 94250N (2015).
373. Ishchenko, O. M. *et al.* Investigating Sequential Vapor Infiltration Synthesis on Block-Copolymer-Templated Titania Nanoarrays. *J. Phys. Chem. C* **120**, 7067–7076 (2016).
374. Yin, J., Xu, Q., Wang, Z., Yao, X. & Wang, Y. Highly ordered TiO2 nanostructures by sequential vapour infiltration of block copolymer micellar films in an atomic layer deposition reactor. *J. Mater. Chem. C* **1**, 1029–1036 (2013).
375. Peng, Q., Tseng, Y. C., Darling, S. B. & Elam, J. W. Nanoscopic patterned materials with tunable dimensions via atomic layer deposition on block copolymers. *Adv. Mater.* **22**, 5129–5133 (2010).
376. Malvern & Instruments, M. Dynamic Light Scattering : An Introduction in 30 Minutes. *Technical Note MRK656-01* 1–8 (2011).
377. Aliano, A. *et al.* AFM, Tapping Mode. in *Encyclopedia of Nanotechnology* 99–99 (Springer Netherlands, 2012). doi:10.1007/978-90-481-9751-4_33
378. Zhang, L. & Fang, M. Nanomaterials in pollution trace detection and environmental improvement. *Nano Today* **5**, 128–142 (2010).
379. Cai, J. & Qi, L. Recent advances in antireflective surfaces based on nanostructure arrays. *Mater. Horizons* **2**, 37–53 (2015).
380. Bunaciu, A. A., Hoang, V. D. & Aboul-Enein, H. Y. Vibrational Micro-Spectroscopy of Human Tissues Analysis: Review. *Crit. Rev. Anal. Chem.* **47**, 194–203 (2017).
381. Liu, Y., Jaiswal, A., Poggi, M. A. & Wilson, W. D. Surface Plasmon Resonance and Quartz Crystal Microbalance Methods for Detection of Molecular Interactions. in *Chemosensors* 329–344 (John Wiley & Sons, Inc., 2011). doi:10.1002/9781118019580.ch16
382. Singh, P. *Surface plasmon resonance*. *Surface Plasmon Resonance* (2014). doi:10.1007/978-981-10-6156-1_109
383. Guerrini, L. & Graham, D. Molecularly-mediated assemblies of plasmonic nanoparticles for Surface-Enhanced Raman Spectroscopy applications. *Chem. Soc. Rev.* **41**, 7085–7107 (2012).
384. Dodson, S. *et al.* Optimizing Electromagnetic Hotspot in Plasmonic Bow-Tie Antennae. *J. Phys. ...*

(2013).
385. Xiao, R., Wang, C. W., Zhu, A. N. & Long, F. Single functional magnetic-bead as universal biosensing platform for trace analyte detection using SERS-nanobioprobe. *Biosens. Bioelectron.* **79**, 661–668 (2016).
386. Zhao, Q. *et al.* SERS-based ultrasensitive detection of organophosphorus nerve agents via substrate's surface modification. *J. Hazard. Mater.* **324**, 194–202 (2017).
387. Yaseen, T., Pu, H. & Sun, D. W. Functionalization techniques for improving SERS substrates and their applications in food safety evaluation: A review of recent research trends. *Trends Food Sci. Technol.* **72**, 162–174 (2018).
388. Plech, A. *et al.* Turkevich method for gold nanoparticle synthesis revisited. *J. Phys. Chem. B* **110**, 15700–15707 (2006).
389. Armbruster, D. A. & Pry, T. Limit of blank, limit of detection and limit of quantitation. *Clin. Biochem. Rev.* **29 Suppl 1**, S49-52 (2008).
390. Kankare, J. Sauerbrey Equation of Quartz Crystal Microbalance in Liquid Medium. *Langmuir* **18**, 7092–7094 (2002).
391. Olmon, R. L. *et al.* Optical dielectric function of gold. *Phys. Rev. B - Condens. Matter Mater. Phys.* **86**, (2012).
392. Adamczyk, Z., Zembala, M., Siwek, B. & Warszyński, P. Structure and ordering in localized adsorption of particles. *J. Colloid Interface Sci.* **140**, 123–137 (1990).
393. Adamczyk, Z., Nattich, M. & Barbasz, J. Deposition of colloid particles at heterogeneous and patterned surfaces. *Adv. Colloid Interface Sci.* **147**–**148**, 2–17 (2009).
394. Wilchek, M., Bayer, E. A. & Livnah, O. Essentials of biorecognition: The (strept)avidin-biotin system as a model for protein-protein and protein-ligand interaction. *Immunol. Lett.* **103**, 27–32 (2006).
395. Green, N. M. Avidin. *Adv. Protein Chem.* **29**, 85–133 (1975).
396. Mendez-Gonzalez, D. *et al.* Oligonucleotide Sensor Based on Selective Capture of Upconversion Nanoparticles Triggered by Target-Induced DNA Interstrand Ligand Reaction. *ACS Appl. Mater. Interfaces* **9**, 12272–12281 (2017).
397. Kang, T., Yoo, S. M., Yoon, I., Lee, S. Y. & Kim, B. Patterned multiplex pathogen DNA detection by Au Particle-on-wire SERS sensor. *Nano Lett.* **10**, 1189–1193 (2010).
398. Holmberg, A. *et al.* The biotin-streptavidin interaction can be reversibly broken using water at elevated temperatures. *Electrophoresis* **26**, 501–510 (2005).
399. Mahajan, S., Baumberg, J. J., Russell, A. E. & Bartlett, P. N. Reproducible SERRS from structured gold surfaces. *Phys. Chem. Chem. Phys.* **9**, 6016–6020 (2007).
400. Yu, W. & Mittra, R. A Conformal Finite Difference Time Domain Technique for Modeling Curved Dielectric Surfaces. *IEEE Microw. Wirel. Components Lett.* **11**, 25–27 (2001).
401. Nedyalkov, N. N. *et al.* Far- and near-field optical properties of gold nanoparticle ensembles. *Quantum Electron.* **42**, 1123–1127 (2012).
402. Wang, Z. B. *et al.* The influences of particle number on hot spots in strongly coupled metal nanoparticles chain. *J. Chem. Phys.* **128**, (2008).
403. Romero, I., Aizpurua, J., Bryant, G. W. & García De Abajo, F. J. Plasmons in nearly touching metallic nanoparticles: singular response in the limit of touching dimers. *Opt. Express* **14**, 9988 (2006).
404. Pérez, I. Plasmon interaction in coupled nanoparticles and nanovoids. (Universidad del País Vasco - Euskal Herriko Unibertsitatea, 2013).
405. Weber, P. C., Wendoloski, J. J., Pantoliano, M. W. & Salemme, F. R. Crystallographic and thermodynamic comparison of natural and synthetic ligands bound to streptavidin. *J. Am. Chem. Soc.* **114**, 3197–3200 (1992).
406. Drachev, V. P. & Shalaev, V. M. Biomolecule Sensing with Adaptive Plasmonic Nanostructures. *Surface-Enhanced Raman Scatt.* **366**, 351–366 (2006).
407. Chu, Y. & Crozier, K. B. Experimental study of the interaction between localized and propagating surface plasmons. *Opt. Lett.* **34**, 244 (2009).
408. Yamamoto, N., Ohtani, S. & García De Abajo, F. J. Gap and mie plasmons in individual silver nanospheres near a silver surface. *Nano Lett.* **11**, 91–95 (2011).
409. Mock, J. J. *et al.* Distance-dependent plasmon resonant coupling between a gold nanoparticle and gold film. *Nano Lett.* **8**, 2245–2252 (2008).
410. Hu, M., Ghoshal, A., Marquez, M. & Kik, P. G. Single particle spectroscopy study of metal-film-induced tuning of silver nanoparticle plasmon resonances. *J. Phys. Chem. C* **114**, 7509–7514 (2010).
411. Li, A., Srivastava, S. K., Abdulhalim, I. & Li, S. Engineering the hot spots in squared arrays of gold nanoparticles on a silver film. *Nanoscale* **8**, 15658–15664 (2016).
412. He, L., Smith, E. A., Natan, M. J. & Keating, C. D. The distance-dependence of colloidal Au-

amplified surface plasmon resonance. *J. Phys. Chem. B* **108**, 10973–10980 (2004).
413. Srivastava, S. K., Li, A., Li, S. & Abdulhalim, I. Optimal interparticle gap for ultrahigh field enhancement by LSP excitation via ESPs and confirmation using SERS. *J. Phys. Chem. C* **120**, 28735–28742 (2016).
414. Mubeen, S. *et al.* Plasmonic properties of gold nanoparticles separated from a gold mirror by an ultrathin oxide. *Nano Lett.* **12**, 2088–2094 (2012).
415. Kim, K., Choi, J. Y. & Shin, K. S. Enhanced Raman scattering in gaps formed by planar Au and Au/Ag alloy nanoparticles. *J. Phys. Chem. C* **117**, 11421–11427 (2013).
416. Maurer, T., Adam, P. M. & Lévêque, G. Coupling between plasmonic films and nanostructures: From basics to applications. *Nanophotonics* **4**, 363–382 (2015).
417. Dai, F., Horrer, A., Adam, P. M. & Fleischer, M. Accessing the Hotspots of Cavity Plasmon Modes in Vertical Metal–Insulator–Metal Structures for Surface Enhanced Raman Scattering. *Adv. Opt. Mater.* **8**, (2020).
418. Zhang, X. F. *et al.* Detection of melamine in liquid milk using surface-enhanced Ramanscattering spectroscopy. *J. Raman Spectrosc.* **41**, 1655–1660 (2010).
419. He, X., Yang, S., Xu, T., Song, Y. & Zhang, X. Microdroplet-captured tapes for rapid sampling and SERS detection of food contaminants. *Biosens. Bioelectron.* **152**, 112013 (2020).
420. Wong, C. L., Dinish, U. S., Buddharaju, K. D., Schmidt, M. S. & Olivo, M. Surface-enhanced Raman scattering (SERS)-based volatile organic compounds (VOCs) detection using plasmonic bimetallic nanogap substrate. *Appl. Phys. A* **117**, 687–692 (2014).
421. Lv, L. *et al.* In situ surface-enhanced Raman spectroscopy for detecting microplastics and nanoplastics in aquatic environments. *Sci. Total Environ.* **728**, 138449 (2020).
422. Peláez, E. C. *et al.* Detection and Quantification of HspX Antigen in Sputum Samples Using Plasmonic Biosensing: Toward a Real Point-of-Care (POC) for Tuberculosis Diagnosis. *ACS Infect. Dis.* **6**, 1110–1120 (2020).
423. Rickard, J. J. S. *et al.* Rapid optofluidic detection of biomarkers for traumatic brain injury via surface-enhanced Raman spectroscopy. *Nat. Biomed. Eng.* **4**, 610–623 (2020).
424. Rovey, J. L., Friz, P. D., Hu, C., Glascock, M. S. & Yang, X. Plasmonic force space propulsion. *J. Spacecr. Rockets* **52**, 1163–1168 (2015).
425. Lakowicz, J. R. *et al.* Advances in Surface-Enhanced Fluorescence. **14**, 425–441 (2004).
426. Mei, Z. & Tang, L. Surface-Plasmon-Coupled Fluorescence Enhancement Based on Ordered Gold Nanorod Array Biochip for Ultrasensitive DNA Analysis. *Anal. Chem.* **89**, 633–639 (2017).
427. Fu, Y. & Lakowicz, J. R. Enhanced fluorescence of Cy5-labeled oligonucleotides near silver Island films: A distance effect study using single molecule spectroscopy. *J. Phys. Chem. B* **110**, 22557–22562 (2006).
428. Konradi, R., Textor, M. & Reimhult, E. Using complementary acoustic and optical techniques for quantitative monitoring of biomolecular adsorption at interfaces. *Biosensors* **2**, 341–376 (2012).
429. Laschitsch, A., Menges, B. & Johannsmann, D. Simultaneous determination of optical and acoustic thicknesses of protein layers using surface plasmon resonance spectroscopy and quartz crystal microweighing. *Appl. Phys. Lett.* **77**, 2252–2254 (2000).
430. Komorek, P., Wałek, M. & Jachimska, B. Mechanism of lysozyme adsorption onto gold surface determined by quartz crystal microbalance and surface plasmon resonance. *Bioelectrochemistry* **135**, 107582 (2020).
431. Dahlin, A. B. *et al.* Synchronized quartz crystal microbalance and nanoplasmonic sensing of biomolecular recognition reactions. *ACS Nano* **2**, 2174–2182 (2008).
432. Jonsson, M. P., Jönsson, P. & Höök, F. Simultaneous nanoplasmonic and quartz crystal microbalance sensing: Analysis of biomolecular conformational changes and quantification of the bound molecular mass. *Anal. Chem.* **80**, 7988–7995 (2008).
433. Zhu, J., Huang, S., Ye, J., Zhang, X. & Liu, G. Design of a quartz crystal with transparent electrode used for both QCM-D and LSPR technology. *Sensors Actuators, A Phys.* **229**, 141–146 (2015).
434. Hao, D., Hu, C., Grant, J., Glidle, A. & Cumming, D. R. S. Hybrid localized surface plasmon resonance and quartz crystal microbalance sensor for label free biosensing. *Biosens. Bioelectron.* **100**, 23–27 (2018).
435. Briand, E., Zäch, M., Svedhem, S., Kasemo, B. & Petronis, S. Combined QCM-D and EIS study of supported lipid bilayer formation and interaction with pore-forming peptides. *Analyst* **135**, 343–350 (2010).
436. Rodenhausen, K. B. *et al.* Combined optical and acoustical method for determination of thickness and porosity of transparent organic layers below the ultra-thin film limit. *Rev. Sci. Instrum.* **82**, 103111 (2011).

437. Francis, L. A., Friedt, J.-M., Zhou, C. & Bertrand, P. In situ evaluation of density, viscosity, and thickness of adsorbed soft layers by combined surface acoustic wave and surface plasmon resonance. *Anal. Chem.* **78**, 4200–4209 (2006).
438. Bender, F. *et al.* Development of a combined surface plasmon resonance/surface acoustic wave device for the characterization of biomolecules. *Meas. Sci. Technol.* **20**, 124011 (2009).
439. Friedt, J. M. *et al.* Simultaneous surface acoustic wave and surface plasmon resonance measurements: Electrodeposition and biological interactions monitoring. *J. Appl. Phys.* **95**, 1677–1680 (2004).
440. Sonato, A. *et al.* A surface acoustic wave (SAW)-enhanced grating-coupling phase-interrogation surface plasmon resonance (SPR) microfluidic biosensor. *Lab Chip* **16**, 1224–1233 (2016).
441. Mecea, V. M. From quartz crystal microbalance to fundamental principles of mass measurements. *Anal. Lett.* **38**, 753–767 (2005).
442. Standford Research Systems. Quartz crystal microbalance theory and calibration. *Tech. Reports* **408**, 744–9040 (2004).
443. Dinda, S. *et al.* Quantitative detection with surface enhanced raman scattering (SERS) using self-assembled gold nanoparticle cluster arrays. *Aust. J. Chem.* **66**, (2013).
444. Yap, F. L., Thoniyot, P., Krishnan, S. & Krishnamoorthy, S. Nanoparticle cluster arrays for high-performance SERS through directed self-assembly on flat substrates and on optical fibers. *ACS Nano* **6**, (2012).
445. Johnson, W. L., France, D. C., Rentz, N. S., Cordell, W. T. & Walls, F. L. Sensing bacterial vibrations and early response to antibiotics with phase noise of a resonant crystal. *Sci. Rep.* **7**, 1–12 (2017).
446. Suresh, V., Madapusi, S. & Krishnamoorthy, S. Hierarchically built hetero-superstructure arrays with structurally controlled material compositions. *ACS Nano* **7**, 7513–7523 (2013).
447. Suresh, V., Huang, M. S., Srinivasan, M. P. & Krishnamoorthy, S. In situ synthesis of high density sub-50 nm zno nanopatterned arrays using diblock copolymer templates. *ACS Appl. Mater. Interfaces* **5**, 5727–5732 (2013).
448. Weber, P.C., Ohlendorf, D.H, Wendolski, J.J., Salemme, F. R. Structural Origins of High-Affinity Biotin Binding to Streptavidin. *Am. Assoc. Adv. Sci.* **243**, 85–88 (2016).
449. Reimhult, K., Petersson, K. & Krozer, A. QCM-D analysis of the performance of blocking agents on gold and polystyrene surfaces. *Langmuir* **24**, 8695–8700 (2008).
450. Pieczonka, N. P. W., Goulet, P. J. G. & Aroca, R. F. Applications of the enhancement of resonance Raman scattering and fluorescence by strongly coupled metallic nanostructures. *Top. Appl. Phys.* **103**, 197–216 (2006).
451. Zhang, Y., Dragan, A. & Geddes, C. D. Wavelength dependence of metal-enhanced fluorescence. *J. Phys. Chem. C* **113**, 12095–12100 (2009).
452. Erickson, H. P. Size and shape of protein molecules at the nanometer level determined by sedimentation, gel filtration, and electron microscopy. *Biol. Proced. Online* **11**, 32–51 (2009).
453. Seifert, M., Rinke, M. T. & Galla, H. J. Characterization of streptavidin binding to biotinylated, binary self-assembled thiol monolayers - Influence of component ratio and solvent. *Langmuir* **26**, 6386–6393 (2010).
454. Azzaroni, O., Mir, M. & Knoll, W. Supramolecular architectures of streptavidin on biotinylated self-assembled monolayers. Tracking biomolecular reorganization after bioconjugation. *J. Phys. Chem. B* **111**, 13499–13503 (2007).
455. Rodríguez-Pardo, L., Rodríguez, J. F., Gabrielli, C., Perrot, H. & Brendel, R. Sensitivity, noise, and Resolution in QCM sensors in liquid media. *IEEE Sens. J.* **5**, 1251–1256 (2005).
456. Pan, Y., Zhang, D., Yang, P., Poon, L. L. M. & Wang, Q. Viral load of SARS-CoV-2 in clinical samples. *Lancet Infect. Dis.* **20**, 411–412 (2020).
457. Rusling, J. F., Kumar, C. V., Gutkind, J. S. & Patel, V. Measurement of biomarker proteins for point-of-care early detection and monitoring of cancer. *Analyst* **135**, 2496–2511 (2010).
458. Soler, M., Huertas, C. S. & Lechuga, L. M. Label-free plasmonic biosensors for point-of-care diagnostics: a review. *Expert Rev. Mol. Diagn.* **19**, 71–81 (2019).
459. Masson, J. F. Surface Plasmon Resonance Clinical Biosensors for Medical Diagnostics. *ACS Sensors* **2**, 16–30 (2017).
460. Ejeian, F. *et al.* Biosensors for wastewater monitoring: A review. *Biosens. Bioelectron.* **118**, 66–79 (2018).
461. He, X., Yang, S., Xu, T., Song, Y. & Zhang, X. Microdroplet-captured tapes for rapid sampling and SERS detection of food contaminants. *Biosens. Bioelectron.* **152**, 112013 (2020).
462. Khansili, N., Rattu, G. & Krishna, P. M. Label-free optical biosensors for food and biological sensor applications. *Sensors Actuators, B Chem.* **265**, 35–49 (2018).
463. Wong, C. L., Dinish, U. S., Schmidt, M. S. & Olivo, M. Non-labeling multiplex surface enhanced

Raman scattering (SERS) detection of volatile organic compounds (VOCs). *Anal. Chim. Acta* **844**, 54–60 (2014).
464. Spencer, K. M., Sylvia, J. M., Marren, P. J., Bertone, J. F. & Christesen, S. D. Surface-enhanced Raman spectroscopy for homeland defense. *Chem. Biol. Point Sensors Homel. Def.* **5269**, 1 (2004).
465. Micsa, C. *et al.* Surface Enhanced Raman Scattering in surgery and forensics. *Int. Conf. Transparent Opt. Networks* **2016-Augus**, 16–19 (2016).
466. Fikiet, M. A. *et al.* Surface enhanced Raman spectroscopy: A review of recent applications in forensic science. *Spectrochim. Acta - Part A Mol. Biomol. Spectrosc.* **197**, 255–260 (2018).
467. Xu, H., Bjerneld, E. J., Käll, M. & Börjesson, L. Spectroscopy of single hemoglobin molecules by surface enhanced raman scattering. *Phys. Rev. Lett.* **83**, 4357–4360 (1999).
468. Delfino, I., Bizzarri, A. R. & Cannistraro, S. Time-dependent study of single-molecule SERS signal from yeast cytochrome c. *Chem. Phys.* **326**, 356–362 (2006).
469. Chen, H. Y., Lin, M. H., Wang, C. Y., Chang, Y. M. & Gwo, S. Large-Scale Hot Spot Engineering for Quantitative SERS at the Single-Molecule Scale. *J. Am. Chem. Soc.* **137**, 13698–13705 (2015).
470. Garoli, D., Yamazaki, H., MacCaferri, N. & Wanunu, M. Plasmonic Nanopores for Single-Molecule Detection and Manipulation: Toward Sequencing Applications. *Nano Lett.* **19**, 7553–7562 (2019).
471. Liao, P. F. & Wokaun, A. Lightning rod effect in surface enhanced Raman scattering. *J. Chem. Phys.* **76**, 751–752 (1982).
472. Hatab, N. A. *et al.* Free-standing optical gold bowtie nanoantenna with variable gap size for enhanced Raman spectroscopy. *Nano Lett.* **10**, 4952–4955 (2010).
473. Li, J. *et al.* Large enhancement and uniform distribution of optical near field through combining periodic bowtie nanoantenna with rectangular nanoaperture array. *Opt. Lett.* **36**, 4014 (2011).
474. Baumberg, J. J., Aizpurua, J., Mikkelsen, M. H. & Smith, D. R. Extreme nanophotonics from ultrathin metallic gaps. *Nat. Mater.* **18**, 668–678 (2019).
475. Guerrini, L. & Graham, D. Molecularly-mediated assemblies of plasmonic nanoparticles for Surface-Enhanced Raman Spectroscopy applications. *Chem. Soc. Rev.* **41**, 7085–7107 (2012).
476. Chikkaraddy, R. *et al.* Single-molecule strong coupling at room temperature in plasmonic nanocavities. *Nature* **535**, 127–130 (2016).
477. Li, M. *et al.* Three-dimensional hierarchical plasmonic nano-architecture enhanced surface-enhanced Raman scattering immunosensor for cancer biomarker detection in blood plasma. *ACS Nano* **7**, 4967–4976 (2013).
478. Mitsuishi, M. *et al.* Nanoscale actuation of thermoreversible polymer brushes coupled with localized surface plasmon resonance of gold nanoparticles. *Langmuir* **23**, 7472–7474 (2007).
479. Tokarev, I., Tokareva, I. & Minko, S. Gold-nanoparticle-enhanced plasmonic effects in a responsive polymer gel. *Adv. Mater.* **20**, 2730–2734 (2008).
480. Wang, C. *et al.* Stimuli-responsive plasmonic core-satellite assemblies: I-motif DNA linker enabled intracellular pH sensing. *Chem. Commun.* **49**, 5739–5741 (2013).
481. Lu, Y. & Lal, A. High-efficiency ordered silicon nano-conical-frustum array solar cells by self-powered parallel electron lithography. *Nano Lett.* **10**, 4651–4656 (2010).
482. Schneider, C. A., Rasband, W. S. & Eliceiri, K. W. NIH Image to ImageJ: 25 years of image analysis. *Nat. Methods* **9**, 671–675 (2012).
483. Krishnamoorthy, S., Manipaddy, K. K. & Yap, F. L. Wafer-level self-organized copolymer templates for nanolithography with sub-50 nm feature and spatial resolutions. *Adv. Funct. Mater.* **21**, (2011).
484. Chilkoti, A. & Stayton, P. S. Molecular Origins of the Slow Streptavidin—Biotin Dissociation Kinetics. *J. Am. Chem. Soc.* **117**, 10622–10628 (1995).
485. Bakker, R. M. *et al.* Enhanced localized fluorescence in plasmonic nanoantennae. *Appl. Phys. Lett.* **92**, (2008).
486. Sha, M. Y., Penn, S., Freeman, G. & Doering, W. E. Detection of human viral RNA via a combined fluorescence and SERS molecular beacon assay. *NanoBioTechnology* **3**, 23–30 (2007).
487. Sabanayagam, C. R. & Lakowicz, J. R. Increasing the sensitivity of DNA microarrays by metal-enhanced fluorescence using surface-bound silver nanoparticles. *Nucleic Acids Res.* **35**, 1–9 (2007).
488. Dos Santos, D. S. & Aroca, R. F. Selective surface-enhanced fluorescence and dye aggregation with layer-by-layer film substrates. *Analyst* **132**, 450–454 (2007).
489. Guerrero, A. R. & Aroca, R. F. Surface-enhanced fluorescence with shell-isolated nanoparticles (SHINEF). *Angew. Chemie - Int. Ed.* **50**, 665–668 (2011).

Rishabh RASTOGI

Doctorat : Matériaux, Mécanique, Optique, Nanotechnologie

Année 2020

Points chauds électromagnétiques conçus pour la détection biologique par spectroscopie améliorée par plasmon

La détection nanoplasmonique repose sur des champs électromagnétiques exaltés à proximité de la surface des métaux nanostructurés pour détecter les molécules à des concentrations ultra-faibles. Les exaltations de champ sont fortement prononcées aux jonctions entre les nanostructures adjacentes, ce qui entraîne des points chauds. Les exaltations de champ en ces points chauds augmentent de façon non linéaire en fonction des distances jusqu'au régime inférieur à 10nm. Les analytes présents à ces lacunes peuvent tirer parti de ces exaltations de champ, résultant en une sensibilité ultra-élevée dans la détection. Toutefois, ces lacunes de champ confiné affectent la capacité des grands analytes tels que les biomolécules d'entrer et de tirer ainsi parti des champs EM dans les lacunes. Cela présente des besoins spatiaux pour exalter les champs EM en contradiction avec ceux pour accueillir les interactions biomoléculaires. Cette thèse démontre la conception rationnelle des configurations de réseaux qui permet aux *hotspots* EM d'être mieux exploités par le témoin de l'événement de liaison biomoléculaire. La thèse utilise l'approche moléculaire basée sur l'auto-assemblage pour fabriquer des nanoréseaux plasmoniques reproductibles sur des plaquettes complètes. Plusieurs paramètres sont envisagés, y compris la dimension, la forme et la densité des points chauds, la fonctionnalisation de surface, et le choix des substrats, pour démontrer la détection quantitative des molécules jusqu'aux concentrations picomolaires.

Mots clés : nanoantennas optiques – spectroscopies exaltées de surface – nanophotonique – résonance plasmonique de surface – lithographie – champs électromagnétiques – nanoparticules.

Engineered Electromagnetic Hot-spots for Highly Sensitive (Bio)molecular Detection by Plasmonic Spectrocopies

Nanoplasmonic sensing relies on enhanced electromagnetic fields at the vicinity of nanostructured metal surface to detect molecules at ultra-low concentrations. The EM enhancements are strongly pronounced at junctions between adjacent nanostructures resulting in gap hot-spots. EM enhancements at these hot-spots increase non-linearly as a function of gap distances down to sub-10 regime. Analyte present at these gaps can leverage these EM enhancements, resulting in ultra-high sensitivity in detection. However, such confining gaps affect the ability of large analytes such as biomolecules to enter and thereby leverage EM fields within the gaps. This presents spatial needs to enhance EM fields at odds with those for accommodating biomolecular interactions. This thesis demonstrates the rational design of array configurations that allows the EM hotspots to be better leveraged by the reporter of biomolecular binding event. The thesis uses molecular self-assembly based approach to fabricate reproducible plasmonic nanoarrays on full wafers. Multiple parameters are considered including the dimension, shape, and density of hotspots, surface functionalization, and the choice of substrates, to demonstrate quantitative detection of molecules down to picomolar concentrations.

Keywords: optical nanoantennas – surface-enhanced spectroscopy – nanophotonics – surface plasmon resonance – lithography – electromagnetic fields – nanoparticles.

Thèse réalisée en partenariat entre :

LUXEMBOURG INSTITUTE OF SCIENCE AND TECHNOLOGY | LIST

utt UNIVERSITÉ DE TECHNOLOGIE TROYES

Ecole Doctorale "Sciences pour l'Ingénieur"